Effectively Exploring New Physics: A first EFT interpretation using the $WZ \to \ell\nu\ell\ell$ process with the ATLAS detector at the LHC

by

Maheyer Jamshed Shroff
B.Sc., University of Toronto, 2018
M.Sc., University of Victoria, 2020

A Dissertation Submitted in Partial Fulfillment of the
Requirements for the Degree of

DOCTOR OF PHILOSOPHY

in the Department of Physics and Astronomy

We acknowledge and respect the Lək̓ʷənən (Songhees and Xʷsepsəm/Esquimalt) Peoples on whose territory the university stands, and the Lək̓ʷənən and W̱SÁNEĆ Peoples whose historical relationships with the land continue to this day.

Effectively Exploring New Physics: A first EFT interpretation using the $WZ \to \ell\nu\ell\ell$ process with the ATLAS detector at the LHC

by

Maheyer Jamshed Shroff
B.Sc., University of Toronto, 2018
M.Sc., University of Victoria, 2020

Supervisory Committee

Dr. R. McPherson, Co-Supervisor
(Department of Physics and Astronomy)

Dr. R. Keeler, Co-Supervisor
(Department of Physics and Astronomy)

Dr. I. Trigger, Committee Member
(Department of Physics and Astronomy)

Dr. C. Bohne, Committee Member
(Department of Chemistry)

Abstract

The Standard Model (SM) of particle physics, while highly successful, has known limitations. The decoupling theorem and the effective principle guide Beyond the SM Physics research by allowing us to describe dynamics at relevant length scales without fully understanding smaller-scale interactions. The Standard Model Effective Field Theory (SMEFT) builds on these concepts, treating the SM as a low-energy approximation of a deeper, more fundamental theory. This fundamental theory introduces new heavy particles at a higher energy scale, Λ. By integrating out these beyond-the-Standard-Model (BSM) particles, SMEFT offers a model-independent way to describe their potential effects.

This thesis focuses on electroweak processes involving the coupling of the W and Z bosons, where both bosons decay into leptonic final states. The data used to perform this analysis correspond to the full ATLAS Run-2 dataset, collected from 2015 to 2018, and correspond to an integrated luminosity of 139 fb^{-1} and a centre-of-mass energy of $\sqrt{s} = 13$ TeV.

Multiple kinematic and angular observables are used to constrain the strength of ten SMEFT parameters that affect the WZ channel. Additionally, the thesis includes a study of the interference between different EFT operators, which is a novel contribution to the WZ channel. The results are interpreted in the context of comparing data with the SMEFT predictions and exclusion limits are set at 95% confidence level. No significant deviation from the Standard Model is observed for most of the 1D and 2D particle-level fits. Strong constraints on `cW` and `cHj3` have been obtained across all observables.

These results provide a deeper understanding of potential deviations from the Standard Model and contribute to the ongoing search for new physics.

Table of Contents

List of Tables

List of Figures

Acknowledgements

The work presented in thesis would not be possible without the support and help of several people.

Professor R. Keeler, Thank you very much for everything. Having you as both my Masters and PhD supervisor has been the biggest blessing in my graduate career. Your enthusiasm and knowledge for physics, as well as your patience to teach has been very inspiring. Throughout my time, you have acted as a father figure to me. Thank you very much for going beyond the call of duty to help support and mentor me. I very much appreciate it.

Professor R. McPherson, Thank you very much for your expert input and your continued support in allowing me to grow professionally. I truly appreciate your constant encouragement and always looking out for me.

Professor I. Trigger, Thank you very much for your in depth insight into my work and the analysis in general. Your incredible help and review has made this thesis a million times better. Thank you for always supporting me.

UVic Postdocs, local and at CERN, Merci beaucoup **Clément Camincher**. Je regarde avec beaucoup d'émotion notre séjour au CERN, rempli de travail acharné et de crêpes. Tu es une véritable inspiration. Thank you **Joseph Lambert**, for sharing your knowledge about physics and life in general, sprinkled with your characteristic humour. Thank you **José Pretel** for your support throughout the analysis.

The UVic Physics community, From the faculty to the front-office staff to the janitorial staff, thank you so much for your constant encouragement, warmth and love. For the past eight years, UVic Physics has been home, and I have been very privileged to be part of this wonderful community.

My office-mates, friends, and peers, Thank you for putting up with me! The last few years have been very special, and I truly cherish the memories with all of you. A special shout-out to my roommates: **Juan José Alberto "Robos" Nava Rayo Aquino Jesús Alejandro** and **Charlie "Shunga" Chen**. I'm going to miss you guys! Thank you to **Juan Cristóbal Rivera** as well, who has been in the trenches with me and made life much easier.

My parents, my sister and my family, For their never ending love.

Who determined the path of the sun and stars?
Who is it by whom the moon waxes and wanes again?
Who created waters and plants?
Who bestowed swiftness in the wind and clouds?
Yasna 44.3-44.4

Dedication

To my future nieces and nephews,

“Yours is the Earth and everything that’s in it...”

Declaration

This thesis is a final work as Partial Fulfilment of the Requirements for the Degree of PhD of Science in the Department of Physics and Astronomy at the University of Victoria. Work in this thesis has been been focused mainly on the ATLAS analysis that the author has been a part of. Further work on hardware upgrades that the author has been a part of has also been added to the Appendix of this thesis.

The research presented in this thesis is based on data form the ATLAS experiment at the LHC. ATLAS is a global collaboration of physicists, engineers, technicians, students, and support staff. The collective effort of over 5500 members enables the operation of the experiment, including data collection, software development, and hardware maintenance.

The author has been an active member of the ATLAS WZ leptonic analysis group, a team of approximately 15 members, working collaboratively within the ATLAS collaboration. The SMEFT interpretation of the WZ process has been more localised, involving the University of Victoria group, composed of around 7 members. The collective work of these teams has shaped the direction and scope of the analysis.

The author of this thesis inherited the Inclusive particle level selection code, which he has since modified to suit the requirements of the analysis. The full reconstruction and selection machinery in the analysis has been setup by more senior members of the WZ team. The author was however involved and performed small-scale productions with this machinery. The author also provided modifications to this machinery by adding special angular observables that were used for this study.

The fitting package used in this thesis, `EFTFun`, was pre-existing software built for the ATLAS collaboration's use. While the author did not develop this package, they made minor plotting adjustments to align with the analysis goals.

The author of this thesis has been completely responsible for the production of state-of-the-art 0+1j merged EFT Monte Carlo samples. These samples provided the theoretical predictions used throughout the analysis. The author was solely responsible for their production, validation using NLO generators such as SMEFTatNLO, and ensuring their adequacy for the study.

The author has also been responsible for performing sensitivity studies in an attempt to narrow down which EFT coefficients to study.

Together with his collaborators, the author of this thesis had played a major role producing 1D limits for EFT coefficients, a subsect of the results presented in this document.

Work that is completely novel in this thesis is the introduction of interferences between different EFT dimension-6 operators among themselves and how this could alter predictions. For the first time in the WZ channel at the LHC, 2D limits, constraining two EFT coefficients at a time are provided in this work. This has been the defining work of the author of this thesis, with the guidance of their supervisors and other collaborators. Results of this analysis are to be published in two different formats (both of which have the author of this thesis credited as a core contributor) :

- ATLAS Collaboration. SMEFT reinterpretation of fully leptonic WZ channel production using ATLAS data, **ATLAS Publication Note**, *In progress (Expected Late summer 2025)*
- ATLAS Collaboration. *Measurements and interpretations of $W^{\pm}Z$ production cross-sections in pp collisions at $\sqrt{s} = 13$ TeV with the ATLAS detector*. **arXiv:2507.03500** (submitted to the Journal of High Energy Physics (JHEP), July 2025).

On the hardware side, the Injector Project has been part of the contributions made by the University of Victoria to the ATLAS Liquid Argon Sub-detector group. It has been designed from scratch primarily by the author of this thesis, with the guidance of their supervisor, UVic Staff, and other LASP Firmware group members. It has also been maintained by the author of this thesis. The author of this thesis also performed crucial on-site integration tasks during a 14 month stint at CERN. The author acted as the primary contact for LASP Firmware needs on site. Integration work that has been highlighted in Appendix G of the thesis includes the expert contribution of several LASP members, including the author of this thesis. This has resulted in the following single-author publication:

> Maheyer Shroff. Development of the ATLAS Liquid Argon Calorimeter Readout Electronics for the HL-LHC. *Proceedings of Science*, **EPS-HEP2023**:528, 2024. doi:10.22323/1.449.0528.

All of the work in this document has been written by the author of the thesis. Chapters 1–4 introduce theory and detector material from published sources. Chapter 5 outlines the analysis strategy; its core concepts stem from the WZ analysis team, of which the author is a member. Chapter 6 develops the mathematical framework and modelling applied by the author, while SM predictions from `MATRIX` shown there were produced by WZ collaborators. Chapters 7–9 (figures and tables included) are exclusively done by the author of the thesis, unless otherwise noted.

CHAPTER 1

Introduction

For millennia, humanity has been driven by an insatiable curiosity to understand the fundamental building blocks of nature and the forces that they interact with. In contemporary fundamental physics, two cornerstone theories describe our understanding of all four known fundamental interactions in the universe. Einstein's General Relativity (GR) elegantly describes gravity as the curvature of spacetime caused by mass and energy [1], while the Standard Model of Particle Physics (SM) successfully characterizes the electromagnetic, weak, and strong nuclear forces [2–5].

The Standard Model has not only endured numerous experimental tests over the years but has also provided accurate predictions that subsequent experiments validated. A significant achievement for the theory came in 2012 with the discovery of the Higgs boson by the ATLAS [6] and CMS [7] collaborations at the Large Hadron Collider (LHC), representing the latest milestone in its ongoing success. Despite its successes, both theoretical insights and experimental evidence indicate that the Standard Model is only an approximation of a deeper, more fundamental theory of nature.

Physics, in a sense, is effective. For example, when analysing the motion of a projectile, such as a ball thrown into the air, it is not necessary to account for the detailed interactions of air molecules or the atomic structure of the ball. Instead, engineers and physicists rely on the principles of classical mechanics, which use macroscopic parameters like initial velocity, projection angle, gravity, and air resistance to predict the trajectory. This separation of scales, allows one to study phenomena by focusing on the most relevant factors at a particular scale of observation while effectively disregarding details at other scales. The principle of separation of scales is foundational to the development of effective theories in physics. An effective theory describes a system's behaviour accurately within a specific range or scale without needing to account for all underlying interactions [8].

In this spirit, the Standard Model can be viewed as an effective theory — a low energy approximation of a more fundamental framework that may contain new, yet-undiscovered particles at

a higher energy scale Λ. One powerful approach to systematically explore deviations from the Standard Model is the Standard Model Effective Field Theory (SMEFT) [9], in which higher-dimensional operators are introduced to parameterise potential effects of new physics. These additional operators modify Standard Model interactions. One such interaction includes the triple-gauge coupling (TGC), which governs the behaviour of the electroweak bosons. While the SM explicitly predicts specific, non-zero values for these couplings based on its gauge symmetry, deviations from these predictions (termed anomalous TGCs, aTGCs) can signal potential Beyond the Standard Model (BSM) physics [10, 11].

One of the most promising processes to probe such deviations is the production of WZ boson pairs in proton–proton collisions, specifically in the fully leptonic decay channel, $pp \to WZ \to \ell\nu\ell\ell$. This process is particularly sensitive to modifications in electroweak interactions and can provide insight into the structure of the WWZ triple-gauge coupling. By studying kinematic distributions of the bosons, as well as angular observables related to the decay products of the bosons, it is possible to identify subtle effects that may indicate physics beyond the Standard Model. At high boson energies, new physics contributions could manifest as deviations in the measured cross-section, even if direct discoveries remain out of reach at current collider energies.

This thesis uses the full dataset collected by the ATLAS detector during Run-2 of the LHC (2015–2018), corresponding to an integrated luminosity of 139 fb^{-1} at a centre-of-mass energy of 13 TeV. By analysing both kinematic and angular distributions, this work provides a detailed SMEFT interpretation of the WZ process, not only considering interference between SMEFT and Standard Model operators at first order but also including for the first time, second-order effects where SMEFT operators interact with each other. The use of several angular distributions offers a novel way to probe triple-gauge couplings, as these observables remain independent of boosts.

Through this approach, this study aims to set constraints on relevant SMEFT operators by quantifying the allowed ranges of the strength of new physics effects. In doing so, it contributes to the wider effort to uncover possible physics beyond the Standard Model.

Chapter 2 lays down the foundational theory of the Standard Model, the Effective Field framework and the principles underlying Monte Carlo simulations of collision events. Chapter 2 is completed by a specific focus on the W and Z bosons and their interactions within the Standard Model.

Chapter 3 describes the experimental setup of the LHC and the ATLAS detector that is used to obtain the data from which the interpretation is done.

Chapter 4 explains the methods and algorithms used by the ATLAS collaboration to reconstruct physics objects from raw detector information.

Chapter 5 details the analysis methodology for identifying candidate signal events, including

strategies to address background processes with similar detector signatures. It further explains the observables used to quantify the signal and the systematic uncertainties impacting the measurement.

Chapter 6 provides an overview of the modelling of observables within the SMEFT framework and the statistical modelling used to analyse the collected data and perform statistical inference on physics theories. The setup, generation and validation of the Monte-Carlo samples is also described in this chapter.

Chapter 7 presents comprehensive studies done to select only the EFT operators most sensitive to our channel of interest. Sensitivity studies of the physical observables are also reported in this chapter. This chapter also highlights the effects of the novel cross-terms, and their significance in the total observable distribution. Finally, this chapter is completed by an important validation study that justifies the use of the EFT samples that were generated.

Chapter 8 presents the results and the SMEFT interpretation of the ATLAS Run-2 dataset in the WZ channel. Both 1D and the novel 2D particle-level limits are presented in this chapter.

Chapter 9 provides the conclusions and the outlook of the thesis.

CHAPTER 2

Theory of the Standard Model and Effective Fields

The Standard Model (SM) [2–5, 12, 13] is the cornerstone of modern particle physics, providing a framework to describe all of the elementary particles and the fundamental forces through which the particles can interact. It has been developed through decades of collaboration between theory and experiment, representing one of the most successful scientific endeavours in history. This chapter provides the theoretical foundations of the SM and its limitations. The chapter then provides an introduction to Effective Field Theories. These theories offer a systematic approach to explore deviations from SM predictions and identify potential extensions to our current understanding. Finally, an overview of proton–proton collisions, data from which are used in this thesis, is provided.

2.1 The Standard Model of Particle Physics

The SM is a relativistic quantum field theory that describes the fundamental particles and their interactions. It is based on the principle of local gauge invariance under the symmetry group [12]

$$SU(3)_C \times SU(2)_L \times U(1)_Y \quad , \tag{2.1}$$

which governs the strong, weak, and electromagnetic forces, and is further explained in this chapter.

2.1.1 Particle constituents

In quantum field theory, particles are understood as excitations of underlying fields. This perspective unifies particle physics by describing interactions as exchanges of quanta associated with these fields. A summary of all the SM particles is given in Figure 2.1.

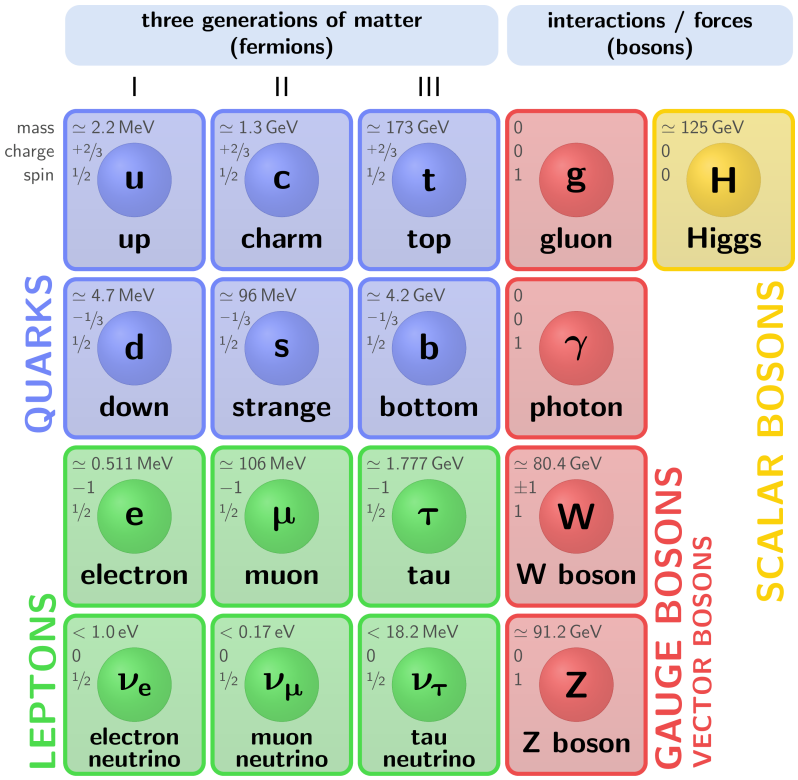

Figure 2.1: *Particle content of the Standard Model (SM). Each type of quark exists in one of three colour charges. For each fermion, there is a corresponding anti-particle with exactly the same mass but with opposite quantum numbers. Taken from [14].*

Forces: The SM encompasses three of the four fundamental forces of nature: electromagnetism, the strong nuclear force, and the weak nuclear force. These forces are mediated by gauge bosons, while gravity remains outside the scope of the model due to the lack of a consistent quantum theory of gravitation.

Fermions: Matter is composed of fermions, which are particles with half-integer spin ($s = 1/2$) that obey the Pauli exclusion principle. Fermions are divided into two categories: quarks and leptons. Quarks exist in six flavours—up, down, charm, strange, top, and bottom—and carry colour charge, allowing them to interact via the strong force. They combine to form composite particles called either mesons or baryons. Leptons include the electron, muon, tau, and their corresponding neutrinos. Unlike quarks, leptons do not carry colour charge, and so do not participate in strong interactions. Electrons, muons and tau leptons do, however, carry an electric charge of -1, whereas neutrinos are electrically neutral. Fermions are organised into three generations, with increasing mass from one generation to the next. Stable matter consists primarily of first-generation fermions, while higher-generation particles decay into lighter ones.

Each fermion has a corresponding antiparticle with identical mass but opposite charges.

Bosons: The interactions between particles are mediated by gauge bosons. The photon is responsible for electromagnetic interactions between charged particles and is massless. The gluons mediate the strong interaction between quarks by exchanging colour charge; there are eight distinct gluons, all of which are massless. The $W^{\pm}$ and Z^0 bosons mediate weak interactions and acquire mass through electroweak symmetry breaking (EWSB).

The Higgs Boson: The Higgs boson plays a pivotal role in the Standard Model as it provides mass to other particles via their interactions with the Higgs field. This electrically neutral scalar particle emerges from EWSB and does not mediate any fundamental force.

2.1.2 Quantum Electrodynamics

Quantum Electrodynamics (QED) [15, 16] is the first step toward the modern SM and describes the interaction between light and matter. This theory is based on the $U(1)$ gauge symmetry, which requires a massless vector field A_μ corresponding to the photon. Photons interact with fermions, with the interaction strength determined by the electric charge of the fermions (q_f). The QED Lagrangian is given by:

$$\mathcal{L}_{\text{QED}} = \underbrace{-\frac{1}{4}F^{\mu\nu}F_{\mu\nu}}_{\text{free photon}} + \underbrace{\sum_f \bar{\psi}_f\big(i\gamma^\mu D_\mu - m_f\big)\psi_f}_{\text{free fermions + interactions}}, \tag{2.2}$$

where $F_{\mu\nu}$ is the electromagnetic field tensor defined as $F_{\mu\nu} = \partial_\mu A_\nu - \partial_\nu A_\mu$, ψ_f represents the Dirac spinor for the fermion f, and m_f is the mass of the fermion. $\sum_f$ runs over all fermion flavours. The covariant derivative D_μ is defined as $D_\mu = \partial_\mu - iq_f A_\mu$. The gamma matrices, γ^μ, also known as Dirac matrices, satisfy the Clifford algebra and are used to construct the generators of the Lorentz group.

2.1.3 Quantum Chromodynamics

The strong force in the standard model is described by Quantum Chromodynamics (QCD) [17], based on the SU(3) colour gauge group. This non-Abelian group has 8 massless spin-1 force carriers, called gluons. The fundamental charge associated with this symmetry group is called colour and comes in 3 types: ‘red’, ‘green’, and ‘blue’. Analogous to QED, colour takes the role of charge.

Quarks $q_f(x)$ are the only matter field that interacts via the strong force. The covariant derivative associated with a local $SU(3)$ symmetry is given by $D_\mu = \partial_\mu - ig_S G^a_\mu \frac{\lambda^a}{2}$ where g_S is the coupling constant of the strong interaction (or equivalently the strong coupling $\alpha_s = \frac{g_s^2}{4\pi}$), G^a_μ are the eight gluon gauge fields, and λ^a are the Gell-Mann matrices. The Lagrangian for QCD is expressed as

$$\mathcal{L}_{\text{QCD}} = -\frac{1}{4} G^a_{\mu\nu} G^{a\mu\nu} + \sum_f \bar{q}_f(x) \left(i\gamma^\mu D_\mu - m_f\right) q_f(x). \tag{2.3}$$

The first term (the kinetic term) introduces self-interactions among the gluon fields.

QCD exhibits two defining phenomena: colour confinement and asymptotic freedom. The non-Abelian nature of $SU(3)$ causes gluon self-interactions, leading to a running coupling constant α_s. At high energies (short distances), α_s decreases, allowing quarks to behave as free particles — a property known as asymptotic freedom. At low energies (large distances), α_s increases, confining quarks into colour-neutral bound states such as mesons (quark-antiquark pairs) and baryons (three quarks). This behaviour ensures that free particles with net colour charge do not exist in nature.

2.1.4 Electroweak theory

The Standard Model unifies electromagnetic and weak interactions under the $SU(2)_L \otimes U(1)_Y$ gauge symmetry [2, 18]. The conserved quantum numbers of this symmetry are weak isospin T_3 and weak hypercharge Y, related to electric charge Q by:

$$Q = T_3 + \frac{1}{2} Y \tag{2.4}$$

It has been experimentally observed [19] that weak interactions with a change in the fermion charge show a $V - A$ structure, which means they only couple to left-handed fermions. It is therefore convenient to introduce the left-handed and right-handed projection operators, that split the fields of the interacting particles into their left and right handed chiral components:

$$\psi = P_L\psi + P_R\psi = \frac{1-\gamma^5}{2}\psi + \frac{1+\gamma^5}{2}\psi = \psi_L + \psi_R \,. \tag{2.5}$$

Under the $SU(2)_L$ symmetry, left-handed fermions form isospin doublets with $T_3 = \pm\frac{1}{2}$:

$$\begin{pmatrix} u \\ d \end{pmatrix}_L, \begin{pmatrix} \nu_e \\ e \end{pmatrix}_L, \qquad \begin{pmatrix} c \\ s \end{pmatrix}_L, \begin{pmatrix} \nu_\mu \\ \mu \end{pmatrix}_L, \qquad \begin{pmatrix} t \\ b \end{pmatrix}_L, \begin{pmatrix} \nu_\tau \\ \tau \end{pmatrix}_L, \tag{2.6}$$

while right-handed fermions are $SU(2)_L$ singlets ($T_3 = 0$):

$$u_R, d_R, e_R \qquad , c_R, s_R, \mu_R \qquad , t_R, b_R, \tau_R. \tag{2.7}$$

Right handed neutrinos were not required in the original SM model, but are generally included following the discovery of massive neutrinos. It should also be noted that in the SM, charged lepton flavour is conserved whilst quark flavour is not. The flavour mixing is given by the Cabibbo-Kobayashi-Maskawa Matrix (CKM-Matrix) [20, 21].

2.1.5 *Electroweak Symmetry Breaking*

The charged fermions and the $W^{\pm}$ and Z bosons have been observed to possess non-negligible mass. This necessitates the inclusion of mass terms in the SM Lagrangian. The Brout-Englert-Higgs model was formulated as a way to solve the mass problem. The model introduces a new complex scalar field (called the Higgs field), which couples to the gauge bosons

$$H = \begin{pmatrix} \phi^+(x) \\ \phi^0(x) \end{pmatrix}. \tag{2.8}$$

The simplest potential of the Higgs field, H, can be written as

$$V(H) = \mu^2 H^\dagger H \ + \lambda \left(H^\dagger H\right)^2. \tag{2.9}$$

where μ and λ are coupling parameters. The shape of this potential depends on the sign of μ^2.

For $\mu^2 < 0$, the potential has a non-zero ground state that does not have the $SU(2)_L \otimes U(1)_Y$ gauge symmetry i.e the ground states are not explicitly invariant under the gauge symmetry. the potential forms a "ring" of minima at a radius given by $v = \sqrt{-\frac{\mu^2}{2\lambda}}$, where v is known as the vacuum expectation value (vev) of the field H. By choosing one ground state, the symmetry is broken as shown in Figure 2.2, where B could be anywhere around that ring-shaped minimum: choosing a place for B breaks the symmetry. This is referred to as Spontaneous Symmetry Breaking [2, 4, 22]. If $\mu^2 > 0$, the potential has a single unique minimum that is symmetric about this point, preventing spontaneous symmetry breaking.

During Electroweak symmetry breaking, the $SU(2)_L \otimes U(1)_Y$ group is spontaneously broken into $U(1)_{\text{QED}}$. This gives rise to three bosonic vector fields W^a_μ, where $a = 1, 2, 3$. The first two components of the W_μ fields mix to create the two charged bosons $W^{\pm}$ which can be written as:

$$W^{\pm}_\mu = \frac{1}{\sqrt{2}} \left(W^1_\mu \mp i W^2_\mu\right). \tag{2.10}$$

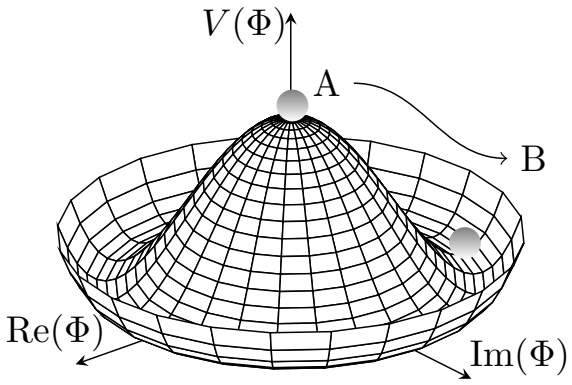

Figure 2.2: *Plot of the Higgs potential as a function of the Higgs Field H (shown as Φ in the diagram). The symmetry is spontaneously broken by choosing an arbitrary ground state B, from an initial state A.*

The B_μ field and the W^3_μ field also mix to create the Z boson and A_μ, the latter of which can be identified with the physical gauge boson of the photon γ:

$$A_\mu = W^3_\mu \sin\theta_W + B_\mu \cos\theta_W, \tag{2.11}$$

$$Z_\mu = W^3_\mu \cos\theta_W - B_\mu \sin\theta_W, \tag{2.12}$$

where θ_W is the weak mixing angle, also called the Weinberg angle. The angle $\sin(\theta_W)$ can be expressed in terms of the coupling strengths for $SU(2)_L$ and $U(1)_Y$ (g and g', respectively) as

$$\sin(\theta_W) = \frac{g'}{\sqrt{g^2 + g'^2}} = \frac{e}{g}\,, \tag{2.13}$$

and e is the electric charge. The quantities θ_W and e are measured.

The boson masses can then be deduced to be

$$m_W = \frac{gv}{2}, \quad m_Z = \frac{v}{2}\sqrt{g^2 + g'^2} = \frac{gv}{2\cos\theta_W}, \quad m_A = 0, \quad m_H = \sqrt{-2\mu^2}. \tag{2.14}$$

Fermion masses

Similarly, if the Higgs field is allowed to couple with fermion fields through a Yukawa term then it allow the fermions to have masses as well, while respecting gauge invariance.

After symmetry breaking, the Yukawa Lagrangian can be written as:

$$\mathcal{L}_{\text{yukawa}} = -\frac{v+h}{\sqrt{2}} \sum_f y_f \bar{\psi}^f_L \psi^f_R\,, \tag{2.15}$$

where y_f is the fermion specific Yukawa couplings. The fermion mass can be expressed in terms of the Yukawa coupling and the vacuum expectation value of the Higgs field v as

$$m_f = \frac{1}{\sqrt{2}} v y_f. \tag{2.16}$$

2.1.6 Complete SM Lagrangian

Adding the pieces of the theories described, the full SM Lagrangian can be written as:

$$\begin{aligned}
\mathcal{L}_{\text{SM}} &= \mathcal{L}_{\text{QCD}} + \mathcal{L}_{\text{EW}} + \mathcal{L}_{\text{Higgs}} + \mathcal{L}_{\text{Yukawa}} \\
&= -\frac{1}{4} G^a_{\mu\nu} G^{a\mu\nu} \\
&\quad - \frac{1}{4} W^j_{\mu\nu} W^{j\mu\nu} - \frac{1}{4} B_{\mu\nu} B^{\mu\nu} + \sum_f \left(i\bar{\psi}_L \gamma^\mu D^L_\mu \psi_L + i\bar{\psi}_R \gamma^\mu D^R_\mu \psi_R \right) \\
&\quad + (D_\mu H)^\dagger D^\mu H - \mu^2 H^\dagger H - \lambda (H^\dagger H)^2 \\
&\quad - \sum_f \left(y_f \bar{\psi}^f_L H \psi^f_R + \text{h.c.} \right)
\end{aligned} \tag{2.17}$$

The field strength tensors are defined as:

$$W^j_{\mu\nu} = \partial_\mu W^j_\nu - \partial_\nu W^j_\mu - g\epsilon^{jkl} W^k_\mu W^l_\nu, \qquad j,k,l \in \{1,2,3\}, \tag{2.18}$$

$$B_{\mu\nu} = \partial_\mu B_\nu - \partial_\nu B_\mu, \tag{2.19}$$

$$G^a_{\mu\nu} = \partial_\mu G^a_\nu - \partial_\nu G^a_\mu - g_s f^{abc} G^b_\mu G^c_\nu, \qquad a,b,c \in \{1,2,...,8\}. \tag{2.20}$$

The terms involving ϵ^{jkl} and f^{abc} contain implicit sums over similar indices, where ϵ^{jkl} and f^{abc} are the structure constants of $SU(2)_L$ and $SU(3)_C$, respectively. The sum over f in the Dirac term contains all the left-handed doublet and right-handed singlet fermion spinors. The covariant derivative D_μ takes the form:

$$D_\mu = \partial_\mu + ig' \frac{Y}{2} B_\mu + ig \frac{\sigma_a}{2} W^a_\mu + ig_S G^a_\mu \frac{\lambda^a}{2} \tag{2.21}$$

2.1.7 Gauge boson couplings

The W and Z bosons can couple to fermions as described in the Lagrangian Eq 2.17 to form a three point vertex as shown in Figure 2.3. The coupling strengths are also indicated.

Figure 2.3: *Three point vertices for the electroweak bosons and their coupling strengths. c_V is the vector coupling, $c_V = T_3 - 2Q\sin^2\theta_W$ and c_A is the axial-vector coupling $c_A = T_3$. Taken from [23].*

The W boson only couples to left-handed fermions (and right-handed anti-fermions), which is manifested by the left-chiral projection operator $P_L = \frac{1}{2}(1-\gamma^5)$.

The Z boson can couple to both left-handed and right-handed fermions, because Z_μ is a mixture of the W^3_μ and B_μ fields. The coupling strengths are conveniently written in terms of the vector coupling, $c_V = T_3 - 2Q\sin^2\theta_W$ and the axial-vector coupling, $c_A = T_3$.

Gauge boson self interactions

The interaction term in Lagrangian Eq 2.17 (first line) results in the self-couplings of the bosons called triple (TGC) and quartic (QGC) gauge couplings. The possible couplings are shown in Figure 2.4. It should be noted that the ZZZ interaction (along with all other neutral TGC and QGC combinations) is forbidden in the SM.

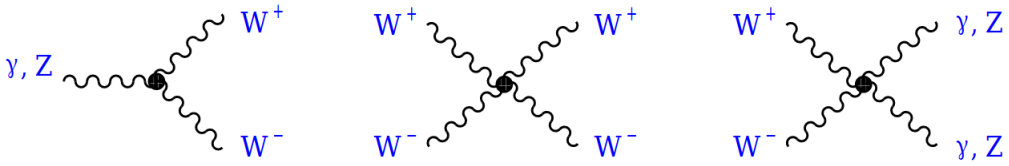

Figure 2.4: *Gauge boson self-interaction vertices [24]. The last diagram illustrates that $WWZZ$, $WW\gamma\gamma$ and $WW\gamma Z$ interactions are allowed.*

The strengths of the gauge couplings are specified by the Standard Model. For the WWZ/γ vertices which are closely related to the subject of this work:

$$g_{WW\gamma} = -e\,, \qquad g_{WWZ} = -e\cot\theta_W\,. \tag{2.22}$$

Any deviations from the predictions will affect the boson pair cross section. Measuring the production of the boson pair therefore provides a stringent test of the electroweak part of the SM.

2.2 Unanswered questions in the SM

Despite being the most successful model in particle physics, the Standard Model still cannot account for several observed phenomena. Below is a short list of the limitations of the SM:

- **Gravity:** The Standard Model does not include the force of gravity. Gravity, which is described by General Relativity, is still not unified with quantum field theory [25].
- **Neutrino Masses:** The Standard Model originally assumed neutrinos to be massless. However, the discovery of neutrino oscillations proved that neutrinos have small but nonzero masses [26, 27]. The Standard Model does not naturally explain the origin of the tiny neutrino masses.
- **Dark Matter:** Astrophysical and cosmological observations for e.g [28] have shown the presence of dark matter, which is unexplained in the Standard Model.
- **Matter-Antimatter Asymmetry:** In the physical world, we know that there is a major imbalance between matter and antimatter proportions [29]. The Standard Model is not able to explain the observed imbalance in the universe
- **Dark energy:** Cosmological observations [30] have shown that the universe is expanding at a accelerating rate. This rate is attributed to an unexplained property of space-time called dark energy, which is estimated to make up around 68 percent of the energy in the universe. Yet there is no explanation of such an energy in the Standard Model.
- **Hierarchy Problem:** The Higgs boson's observed mass is puzzlingly light—quantum corrections would naively drive it to extremely high energies (e.g., Planck scale), requiring an unnatural fine-tuning of parameters to match its measured value [31].

2.3 Effective Field Theory

A *theory of everything* is the Holy Grail of theoretical particle physics, which would unify the Quantum Field Theory (SM) and Einstein's gravity. This theory would be valid at all energy scales and would be UV-complete. However, this ambitious search for a theory of everything has significantly slowed down [32].

The decoupling theorem [33], states that if the energy scale of physics is far greater than the probed energy, the heavy fields effectively decouple in processes with no outgoing heavy particles.

This principle has now guided the focus of theorists and phenomenologists alike to search instead for *theories of something*, which describe physical systems at a particular energy scale. These are called *Effective field theories* (EFTs), as they are not meant to be valid at all energy scales, and the degrees of freedom they describe are more "effective" than fundamental.

EFTs can be viewed as the low-energy limit of a more complete theory. The low-energy behaviour of the full theory is determined by integrating out the heavy fields when they appear as internal components (or propagators) in Feynman diagrams, resulting in effective interactions that involve only the light fields.

A classical example of this is the Fermi theory describing β-decay [34], where in the low-energy limit the massive W boson is integrated out and a simple four-point interaction term arises. While Fermi originally applied it to nuclear β-decay, the same effective interaction also predicts muon decay. This example is detailed in Appendix A.

2.3.1 The Standard Model as an Effective theory

The Standard Model describes all the known elementary particles and the forces between them, and does correctly predict the cross-sections and differential distributions of particles produced in high-energy collisions [35]. However, as shown in Chapter 2.2, we know that the Standard Model is incomplete.

Given the lack of any direct or indirect collider evidence for new physics, it is plausible to consider models where new particles are either too massive to be produced at current collider energies or interact very weakly with the SM. Under this assumption, the SM can be viewed as a low-energy limit of a more complete theory.

In scenarios where Beyond the Standard Model (BSM) particles are considerably heavier than the electroweak scale, their effects can be described in a model-independent manner using EFT methods. The most popular framework for this approach is known as the Standard Model EFT (SMEFT) [9, 36]. SMEFT integrates out heavy BSM particles, encoding their effects through higher-dimensional operators that modify SM interactions.

SMEFT has the same local $SU(3) \times SU(2) \times U(1)$ symmetry as the SM, with the vev of the Higgs field breaking the $SU(2)$ symmetry. Retaining only the SM's field content and gauge symmetry, SMEFT forgoes renormalizability and instead systematically includes every higher mass dimensional D operator allowed by those symmetries.

The SMEFT Lagrangian can therefore be written as an extension of the SM Lagrangian (Eq 2.17) as:

$$\mathcal{L}_{\text{SMEFT}} = \mathcal{L}_{\text{SM}} + \frac{1}{\Lambda}\sum_i c_i^{(5)}\mathcal{O}_i^{D=5} + \frac{1}{\Lambda^2}\sum_i c_i^{(6)}\mathcal{O}_i^{D=6} + \frac{1}{\Lambda^3}\sum_i c_i^{(7)}\mathcal{O}_i^{D=7} + \frac{1}{\Lambda^4}\sum_i c_i^{(8)}\mathcal{O}_i^{D=8} + \ldots \quad (2.23)$$

where $\mathcal{O}_i^D$ is a gauge invariant operator of mass dimension D constructed from the SM fields and required to be invariant under local gauge transformations of the SM symmetry group. The parameters $c_i^{(D)}$are called the Wilson coefficients. These Wilson coefficients can be experimentally measured which would test the presence of their respective operators. Non-zero Wilson coefficients would be signs of new physics.

Note that the leading order term does not contain any dependence on Λ, while the other terms are suppressed by the appropriate powers of the energy scale of new physics, Λ. This is the mass scale at which the new particles are integrated out of the theory.

The leading-order term is the SM Lagrangian which comprises operators of mass dimension $D = 4$. The mass dimensions of the fields, in natural units ($\hbar = c = 1$), can be deduced from the requirement that each term in the Lagrangian must also have mass dimension four:

$$\begin{aligned}
[D_\mu] &= 1\ , && \text{(by definition)} \\
\left[D_\mu H^\dagger D^\mu H\right] &= 4 \ \Rightarrow\ [H] = 1\ , \\
[X_{\mu\nu}X^{\mu\nu}] &= 4 \ \Rightarrow\ [X_{\mu\nu}] = 2 \ \Rightarrow\ [X_\mu] = 1\ , \\
\left[\overline{\psi} D_\mu \psi\right] &= 4 \ \Rightarrow\ [\psi] = \frac{3}{2}\ , \\
\left[\overline{\psi} y_L H \psi\right] &= 4 \ \Rightarrow\ [y_L] = 0\ .
\end{aligned} \quad (2.24)$$

Here, H denotes the Higgs doublet, X_μ is a generic gauge field with associated field strength tensor $X_{\mu\nu}$, ψ represents a fermion field, and y_L is the Yukawa coupling constant.

2.3.2 *Higher order operators*

Dimension 5 operators

The leading correction to the SM has dimension 5, where there is only one single operator, called the Weinberg operator [37]:

$$\mathcal{L}_5 \ = \ \frac{c}{\Lambda}\left(\widetilde{L}\, H\right)\left(\widetilde{H}^\dagger\, L\right), \quad (2.25)$$

where L is the lepton doublet, H is the Higgs doublet.

This operator violates lepton number conservation, $\Delta L = 2$. The most important effect of the Weinberg operator is the appearance of Majorana-type neutrino masses after electroweak

symmetry breaking [38]. Neutrino oscillation experiments tell us that at least two masses of the neutrino are non-zero, and at least one must be equal or larger than 0.06 eV. The scale of new physics from this term therefore can be deduced as (taking $c = 1$):

$$\Lambda \approx \frac{v^2}{m_\nu} \geq 10^{15} \text{ GeV} , \tag{2.26}$$

where v is the vacuum expectation energy (vev) of the Higgs field and m_v is the mass of the neutrino.

This scale of new physics would make the effect of dimension-5 operator practically unobservable in collider experiments and will not be considered further in this thesis.

Dimension-6 operators

The next leading contribution comes from the dimension-6 operators. There are 2499 dimension-6 operators that conserve baryon and lepton number [39]. A need for a complete and non-redundant set of operators has been highlighted as different higher-dimensional operators can produce the same S-matrix elements for SM particle scattering if they can be related through equations of motion, integration by parts, field redefinitions, or Fierz transformations. This results in complex and sometimes unexpected relationships between operators.

Many dimension-6 operators are redundant as they can be expressed as linear combinations of others. Removing these redundant operators simplifies the EFT description and provides a clear mapping from observables to the EFT Wilson coefficients. The first minimal, non-redundant operator basis for $\mathcal{L}^{(6)}$ is referred to as the "Warsaw basis" [39], consisting of 59 independent operators.

The full list of dimension-6 operators in the Warsaw basis is given in Appendix B [40]. A brief explanation of the categories is given below.

- **Boson Self-interaction terms (X^3, H^6)** - These operators describe the boson self-interactions, which give rise to vertices involving three or more bosons. The gluon self-interaction and its CP-odd counterpart are denoted as Q_G and $Q_{\tilde{G}}$. Similarly, the electroweak boson self-interaction and its CP-odd counterpart are denoted as Q_W and $Q_{\tilde{W}}$. The Higgs boson self-coupling operator is Q_H, which affects the minimum of the Higgs potential and changes the vev.

- **Higgs Boson Kinetic term (H^4D^2)** - These operators affect the kinetic terms of the scalar fields. The main consequence of these operators is that the Wilson coefficients are recast into an overall rescaling of all SM Higgs couplings.

- **Higgs Gauge (X^2H^2)** - Upon Electroweak Symmetry Breaking (EWSB), the operators $Q_{HG}, Q_{HW}, Q_{HB}, Q_{HWB}$ induce corrections to the kinetic terms of the gauge boson indicated by the 2nd subscript. The first three lead to overall rescaling of the kinetic term of the gauge boson, while Q_{HWB} introduces a kinetic mixing between the B and W^3 fields. As a result, Q_{HWB} modifies all γ and Z couplings.

- **Yukawa operators (ψ^2H^3)** - Upon EWSB, these operators modify the Yukawa interaction with the Higgs boson, thus modifying both the fermion masses and their Yukawa couplings to the Higgs boson. The fermion couplings to the Higgs boson now are not just proportional to the fermion masses like in the SM, but also depend on the strength of these operators.

- **Higgs-fermion (ψ^2H^2D)** After EWSB, these operators introduce modifications to the Higgs and fermion coupling terms. These therefore cause modifications in both the Higgs and electroweak sector.

- **Dipole moment (ψ^2XH)** These operators contribute to the anomalous magnetic and electric dipole moments of all fundamental particles.

- **Four fermion (ψ^4)** These operators model point interactions and affect different possible quartets of fermions. They are divided by fermions chirality as $(\bar{L}L)(\bar{L}L), (\bar{R}R)(\bar{R}R)$, $(\bar{L}L)(\bar{R}R)$ and the mixed $(\bar{L}R)(\bar{R}L) + (\bar{L}R)(\bar{L}R)$

2.3.3 Flavour symmetries in Dimension-6 operators

Without any flavour symmetry, there are 1350 CP-even and 1149 CP-odd independent dimension-6 operators in the SMEFT Lagrangian. Constraining such a large parameter space is challenging. In particular, experimental observations cannot differentiate the flavour of underlying light quarks that participate in high-energy processes. This introduces a flavour symmetry, which can reduce the number of operators. It should be noted that these symmetries are not necessarily fundamental symmetries of the underlying complete theory, but could be accidental.

The following flavour symmetries [40] considered in this thesis are listed below:

- Maximal $U(3)^5$ symmetry: This flavour symmetry consists of the largest group of transformations compatible with the gauge symmetries of the SM (assuming no right-handed neutrinos):

$$U(3)^5 = \underbrace{U(3)_{Q_L}}_{\substack{\text{Left-handed}\\ \text{quark doublets}}} \times \underbrace{U(3)_{u_R}}_{\substack{\text{Right-handed}\\ \text{up-type quarks}}} \times \underbrace{U(3)_{d_R}}_{\substack{\text{Right-handed}\\ \text{down-type quarks}}} \times \underbrace{U(3)_{L_L}}_{\substack{\text{Left-handed}\\ \text{lepton doublets}}} \times \underbrace{U(3)_{e_R}}_{\substack{\text{Right-handed}\\ \text{charged leptons}}}$$

In the limit where the Yukawa couplings are small, $U(3)^5$ essentially states that fermions with the same electroweak quantum numbers are not distinguished by gauge interactions.

- `topU3l`: Because the top and bottom quarks are experimentally distinguishable, it is reasonable to assume that they are different than the other lighter quarks. This flavour symmetry imposes separate operators for modelling top and bottom quarks.
- `top`: This is the least restrictive scheme where all leptons are distinguishable from each other, in addition to the separate operators for parameterising top and bottom quarks.

The number of parameters for each flavour assumption is given in Table 2.1.

	$U(3)^5$		topU3l		top		general	
	all	$\not{CP}$	all	$\not{CP}$	all	$\not{CP}$	all	$\not{CP}$
X^3	4	2	4	2	4	2	4	2
H^6	1	-	1	-	1	-	1	-
H^4D^2	2	-	2	-	2	-	2	-
X^2H^2	8	4	8	4	8	4	8	4
ψ^2H^3	6	3	10	5	14	7	54	27
ψ^2XH	16	8	28	14	36	18	144	72
ψ^2H^2D	9	1	15	2	21	2	81	30
$(\bar{L}L)(\bar{L}L)$	8	-	16	-	31	-	297	126
$(\bar{R}R)(\bar{R}R)$	9	-	27	2	40	2	450	195
$(\bar{L}L)(\bar{R}R)$	8	-	31	4	54	4	648	288
$(\bar{L}R)(\bar{L}R), (\bar{L}R)(\bar{R}L)$	14	7	40	20	64	32	810	405
total	85	25	182	53	275	71	2499	1149

Table 2.1: *Number of independent parameters for each class of dimension-6 operators as defined in the Warsaw basis under different flavour assumptions. $\not{CP}$ categorises those operators that violate Charge-Parity (CP).Taken from [40].*

2.3.4 Input parameters in SMEFT

The Standard Model can generate accurate predictions only when certain parameters, determined through experiments, are provided as inputs. Assuming all three neutrinos are massive, a total of 26 input parameters are needed [41].

The Lagrangian parameters are determined by imposing a set of defining conditions that relate them to (pseudo-)observables. For a Lagrangian with N independent parameters $g =$

$\{g_i \dots g_N\}$, at least $M \geq N$ independent input observables $\mathcal{O} = \{\mathcal{O}_1 \dots \mathcal{O}_M\}$ need to be selected. By computing each $\mathcal{O}_n$ in the theory at a chosen perturbative order, one obtains the relations

$$\mathcal{O}_n = F_n^{(0)}(g), \quad n = 1 \dots M \tag{2.27}$$

where $F_n^{(0)}$ denotes a function of the parameters g. If $M = N$, the system is invertible and we can recover the measured values of g from functions K of the observables $\mathcal{O}$ as $g_i = K_i^{(0)}(\mathcal{O})$ for $i = 1, \dots, N$.

The Standard Model includes 4 independent parameters describing the electroweak symmetry breaking, $g = \{g, g', v, \lambda\}$. These parameters can be determined by measuring observables from the set $\mathcal{O} = \{\alpha_{\text{em}}, G_F, m_W, m_Z, m_h\}$. The Higgs boson mass m_h is always required to determine λ, but the selection of the remaining three observables is flexible. There are three different schemes available for choosing the electroweak input observables.

SMEFT introduces a large number of additional parameters, namely the cutoff scale Λ and the Wilson coefficients $c_i^{(d)}$. An issue arises because the observables $\mathcal{O}$, which are used to determine the values of the SM parameters g, will also be influenced by contributions from the SMEFT parameters.

Historically, the $\{\alpha_{\text{em}}, G_F, m_Z\}$ set was used and contains the most precisely known parameters from the set. However, m_W in that case receives SMEFT corrections, leading to a highly non-linear dependence of predictions upon Wilson coefficients. The remaining two schemes, $\{\alpha_{\text{em}}, m_W, m_Z\}$ and $\{m_W, m_Z, G_F\}$ are used in SMEFT, both with their downsides. The former has to always consider SMEFT corrections to the Fermi constant G_F. The latter can lead to slightly worse electroweak convergences both in the SM and in SMEFT [41]. The work done in this thesis uses the $\{m_W, m_Z, G_F\}$ scheme.

2.4 Proton–Proton collisions and Monte-Carlo Simulation

The events studied in this thesis consist of highly energetic proton–proton collisions. This section describes the theoretical framework for proton–proton collisions and the Monte-Carlo simulation techniques used to model these complex interactions.

2.4.1 Proton Structure and Parton Distribution Functions

Protons are composite particles comprising two up quarks and one down quark (valence quarks), along with gluons and sea quarks. At high energies, quantum fluctuations generate quark–

antiquark pairs, introducing sea quarks into the proton. The prevalence of gluons and sea quarks increases significantly at higher energy scales, enabling the probing of heavier quarks within the proton.

The internal structure of the proton is parameterised using Parton Distribution Functions (PDFs). A PDF $f_{q/p}(x_q, Q^2)$ represents the probability of finding a parton q (quark or gluon) within the proton carrying a fraction x_q of the proton's longitudinal momentum at an energy scale Q.

PDFs depend on the energy scale Q at which the proton is probed, with this scale dependence governed by the DGLAP equations [42]. To separate perturbative QCD (high-energy) from non-perturbative QCD (low-energy) processes, a factorisation scale μ_F is introduced. This scale determines which interactions are absorbed into the PDFs and which are treated perturbatively. Consequently, PDFs are evaluated at the scale μ_F.

Since PDFs cannot be calculated directly from first principles due to their non-perturbative nature, they are obtained through global fits to experimental data from various processes, such as deep inelastic scattering and proton–proton collisions. Once determined at a reference scale, PDFs can be mathematically evolved to different energy scales.

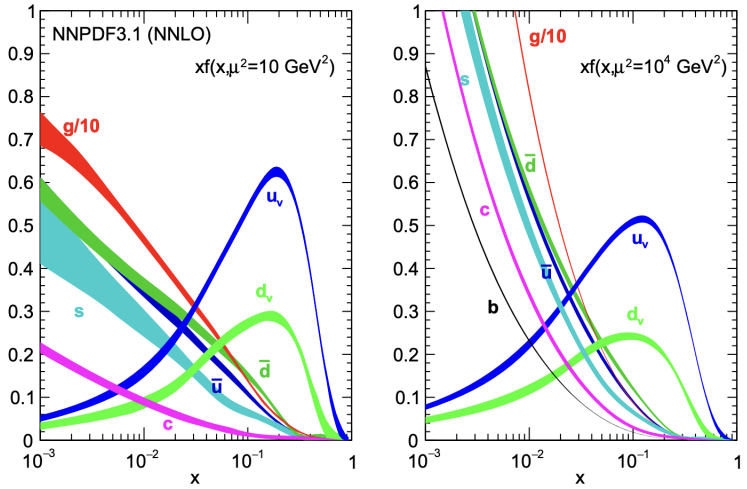

Figure 2.5: *The NNPDF3.1 NNLO PDFs, evaluated at $\mu^2 = 10$ GeV^2 (left) and $\mu^2 = 10^4$ GeV^2 (right). The y-axis represents $xf(x, \mu^2)$, the momentum-weighted parton distribution function. Taken from [43].*

Figure 2.5 illustrates the evolution of PDFs at two different energy scales: 3.16 GeV and 100 GeV. Notable features include a large gluon and sea quark PDF at low momentum fractions and valence quark distributions peaking around $x \approx \frac{1}{3}$.

2.4.2 *Factorisation and Cross-section Calculation*

High-energy proton–proton (pp) collisions primarily involve interactions between individual partons within the protons. Due to asymptotic freedom, these partons behave as nearly free particles at high energies, allowing the application of perturbative QCD.

The factorisation theorem [44] enables the approximation of the overall cross-section as a convolution of parton distribution functions and partonic cross-sections:

$$\sigma(p_A p_B \to X) = \int dx_a \, dx_b \, f_{a/A}(x_a, \mu_F^2) \, f_{b/B}(x_b, \mu_F^2) \, \sigma(q_a q_b \to X; \alpha_s(\mu_R^2), \mu_R^2), \tag{2.28}$$

where:

- $f_{a/A}(x_a, \mu_F^2)$ and $f_{b/B}(x_b, \mu_F^2)$ are the PDFs for partons a and b in protons A and B, evaluated at the factorisation scale μ_F.
- $\sigma(q_a q_b \to X; \alpha_s(\mu_R^2), \mu_R^2)$ is the partonic cross section for the subprocess $q_a q_b \to X$, calculated using perturbative QCD at the renormalisation scale μ_R.
- x_a and x_b are the momentum fractions carried by the partons a and b.
- s is the square of the centre-of-mass energy of the pp system.

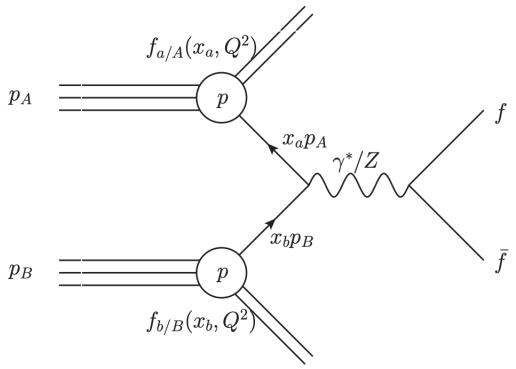

Figure 2.6: *Components of the factorisation formula for the hard scattering cross section yielding the final state $\sigma(pp \to X)$. Taken from [45].*

Figure 2.6 visually represents the elements of Equation 2.28, illustrating how the hard scattering process is combined with the non-perturbative PDFs to yield the overall cross-section for producing a final state X.

2.4.3 *Monte-Carlo Simulation of Proton–Proton Collisions*

In experimental particle physics, theories are verified by simulating events according to theoretical predictions and comparing them with experimental data. Due to the complexities of proton constituents and collision energies, Monte-Carlo (MC) simulations are conducted in a series of steps that model the different aspects of a proton–proton collision.

Figure 2.7 illustrates all the processes involved in a proton–proton collision, including the hard parton-parton interaction, parton showers, hadronisation, and initial and final state radiation.

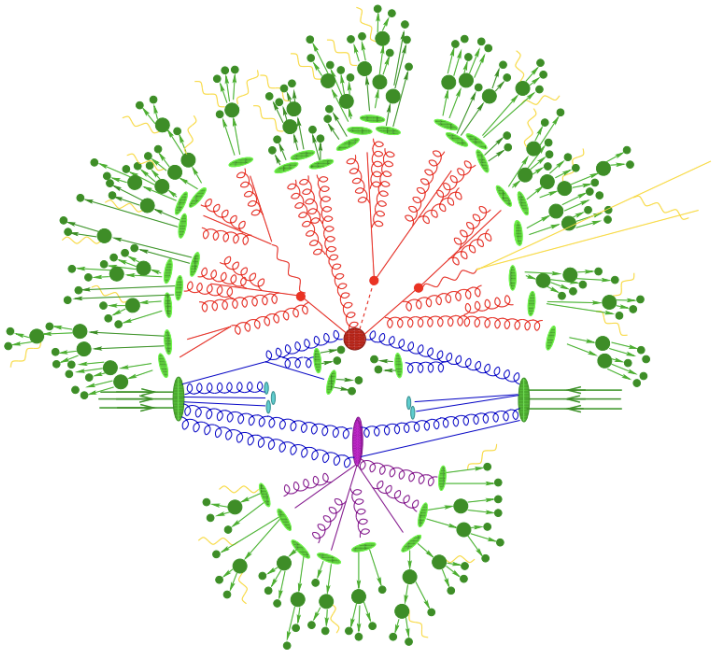

Figure 2.7: *Sketch of a hadron-hadron collision. The red blob in the centre represents the hard collision, surrounded by the parton showers and hard final states resulting from the hard interaction painted red. The purple blob indicates a secondary hard scattering event. Parton-to-hadron transitions are represented by light green blobs, dark green blobs indicate hadron decays, while yellow lines signal soft photon radiation. Taken from [46].*

Hard Proton–Proton Interaction The first simulation step involves the fundamental hard proton–proton collision represented by the red blob in the centre of Figure 2.7. In hard scattering events, which involve large momentum transfers, perturbative QCD can be applied to calculate the partonic cross-sections.

For any given process, the matrix element $\mathcal{M}$ describes the probability amplitude of a transition between initial and final states. MC generators calculate this quantity using Feynman rules

applied to all possible diagrams connecting the two states. When the interaction couplings are less than 1, higher-order diagrams contribute less significantly, allowing a focus on the lowest-order diagrams (leading order, LO). Diagrams including an additional interaction are called next-to-leading order (NLO).

The matrix element feeds into the calculation of the cross-section given in Equation 2.28, where the perturbative (high-energy) regime term

$$\sigma(x_a x_b s, \mu_R^2) \propto \int |\mathcal{M}|^2 d\Phi;, \tag{2.29}$$

and $d\Phi$ represents an infinitesimal phase-space volume. The phase space integration is performed using Monte Carlo methods, after which the phase space is sampled to produce events.

Parton Shower Parton showers, represented by the red lines surrounding the central red blob in Figure 2.7, describe the process where high-energy quarks and gluons emit additional partons as they move apart after a high-energy collision. Typically, only the most energetic QCD emissions (those above the factorisation scale) are included directly in the hard matrix element. The remaining lower-energy emissions are generated using a Markov chain method, where partons are emitted one after another based on splitting functions until their energy becomes too low to continue [47].

Following a hard scattering event, the outgoing partons undergo a series of emissions. Partons may emit gluons, which can split into quark–antiquark pairs or additional gluons. As the energy scale decreases, the strong coupling constant α_s increases, making non-perturbative effects significant. In practice, the parton shower uses a PDF to model initial-state radiation through backward evolution. This PDF is often distinct from the one employed in the hard-scattering matrix element calculation, as the shower typically relies on a leading-order set tuned for compatibility with the shower algorithm and hadronisation model.

Hadronisation The light green blobs in Figure 2.7 represent hadronisation. Due to colour confinement, quarks and gluons produced in hard processes and parton showers cannot be directly observed. Instead, only hadrons or their decay products can be detected. Since hadronisation occurs at low energies where perturbative QCD calculations do not converge, phenomenological models based on experimental data are used to describe this process.

The string model approach [48], implemented in `Pythia`, is commonly employed. In this model, quarks and antiquarks are connected by strings representing the potential energy between them. As the distance between them increases, the potential energy rises. Once this

energy becomes too great, the string breaks, resulting in the formation of a new quark-antiquark pair.

The cascade of emissions and subsequent hadronisation leads to the formation of hadron jets—collimated sprays of hadrons that propagate in the direction of the original partons and are key observables in collider experiments.

Decay Many hadrons produced during hadronisation, along with τ leptons, are unstable and decay either in the beam pipe or inside the detector. These decays also need to be accurately simulated, with careful attention to modelling spin correlations correctly. Dedicated MC packages like `EvtGen` [49] are used for this purpose. The decay process is shown in dark green in the outer layer of Figure 2.7.

Soft Photon Radiation The yellow lines in Figure 2.7 represent QED radiation, which can occur at any stage of event generation where charged particles are present. One approach to simulating this radiation uses an algorithm similar to that used for the QCD shower, modelling the emission of photons by charged particles in a cascading manner where emission is governed by splitting functions.

Underlying Event All processes occurring in the proton–proton collision that are not directly associated with the hard interaction are collectively termed the underlying event. This includes secondary interactions between partons in the protons (shown as the purple blob in Figure 2.7), beam-beam remnants, and initial and final state radiation not related to the hard-scattering event. Since factorisation theorems do not handle this scenario, underlying events are simulated using phenomenological models [50].

Renormalisation and Factorisation Scales Perturbative calculations of the partonic cross-section depend on the renormalisation scale μ_R and the factorisation scale μ_F. While physical observables should be independent of these scales, practical calculations truncated at a finite order in perturbation theory exhibit residual dependencies. Varying μ_R and μ_F within reasonable ranges provides an estimate of the theoretical uncertainties associated with the perturbative expansion.

Monte-Carlo Generator Implementations Modern simulations employ specialised tools for different aspects of collision modelling. `Pythia` [51] implements parton showers using transverse-momentum ordered radiation and hadronisation via the string model. `Sherpa` [52] specialises

in automated merging of multi-jet matrix elements with parton showers through its `OpenLoops` frameworks. For next-to-leading order (NLO) calculations, `aMC@NLO` combines `MadGraph`'s matrix-element generation with phase-space integration [53], while `Powheg` [54–56] provides a matching scheme between NLO computations and parton showers. These generators often interface collaboratively, with `MadGraph/Powheg` typically handling hard process generation and `Pythia` managing the showering and hadronisation processes.

2.5 WZ Production and Decay Dynamics

2.5.1 WZ Production Mechanisms in Proton-Proton Colliders

Leading Order Production

At Leading Order (LO), WZ pairs predominantly form through quark-antiquark ($q\bar{q}$) interactions via three distinct channels shown in Figure 2.8:

- t- **and** u**-channel processes**: Radiation of gauge bosons from initial-state quarks with space-like propagators, where W and Z bosons emerge from separate quark lines
- s**-channel process**: Quark-antiquark annihilation through $W^{\pm}$ propagator that radiates the Z boson via the triple gauge vertex WWZ, producing real (on-shell) W and Z bosons

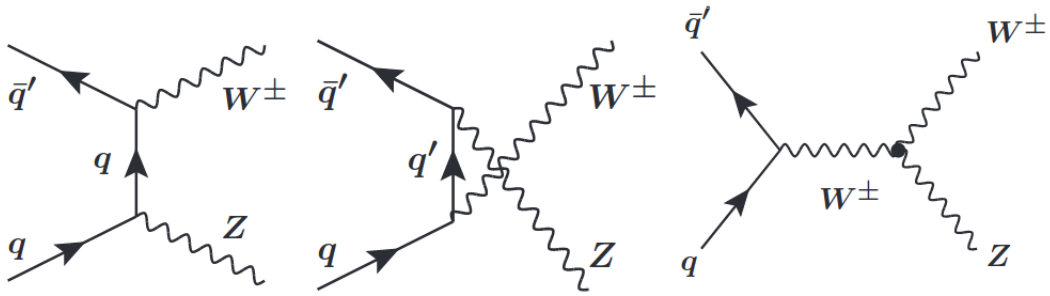

Figure 2.8: *LO Feynman diagrams of WZ production processes in a hadron collider. Taken from [57]. The convention that time increases from left to right is used.*

At LO, a $u\bar{d}$ quark pair produces a $W^{+}Z$ boson pair, while a $d\bar{u}$ quark pair produces a a $W^{-}Z$ boson pair. The u- valence quark density is larger in protons than the d- valence quark density, whilst the $\bar{u}$ and $\bar{d}$ contents in the proton are approximately the same. For this reason, the cross-section for $W^{+}Z$ production is about 30% larger than that for $W^{-}Z$ in pp colliders[58].

Next-to-Leading Order Contributions

NLO processes introduce gluon-initiated production channels critical for precision predictions. These contributions significantly enhance prediction accuracy given gluons' substantial proton momentum fraction, as shown and explained in Figure 2.5. Figure 2.9 shows the Feynman diagrams for WZ production at NLO QCD. Feynman diagrams 2.9(a), 2.9(b), 2.9(c), 2.9(f) and 2.9(g) result in an additional quark in the final state. Feynman diagrams 2.9(d) and 2.9(e) show the $q\bar{q}$ initiated process with gluon bremsstrahlung in the final state. Diagrams 2.9(h) - 2.9(k) are the virtual contributions with internal gluon loops .

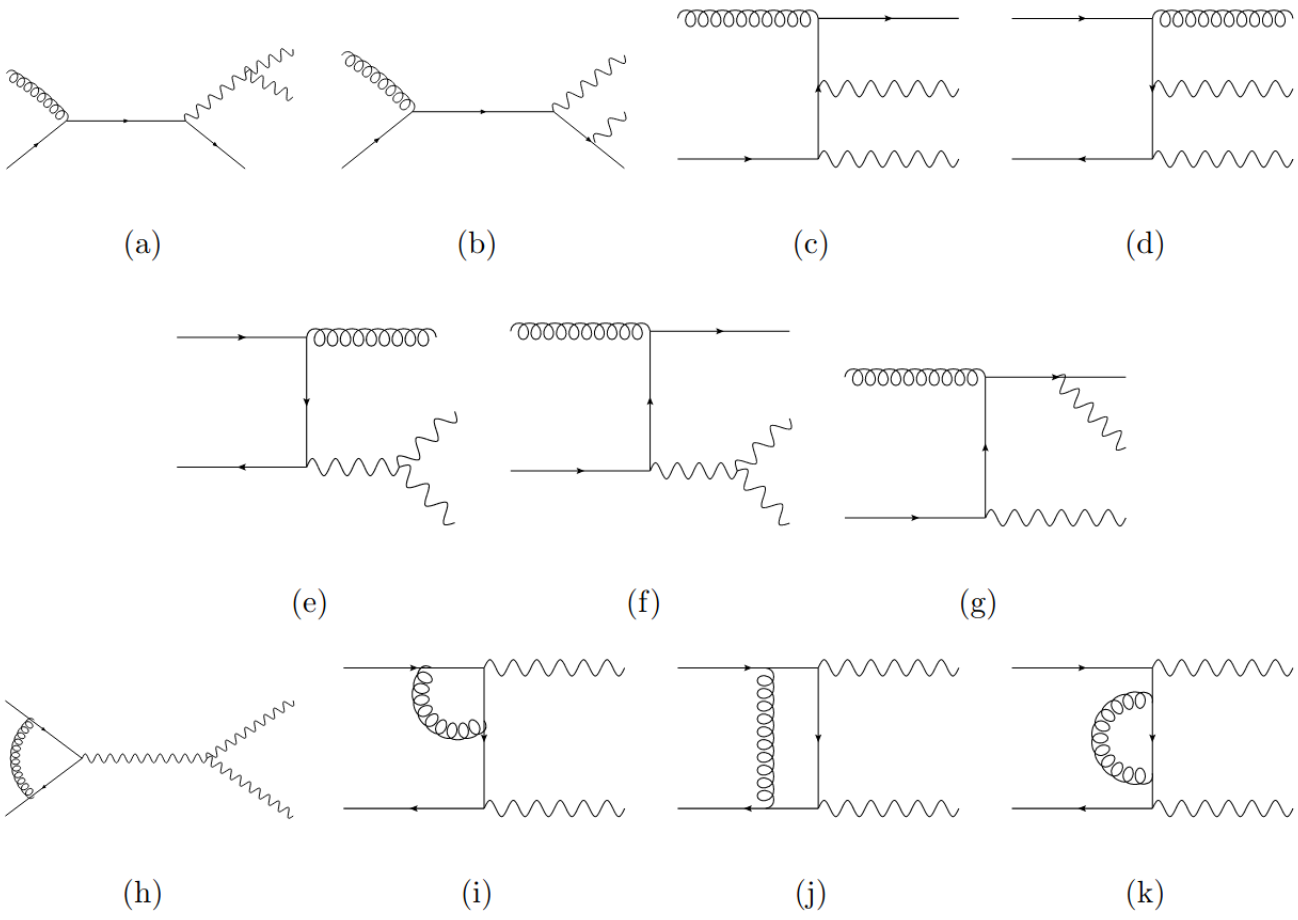

Figure 2.9: *QCD NLO Feynman diagrams for WZ production. Straight lines represent quarks, gluons are shown by spiralling lines, and wavy lines correspond to W or Z bosons. Taken from [59].*

2.5.2 *Decay Characteristics*

Boson Decay Branching Ratios

The W boson decays exclusively to left-handed fermion doublets, while the Z boson couples to both left- and right-handed fermions.

$W^{\pm}$ **Decay Modes**	%
$e^{\pm}\nu$	10.71
$\mu^{\pm}\nu$	10.63
$\tau^{\pm}\nu$	11.38
qq'	67.41

Z **Decay Modes**	%
e^+e^-	3.36
$\mu^+\mu^-$	3.37
$\tau^+\tau^-$	3.37
$q\bar{q}$	69.91
Invisible	20.00

WZ **Combined**	%
$\ell^{\pm}\nu_{\ell}\ell'^{+}\ell'^{-}$ (per flavour combination)	0.35
$\ell^{\pm}\nu_{\ell}$ + invisible (per lepton flavour)	2.18
Hadronic	90.29

Table 2.2: *Measured branching ratios from PDG [42]. Invisible Z decays include $\nu\bar{\nu}$ pairs. Hadronic modes exclude top quarks and contain negligible b-quark content. Prime notation (qq') indicates distinct quark flavours in W decays. The first row in the WZ combined table refers to fully leptonic decays with fixed-flavour configurations (e.g., $W \to e\nu_e$, $Z \to \mu^+\mu^-$). The second row considers $W \to \ell\nu$ for a given lepton flavour, with $Z \to \nu\bar{\nu}$.*

The fully leptonic $WZ \to \ell^{\pm}\nu\ell'^{+}\ell'^{-}$ channel (3.2% total branching fraction) provides clean experimental signatures despite its rarity, enabling precise TGC measurements.

CHAPTER 3

The ATLAS experiment at the Large Hadron Collider

3.1 The Large Hadron Collider

The Large Hadron Collider (LHC) [60] is the world's largest and most powerful particle accelerator and collider, located at CERN (the European Organisation for Nuclear Research) in Geneva. It is a circular collider with a circumference of 26.7 km, situated underground at depths ranging from 45 m to 170 m.

At the LHC, protons are accelerated to unprecedented high energies. Currently, the LHC achieves a centre-of-mass energy of $\sqrt{s} = 13.6$ TeV, colliding protons at four Interaction points (IP). Dedicated experiments are located at each of these interaction points. Two general-purpose detectors, ATLAS [61] and CMS [62], are designed to collect high luminosity data, while the other two IPs have specialised low luminosity experiments: ALICE [63], optimised for measuring heavy ion collisions, and LHCb [64], specialised for b-physics.

3.1.1 The accelerator complex

In the LHC, two proton beams travel in opposite directions at nearly the speed of light, confined to a circular orbit by 1,232 superconducting dipole magnets (8 T field strength, 12000 A current) cooled to 1.9 K with superfluid helium. Quadrupole magnets are used to focus the beams.

Protons are accelerated by 400 MHz RF cavities and collide in bunches of approximately 10^{11} protons [60].

Before injection into the LHC, protons are pre-accelerated by LINAC4[1] (160 MeV), the PS Booster (1.4 GeV), the Proton Synchrotron (PS, 26 GeV), and the Super Proton Synchrotron

[1] LINAC4 succeeded LINAC2 during the 2019–20 shutdown. For data used in this thesis, LINAC2 was operating, accelerating protons to 50 MeV.

(SPS, 450 GeV). A diagram of the CERN accelerator facilities and the LHC accelerator chain is shown in Figure 3.1.

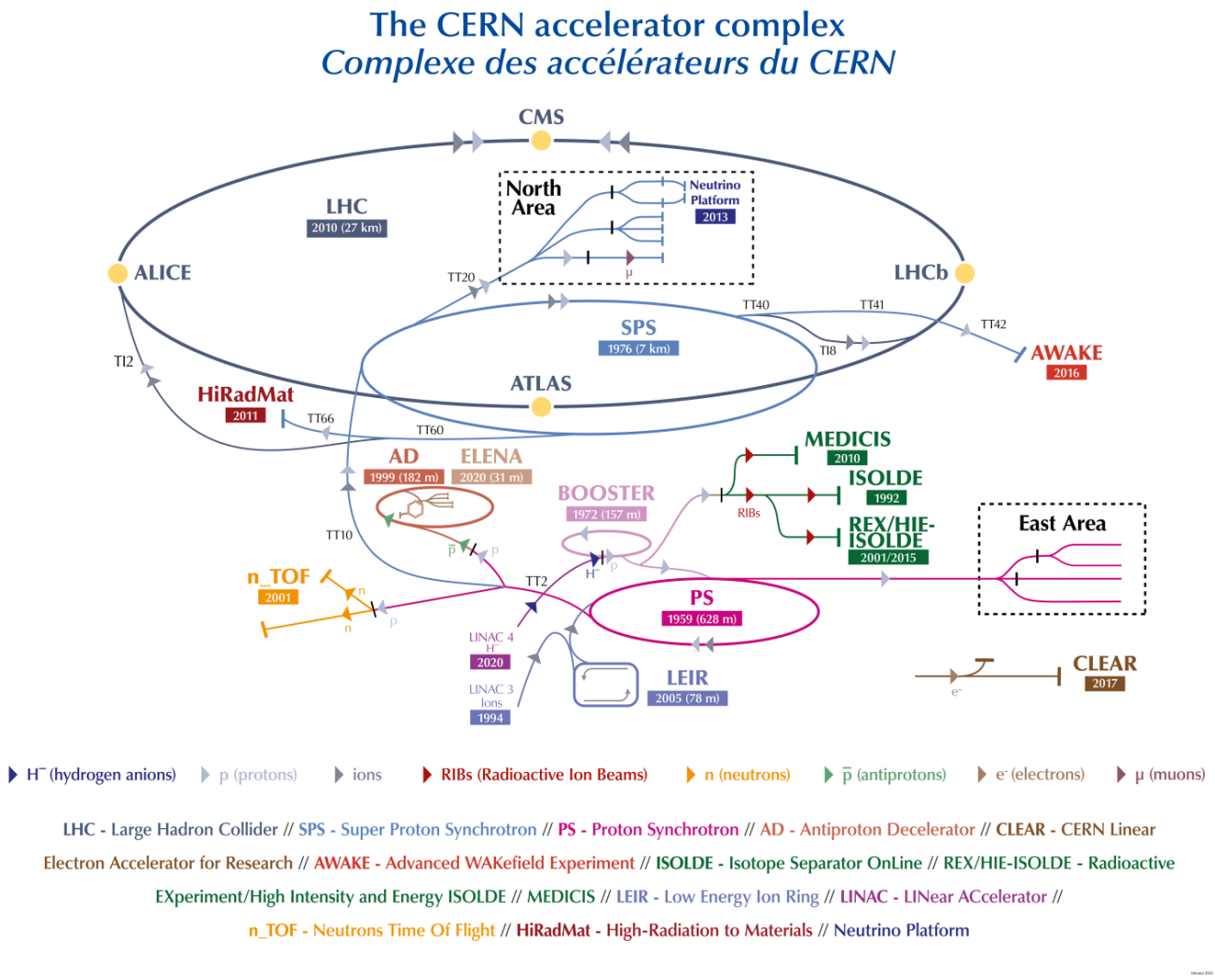

Figure 3.1: *The CERN accelerator complex showing the Large Hadron Collider (dark blue) along with its preaccelerators and affiliated experiments. Diagram taken from [65].*

The LHC began operations in 2008, with the first collisions occurring in 2009. Data collected from 2010 to 2013 is known as "Run-1". The bulk of this run was recorded at $\sqrt{s}$ =7 TeV and later at 8 TeV. After Long Shutdown 1 (LS1, 2013-2014), Run-2 (2015-2018) ran at $\sqrt{s}$ =13 TeV. Following Long Shutdown 2 (LS2, 2018-2022), Run-3 began in July 2022 at $\sqrt{s} = 13.6$ TeV and is expected to continue until 2026.

The data pertinent to this thesis were recorded during Run-2.

3.1.2 LHC luminosity

Instantaneous luminosity L serves as a proportionality constant that links the cross-section σ of a particular process to the number of events N produced. The relationship is given by the formula:

$$N = L\sigma. \tag{3.1}$$

The machine luminosity depends on the beam parameters and, for a Gaussian beam distribution, can be written as [60]

$$L = \frac{N_b^2 n_b f_{\text{rev}} \gamma_r F}{4\pi \epsilon_n \beta^*}, \tag{3.2}$$

where N_b and n_b are respectively the number of particles per bunch and the number of bunches in the beam, f_{rev} is the revolution frequency, γ is the relativistic factor. ϵ_n is the normalised transverse beam emittance and is related to the transverse size of the beam. The envelope of the beam is given by the β-function and β^* is the value of the β-function at the interaction point. F is the geometric luminosity reduction factor and is related to the beam crossing angle, transverse RMS beam size and RMS bunch length at the interaction point.

3.1.3 Pile-up at the LHC

A proton–proton scattering event at the LHC does not occur in isolation. Protons collide in bunches, with bunch crossings happening every 25 ns, and multiple interactions can occur during each crossing.

Interactions that influence the collision of interest due to their proximity in space and time are known as “pile-up”. Pile-up, denoted by μ, can be thought of as the mean number of collisions per bunch crossing. Naturally, pile-up increases with instantaneous luminosity. The two kinds of pile-up are in-time pile-up and out-of-time pile-up [57].

In-time pile-up refers to collision events that occur within the same bunch crossing as the collision of interest, potentially affecting the detector signals. Out-of-time pile-up involves similar events, but the additional collisions happen shortly before or after the collision of interest, such as during a previous or subsequent bunch crossing. The response time of ATLAS subdetectors exceeds the time between collisions, so energy deposits from these out-of-time pile-up events can also impact the signal from the collision of interest [66].

Figure 3.2(b) shows the number of interactions per bunch crossing during Run-2 at the LHC. There are on average about 30 collisions per bunch crossing.

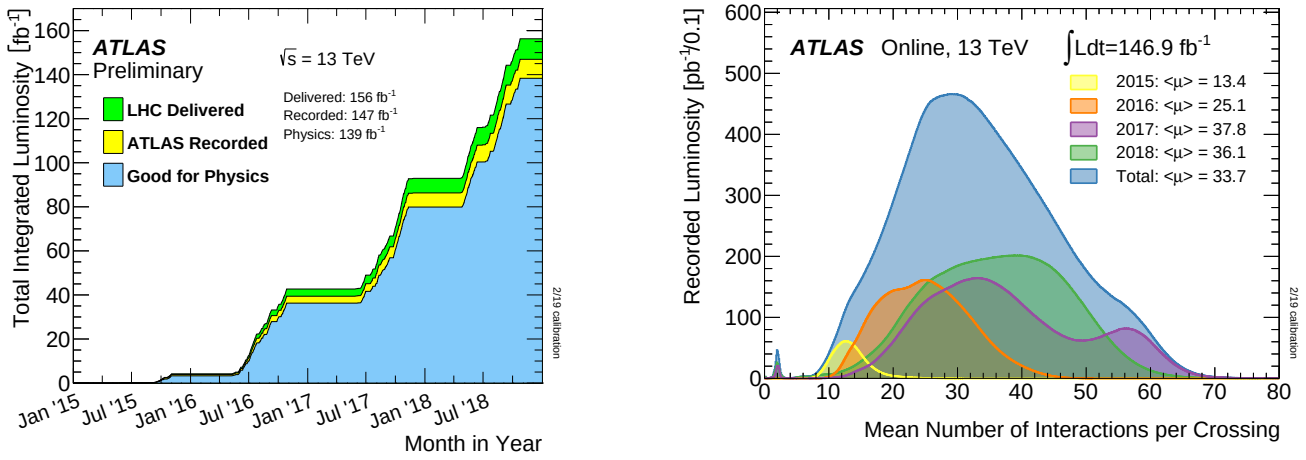

(a) **(b)**

Figure 3.2: *(a) The cumulative luminosity delivered to ATLAS during stable beam operations for proton–proton collisions at $\sqrt{s} = 13$ TeV throughout LHC Run-2. (b) The luminosity-weighted distribution of pile-up $\langle\mu\rangle$, during Run-2. The average pile-up is approximately 30 for the data-taking period. Taken from [67].*

3.2 The ATLAS Experiment

The ATLAS detector, described in Ref. [61] and references therein, is a multi-purpose detector designed to study the collisions occurring within the LHC. It is situated at one of the Interaction Points around the LHC ring. The detector is able to identify particles created from hadron-hadron collisions and measure the energy, momentum and charge of hadronic jets, leptons and photons.

ATLAS is a cylindrically shaped detector measuring 44 metres in length and 25 metres in diameter, with a total weight of approximately 7,000 tonnes.

Particle collisions occur at the detector's centre, surrounded by layered sub-detectors. The central cylindrical section, known as the barrel, contains concentric layers of tracking systems and calorimeters aligned parallel to the beam axis. This is complemented by end-cap structures at both extremities of the barrel – disc-shaped assemblies of sub-detectors oriented perpendicular to the beamline. Together, this barrel–end-cap configuration achieves nearly 4π steradians of solid-angle coverage, minimising undetected regions.

ATLAS consists of three main sub-systems:

- Inner Detector - Comprising Pixel detectors, Silicon Microstrip Trackers (SCT), and Transition Radiation Trackers (TRT), immersed in a 2T axial magnetic field from the central superconducting solenoid. This configuration enables precise tracking of charged particle trajectories through Lorentz force-induced curvature, allowing momentum measurement and charge identification. Further details are provided in Section 3.2.2.

- Electromagnetic and Hadronic Calorimeters - Determine energy deposits from electrons, photons, and hadrons through cascading particle showers. This subdetector is elaborated upon in Section 3.2.3.
- Muon Spectrometer - Operates in a separate toroidal magnetic field, and uses monitored drift tubes and cathode strip chambers to track high-momentum muons and measure their charge. Further details are provided in Section 3.2.4.

A dedicated trigger (further elaborated in Section 3.2.5) preselects potentially interesting events and rejects the rest. A more complete description can be found in [61].

Figure 3.3 illustrates the ATLAS detector in its Run-2 configuration, and its various sub-detectors.

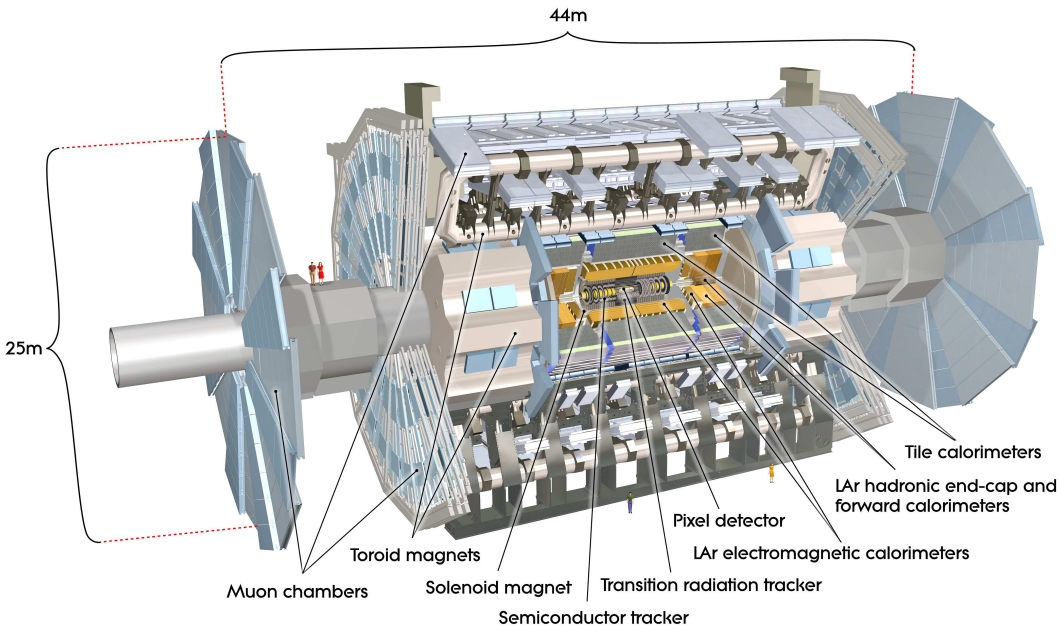

Figure 3.3: *Cut-away view of the ATLAS detector. Taken from [61].*

3.2.1 The ATLAS coordinate system

In the ATLAS experiment, the primary interaction point of a collision serves as the origin of a right-handed coordinate system. The positive x-axis points radially inward towards the centre of the LHC ring, the positive y-axis extends vertically upwards, and the z-axis points along the beam pipe.

Given that the detector is approximately rotationally symmetric around the beam axis, a spherical coordinate system (R, θ, ϕ) is also used, where the azimuthal angle ϕ is measured

around the beam axis in the $x-y$ plane, and the polar angle θ represents the angle relative to the beam axis. The radial distance R indicates the distance in the transverse plane.

Transverse quantities such as transverse momentum (p_T), transverse energy (E_T), and missing transverse energy (E_T^{miss}) are defined as the component of the momentum/energy in the $x-y$ plane.

In place of the polar angle θ, the rapidity y is often used, which is given by $y = \frac{1}{2}\ln\left(\frac{E+p_z}{E-p_z}\right)$ where E is the particle's energy and p_z is its momentum along the beam axis. The benefit of using rapidity is that it remains unchanged under Lorentz boosts along the beam axis.

For proton–proton collisions, where partons collide with unknown momentum fractions and the boost along the z-axis is not known, rapidity acts as a more suitable description. In the ultra-relativistic limit, where the mass $m \approx 0$, rapidity can be approximated by pseudo-rapidity η, which is calculated from the polar angle θ as $\eta = -\ln(\tan(\theta/2))$. Differences in η are approximately invariant under Lorentz boosts along the beam axis, making it a more convenient variable than θ.

The distance between two particles in the detector, ΔR, is defined as $\Delta R = \sqrt{(\Delta\phi)^2 + (\Delta\eta)^2}$ where $\Delta\phi$ is the difference in azimuthal angle (measured in radians), and $\Delta\eta$ is the difference in pseudo-rapidity.

3.2.2 The ATLAS Inner Detector

The ATLAS Inner Detector (ID) is a complex system designed to detect and track charged particles produced in collisions, measure their momentum, and determine the origin of particle tracks, a process known as vertexing. To do precision physics, high granularity and low noise measurements are needed. The design specification for the momentum resolution of the tracks is $\frac{\sigma_{p_T}}{p_T} = 0.05\% p_T$ [GeV] $\bigoplus 1\%$ [61].

The ID comprises three sub-detectors: the pixel detector, semiconductor tracker (SCT), and transition radiation tracker (TRT). These are arranged cylindrically around the beam pipe within a 2T axial magnetic field which bends the trajectories of charged particles to help determine their momentum. A schematic view of the Inner Detector is shown in Figure 3.4.

The ID employs two principal detection technologies: silicon sensors and straw drift tubes. Charged particles traversing silicon sensors create electron-hole pairs, which are collected via an applied electric field to record position measurements. In the TRT's straw drift tubes (so named for their cylindrical shape and dimensions, typically $4\,\mathrm{mm}$ in diameter and up to $150\,\mathrm{cm}$ in length), ionisation electrons drift towards a central anode wire under an electric field, where they are detected, with the resulting signals transmitted along the wire to readout electronics at

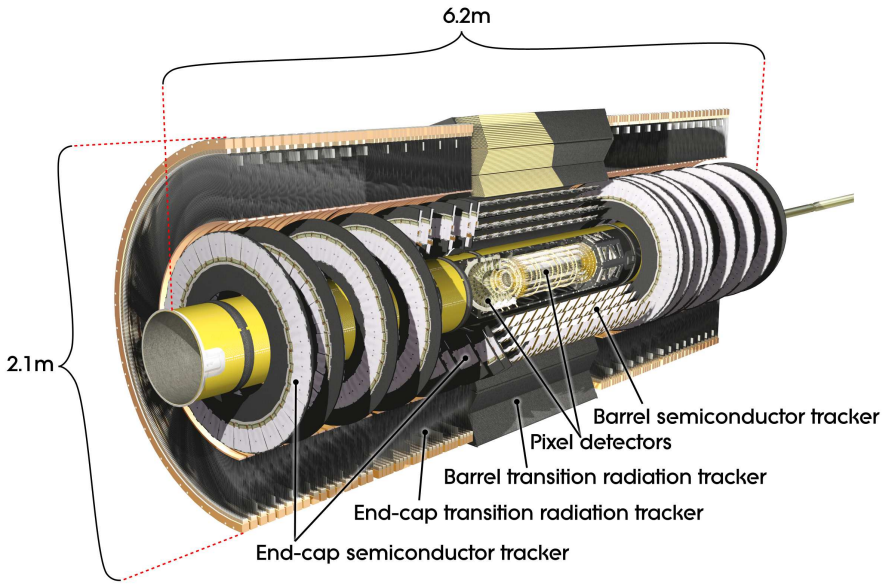

Figure 3.4: *Cutaway view of the ATLAS Inner Detector. Taken from [61]*

the ends of the straws.

- **Pixel Detector:** Innermost sub-detector with finest granularity. Features four barrel layers (including the Insertable B-Layer at $3.3\,\mathrm{cm}$ radius) and two end-cap discs. Covers $|\eta| < 2.5$ with $50 \times 250\ \mu\mathrm{m}^2$ pixels.
- **Semiconductor Tracker (SCT):** Four barrel layers and nine end-cap discs of double-sided silicon strip layers, with each layer comprising two sensors arranged in a stereo configuration with a $40\,\mathrm{mrad}$ angle between strips to provide three-dimensional hit reconstruction. Covers $|\eta| < 2.5$ with $17\,\mu\mathrm{m}$ R-ϕ and $580\,\mu\mathrm{m}$ z resolution. Both SCT and pixel detectors operate at $-5\,^{\circ}\mathrm{C}$ to $-10\,^{\circ}\mathrm{C}$.
- **Transition Radiation Tracker (TRT):** Approximately 300,000 straw drift tubes filled with Xe, CO_2, and O_2 gas mixture. Covers $|\eta| < 2$. Differentiates electrons from charged hadrons by detecting transition radiation photons, which are more likely to be emitted by high-γ particles such as electrons.

3.2.3 Calorimeters

The ATLAS calorimeter system is designed to measure the energy of particles through two main components: the electromagnetic calorimeter (ECAL) and the hadronic calorimeter (HCAL). These components work by making particles deposit all of their energy through electromagnetic and strong interactions. A schematic view of the calorimeters is shown in Figure 3.5.

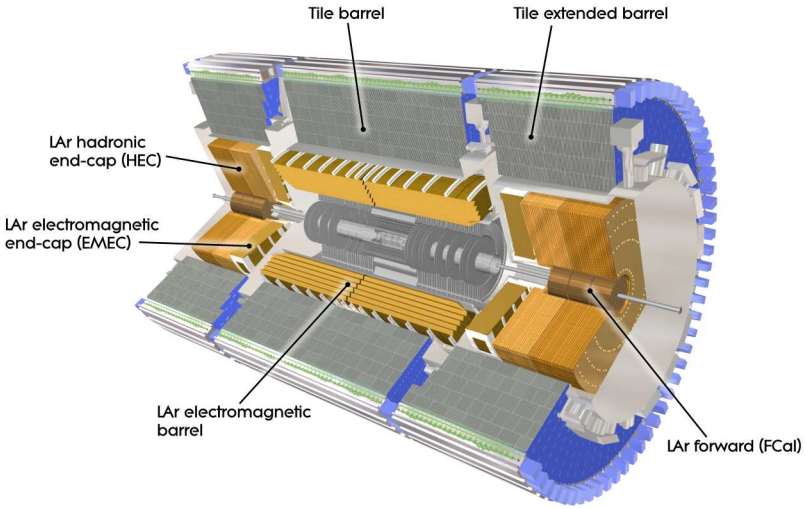

Figure 3.5: *Cutaway view of the ATLAS calorimeter system. Taken from [61].*

The calorimeters are sampling calorimeters, meaning they consist of alternating layers of high-density absorbing material and active material that measures energy. When particles enter the calorimeter, they interact with high-density materials causing them to shower. The active layers measure ionisation caused by charged particles in these showers, allowing an estimation of the total energy deposited.

The Electromagnetic Calorimeter

The ATLAS electromagnetic calorimeter (ECAL)is a sampling calorimeter that uses lead plates as the absorber material and liquid argon (LAr) as the active material. In some forward regions, copper is used instead of lead due to its electrical conductivity properties under high flux conditions. When photons and electrons interact electromagnetically within the ECAL, they ionise atoms and generate secondary particles through processes such as pair production, bremsstrahlung, Compton scattering, and the photoelectric effect. These secondary particles then interact with the lead or copper absorber material, producing a cascade of particles known as a shower. This process continues until the electrons or photons lose sufficient energy to no longer produce secondary particles and instead lose their remaining energy through collisions with atoms.

The shape of the resulting shower—its width, length, and location of its maximum—provides critical information about the identity of the initial particle. Lead is chosen as an absorber material due to its short radiation length, which allows for a more compact construction of the ECAL. In the active LAr material, argon atoms are ionised by charged particles in the shower.

The resulting charge drifts to readout electrodes situated in gaps between absorber plates due to a high voltage applied across these electrodes.

The ECAL achieves an energy resolution of: $\frac{\sigma_E}{E} = \frac{10\%}{\sqrt{E[\text{GeV}]}} \bigoplus 0.7\%$ [61].

The ECAL is divided into three subsystems: the electromagnetic barrel calorimeter (EMB), the electromagnetic end-cap calorimeter (EMEC), and part of the forward calorimeter (FCAL), which has an electromagnetic component optimised for measurements in very forward regions ($3.1 < |\eta| < 4.9$). These subsystems use Liquid Argon as their active material; however, their absorber materials differ depending on their position relative to the beam axis.

The EMB covers $|\eta| < 1.475$, while the EMEC covers $1.375 < |\eta| < 3.2$. Both use lead as their absorber material. The FCAL includes copper for its electromagnetic module due to its suitability for high flux regions.

The EMB and EMEC consist of four layers with different granularity optimised for precision measurements up to $|\eta| < 2.5$. Table 3.1 summarises these layers.

Layer	$\lvert\eta\rvert$ **Coverage**	$\eta \times \phi$ **Granularity**	**Thickness**	**Notes**
Presampler	$\lvert\eta\rvert < 1.8$	0.025×0.1	$1.7X_0$	Corrects for energy loss upstream of calorimeter
Front Layer	$\lvert\eta\rvert < 1.4$ $1.5 < \lvert\eta\rvert < 1.8$ $2.4 < \lvert\eta\rvert < 2.5$	0.003125×0.1 Transitioning granularity 0.025×0.1	$4.3X_0$	Fine granularity for precise position measurements.
Middle Layer	$\lvert\eta\rvert < 2.5$	0.025×0.025	$16X_0$	Captures majority of energy deposits.
Back Layer	$\lvert\eta\rvert < 1.35$ $1.5 < \lvert\eta\rvert < 2.5$	0.050×0.025 0.050×0.025	$2X_0$	Captures shower tail.

Table 3.1: *Details of the EMB and EMEC Layers*

It is worth noting that all EM subsystems utilise a clever accordion geometry that ensures complete coverage without gaps in azimuthal angle (ϕ).

The Hadronic Calorimeter

The hadronic calorimeter (HCAL) in ATLAS consists of three main components: the Tile Calorimeter (Tile-Cal) in the barrel region, the Hadronic End-Cap Calorimeter (HEC), and part of the Forward Calorimeter (FCAL). The HEC and FCAL are distinct from the ECALs but share cryostats with them. The hadronic barrel and end-cap calorimeters have an energy resolution of $\sigma_E/E = 50\%/\sqrt{E[\text{GeV}]} \oplus 3\%$ [61].

The Tile-Cal is situated outside (downstream) of the ECAL and uses steel as its absorber material and scintillator tiles as its active material. Hadronic interactions with steel produce particle cascades larger than electromagnetic showers due to strong interactions dominating over electromagnetic ones at higher energies.

The HEC covers $1.5 < |\eta| < 3.2$ and consists of two independent wheels located forward relative to the EMEC in each end-cap cryostat.

The FCAL extends ATLAS coverage to very forward regions ($3.1 < |\eta| < 4.9$). It consists of three layers: one copper/LAr layer optimised for electromagnetic measurements and two tungsten/LAr layers optimised for hadronic measurements due to tungsten's high density and short interaction length.

These design choices address challenges posed by high particle fluxes in forward regions while ensuring accurate measurement capabilities across all pseudorapidity ranges.

3.2.4 Muon Spectrometer

The muon spectrometer, located in the outermost part of ATLAS (Figure 3.6), detects and measures charged particles that penetrate through the calorimeters. Muons lose minimal energy via ionisation and typically pass through all detector layers. Dedicated toroidal magnets bend muon trajectories to enable momentum measurement - superconducting barrel coils produce a 4 T field for $|\eta| < 1.4$, while end-cap toroids cover $1.6 < |\eta| < 2.7$. In the transition region ($1.4 < |\eta| < 1.6$), combined magnetic fields enable track reconstruction. This toroidal configuration maximises the bending power over a large volume, achieving $\sigma_{p_T}/p_T = 10\%$ at $p_T = 1$ TeV where tracks become nearly straight [61]. For electrons at these energies, momentum measurement relies entirely on calorimetry.

Tracking chambers surrounding the toroids record muon trajectories using complementary technologies:

Tracking Chambers

The primary tracking system uses three layers of Monitored Drift Tubes (MDTs) in the barrel region and two layers in the end-caps. These 30 mm diameter drift tubes contain Ar:CO_2 gas where ionisation electrons drift to a central anode wire. Position resolution of $\sim$100 μm is achieved by measuring electron arrival times.

In the high-rate forward region ($2.0 < |\eta| < 2.7$), Cathode Strip Chambers (CSCs) were used instead of MDTs due to their better performance in high-rate environments. CSCs use orthogonal cathode strips and anode wires to provide 1 mm spatial resolution in both η and ϕ coordinates,

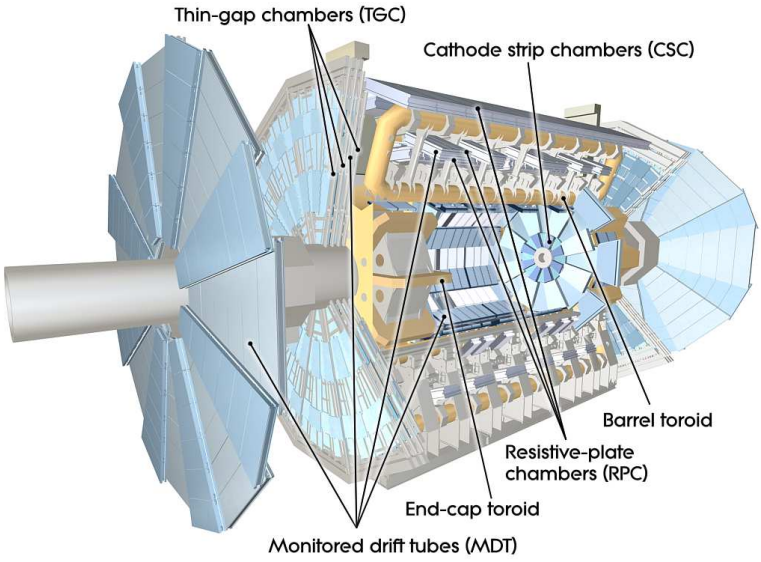

Figure 3.6: *Cut-away view of the ATLAS muon system. Taken from [61].*

with 20 ns maximum drift time for high-rate capability. MDTs are the primary precision tracking detectors, covering $|\eta| < 2.7$ except in the CSC regions.

Triggering Chambers

Resistive Plate Chambers (RPCs) in the barrel and Thin Gap Chambers (TGCs) in the end-caps provide ϕ coordinate measurements and fast trigger signals. Because MDTs measure only the precision coordinate, RPCs and TGCs are used to provide ϕ information for all tracks. The RPC system consists of:

- Two double-gap RPC layers surrounding the middle MDT layer
- One double-gap RPC layer behind the outer MDT layer

RPCs use 2 mm gas gaps between resistive bakelite plates, achieving $\sim$10 mm resolution in ϕ (precision coordinate) and $\sim$30 mm in r for MDT matching. TGCs in the end-caps employ 1.4 mm wire-cathode gaps, providing 2-5 mm spatial resolution with few-nanosecond time resolution.

3.2.5 Triggering and Data Acquisition

Proton collisions occur every 25 ns at the LHC, corresponding to an initial event rate of 40 MHz. Storing the resulting data stream of $\mathcal{O}(60$ TB/s$)$—equivalent to 40 million events per second

at 1.6 MB per event after zero suppression [61]— is not feasible and requires a sophisticated multi-stage trigger system to reduce the data to something manageable. Figure 3.7 shows the ATLAS Trigger and Data Acquisition (TDAQ) architecture with its rate reduction stages.

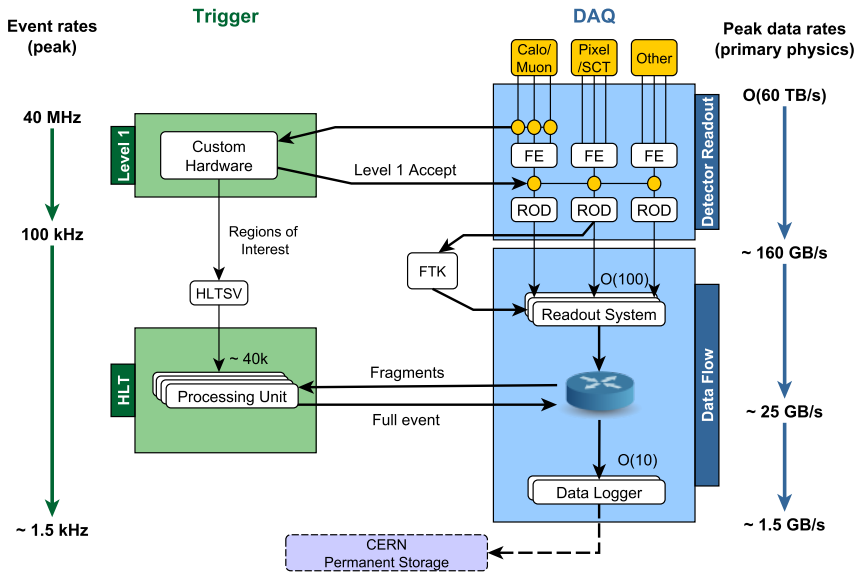

Figure 3.7: *ATLAS Trigger and Data Acquisition system in Run-2 showing expected peak rates and bandwidths. Taken from [68].*

The trigger system comprises two principal components. The Level 1 (L1) trigger is a hardware-based system that identifies Regions of Interest (ROIs) using coarse-grained muon spectrometer data, simplified calorimeter information detecting high-p_T objects ($p_T > 20$ GeV), and missing transverse energy (E_T^{miss}) calculations. L1 reduces the event rate from 40 MHz to 100 kHz with 2.5 μs latency. During decision-making, event data is buffered in front-end electronics before transfer to Read-Out Drivers (RODs).

The High-Level Trigger (HLT) is a software-based system operating on approximately 40,000 CPU cores [69]. It performs full-granularity detector reconstruction, track-to-calorimeter cluster matching, and advanced physics object identification such as b-jets and τ leptons. The HLT further reduces rates to 1–1.5 kHz, peaking at 1.5 kHz during high-luminosity runs. Selected events are permanently stored and distributed to CERN's Tier-0 facility for initial processing, then globally distributed to regional Tier-1 centres such as Simon Fraser University in Vancouver, Canada and other sites worldwide.

CHAPTER 4

Reconstruction of particles in ATLAS

To transform detector signals into physics objects usable for analysis, specialised reconstruction and identification algorithms are developed. The ATLAS collaboration centrally implements these algorithms within the ATHENA framework [70]. ATHENA is a comprehensive software framework that manages all levels of ATLAS data processing, from high-level triggering to event simulation, reconstruction, and analysis, ensuring consistency across various applications and analyses.

The reconstructed objects, such as electrons, muons, or jets, are then calibrated to account for detector-specific effects. This chapter briefly summarizes the reconstruction algorithms used to obtain physics objects that enter the different measurements used in this thesis.

The ATLAS detector can detect the following final-state particles: electrons, photons, muons, hadrons (such as protons, neutrons, pions and kaons) and neutrinos (whose presence can be inferred). The signature of each of these particles as they interact with the different sub-detectors within ATLAS is used in reconstruction algorithms to identify the particle. Figure 4.1 shows a diagram of different particle paths in the detector.

The process of reconstructing physics objects starts with high-level detector data, such as tracks and vertices from the Inner Detector, tracks from the Muon Spectrometer, and topological calorimeter clusters [72]. Physics objects are then constructed from these data points based on their anticipated detector signatures. Detector signatures, however, are not unique and a signal can be confused with background objects with similar signatures. Specialised algorithms integrate various detector information to accurately select candidate objects. Different identification working points are used to strike a balance between signal efficiency and background rejection. Furthermore, objects can be subjected to isolation criteria, which reject candidates if there is significant additional detector activity nearby.

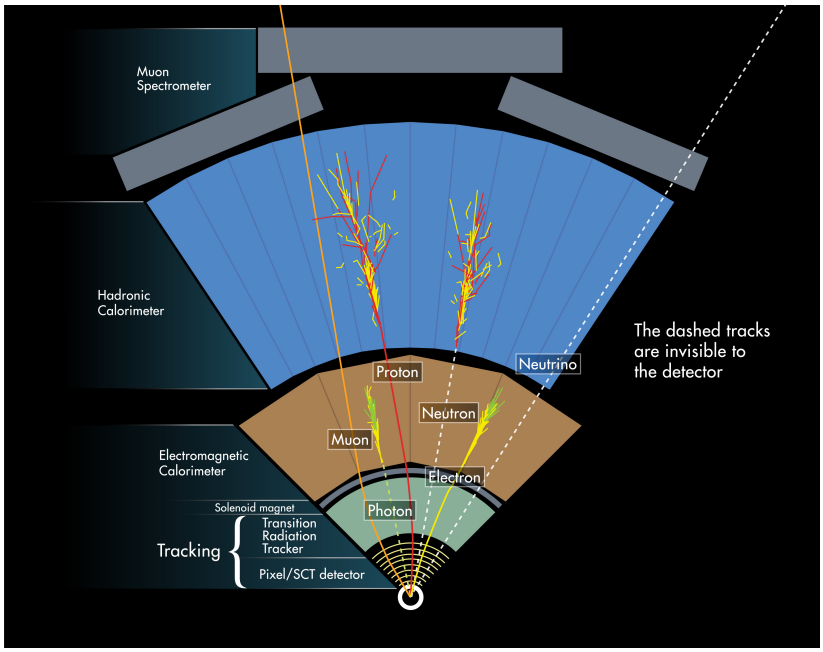

Figure 4.1: *Diagram illustrating the interactions of various particles with different ATLAS sub-detectors in the transverse plane. [71]*

4.1 Track and Vertices

Tracks are the trajectories of charged particles, and their reconstruction is done in the Inner Detector (ID) and Muon Spectrometer (MS) [73, 74].

The track reconstruction process starts with three-dimensional space points derived from clusters in the Pixel and SCT detectors and drift circles in the TRT. Two primary algorithms are employed for this purpose: the inside-out algorithm and the outside-in algorithm.

- The **inside-out algorithm** begins from the innermost layers of the detector (closest to the beam pipe) and extends outward. It starts with precise measurements from the Pixel and SCT detectors, forming initial track seeds. A "seed" is an initial estimate of a particle's trajectory based on a few early measurements. These seeds are then extended through the remaining detector layers, incorporating additional measurements to refine the track parameters. This algorithm is particularly effective in leveraging the high precision of the inner layers to initiate accurate track reconstruction.

- The **outside-in algorithm** starts from the outer layers of the detector and works its way inward. This method is used to recover tracks that might have been missed by the inside-out approach, especially those that do not have sufficient initial measurements in the innermost layers. This may happen with charged particles produced from decay chains of long-lived

particles such as b or c hadrons. The algorithm begins with track seeds from the TRT and outer SCT layers, then extends inward, incorporating measurements from the inner layers to complete the track reconstruction.

Vertices, representing the intersections of charged particle trajectories, are reconstructed using an iterative vertex finding and fitting procedure [75]. The algorithm relies on the transverse impact parameter d_0, defined as the radial distance of a track's closest approach to the beam axis in the r–ϕ plane, and the longitudinal impact parameter z_0, which is the z-coordinate of this closest approach along the beam axis. Tracks compatible with a vertex seed are iteratively added, and the vertex position is updated by weighting tracks according to their compatibility. Tracks associated with a vertex are refit under the assumption that they originate from that vertex.

Tracks not matching an identified vertex are used as seeds for finding additional vertices, and this process continues until no further vertices can be formed. Vertices with at least two associated tracks having $p_{\mathrm{T}} > 0.5$ GeV are considered valid candidates. Among these, the vertex with the largest sum of squared p_{T} values of its associated tracks is selected as the primary vertex. While this selection aims to identify the hard-scattering interaction, it may not always correspond to it in high-pileup conditions.

4.2 Electrons

Electrons are reconstructed by combining information from the Inner Detector (ID) and the Electromagnetic Calorimeter (ECAL). As electrons traverse the detector, they may radiate a significant amount of energy through bremsstrahlung due to their small mass. When these high-energy photons interact with the detector material, they can convert into electron-positron pairs, a process known as *photon conversion*. This radiated energy can result in the production of additional photons and, in some cases, electron-positron pairs, leading to a more complex energy deposition pattern.

In the central region ($|\eta| < 2.47$), the reconstruction of electrons uses a dedicated algorithm that combines tracking and calorimeter information [76–78]. The direction of the electron is inferred from its trajectory in the ID, while its energy is measured from the deposits in the ECAL. Figure 4.2 illustrates the typical path of an electron through the ATLAS detector, including possible bremsstrahlung photon emission.

Electron reconstruction begins with the formation of topological clusters (topo-clusters) in the ECAL. The ECAL is composed of cells, each of which records the energy deposited by particles passing through. A significance-based clustering algorithm identifies seed cells where the energy

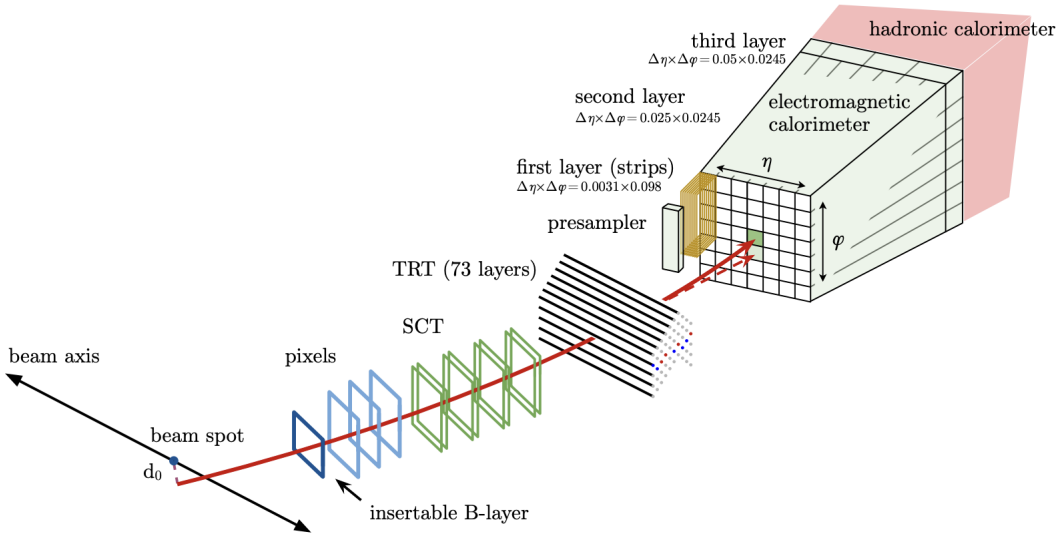

Figure 4.2: *A schematic illustration of the electron path through ATLAS. The electron path is shown as a solid red line while the dashed red line illustrates a bremsstrahlung photon, which causes an adjacent energy deposit in the ECAL. Taken from [76].*

deposit exceeds the expected electronic noise by a significant margin (i.e. a high signal-to-noise ratio), and then aggregates neighbouring cells based on similar criteria. These topo-clusters are subsequently merged by a supercluster-building algorithm [79], which accounts for energy from bremsstrahlung photons and photon conversions. The resulting superclusters are calibrated to the EM scale, which is defined such that the measured energy corresponds to the true energy of electrons and photons. This scale is derived from test-beam data and well-known physics processes, such as $Z \to ee$ and $J/\Psi \to ee$ decays.

To reconstruct the electron's trajectory, tracks in the ID are matched to the calorimeter clusters. Initially, a pattern recognition algorithm assumes that the track was produced by a charged pion, using a model that accounts for typical energy loss due to interactions with the detector material. If this model fails to explain the match between the track and the EM cluster—particularly in cases with significant bremsstrahlung—the energy loss model is updated to account for larger-than-expected energy loss. A Gaussian Sum Filter (GSF) algorithm [80] is then used to better model the distorted curvature of the electron track caused by bremsstrahlung radiation, improving the reconstruction accuracy.

Electron candidates are classified as either *prompt* or *non-prompt*. Prompt electrons originate directly from the primary interaction vertex (e.g., $Z \to ee$), while non-prompt electrons arise from secondary processes such as heavy-flavour hadron decays ($b \to ce\nu$) or photon conversions. Non-prompt electrons are often accompanied by nearby tracks or additional energy deposits.

To suppress non-prompt backgrounds, a likelihood-based discriminant combines multiple variables such as shower shape, track quality, and isolation criteria. Three working points are defined:

- **Loose**: Maximises signal efficiency (95%), allowing more background.
- **Medium**: Balances efficiency (85%) and background rejection.
- **Tight**: Prioritises background rejection with reduced efficiency (70%).

Several isolation working points exist, which define thresholds on the energy sum within a cone of $\Delta R < 0.2$ around the electron. Candidates with excess energy in this region are rejected.

Some variables used in electron identification and isolation are not always well-modelled in MC simulations. To ensure that selection efficiencies observed in data are accurately reflected in the simulation, scale factors are applied to correct for differences between data and MC predictions. These scale factors are derived using the Tag-and-Probe method [81], which exploits well-known decay channels such as $Z \to ee$ or $J/\Psi \to ee$, taking advantage of their clean invariant mass peaks and isolation properties.

4.3 Muons

Muons are identified by their signals in the Muon Spectrometer (MS), the Inner Detector (ID), and the calorimeters. The primary reconstruction relies on combining information from the MS and ID, while in regions not covered by the MS, the muon's energy loss in the calorimeters provides additional discrimination. Conversely, in areas lacking ID coverage, muons can still be reconstructed using MS data alone [82].

In the ID, tracks are reconstructed as described in Section 4.1. The MS consists of several layers of muon chambers arranged in stations, typically three in total: an inner, middle, and outer station, with each containing multiple detector layers separated by large distances to accommodate the magnetic field and provide precise momentum measurements. Within these stations, an algorithm identifies groups of aligned hits, referred to as segments, which represent straight-line approximations of the muon's path in a single chamber layer. These segments, once identified, are combined across different stations using a combinatorial search to form muon track candidates. The quality of these candidates is evaluated based on hit multiplicity and fit quality, with at least two matching segments required to form a viable track.

A global χ^2 fit is then performed across all hits forming a candidate. If certain hits contribute disproportionately to the total χ^2, they may be excluded in a refit to improve the overall quality.

Furthermore, the reconstruction algorithm searches for any additional hits near the candidate trajectory that were not initially included [82].

Muons in ATLAS can be reconstructed in several ways, depending on detector coverage and the quality of the track information. The most common type are combined muons, which use tracks from both the MS and ID, merged using a combined fit that accounts for all relevant hits and calorimetric energy loss.

Minimum-ionising particles (MIPs) are charged particles that lose a minimal amount of energy per unit length as they traverse a detector medium. In ATLAS, muons are typically MIPs when passing through the calorimeters, as they do not undergo strong interactions like hadrons and deposit only a small, consistent amount of energy.

Not all muons originate directly from the hard scatter process at the interaction point. Other processes such as decays of hadrons containing heavy-flavour quarks (e.g. b or c), as well as in-flight decays of charged pions and kaons, can also produce muons. These are collectively referred to as non-prompt muons. Compared to prompt muons, they are generally less isolated and their tracks often do not point back precisely to the primary vertex.

To discriminate between prompt and non-prompt muons, dedicated identification working points are defined. These include Low-p_T, Loose, Medium, Tight, and High-p_T selections, each offering a trade-off between background rejection and signal efficiency. The criteria for these working points depend on the type of reconstructed muon and on variables that quantify the track quality and consistency between the ID and MS information, when available.

As with electrons, isolation requirements—based on either calorimeter or tracking information—are applied to further reduce backgrounds from non-prompt muons and other sources.

The muon energy scale is calibrated to the per-mille level using well-known resonances such as $Z \to \mu\mu$ and $J/\psi \to \mu\mu$. These same processes are also used in tag-and-probe methods to evaluate the efficiency of muon reconstruction, identification, and isolation in data. Correction factors derived from these measurements are applied to simulated events to ensure accurate modelling of muon performance.

4.4 Hadronic Jets

Hadronic jets are reconstructed using the anti-k_t algorithm [83], which clusters nearby energy deposits and tracks into jets based on their distance in η–ϕ space. In this analysis, jets are built using the particle-flow algorithm [84], which combines signals from the calorimeters with tracks in the ID to improve the accuracy of the reconstructed jet properties. This method helps to better resolve the energy and direction of jets and also reduces the impact of pile-up.

Jets are reconstructed with a fixed radius parameter, R, which determines how wide the jet can be in angular space. Two types of jets are used, based on the chosen value of R. Jets with $R = 0.4$ are referred to as small-R jets and are commonly used to identify the hadronisation of individual quarks or gluons. Jets with $R = 1.0$ are known as large-R jets and are used to capture the decay products of boosted heavy particles, such as W or Z bosons, that are produced with high momentum and decay into collimated jets.

To ensure the reconstructed jets are of good quality, corrections are applied to account for the detector response, and additional criteria are used to reduce contamination from pile-up or noise in the calorimeters.

4.5 Missing transverse energy: neutrino reconstruction

Neutrinos are the only SM particles that cannot be detected in the ATLAS detector, since they interact only weakly, with extremely small interaction cross-sections.

Neutrinos can be inferred indirectly by using energy and momentum conservation in the transverse plane. Since the incoming partons have no initial transverse momentum, the vector sum of the momenta of all outgoing particles must be close to zero in this plane. The missing transverse energy ($E_{\mathrm{T}}^{\mathrm{miss}}$) is defined as the magnitude of this momentum imbalance. It is calculated from its components along the x- and y-axes.

The individual components $E_{\mathrm{x}}^{\mathrm{miss}}$ and $E_{\mathrm{y}}^{\mathrm{miss}}$ are computed by summing contributions from all calibrated final state objects, along with an additional track-based soft term that accounts for tracks not associated with any specific object but still compatible with the primary vertex [85, 86]:

$$E_{x(y)}^{\mathrm{miss}} = -E_{x(y)}^{\mathrm{miss,\ soft,\ trk}} - \sum_{i \in \mathrm{objects}} E_{x(y)}^{\mathrm{miss,\ i}} \quad , \tag{4.1}$$

where the sum includes contributions from muons (μ), electrons (e), photons (γ), hadronically decaying τ-leptons, and jets along the x and y axes as

$$\sum_{i \in \mathrm{objects}} E_{x/y}^{\mathrm{miss,\ i}} = E_{x/y}^{\mathrm{miss,\ }\mu} + E_{x/y}^{\mathrm{miss,\ e}} + E_{x/y}^{\mathrm{miss,\ }\gamma} + E_{x/y}^{\mathrm{miss,\ }\tau} + E_{x/y}^{\mathrm{miss,\ jets}} \quad . \tag{4.2}$$

A specialised overlap removal procedure is implemented to prevent double counting of signatures. Since $E_{\mathrm{T}}^{\mathrm{miss}}$ depends on the entire event's activity, it is a measurement with a higher uncertainty than other reconstructed objects.

CHAPTER 5

Inclusive Run-2 $WZ \to \ell\nu\ell\ell$ analysis methodology

5.1 Inclusive Phase Space Definition

This thesis describes the study of the process

$$pp \to W^{\pm}Z + X$$

where X indicates possible additional particles in the final state, and the bosons decay as:

$$Z \to e^{+}e^{-} \quad \text{or} \quad Z \to \mu^{+}\mu^{-}$$

$$W^{\pm} \to e^{\pm}\nu_{e} \quad \text{or} \quad W^{\pm} \to \mu^{\pm}\nu_{\mu}$$

Differential cross-section measurements from different observables are performed in the inclusive fiducial phase space. The inclusive fiducial phase space is defined to be close to the measurement phase space given by the detector acceptance and the selection cuts to minimize extrapolation uncertainties. An extrapolation to the total phase space is also implemented, whereas the total phase space is defined as the total production cross section of the WZ with the bosons decaying to all possible final states in the complete solid angle.

The total phase space encompasses all WZ events in the complete solid angle and all decays. The fiducial phase space is a subset of the total phase space and considers only fully leptonic decays of the WZ pair within the detector's acceptance range and satisfying the applied selection criteria. Finally, the detector phase space includes events which are reconstructed in the detector. As not all generated WZ events are reconstructed in the detector, the fiducial phase space is larger than the detector phase space. However, it is not a subset as events which are generated outside the fiducial phase space can be reconstructed inside the detector.

This analysis exclusively considers decays involving Z bosons. Leptons ($\ell^+\ell^-$) resulting from Z boson decay must conform to the stringent invariant mass requirement: 66 GeV $\leq m_{\ell^+\ell^-} \leq 116$ GeV.

Table 5.1 presents a comprehensive overview of the requirements imposed upon both the fiducial and total phase spaces:

Parameter	**Total**	**Fiducial inclusive**
Lepton $\lvert\eta\rvert$	—	< 2.5
p_{T} of ℓ_Z, ℓ_W [GeV]	—	> 15, > 20
m_Z range [GeV]	$66 - 116$	$\lvert m_Z - m_Z^{\mathrm{PDG}}\rvert < 10$
m_{T}^W [GeV]	—	> 30
$\Delta R(\ell_Z^+, \ell_Z^-)$, $\Delta R(\ell_Z, \ell_W)$	—	> 0.2, > 0.3

Table 5.1: *Definitive criteria for fiducial and total phase spaces.*

where the transverse mass of the W boson is defined in terms of the lepton transverse momentum p_T^ℓ, the neutrino transverse momentum p_T^ν, and the angle $\Delta\phi$ between the lepton direction and the missing transverse momentum (p_T^ν),

$$m_T^W = \sqrt{2p_T^\ell p_T^\nu (1 - \cos\Delta\phi)}. \tag{5.1}$$

Estimates of the predicted cross-sections, as well as extrapolation and correction factors, are derived using MC simulations at generator level, employing so-called truth particles—i.e., particles before any detector simulation is applied. Reconstruction of these truth-level events does not follow the same approach as that used for data events, outlined in Section 5.2. Instead, a dedicated method known as the resonant-shape algorithm [87, 88] is used. This algorithm is constructed to be independent of the details of the MC generator.

Although this method yields a more efficient reconstruction than that achievable at detector level, it is not applicable to real data due to the lack of full kinematic information, particularly for neutrinos. The algorithm reconstructs events based on the expected kinematic features of the WZ final state, specifically making use of the invariant masses and decay widths of the two bosons. Among all possible configurations of truth particles to the W and Z bosons, the one that maximises the following likelihood-based estimator is selected:

$$P = \left| \frac{1}{m^2_{(\ell^+,\ell^-)} - \left(m_Z^{\mathrm{PDG}}\right)^2 + i\,\Gamma_Z^{\mathrm{PDG}}\, m_Z^{\mathrm{PDG}}} \right|^2 \times \left| \frac{1}{m^2_{(\ell',\nu_{\ell'})} - \left(m_W^{\mathrm{PDG}}\right)^2 + i\,\Gamma_W^{\mathrm{PDG}}\, m_W^{\mathrm{PDG}}} \right|^2, \tag{5.2}$$

Here, m_W^{PDG} and m_Z^{PDG} refer to the world-average masses of the W and Z bosons, while Γ_W^{PDG} and Γ_Z^{PDG} represent their respective total decay widths, as calculated by the Particle Data Group [42].

All quoted differential results are unfolded from reconstruction-level data to the fiducial particle (dressed) level, further described in Section 5.5.

5.2 Object and Event Selection

5.2.1 Lepton Selection

The identification of WZ event candidates involves selecting events with leptons that meet specific signal requirements, followed by a refined selection that leverages the unique topology and kinematics of the signal to assign leptons to the W and Z bosons. This section outlines the selection criteria for leptons, emphasising the importance of these criteria in differentiating signal from background events, particularly those with misidentified leptons or more than three leptons, such as ZZ events.

The lepton selection process is structured in three levels of increasing stringency, where each level is a subset of the previous one. Initially, the leptons must pass a baseline selection. Leptons assigned to the Z boson must pass the Z-lepton selection, while those assigned to the W boson must meet the even stricter W-lepton selection. This is because background noise is more likely to come from W-leptons. Consequently, W-leptons are a subset of Z-leptons, and both must satisfy the baseline criteria. W or Z leptons are also referred to as signal leptons. The detailed electron and muon reconstruction and identification processes, which motivate the selection criteria described here, are explained in Sections 4.2 and 4.3.

One of the main purposes of the baseline selection is to construct a veto for events with more than three leptons, thus reducing contamination from ZZ decays, which yield four leptons. The baseline requirements are as follows:

- $p_T > 5$ GeV,
- `Loose` [77, 89] identification criteria for both electrons and muons,
- Electrons must be within the ID range ($|\eta| < 2.5$), and muons must be within the precision muon chambers' range ($|\eta| < 2.7$),
- Matching with the primary vertex, with transverse impact parameter significance $|d_0/\Delta d_0|$ less than three for muons and five for electrons, and longitudinal impact parameter $|z_0 \cdot$

$\sin(\theta)| < 0.5$ mm for both of them,

- Baseline electrons must meet the `Loose_VarRad` [77] isolation criterion, while baseline muons must meet the `PflowLoose_FixedRad` [89] isolation criterion,
- Baseline electrons must pass the `LooseLH+BLayer` [77] identification criterion, ensuring a selection efficiency of 84 - 96% for electrons with $10 < p_T < 80$ GeV,
- To avoid double-counting, if a track can be reconstructed as part of either an electron or a muon candidate, it will be used to reconstruct the muon only. If a track can be reconstructed as part of two different electrons, it will be used to reconstruct the electron with the larger transverse momentum. This overlap removal is crucial for accurate event counting and reducing background.

For signal leptons assigned to Z bosons, the optimised criteria are:

- Z-electrons and Z-muons must meet `Medium` [77, 89] identification criteria,
- Z-electrons must pass the `HighPtCaloOnly` [77] isolation,
- Leptons near hadronic jets are excluded to suppress misidentification; electrons within $0.2 < \Delta R < 0.4$ of a jet ("e-to-jet overlap removal") and muons within $\Delta R < 0.4$ of a jet with fewer than three tracks are removed ("μ-jet Overlap Removal").

W-lepton candidates are subjected to even stricter criteria:

- W-electrons must meet `TightLH` identification criteria and `Tight_VarRad` [77] isolation whilst W-muons must meet `PflowTight_FixedRad` [89] isolation requirements,
- Electrons produced from photon conversions are typically more isolated than those from hadron decays. Although they are genuine isolated electrons, they do not originate from the primary interaction point, classifying them as non-prompt leptons. To address this, a custom tool (`EGammaAmbiguityTool`) is utilised to distinguish between electrons and photons. This tool helps identify candidates that pass either the electron reconstruction alone or both the electron and photon reconstructions. Background events from $Z + \gamma$ decay contribute significantly to misidentified lepton events in the analysis. To mitigate the impact of photon conversions, any W-electron candidates that also pass the photon reconstruction criteria are excluded. This selection criterion introduces an inefficiency of approximately 5% for genuine electrons originating from W-boson decays. Additionally,

the DFCommonAddAmbiguity tagger [90] is used to reject misidentified converted photons. Electrons flagged by DFCommonAddAmbiguity are excluded in the W-selection. This requirement introduces a small inefficiency of around 0.5% for true electrons from W-boson decays but reduces $Z + \gamma$ background events by approximately 35% in the inclusive $W^{\pm}Z$ event selection.

Additionally, stricter p_T thresholds are imposed: Z-leptons require $p_T > 15$ GeV, and W-leptons require $p_T > 20$ GeV. Electrons are excluded from the barrel-endcap transition region, and muons must have tracker information available, limiting their range to $|\eta| < 2.5$.

Tables 5.2 and 5.3 provide detailed criteria for the baseline, Z, and W-lepton selections for electrons and muons, respectively. These tables illustrate the progression from loose to tight selection criteria, designed to optimize signal detection and background rejection.

Selection	**Baseline selection**	**Z selection**	**W selection**
$p_T > 5$ GeV	✓	✓	✓
Electron object quality	✓	✓	✓
$\lvert\eta_{\text{cluster}}\rvert < 2.47, \lvert\eta\rvert < 2.5$	✓	✓	✓
LooseLH+BLayer identification	✓	✓	✓
$\lvert d_0^{\text{BL}}/\sigma(d_0^{\text{BL}})\rvert < 5$	✓	✓	✓
$\lvert\Delta z_0^{\text{BL}} \sin\theta\rvert < 0.5$ mm	✓	✓	✓
Loose_VarRad isolation	✓	✓	✓
e-to-μ and e-to-e overlap removal	✓	✓	✓
e-to-jets overlap removal		✓	✓
$p_T > 15$ GeV		✓	✓
Exclude $1.37 < \lvert\eta_{\text{cluster}}\rvert < 1.52$		✓	✓
MediumLH identification		✓	✓
HighPtCaloOnly isolation		✓	✓
$p_T > 20$ GeV			✓
TightLH identification			✓
Tight_VarRad isolation			✓
Unambiguous author			✓
DFCommonAddAmbiguity ≤ 0			✓

Table 5.2: *Three levels of electron object selection used in the analysis.*

5.2.2 Missing transverse Energy and Neutrino Reconstruction

Since the ATLAS detector cannot detect neutrinos, their properties must be inferred from all the other detected measurements in the event. Assuming the initial transverse momentum before the

Selection	**Baseline selection**	Z **selection**	W **selection**
$p_T > 5$ GeV	✓	✓	✓
$\|\eta\| < 2.7$	✓	✓	✓
`Loose` quality	✓	✓	✓
$\|d_0^{\text{BL}}/\sigma(d_0^{\text{BL}})\| < 3$ (for $\|\eta\| < 2.5$ only)	✓	✓	✓
$\|\Delta z_0^{\text{BL}} \sin\theta\| < 0.5$ mm (for $\|\eta\| < 2.5$ only)	✓	✓	✓
`PflowLoose_FixedRad` isolation	✓	✓	✓
μ-jet Overlap Removal		✓	✓
$p_T > 15$ GeV		✓	✓
$\|\eta\| < 2.5$		✓	✓
`Medium` quality		✓	✓
$p_T > 20$ GeV			✓
`Tight` quality			✓
`PflowTight_FixedRad` isolation			✓

Table 5.3: *Three levels of muon object selection used in the analysis.*

pp collision is zero, the neutrino's transverse momentum can be calculated as shown in Equation 4.2.

However, there is no direct constraint on the longitudinal momentum of the proton's constituents before the collision. The Parton Distribution Function only provides a probabilistic distribution of the parton momenta within the proton.

To solve this problem, one can constrain the mass of the W, to find the missing z-momentum of the ν, under the assumption that all the missing transverse energy comes from the neutrino (which is the decay product of the W), and the W is on-shell.
For a $W^{\pm} \to l^{\pm} v$ decay:

$$\begin{aligned} \frac{m_W^2}{2} &= E^{\ell} E^{\nu} - \vec{p_T^{\ell}} \cdot \vec{p_T^{\nu}} - p_z^{\ell} p_z^{\nu}, \\ \Rightarrow \left(\xi - p_z^{\ell} p_z^{\nu}\right)^2 &= E^{\ell 2} E^{\nu 2} = E^{\ell 2}\left(p_T^{\nu\,2} + p_z^{\nu 2}\right) \quad \text{with} \quad \xi = \frac{m_W^2}{2} + \vec{p_T^{\ell}} \cdot \vec{p_T^{\nu}}. \end{aligned} \tag{5.3}$$

Simplifying and solving the previous equation brings:

$$p_z^{\nu} = \frac{p_z^{\ell}\xi \pm \sqrt{\Delta}}{p_T^{l\,2}}, \tag{5.4}$$

where:

$$\Delta = p_z^{l\,2}\xi^2 - p_T^{l\,2}\left[E^{l 2} p_T^{\nu\,2} - \xi^2\right]. \tag{5.5}$$

For cases where $\Delta > 0$, the solution with the smaller absolute value is chosen. For cases where $\Delta < 0$ and there are no physical solutions (which can happen due to the natural decay width of the W, or incorrectly measuring $E_{\mathrm{T}}^{\mathrm{miss}}$ due to detector noise or by misidentification of leptons or background events), the real part of the complex solution is chosen [91].

The ATLAS Run-2 WZ analysis team has also developed a neural network (NN) regression model using TensorFlow v1.3 [92] with the Keras v2.2.4-tf [93] backend to estimate p_Z^ν. The NN was trained on a WZ-inclusive NLO Powheg+Pythia sample to reconstruct p_Z^ν, using the inputs:

- p_T and η of the charged lepton associated with the W boson,
- Missing transverse momentum components along and perpendicular to the direction of the charged lepton associated with the W boson,
- The reconstructed p_z^ν from the baseline analytic method (choosing the smallest $|p_z^\nu|$ if $\Delta > 0$ or the real part if $\Delta < 0$).

This input selection exploits rotational symmetry, reducing the number of inputs to five, which leads to faster training and better overall performance.

To ensure the neural network regression aligns with the W boson mass constraint, a new Keras layer was implemented to compute the W mass from the regressed neutrino momentum and the true momentum of the charged lepton. This layer, devoid of trainable parameters, is utilised to formulate a loss function targeting W mass reconstruction.

The final loss function for training the NN combines the mean squared errors of the neutrino momentum components and the W mass. The true value of m_W is used as the target, allowing the NN to account for the natural width of the W boson, contrasting with the analytic method above, which forces the W boson to be on shell. Further details of the implementation of the NN are found in [88].

5.2.3 *Reconstruction of m_T^{WZ}*

The Z boson can now be reconstructed by summing the four-momentum of the two leptons from the decaying Z. The four-momentum of the W-lepton and the four-momentum of the neutrino, obtained by E_T^{miss} and the NN output of p_z^ν, can also be summed to reconstruct the W boson.

The vector sum of the W and Z boson's four-momenta, is called the "WZ-system". The transverse mass of the WZ is reconstructed by taking the four-vectors of the final state leptons, associated to the W and Z bosons, projected on the transverse plane by neglecting their longitudinal component. Then the m_T^{WZ} is defined as the invariant mass of the system built with the projected four-vectors of the three leptons and E_T^{miss}:

$$m_T^{WZ} = \sqrt{\left(\sum_{\ell=1}^{3} p_T^{\ell} + E_T^{\text{miss}}\right)^2 - \left(\sum_{\ell=1}^{3} p_x^{\ell} + E_x^{\text{miss}}\right)^2 - \left(\sum_{\ell=1}^{3} p_y^{\ell} + E_y^{\text{miss}}\right)^2}. \quad (5.6)$$

5.2.4 *Selection of WZ Candidate Events*

The selection process for WZ candidate events involves several steps, which are summarised in Table 5.4

- At first, basic data quality requirements are imposed on the event so that corrupted events detected by LAr, Tile, or the SCT are vetoed. Event cleaning is further done by rejecting events consistent with having at least one misidentified jet from pile-up or beam interactions. Events are required to have a primary vertex with at least two associated tracks.

- Events are selected with a dedicated trigger algorithm that identifies electron and muon candidates that fulfil isolation and minimal energy requirement: 25 GeV in 2015 and 27 GeV in 2016-2018, due to the higher instantaneous luminosity in the later data taking period.

- Events are required to have less than four baseline leptons to decrease the background contribution from ZZ processes with four leptons.

- Events must have exactly three leptons satisfying the Z-selection and one of these leptons has to be identified as satisfying the trigger.

- A Z boson candidate is formed with two same-flavour, opposite-charge (SFOC) leptons. If more than one pair is possible, the pair whose dilepton invariant mass m_{ll} is closest to the Z boson mass m_Z^{PDG} is taken as the Z boson candidate. This Z boson candidate must have an invariant mass within a window of 10 GeV around m_Z^{PDG}.

- The third and remaining lepton is required to pass the W lepton selection criteria. The W boson is reconstructed from this lepton and E_T^{miss}. The transverse mass (defined in Equation 5.1) of the W candidate is required to be above 30 GeV, or else the event is disregarded.

Inclusive event selection	
Event cleaning	Reject LAr, Tile and SCT corrupted events and incomplete events
Primary vertex	Hard scattering vertex with at least two tracks
ZZ **veto**	Less than 4 baseline leptons
N **leptons**	Exactly three leptons passing the Z lepton selection
Leading lepton p_T	$p_T^{\text{lead}} > 25$ GeV (in 2015) or $p_T^{\text{lead}} > 27$ GeV (in 2016-2018)
Z **leptons**	Two same flavour oppositely charged leptons passing Z-lepton selection
Mass window	$\lvert M_{\ell\ell} - M_Z \rvert < 10$ GeV
W **lepton**	Remaining lepton passes W-lepton selection
W **transverse mass**	$m_T^W > 30$ GeV

Table 5.4: *Overview of the inclusive event selection. Leading lepton refers to the lepton with the highest transverse momentum p_T in a given event.*

5.3 Background estimation

Various background processes produce final states that mimic those expected from WZ production, affecting the event selection. These processes can be grouped into two broad categories:

1. **Irreducible Background**: These are processes with at least three real leptons in the final state. Leptonic decays of ZZ events are the dominant contribution to irreducible background processes, followed by $t\bar{t}V$ events. Some other processes such as VVV and tZ also contribute slightly to this kind of background. V refers to either the W or Z vector boson.

2. **Reducible Background:** These are processes that include at least one non-prompt (or "fake") lepton. These leptons arise when jets are incorrectly identified as leptons or when non-prompt leptons emerge within jets. Common sources include processes such as Z+jets, $Z\gamma$, $t\bar{t}$, Wt, and WW. A data-driven approach called the Matrix Method [94] is employed to estimate this background.

5.3.1 Irreducible Background

ZZ events

The largest background contribution to the signal region comes from the process $ZZ \to \ell^+\ell^-\ell^+\ell^-$, where one lepton fails the lepton identification requirements or falls outside the acceptance of the detector. Such events are minimised by vetoing events with more than three leptons (Table 5.4).

Dedicated MC events with $q\bar{q} \to ZZ$ and $gg \to ZZ$ processes are simulated to estimate the amount of ZZ events that survive in the WZ selection. The MC is validated in a dedicated control region (CR) enriched in ZZ events. (A control region is defined by a set of selection criteria that isolates a subset of events enriched in a specific background process and depleted in the signal of interest.) The definition of the four-lepton control region is the same as the final WZ event selection (Table 5.4), except that the ZZ veto condition is reversed.

In the ZZ control region, selected events must contain two leptons of the same flavour but opposite charge, and their invariant mass must be within 10 GeV of the Z boson mass ($|M_{\ell\ell} - M_Z| < 10$ GeV). If more than one pair of leptons can form a Z candidate, the pair with the invariant mass closest to the Z boson mass m_Z^{PDG} is chosen. These leptons must pass the Z-lepton criteria specified in Tables 5.2 and 5.3. In addition, the event must include two more leptons: one that fulfils the W-lepton criteria and has a $p_T > 15$GeV and the other that fulfils the baseline lepton criteria and has a $p_T > 5$GeV.

In the control region, a high purity of ZZ events of 88% is obtained. Based on the total event yield observed in data compared to MC in this region, the ZZ MC prediction is scaled by a global factor of 1.10 to normalise the MC prediction to the observed yield in the control region. A global normalisation uncertainty of 10% is additionally assigned to this background to account for theoretical and modelling uncertainties such as scale and PDF variations, following the prescription used in ATLAS Run 2 analysis for this channel [95]. Figure 5.1 shows the key kinematic distributions in the ZZ control region.

$t\bar{t}V$ events

The modelling of $t\bar{t}V$ events uses another control region. This region is selected by applying the full WZ selection criteria (Table 5.4), but in addition requiring two hadronic jets, identified with a b-tag [96], which are assumed to originate from the decay of a b-hadron. Jets in in the central region ($|\eta| < 2.5$) and with $p_T > 25$ GeV are tagged with an 85% b-hadron tagging efficiency [88].

In this control region, a high purity in $t\bar{t}V$ events of 83% is obtained. The $t\bar{t}V$ MC prediction is scaled by a factor of 1.30, derived from the ratio of observed to expected event yields in the $t\bar{t}V$ control region. A 15% global normalisation uncertainty is also assigned to this background, accounting for theoretical modelling uncertainties including scale and generator choices, as recommended in the ATLAS Run 2 analysis for this channel [97]. Figure 5.2 shows the m_T^W distribution in this control region.

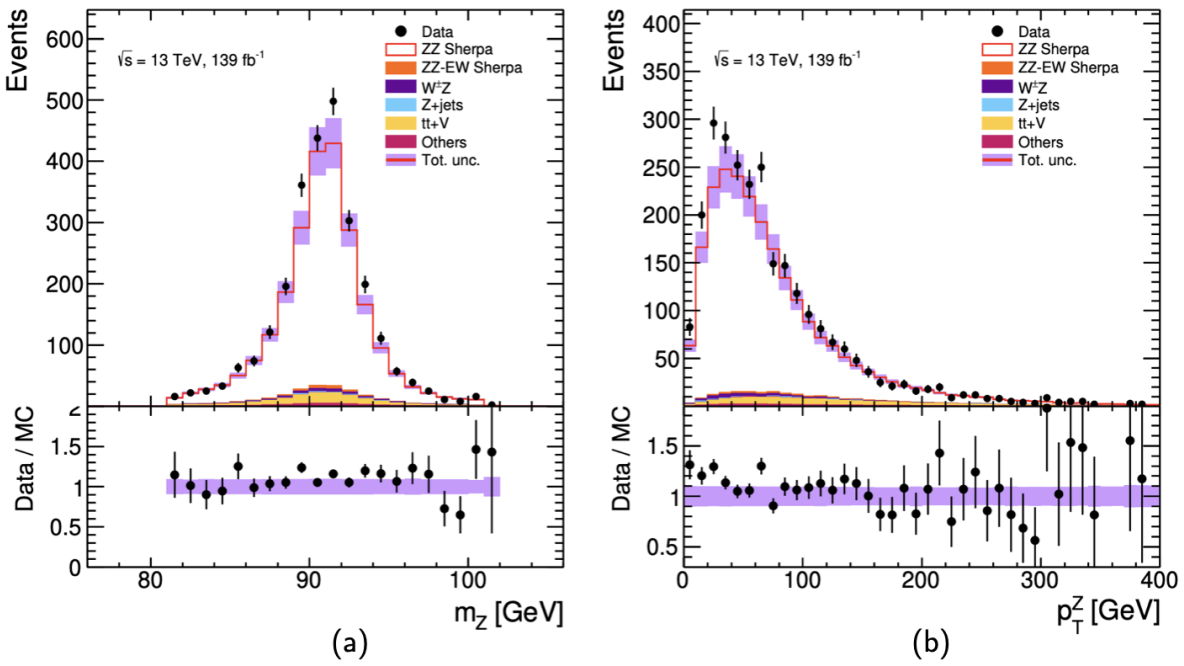

Figure 5.1: *Control distributions in the ZZ control regions of the first Z boson's (a) invariant mass, m_Z, (b) transverse momentum p_T^Z. The violet band represents systematic uncertainties which include a global normalisation uncertainty of 10% on the MC contribution. Taken from [88].*

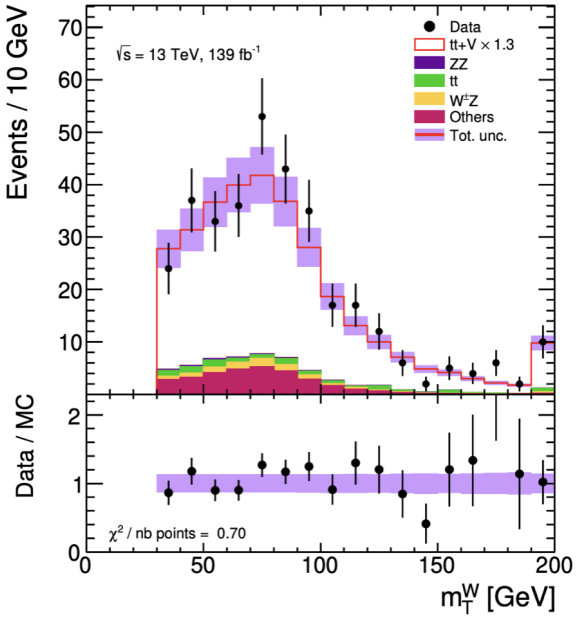

Figure 5.2: *Control distributions in the $t\bar{t}V$ control region for m_T^W. The violet band represents systematic uncertainties which include a global normalisation uncertainty of 15% on the MC contribution. Taken from [88].*

5.3.2 *Reducible Background and the Matrix Method*

The previous section talked about irreducible backgrounds which are estimated using MC simulations and validated in control regions. This approach assumes that the simulation accurately models the identification and isolation criteria for real leptons. However, accurately simulating the detector's response to real leptons is challenging, and discrepancies are typically corrected with scale factors. While these scale factors adjust for discrepancies in real lepton detection, no such corrections exist for objects misidentified as leptons. Consequently, MC simulations might not accurately predict the yield of these misidentified objects in the signal selection. Given these limitations, data-driven methods are preferred for estimating these backgrounds. In this WZ analysis, the Matrix Method is used to estimate this misidentified background.

The Matrix Method is a well-established data-driven technique, previously utilised in several particle physics analyses (for example in [94]). The purpose is to determine, statistically, how many events in the signal region arise from objects misidentified as prompt leptons.

Since fake leptons cannot be identified on an event-by-event basis in data, the estimation must be done using statistical methods. The approach begins by defining a Loose Signal Region (LSR) — a set of events that satisfy the kinematic selections of the signal region but contain leptons that do not pass the Tight lepton selection criteria. These Loose leptons satisfy basic identification requirements but fail stricter cuts, such as isolation.

To estimate how many fake leptons pass the Tight selection and thus contribute to the signal region, a fake factor (F) is introduced. This is measured in a control region that is enriched in fake leptons, such as events dominated by multijet production. The fake factor is defined as:

$$F_i = \frac{f_i}{\bar{f}_i} = \frac{N_T}{N_{!T}}, \tag{5.7}$$

where f_i is the probability that a fake lepton in p_T bin i passes the Tight criteria, and $\bar{f}_i = 1 - f_i$ is the probability that it fails. N_T is the number of fake leptons passing the tight lepton requirements and $N_{!T}$ is the number of fake leptons failing the tight lepton requirements. The fake factor is used to extrapolate from the LSR to predict the number of background events in the Tight signal region.

An illustration of the methodology is shown in Figure 5.3, where the transfer factor F is derived from a control region enriched in fake leptons and applied to the Loose Signal Region. This visual helps clarify how the method statistically extrapolates fake backgrounds into the signal region using data-driven control measurements.

Corrections are applied to account for differences between control and signal regions, such as

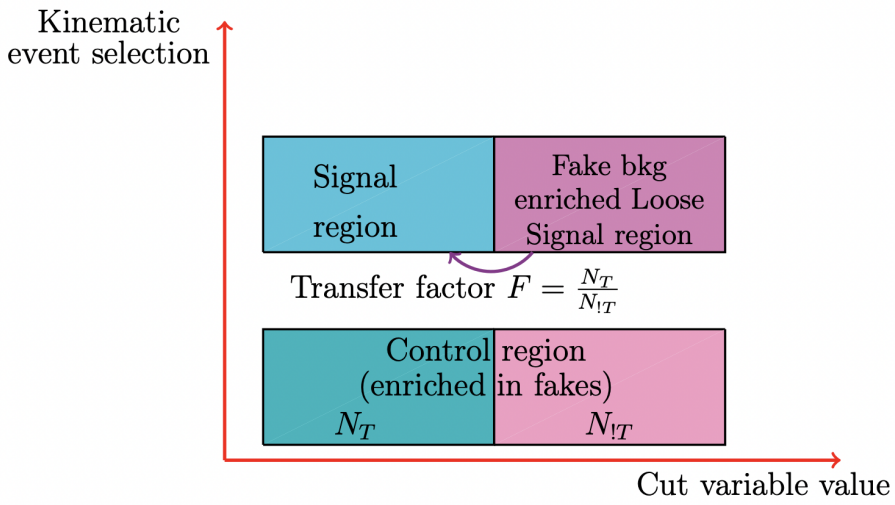

Figure 5.3: *Illustration of the Matrix Method methodology. The transfer factor $F = N_T/N_{!T}$ is measured in a control region enriched in fake leptons and applied to the Loose Signal Region to estimate the fake background in the signal region. Taken from [57].*

detector effects, kinematic mismodelling, or variations in the fake lepton composition.

The Matrix Method provides a formalism for this estimation by categorising events based on whether leptons pass or fail the Tight selection. In this method, leptons are classified as follows:

- **Real Leptons (R):** Prompt electrons or muons produced from the decay of W or Z bosons.
- **Fake, non-prompt Leptons (F):** Objects that are not true leptons but pass the lepton selection criteria, such as hadrons, non-isolated leptons from heavy-flavour decays, or electrons from photon conversions.
- **Tight Leptons (T):** Leptons passing the full signal selection, including identification and isolation criteria (see Tables 5.2 and 5.3). These may include both real and misidentified fake leptons.
- **Loose Leptons (L):** Leptons passing a looser set of criteria (Table 5.5) but failing the Tight selection.

In $W^{\pm}Z$ events, the three leptons in the final state are organised as: the lepton from the W decay, the highest-p_T lepton from the Z, and the second lepton from the Z. Events may contain both real and fake leptons and are categorised as:

- N_{RRR}: Events with three real leptons from prompt decays. This includes genuine $W^{\pm}Z$ events and irreducible backgrounds such as ZZ and $t + Vj$.

Electrons	Muons
$p_T > 15$ GeV	$p_T > 15$ GeV
$\|\eta\| < 2.47$	$\|\eta\| < 2.7$
$!(1.37 < \|\eta\| < 1.52)$	-
Pass `Loose` LH ID	Pass `Medium` LH ID
$\|\Delta z_0 \sin\theta\| < 0.5$ mm	$\|\Delta z_0 \sin\theta\| < 0.5$ mm
$\|d_0/\sigma(d_0)\| < 5$	$\|d_0/\sigma(d_0)\| < 3$

Table 5.5: *Baseline requirements for leptons considered in the Matrix Method. Loose leptons satisfy this selection but fail the tighter signal criteria, whereas Tight leptons pass both. LH ID represents the Likelihood Identification criteria.*

- N_{FRR}: One fake lepton (from W), two real leptons (from Z); dominant in processes like Z+jets, $Z+\gamma$, $t\bar{t}$.
- N_{RRF} and N_{RFR}: One fake lepton misassociated with the Z; seen in Z+jets, $Z+\gamma$, and $t\bar{t}$.
- N_{FFR}, N_{FRF}, N_{RFF}, N_{FFF}: Events with two or more fake leptons; rarer, originating from W+jets, $t\bar{t}$, and QCD.

We define e as the probability that a real lepton is identified as Tight, and f as the probability that a fake lepton is misidentified as Tight. The complementary probabilities are $\bar{e} = 1 - e$ and $\bar{f} = 1 - f$.

The expected event yields in data can be written as an 8×8 matrix equation:

$$\begin{pmatrix} N_{TTT} \\ N_{TTL} \\ N_{TLT} \\ N_{LTT} \\ N_{TLL} \\ N_{LTL} \\ N_{LLT} \\ N_{LLL} \end{pmatrix} = \begin{pmatrix} e_1e_2e_3 & e_1e_2f_3 & e_1f_2e_3 & e_1f_2f_3 & f_1e_2e_3 & f_1e_2f_3 & f_1f_2e_3 & f_1f_2f_3 \\ e_1e_2\bar{e}_3 & e_1e_2\bar{f}_3 & e_1f_2\bar{e}_3 & e_1f_2\bar{f}_3 & f_1e_2\bar{e}_3 & f_1e_2\bar{f}_3 & f_1f_2\bar{e}_3 & f_1f_2\bar{f}_3 \\ e_1\bar{e}_2e_3 & e_1\bar{e}_2f_3 & e_1\bar{f}_2e_3 & e_1\bar{f}_2f_3 & f_1\bar{e}_2e_3 & f_1\bar{e}_2f_3 & f_1\bar{f}_2e_3 & f_1\bar{f}_2f_3 \\ \bar{e}_1e_2e_3 & \bar{e}_1e_2f_3 & \bar{e}_1f_2e_3 & \bar{e}_1f_2f_3 & \bar{f}_1e_2e_3 & \bar{f}_1e_2f_3 & \bar{f}_1f_2e_3 & \bar{f}_1f_2f_3 \\ e_1\bar{e}_2\bar{e}_3 & e_1\bar{e}_2\bar{f}_3 & e_1\bar{f}_2\bar{e}_3 & e_1\bar{f}_2\bar{f}_3 & f_1\bar{e}_2\bar{e}_3 & f_1\bar{e}_2\bar{f}_3 & f_1\bar{f}_2\bar{e}_3 & f_1\bar{f}_2\bar{f}_3 \\ \bar{e}_1e_2\bar{e}_3 & \bar{e}_1e_2\bar{f}_3 & \bar{e}_1f_2\bar{e}_3 & \bar{e}_1f_2\bar{f}_3 & \bar{f}_1e_2\bar{e}_3 & \bar{f}_1e_2\bar{f}_3 & \bar{f}_1f_2\bar{e}_3 & \bar{f}_1f_2\bar{f}_3 \\ \bar{e}_1\bar{e}_2e_3 & \bar{e}_1\bar{e}_2f_3 & \bar{e}_1\bar{f}_2e_3 & \bar{e}_1\bar{f}_2f_3 & \bar{f}_1\bar{e}_2e_3 & \bar{f}_1\bar{e}_2f_3 & \bar{f}_1\bar{f}_2e_3 & \bar{f}_1\bar{f}_2f_3 \\ \bar{e}_1\bar{e}_2\bar{e}_3 & \bar{e}_1\bar{e}_2\bar{f}_3 & \bar{e}_1\bar{f}_2\bar{e}_3 & \bar{e}_1\bar{f}_2\bar{f}_3 & \bar{f}_1\bar{e}_2\bar{e}_3 & \bar{f}_1\bar{e}_2\bar{f}_3 & \bar{f}_1\bar{f}_2\bar{e}_3 & \bar{f}_1\bar{f}_2\bar{f}_3 \end{pmatrix} \begin{pmatrix} N_{RRR} \\ N_{RRF} \\ N_{RFR} \\ N_{FRR} \\ N_{RFF} \\ N_{FRF} \\ N_{FFR} \\ N_{FFF} \end{pmatrix} \tag{5.8}$$

The matrix coefficients encode the probabilities that real or fake leptons pass or fail the Tight criteria. Since N_{FFF} and N_{LLL} are negligible, they are removed, reducing the system to a 7×7 matrix.

After inverting Equation 5.8, one can solve for the number of events in each category [88]. In particular, the number of fake leptons contributing to the signal region is estimated using:

$$N_{\text{fake}} = \sum_i N_{\text{TTL}}^{\text{red},i} F_Z^i + \sum_i N_{\text{TLT}}^{\text{red},i} F_Z^i + \sum_i N_{\text{LTT}}^{\text{red},i} F_W^i - \sum_{i,j} N_{\text{TLL}}^{\text{red},ij} F_Z^i F_Z^j - \sum_{i,j} N_{\text{LTL}}^{\text{red},ij} F_W^i F_Z^j - \sum_{i,j} N_{\text{LLT}}^{\text{red},ij} F_W^i F_Z^j \,, \tag{5.9}$$

where i and j run over bins in fake lepton p_T. F_W^i and F_Z^j are fake factors for fake leptons originating from W and Z selections, respectively. N_{ijk}^{red} denotes the number of events in the LSR after subtracting irreducible backgrounds (from MC):

$$N_{ijk}^{\text{red}} = N_{ijk} - N_{ijk}^{\text{irr}} \,. \tag{5.10}$$

Electrons and muons from W and Z boson candidates have different isolation and identification criteria, so separate fake efficiencies are calculated for each. The control regions (CRs) used to measure these fake factors must closely match the composition of the signal regions. The main sources of fake leptons are:

- **W leptons**: Mainly from Z+jets or and Zγ processes.
- **Z leptons**: Dominantly from $t\bar{t}$ events.

The different selection criteria for each of the control region is listed in Table 5.6.

To validate the methodology, a closure test is performed using Monte Carlo simulation. The first row of Table 5.7 shows the number of events in the signal region containing at least one fake lepton, as identified directly in MC using truth-level information. This includes contributions from , Z+jets, and $Z\gamma$ events. The second row shows the fake background estimated using the Matrix Method, where fake factors are derived from MC control regions and applied to Loose Signal Regions, mirroring the data-driven approach. The final row presents the ratio of the Matrix Method prediction to the MC truth. Good agreement within uncertainties across all channels confirms the reliability and robustness of the estimation procedure.

	Z+jets CR	**Photon conversion CR**	$t\bar{t}$ **CR**
Object selection	• ≥ 2 Z-type leptons ℓ, same flavour, opposite charge • $\lvert m_{\ell\ell} - m_Z^{PDG} \rvert < 15$ GeV • Fake lepton is highest p_T Matrix Method lepton • Construct "fake W" from fake and E_{miss}^T • $m_T^W < 30$ GeV • $E_{\text{miss}}^T < 30$ GeV (if fake electron) • $m_{\ell\ell} > 81$ GeV (if fake electron)	• ≥ 2 Z-type muons, opposite charge ($\mu^+\mu^-$) • $55 < m_{\mu\mu} < 85$ GeV • Fake lepton is highest p_T Matrix Method lepton • Construct "fake W" from fake and E_{miss}^T • $m_T^W < 30$ GeV • $E_{\text{miss}}^T < 30$ GeV • $m_{\mu^+,\mu^-,\text{fake}} < 105$ GeV	• ≥ 1 Z-type electron e_Z • ≥ 1 Z-type muon μ_Z • charge(μ_Z) · charge(e_Z) < 0 • Fake lepton is highest p_T Matrix Method lepton • Lepton with different flavour than fake passes W-lepton requirements: l_W • charge(fake) · charge(l_W) > 0

Table 5.6: *Summary of the control regions selection. Taken from [88].*

Source	eee	$e\mu\mu$	μee	$\mu\mu\mu$	**Total**
($t\bar{t}$ + Z+jets + Zγ) MC	272.4 ± 8.6	337.9 ± 9.8	129.7 ± 6.4	274.7 ± 8.8	1014.7 ± 17.0
Matrix Method result	271.4 ± 26.2	344.3 ± 28.2	129.5 ± 7.6	275.1 ± 16.0	1020.3 ± 77.6
Ratio	1.004 ± 0.102	0.981 ± 0.085	1.001 ± 0.077	0.999 ± 0.066	0.994 ± 0.077

Table 5.7: *Comparison between $t\bar{t}$ + Z+jets + Zγ MC and the Matrix Method result [88].*

5.4 Observables of Interest

The results of this analysis are derived from the measurement of observables related to the W, Z, and WZ system. These measurements are made by reconstructing the bosons from the detected leptons. Broadly speaking, the observables fall into two categories: Kinematic observables and angular observables. Kinematic observables are those directly measured or calculated from the detector data, reflecting the intrinsic properties of the particles or systems in the lab frame. In contrast, angular observables are derived from these kinematic measurements, often requiring transformations into different reference frames to reveal the angular relationships between particles.

5.4.1 Kinematic observables

The following kinematic observables are studied within the scope of the thesis. Differential distributions of each of these observables are made in binned histograms.

p_T^Z

The transverse momentum of the Z is calculated by adding the 4-momentum vectors of the two reconstructed Z-leptons. The transverse momentum (p_T) of the Z boson gives an indication of how much the Z boson has been accelerated or 'boosted' in the transverse plane. This boost affects the energy and momentum distribution of the decay products.

p_T^W

The transverse momentum of the W is calculated by adding the transverse vectors of the reconstructed neutrino and the reconstructed W-lepton. This measurement gives an indication of how much the W boson has been accelerated in the transverse plane. Because it is in the transverse plane, the inaccurate estimation of the longitudinal component of the neutrino, p_z^ν, is avoided.

m_T^{WZ}

The m_T^{WZ} observable (Equation 5.6) is the invariant mass of the "WZ-system" in the transverse plane. It is constructed from adding the 4-momentum vectors of the reconstructed W and Z bosons. Because this is a quantity of the WZ system, it is a good probe of the triple-gauge vertex in the s-channel production mode (see Chapter 2.5.1).

p_T^ν

The transverse momentum of the neutrino, p_T^ν, is determined by the E_T^{miss} of the event.

5.4.2 *Angular observables*

The 4-vectors of the reconstructed bosons, and all their corresponding quantities listed above are calculated in the lab frame. This has the draw-back that because events will have different WZ system momenta, the decay products will be boosted differently.

Angular distributions are useful because one can transform the event to the centre of mass (CM) frame, which will give observable distributions that are independent of the boost. Angles, being ratios of measured quantities, often have reduced systematic uncertainties because many detector-related errors cancel out when taking ratios. This makes angular observables particularly useful for precision measurements. The following angles are considered in the analysis:

$|\cos\theta_V|$

The reconstructed W and Z four vectors build the WZ system rest frame. By definition, in this rest frame, the W and Z bosons will be back to back, with equal and opposite momentum. The angle of the boson with respect to the beam-line (z axis) can then be found and the cosine of this angle is denoted as $\cos\theta_W$ or $\cos\theta_Z$, shown in Figure 5.4. Because the decay is back to back, the magnitude for cosine of both the angles are the same. Since the reconstruction of the Z boson is better, the absolute value of this is taken as the measurement for the observable $|\cos\theta_V|$. However, it should be noted that to obtain the WZ rest-frame, information about the p_z^ν is needed, and so while the Z boson is very well measured, this observable is affected by the uncertainty of the neutrino reconstruction.

$\cos\theta^*_{Z_\ell}$ **and** $\cos\theta^*_{W_\ell}$

Also considered is the angle at which the leptons decay relative to the direction of their parent bosons. The leptons are thus boosted twice: the first boost takes them from the lab frame to the WZ system rest frame and the second boost takes them to their parent boson rest frame. In this rest frame, the cosine of the angle the lepton makes with respect to the direction of the parent boson is calculated. This is also shown in Figure 5.4.

For the case of Z, the lepton (negatively charged) is considered. For the case of W, the cosine of the angle is multiplied by the charge of the lepton (as the lepton can be either positively or negatively charged).

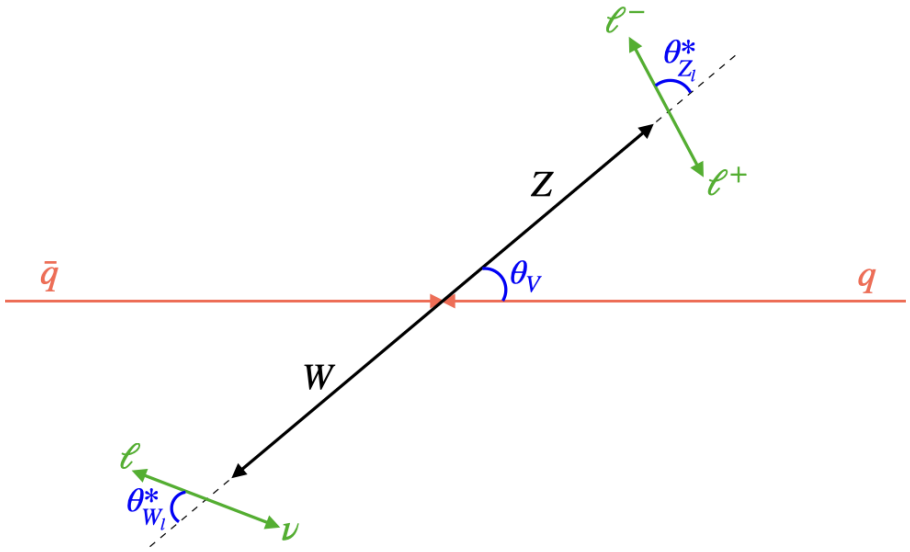

Figure 5.4: *Illustration of the cosine angular observables. θ_V is the angle that the Z boson makes with the beamline in the WZ rest frame. $\theta^*_{Z_\ell}$ and $\theta^*_{W_\ell}$ are the angles that the leptons make with respect to the parent boson direction in the rest frame of the boson.*

$\phi^*_{Z_\ell}$ and $\phi^*_{W_\ell}$

For these angles, a new plane is defined using the direction of the boson and the beam direction. Specifically, in the rest frame of each boson $V = W, Z$, a right-handed coordinate system (x', y', z') is constructed as follows:

- The z'-axis is aligned with the boson momentum direction $\hat{b} = \vec{p}_V/|\vec{p}_V|$, as observed in the WZ centre-of-mass frame,
- The y'-axis is given by $\hat{y}' = \hat{z}_{\text{beam}} \times \hat{b}$, where $\hat{z}_{\text{beam}}$ is the beam direction in the laboratory frame,
- The x'-axis is then defined to complete a right-handed basis, $\hat{x}' = \hat{y}' \times \hat{b}$.

The azimuthal angles $\phi^*_{Z_\ell}$ and $\phi^*_{W_\ell}$ are defined as the angles between the projection of the charged lepton momentum (from the respective boson decay) onto the (x', y') plane and the x'-axis. A schematic illustrating this construction is shown in Figure 5.5.

It is important to note that this angle, like the polar angle, is defined in the parent boson rest frame. The choice of this frame ensures consistency and allows for a proper interpretation of spin correlation effects.

In the case of Z bosons, the negatively charged lepton is considered for defining $\phi^*_{Z_\ell}$. For W bosons, however, no charge multiplication is applied to the angle. This is motivated by the

observation that the azimuthal angle the negative lepton makes around the W^- is equivalent (up to a sign) to the angle the positive lepton makes around the W^+. Therefore, summing the distributions of $\phi^*_{W_\ell}$ for both W^+ and W^- preserves all relevant information and does not wash out physical effects.

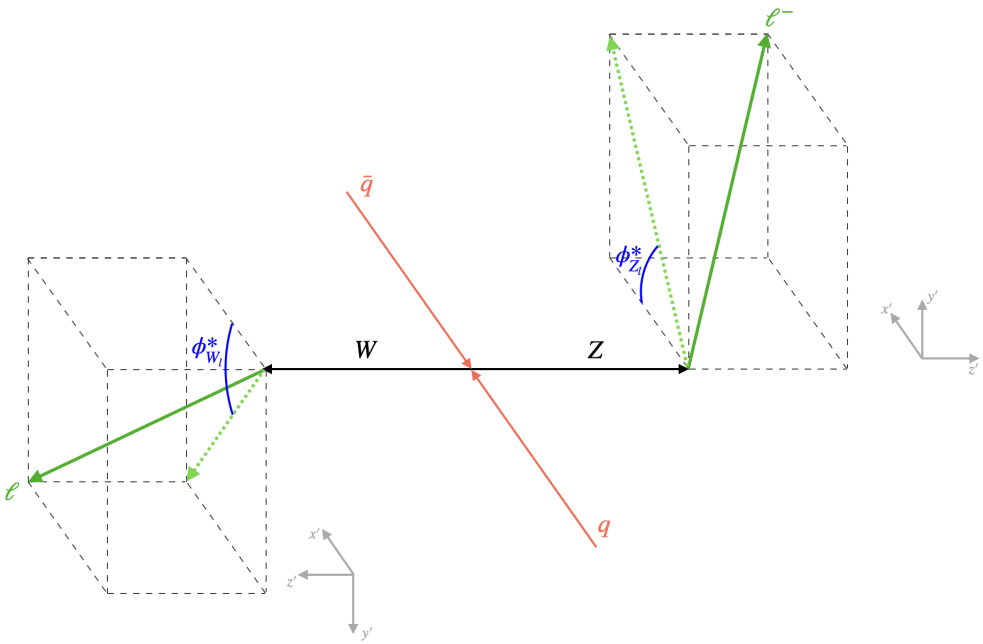

Figure 5.5: *Illustration of the ϕ^* of the leptons with respect to the plane defined by the beam direction and the parent boson direction, in the rest frame of the parent boson. A right-handed axis convention is used, as defined in the text.*

5.5 Unfolding

5.5.1 Particle level definition

To allow a direct comparison between detector-level measurements and theoretical predictions, it is necessary to correct the observed data for detector effects such as limited resolution, acceptance, and reconstruction efficiency. This procedure is known as unfolding. The goal of unfolding is to recover the underlying particle level (truth-level) distributions that would be measured by an ideal detector. In this analysis, the measurement is unfolded to the level of *dressed leptons*.

Dressed leptons are defined by incorporating nearby photons that originate from final state radiation (FSR), a process in quantum electrodynamics (QED) in which charged leptons emit photons after the hard scattering process. This radiation can significantly alter the measured

momentum and direction of the lepton, particularly for electrons. Therefore, accurate treatment of FSR is essential when defining lepton-level observables.

In experimental and theoretical contexts, leptons are typically categorised into three different definitions based on how QED radiation is treated:

- **Bare leptons:** Leptons after final state radiation has occurred, excluding any radiated photons. These represent the particles directly produced by the interaction but do not account for energy lost to photon emission.
- **Dressed leptons:** Leptons reconstructed by combining the bare lepton with all photons radiated within a small angular cone around it. In this analysis, photons within $\Delta R < 0.1$ of the lepton are included. This reflects the way electrons and muons are reconstructed in the detector, where nearby photon energy is typically clustered with the lepton, especially in the case of electromagnetic showers.
- **Born leptons:** Leptons at the Born (tree-level) stage of the interaction, before any QED radiation has taken place. These are useful for theoretical calculations but do not correspond to directly measurable quantities.

5.5.2 Unfolding methodology

In this analysis each observable defined in Section 5.4 (after the event and object selections of Sections 5.2) is filled into a reconstructed (detector-level) histogram using the selected reconstructed electrons, muons and MET objects. Background contributions b_i (irreducible from MC, reducible from the Matrix Method) are subtracted bin-by-bin. The resulting background-subtracted reconstructed spectrum is then unfolded, observable by observable, to the fiducial particle level defined with dressed leptons. Dressing is applied only on the truth side when building the response; reconstructed leptons are used as "undressed".

The relation between observed data at the detector level and the true underlying distribution at the particle level is written as

$$n_i = \sum_j R_{ij}\, s_j + b_i, \tag{5.11}$$

where n_i denotes the total number of observed events in the i-th reconstructed bin, s_j is the number of signal events in the j-th truth (fiducial) bin, R_{ij} is the response matrix, which maps the migration of signal events from the fiducial bins to the reconstructed bins and b_i represents the background events present in the i-th bin.

The response matrix R_{ij} combines the effects of :

- **Efficiency correction**: This accounts for both inefficiencies in the detector and events migrating out of the signal region due to finite resolution and limited acceptance. It is defined as the ratio of simulated events passing both the reconstructed and fiducial selections to those passing only the fiducial selection. The efficiency correction is applied in bins based on the fiducial phase-space.

- **Migration matrix**: The migration matrix captures how events move between the truth and reconstructed regions. Specifically, the entry ij describes the probability that an event generated in the j-th truth bin is reconstructed in the i-th bin.

- **Fiducial correction**: This correction addresses effects that cause events generated outside the fiducial region to be reconstructed inside the signal region. It is defined as the ratio of events passing both reconstructed and fiducial selection criteria over those passing only the reconstructed selection. This correction is applied on a per-reconstructed-bin basis.

Two other parameters called Stability and Purity also inform the unfolding procedure. Stability is the fraction of truth events in a bin that are reconstructed in the same bin, while purity is the fraction of reconstructed events in a bin that originated from the same truth bin.

A schematic of the unfolding components is shown in Figure 5.6 and can be mathematically described as an inversion of Equation 5.11:

$$s_j = \sum_i R_{ij}^{-1} \left(n_i - b_i\right). \tag{5.12}$$

Direct algebraic manipulation of the response matrix is usually not feasible due to potential issues of the matrix being singular, which can lead to numerical instability. Additionally, this approach often results in large statistical fluctuations and uncertainties. Multiple approaches exist to unfold the data in a more regularised way. This analysis uses the Bayesian Iterative method [99].

In this approach, a prior guess of the true distribution is made. Using the response matrix, Bayes' theorem is applied iteratively to refine the guess. After each iteration, the estimate of the true distribution is updated based on the measured data. The process continues until the estimate stabilizes, providing a corrected distribution that accounts for detector effects.

The Iterative Bayes technique is implemented in the VIPUnfolding framework which calls the RooUnfold [100] package. The framework implements the determination of data statistical uncertainty using multiple pseudo-datasets (called "toys") as was done in [94].

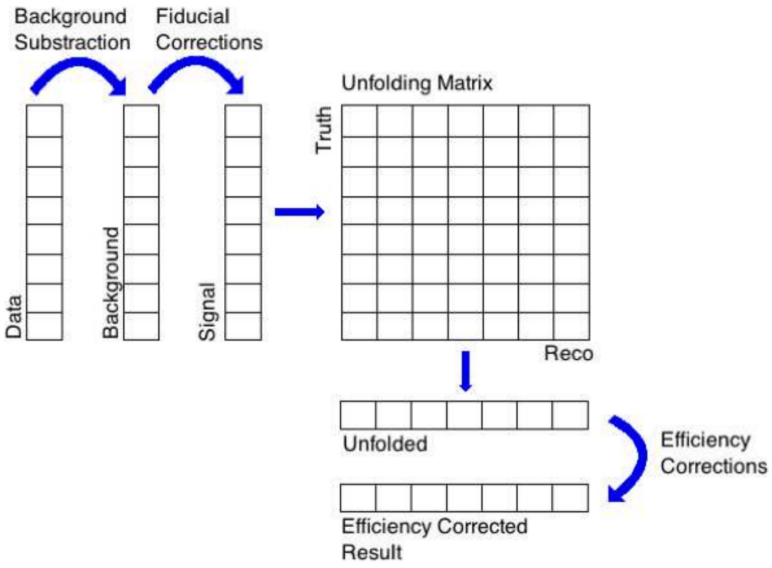

Figure 5.6: *Schematic view of the unfolding procedure. Taken from [98].*

5.6 Systematic Uncertainties

5.6.1 Systematic uncertainties from particle reconstruction

Sources of systematic uncertainty from particle reconstruction are related to the physics objects used in this analysis. These uncertainties are centrally derived by specialised performance groups within ATLAS. These groups compile sets of variations that encompass all potential uncertainties, typically covering object identification, reconstruction, isolation, and kinematics measurements. The variations are applied to all MC samples, and their effects are propagated to the final yields and distributions.

Sources of experimental systematic uncertainty include pile-up reweighting, as well as uncertainties in electron energy, muon momentum, missing transverse energy (E_T^{miss}), and jet energy scales and resolutions (see Chapter 4). Additional uncertainties come from the scale factors applied to simulations to match data for trigger, reconstruction, identification, and isolation efficiencies. These uncertainties affect both signal predictions and MC-based background estimates.

5.6.2 Luminosity uncertainty

The uncertainty in the combined 2015–2018 integrated luminosity is 0.83% [101], determined using the LUCID-2 detector [102]. This uncertainty is applied to the normalisation of the signal and to all background estimates based solely on MC simulations (irreducible backgrounds).

5.6.3 *Background uncertainty*

Uncertainty in the reducible background events is determined via the data-driven Matrix method approach detailed in Section 5.3.2. The reducible backgrounds have a total uncertainty of the order of 20% - 25% [88].

A flat normalisation uncertainty is applied to irreducible backgrounds, meaning that the same percentage uncertainty is assigned uniformly across all bins of the distribution. The overall magnitude of these uncertainties is estimated either from scale and PDF uncertainties or by comparing the predicted and observed cross-sections in dedicated analyses. These are listed in Table 5.8.

Background	**Unc.**
$t\bar{t}+V$	15%
tZ	15%
$WZjj$–EW	25%
VVV	30%
ZZ	10%

Table 5.8: *Flat normalisation uncertainties for the irreducible background processes.*

5.6.4 *Parton Distribution Function (PDF) uncertainty*

The PDF set used for simulating the MC WZ samples is the `NNPDF 3.0` PDF set. Following the PDF4LHC recommendations [103], a 68% confidence level for the PDF uncertainty is obtained. The PDF uncertainty is evaluated as the standard deviation of results computed using the 100 `NNPDF 3.0` replicas, which corresponds to a 68% confidence level. In the NNPDF framework each replica is produced by refitting a bootstrap replica of the experimental data, so the ensemble of replicas samples the full statistical and systematic spread allowed by current measurements. For each bin i in the observable's histogram, the uncertainty is calculated as:

$$\Delta_{\text{PDF}} N_i = \sqrt{\frac{1}{n_{\text{rep}}-1}\sum_{k=1}^{n_{\text{rep}}}\left(N^{(k)}_{i,\text{NNPDF}} - \langle N_{i,\text{NNPDF}}\rangle\right)^2}, \tag{5.13}$$

where $k \in \{0, 1, 2, \ldots, n_{\text{rep}}\}$, and $n_{\text{rep}} = 100$, with $k = 0$ corresponding to the central PDF. The mean of the PDFs is calculated as:

$$\langle N_{i,\text{NNPDF}}\rangle = \frac{1}{n_{\text{rep}}}\sum_{k=1}^{n_{\text{rep}}} N^{(k)}_{i,\text{NNPDF}}. \tag{5.14}$$

5.6.5 QCD scale uncertainty

The matrix element of a process depends not only on the kinematics of the incoming and outgoing particles but also on the renormalisation scale μ_R and the factorisation scale μ_F (see Section 2.4.1). Ideally, the choice of these scales would have no impact on the results if all orders of perturbation theory could be considered, but this is not currently feasible. To account for the uncertainty introduced by the scale choices, a procedure is employed where each scale is varied independently by factors of 0.5 and 2.0 relative to its nominal value. Excluding the extreme cases of $\{0.5, 0.5\}$ and $\{2, 2\}$ for (μ_R, μ_F) (as they represent the largest possible deviations from the nominal scales which can lead to unrealistic uncertainty estimates) the maximum and minimum values of the cross-sections are taken. The differences between these values and the nominal cross-section are used to define the positive and negative scale uncertainties.

CHAPTER 6

SMEFT Predictions, Setup and Statistical Framework

6.1 Predictions and observables in SMEFT

Beyond the Standard Model effects can manifest themselves in observables that can be seen with the detector. Truth-level distributions are then be obtained through unfolding (section 5.5). This analysis examines all angular observables from Section 5.4.2 and the m_T^{WZ} kinematic observable. For this high-statistics process, cross-sections are analysed differentially as binned distributions.

6.1.1 Parameterisation of SMEFT - The Decomposition method

In SMEFT, the coupling strength of the new physics operators is parameterised through the Wilson coefficients. From the Effective Lagrangian given in Equation 2.23, the amplitude matrix element can be found. The square of the amplitude matrix element ($\mathcal{A}$) gives the cross-section in terms of the Wilson coefficients:

$$\begin{aligned}\sigma_{\text{SMEFT}} \propto |\mathcal{A}_{\text{SMEFT}}|^2 &= |\mathcal{A}_{\text{SM}} + \sum_i \mathcal{A}_i^{(6)}|^2 \\ &= |\mathcal{A}_{\text{SM}}|^2 \\ &\quad + \sum_i \frac{c_i^{(6)}}{\Lambda^2} 2\Re\left(\mathcal{A}_i^{(6)} \mathcal{A}_{\text{SM}}^*\right) \\ &\quad + \sum_i \left(\frac{c_i^{(6)}}{\Lambda^4}\right)^2 |\mathcal{A}_i^{(6)}|^2 \\ &\quad + \sum_{i<j} \frac{c_i^{(6)} c_j^{(6)}}{\Lambda^4} 2\Re\left(\mathcal{A}_i^{(6)} \mathcal{A}_j^{(6)*}\right) \quad ,\end{aligned} \tag{6.1}$$

where only dimension-6 or lower operators are considered. The first term in the expansion is the square of the purely SM amplitude. The second term is the interference term of the SM and the SMEFT amplitudes (also called the linear term). The third term is called the quadratic term which is the square of the SMEFT amplitude, and the fourth term is called the cross-term which is the interference of a SMEFT operator's amplitude with another SMEFT operator's amplitude.

The cross-section predictions can be broken down (i.e. "decomposed") into the parts described above:

$$\sigma_{\text{SMEFT}} = \sigma_{\text{SM}} + \sigma_{\text{int}} + \sigma_{\text{quad}} + \sigma_{\text{cross}} \quad . \tag{6.2}$$

This procedure is known as the Decomposition method. To minimize the perturbative QCD uncertainties in extracting the SMEFT Wilson coefficients, the parameterisation of the predicted cross-section can be calculated as a relative correction to the Standard Model prediction at the highest available order for each process:

$$\sigma_{\text{SMEFT}} = \sigma_{\text{SM}}^{\text{(N)NLO}} \times \left(1 + \frac{\sigma_{\text{int}}^{\text{(N)LO}}}{\sigma_{\text{SM}}^{\text{(N)LO}}} + \frac{\sigma_{\text{quad}}^{\text{(N)LO}}}{\sigma_{\text{SM}}^{\text{(N)LO}}} + \frac{\sigma_{\text{cross}}^{\text{(N)LO}}}{\sigma_{\text{SM}}^{\text{(N)LO}}}\right). \tag{6.3}$$

Therefore, any observable O_b, such as the cross-section of a specific process in a measurement bin b, can be expressed as:

$$O_b = O_b^{\text{SM}} \left(1 + \sum_i A_{bi} c_i + \sum_i B_{bi} c_i^2 + \sum_{i<j} C_{bij} c_i c_j\right), \tag{6.4}$$

where O_b^{SM} is the Standard Model (SM) value, and A_{bi}, B_{bi}, and C_{bij} represent the linear, quadratic, and cross-term coefficients of the weights relative to the SM value. Once the values of A_{bi}, B_{bi}, and C_{bij} are known, a continuous prediction of O_b in terms of the Wilson coefficients is available.

The σ_{quad} and σ_{cross} terms are suppressed by a factor of Λ^{-4}. The lowest-order cross-section terms generated by dimension-8 operators that involve interference between SM and dimension-8 SMEFT operators are also suppressed by a factor Λ^{-4}. Since this analysis focuses exclusively on dimension-6 operators with at most two non-zero Wilson coefficients at a time, we consistently set all dimension-8 operator coefficients to zero. This simplified approach is justified because we are specifically interested in isolating and constraining the effects of individual dimension-6 operators and their pairwise interactions, without the additional complexity introduced by dimension-8 contributions that would compete at the same order as our quadratic and cross-terms.

6.2 SMEFT Monte-Carlo Generation

Observables for different configurations of Wilson coefficient parameters are estimated using Monte Carlo simulations. SMEFT Universal FeynRules Output (UFO) [104] models, like `SMEFTsim 3.0` [40] and `SMEFTatNLO` [105], are integrated with Monte Carlo generators such as `MadGraph5_aMC@NLO` [53] for simulating the hard-scatter process. Following this, `PYTHIA` [51] is used for particle showering to simulate particle-level events. These events can then be processed through detector simulations to obtain the observable distributions at the detector level.

SMEFT UFO models in MadGraph allow for generating separate contributions of the matrix element squared, $|\mathcal{A}_{\text{SMEFT}}|^2$, by making use of syntax that separates the different terms arising from the matrix element squared equation. For instance, in `SMEFTsim`, it is possible to generate separately the distributions[1] for σ_{SM}, σ_{int}, and σ_{quad} or σ_{cross} [40].

For the thesis, the effect of SMEFT operators is simulated at leading order with the $\{m_W, m_Z, G_F\}$ electroweak input parameter scheme. All lepton generations and the first two quark generations are treated as massless. The `top` (section 2.3.3) flavour symmetry is used, to be as general as possible.

Dedicated samples for the SM as well as the linear and quadratic effects of dimension-6 operators, including cross terms, are generated at leading order using `MadGraph5_aMC@NLO version 2.9.9` and the `SMEFTsim 3.0` model. These events are interfaced with `Pythia 8.244` for parton showering and hadronisation. Decays of bottom and charm hadrons are handled by `EvtGen` [49]. Particle-level events are subsequently analysed in the inclusive phase space defined in Section 5.1 using `Rivet 3.1.2` [106] (a generator-independent framework that applies particle-level analyses to Monte-Carlo events to validate and tune Monte Carlo generators).

The presence of dimension-6 operators can alter the mass and width of intermediate particles, particularly when these particles are on-shell (at resonance). This occurs because these higher-dimensional operators introduce modifications to the particle self-energies and couplings, which directly affect their physical properties. When particles are on-shell, these modifications become especially significant as they alter the position and shape of the resonance peak in scattering amplitudes, leading to measurable deviations in experimental observables. These effects are treated in calculations by computing propagator corrections using linearised SMEFT expansions while neglecting quadratic terms, as implemented in tools like `SMEFTsim 3.0` [40, 107].

Higher-order QCD and electroweak corrections (section 2.5.1) are approximately included

[1] SM only: `NP^2==0`. With only c_i nonzero, `NP^2==1` isolates the linear piece A_{bi} in σ_{int}; `NP^2==2` gives the quadratic B_{bi} in σ_{quad}. For the cross term C_{bij}, turn on c_i and c_j with `NP^2==2` and subtract the individual B_{bi} and B_{bj}.

under the assumption that their relative effect remains unchanged by the presence of dimension-6 SMEFT operators [107]. To emulate NLO QCD effects, a 'merged' Monte Carlo generation strategy is employed. This involves simulating an additional process that includes the final states of interest as well as an extra jet. This approach incorporates leading-order proton–proton diagrams that produce a jet in the final state, effectively including all next-to-leading-order process that do not involve loops, by modelling an additional hard jet in the matrix element calculation instead of the Parton shower. This method is referred to as the "0+1j" strategy, where both the signal process and the signal plus one jet process are simulated.

When multiple processes are specified, `MadGraph5_aMC@NLO` automatically calculates the cross-section for each process. The program then generates events for each process in proportion to these calculated cross-sections.

6.2.1 Validation of the merged sample strategy with the best SM prediction

The 'merged' MC strategy of adding new processes with the same final state but including a jet is a way to include some NLO QCD effects while still generating the process at LO. This strategy is not only computationally efficient but also provides the opportunity to probe multiple EFT operators simultaneously using the decomposition method: a feature not available with `SMEFTatNLO` [105, 108]. It is pertinent to note, however, that the 0+1j merged solution tries to only model NLO behaviour by modelling of additional jet radiation - not by considering virtual corrections such as loops.

A state-of-the-art $WZ \to \ell\nu\ell\ell$ SM MC sample is produced using the `POWHEGBOX v2` [109–111] generator, which simulates the WZ [112] production processes at NLO accuracy in QCD. Events were interfaced to `PYTHIA v8.210` [51] for the modelling of the parton shower, hadronisation, and underlying event, with parameters set according to the `AZNLO` tune [113]. The `CT10` PDF set [114] was used for the hard-scattering processes, whereas the `CTEQ6L1` PDF set [115] was used for the parton shower. The `EVTGEN v1.2.0` program [49] was used to decay bottom and charm hadrons. The factorisation and renormalisation scales (section 2.4.2) were set to half the invariant mass of the boson pair ($m_{WZ}/2$) [94]. An invariant mass of $m_{\ell\ell} > 4$ GeV was required at matrix-element level for any pair of same-flavour charged leptons [88].

The influence of higher-order QCD and electroweak corrections on both SM predictions for WZ production is evaluated using fixed-order calculations performed with `MATRIX` [116]. These predictions achieve NNLO accuracy in QCD and NLO in electroweak theory. Photon-induced contributions are included at NLO electroweak accuracy, using the `NNPDF3.1@nnlo` PDF set, with photon content incorporated through the `LUX`QED method [117]. The electroweak couplings are

derived from gauge-boson masses in the G_μ scheme [88]. The dynamic QCD scales are defined as half the sum of the transverse masses of the two gauge bosons [88].

Predictions from MATRIX are compared with those from POWHEG+PYTHIA in bins of the observables of interest. Figure 6.1 presents the differential distributions for the full list of observables, including $\cos\theta^*_{W\ell}$, $\cos\theta^*_{Z\ell}$, $\phi^*_{W\ell}$, $\phi^*_{Z\ell}$, $|\cos(\theta_V)|$, and m_T^{WZ} (see Section 5.4). Since NLO QCD predictions alone are insufficient to fully describe the data, as demonstrated in Figure 6.1, POWHEG+PYTHIA predictions are scaled to match MATRIX predictions described in the previous paragraph.

The POWHEG+PYTHIA8 predictions are rescaled using the following strategy:

- A bin-by-bin rescaling to MATRIX predictions is performed to incorporate higher-order corrections to NNLO QCD $\oplus$ NLO EW in the matrix element calculation.

Now that a method has been established to scale the SM NLO in QCD sample to the state-of-the-art WZ MATRIX correction, the validation of the 0+1j merged scheme methodology can be done for the SM.

The 0+1j scheme includes a subset of the NLO QCD processes that are fully incorporated in the POWHEG+PYTHIA sample. Table 6.1 compares the fiducial cross-sections of three SM MC samples to the MATRIX prediction: the MadGraph 0+1j, MadGraph 0j, and the POWHEG+PYTHIA generation.

Generator and Scheme	**Fiducial Cross-section [fb]**	**% difference to MATRIX**
MATRIX NNLO QCD $\oplus$ NLO EWK	63.26	0.00%
POWHEG + PYTHIA NLO QCD	52.06	17.70%
MadGraph + PYTHIA LO: 0+1j merged	45.92	27.41%
MadGraph + PYTHIA LO: 0j	30.14	52.35%

Table 6.1: *Comparison of Fiducial Cross-sections and their differences to the MATRIX NNLO QCD $\oplus$ NLO EWK prediction of SM generated samples*

The difference in fiducial cross-section between POWHEG + PYTHIA NLO QCD and MadGraph + PYTHIA LO 0+1j merged samples is 27.4%, much lower than 52.4%, which is the difference with the 0j MadGraph + PYTHIA sample.

Figure 6.2 shows the difference in observable distributions between the 3 SM MC generations.

Of particular interest is the degree of flatness between the ratio of POWHEG to the MadGraph samples, as can be seen especially in the angular plots of Figure 6.2.

The m_T^{WZ} distribution shows rather non-flat behaviour for the 0+1j compared to the POWHEG production. This disagreement can be attributed to the fact that the 0+1j merged solution at-

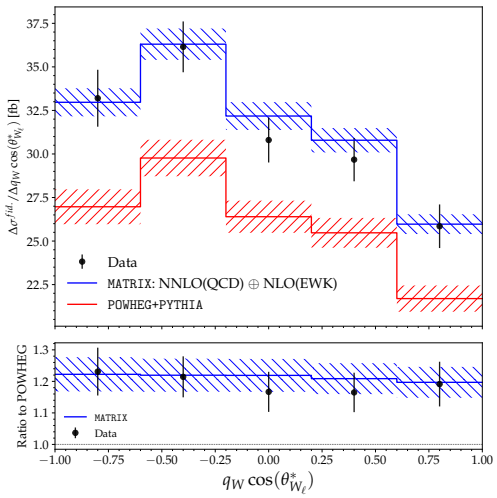

(a)

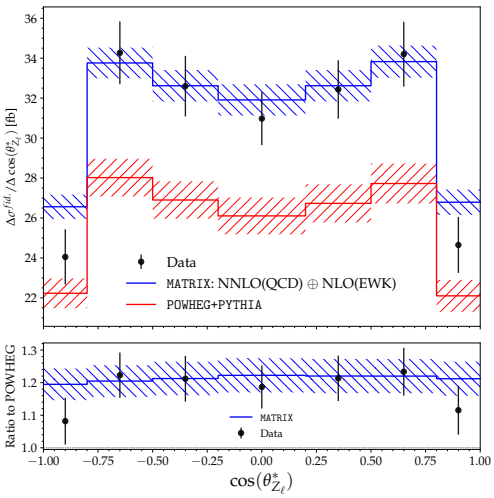

(b)

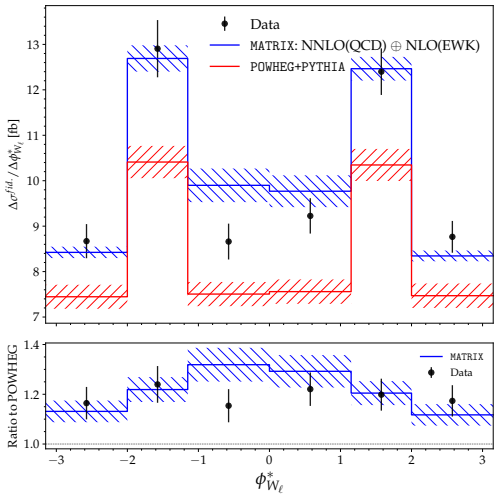

(c)

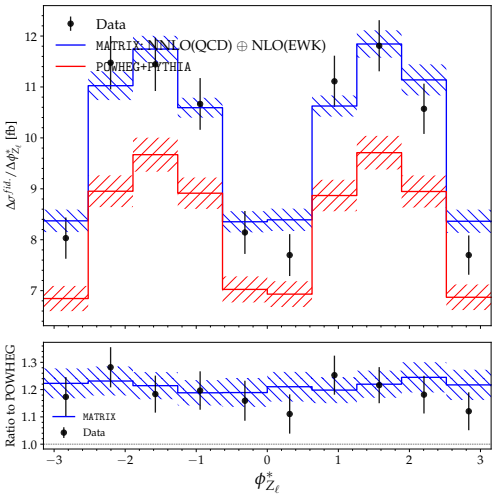

(d)

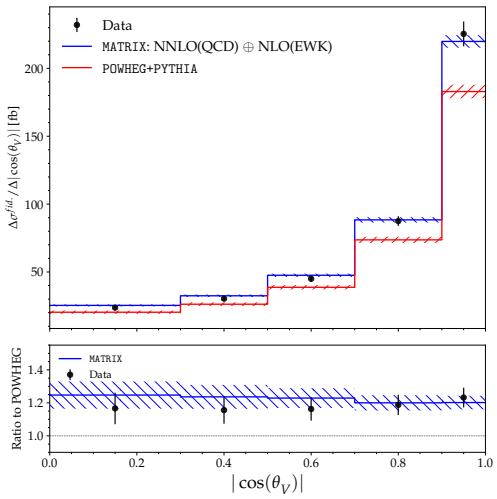

(e)

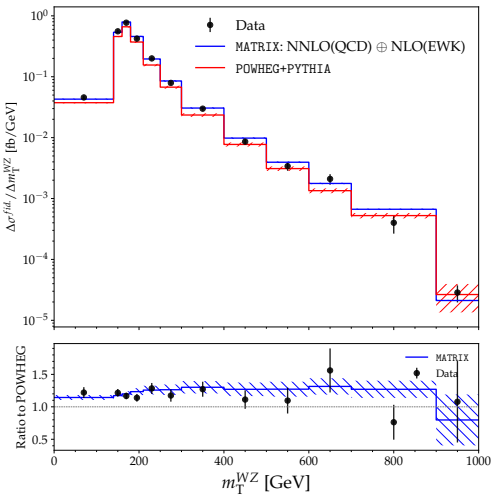

(f)

Figure 6.1: *Differential distributions of observables (described in Section 5.4) for the WZ system, comparing `POWHEG + PYTHIA` NLO QCD predictions, `MATRIX` predictions with NLO EWK and NNLO QCD corrections, and unfolded ATLAS Run-2 data. The hatched bands represent the scale and PDF uncertainties in the generation. Data error bars include both systematic and statistical errors.*

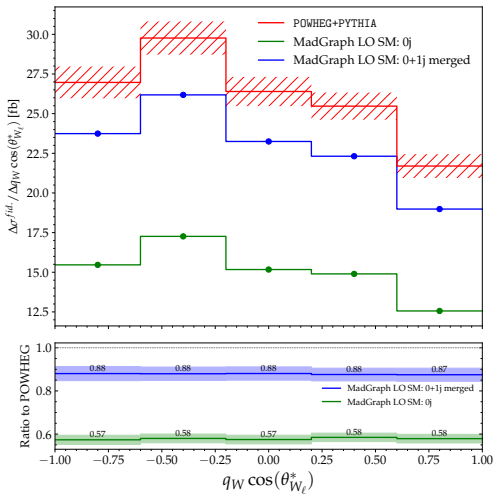

(a)

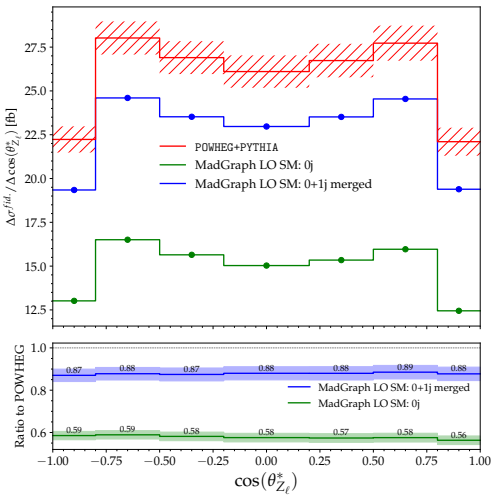

(b)

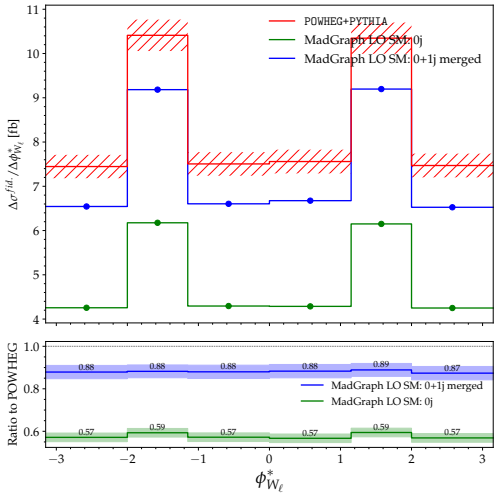

(c)

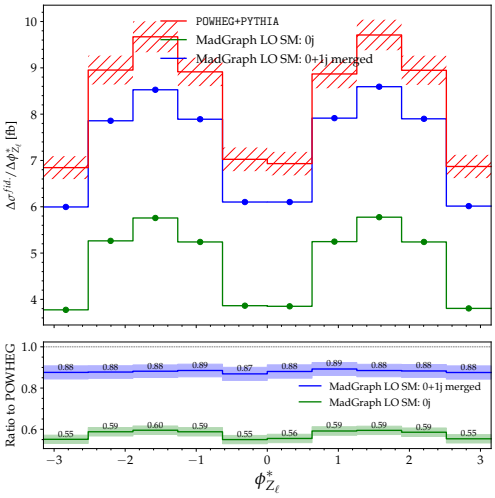

(d)

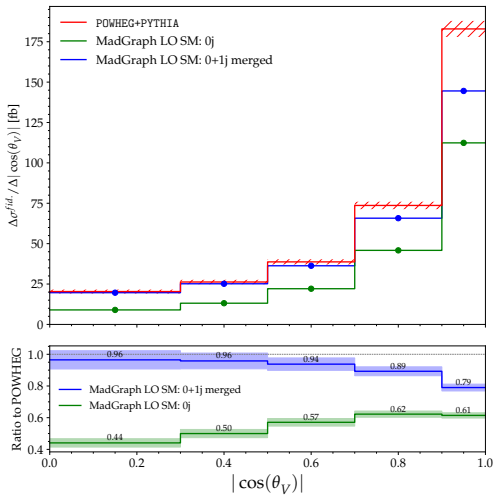

(e)

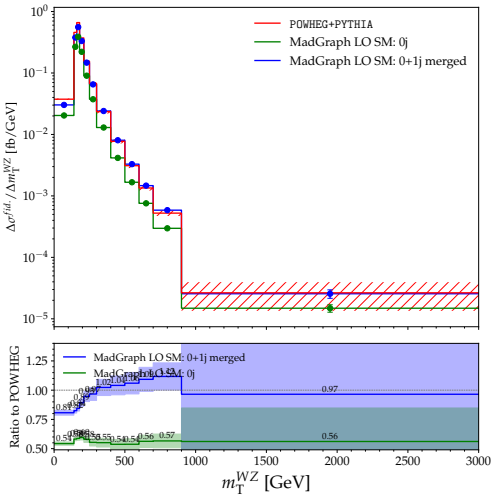

(f)

Figure 6.2: *Differential distributions of observables (described in Section 5.4) for the WZ system, comparing predictions from three generators: `POWHEG + PYTHIA`, `MadGraph 0+1j LO`, and `MadGraph 0j LO`. The hatched bands represents the scale and PDF uncertainties of the POWHEG generation. The ratio between the POWHEG and the 0+1j merged prediction is listed for every bin. The envelope in the ratio plot propagates the scale and PDF uncertainties of the POWHEG generation as well as the statistical uncertainties.*

tempts to model only NLO behaviour by including additional jet radiation, rather than incorporating virtual corrections such as loop diagrams. For kinematic variables like m_T^{WZ}, these virtual NLO corrections are not accurately modelled by the 0+1j merged scheme.

Through the validation of the SM prediction in both the fiducial cross-section as well as the differential distributions of the observables, it is quite evident that the 0+1j merged scheme offers a far better solution than 0j scheme. Thus this strategy of MC generation is used for SM as well as SMEFT operators.

Validation of the 0+1j merged strategy for the `MadGraph` modelling of the SMEFT operators is deferred to Section 7.4.

6.3 Likelihood model and Inference

In searches for new physics within the framework of SMEFT, it is essential to evaluate whether the observed data is consistent with the Standard Model-only hypothesis or suggests the presence of additional new physics due to higher-dimensional EFT operators. This evaluation process is known as a statistical hypothesis test.

The likelihood function represents the joint probability distribution of observed data as a function of the parameters within a statistical model. Maximizing the likelihood function is a technique for estimating the parameters of a model given a finite sample of data [118].

In particle physics, the simplest form of a likelihood function is often based on a counting experiment, typically described by a Poisson distribution. This distribution involves one observable, the observed event count N_{obs}, and one parameter, the expected event count N_{exp}, and is given by:

$$\text{Poisson}(N_{\text{obs}}|N_{\text{exp}}) = \frac{(N_{\text{exp}})^{N_{\text{obs}}}}{N_{\text{obs}}!} e^{-N_{\text{exp}}}. \tag{6.5}$$

In practice, N_{exp} is divided into an expected signal count s and an expected background count b. A parameter μ is introduced to scale the signal count s, allowing for deviations from the nominal expectation, such that $N_{\text{exp}} = \mu \cdot s + b$. To model distributions, the overall likelihood is constructed as the product of Poisson likelihoods for each bin:

$$L(x|\mu) = \prod_{i \in \text{bins}} \text{Poisson}(N_i|\mu s_i + b_i), \tag{6.6}$$

where N_i is the number of events in each bin, x represents the entire dataset $x = \{N_i\}$, and s_i and b_i are the expected signal and background counts in each bin. The parameter $\mu = \{\mu_i\}$

denotes the set of signal strengths across the bins.

Systematic uncertainties, both experimental and theoretical, are incorporated as nuisance parameters θ in the likelihood function. This results in:

$$L(x|\mu,\theta) = \prod_{i\in\text{bins}} \text{Poisson}(N_i|\mu s_i(\theta) + b_i(\theta)) \prod_{j\in\theta} \text{Gauss}(0|\theta_j, 1), \tag{6.7}$$

where each nuisance parameter θ_j accounts for a source of systematic uncertainty, and we have assumed a Gaussian constraint of mean = 0 and a variance of 1.

In terms of SMEFT, the predictions depend on the value of the Wilson coefficients **c** that are also subject to theory systematics, parameterised by nuisance parameters.

The predicted measurement in a bin b of the unfolded distribution is parameterised as explained in Equation 6.4, but now rescaling the prediction with a linear approximation of the effects of the nuisance parameters:

$$x_b^{\text{pred}}(\boldsymbol{c},\boldsymbol{\theta}) = x_b^{\text{SM}} \left(1 + \sum_i A_{bi}c_i + \sum_i B_{bi}c_i^2 + \sum_{i<j} C_{bij}c_ic_j\right) \times \prod_{j=1}^{n_{\text{syst}}} (1 + \theta_j u_{bj}), \tag{6.8}$$

where x_b^{SM} is the nominal SM cross prediction, $\boldsymbol{c}$ are the Wilson coefficients, $\boldsymbol{\theta} = (\theta_1, \ldots, \theta_{n_{\text{syst}}})$ are nuisance parameters, n_{syst} is the number of nuisance parameters, and u_{bj} represents the relative impact of systematic uncertainty j in bin b, and θ_j are standardised nuisance parameters with nominal value $\theta_j = 0$ corresponding to the central prediction.

For large event counts, the Poisson distribution can be approximated by a Gaussian distribution due to the Central Limit Theorem [119]. This approximation allows us to simplify the likelihood function written in Equation 6.7.

$$\text{Poisson}(N_i|x_i^{\text{pred}}) \approx \frac{1}{\sqrt{2\pi x_i^{\text{pred}}}} \exp\left(-\frac{(N_i - x_i^{\text{pred}})^2}{2x_i^{\text{pred}}}\right). \tag{6.9}$$

Using this Gaussian approximation, we can rewrite the likelihood function for each bin in terms of a Gaussian distribution. The overall likelihood function becomes:

$$L(\boldsymbol{x}|\boldsymbol{c},\boldsymbol{\theta}) = \prod_{i\in\text{bins}} \frac{1}{\sqrt{2\pi\sigma_i^2}} \exp\left(-\frac{(x_i^{\text{meas}} - x_i^{\text{pred}})^2}{2\sigma_i^2}\right) \prod_{j\in\theta} f_i(\theta_i), \tag{6.10}$$

where $x_i^{\text{pred}} = \mu s_i(\boldsymbol{\theta}) + b_i(\boldsymbol{\theta})$ and $\sigma_i^2 = x_i^{\text{pred}}$ for simplicity in the Gaussian approximation. The constraint terms $f_j(\theta_j)$ in the likelihood encode prior knowledge about systematic uncertainties. These take the standardised Gaussian constraints form (assuming θ_j being centred at 0 with unit

variance) :

$$f_i(\theta_i) = \frac{1}{\sqrt{2\pi}} \exp\left(-\frac{1}{2}\theta_i^2\right). \tag{6.11}$$

To further simplify the likelihood expression and provide a more compact form, we rewrite the likelihood function in matrix notation. Let $\Delta\boldsymbol{x}(\boldsymbol{c},\boldsymbol{\theta}) = \boldsymbol{x}^{\text{meas}} - \boldsymbol{x}^{\text{pred}}$, where $\boldsymbol{x}^{\text{meas}}$ is the vector of observed counts and $\boldsymbol{x}^{\text{pred}}$ is the vector of expected counts. The covariance matrix C incorporates the uncertainties in the expected counts. The Gaussian likelihood function then becomes:

$$L(\boldsymbol{x}|\boldsymbol{c},\boldsymbol{\theta}) = \frac{1}{\sqrt{(2\pi)^{n_{\text{bins}}}\det(C)}} \exp\left(-\frac{1}{2}\Delta\boldsymbol{x}^T(\boldsymbol{c},\boldsymbol{\theta})C^{-1}\Delta\boldsymbol{x}(\boldsymbol{c},\boldsymbol{\theta})\right) \prod_{i=1}^{n_{\text{syst}}} f_i(\theta_i). \tag{6.12}$$

In this form, n_{bins} is the number of bins, and n_{syst} is the number of systematic uncertainties modelled by the functions $f_i(\theta_i)$.The f_i correspond to the Gaussian constraints on nuisance parameters, while the vector $\Delta\boldsymbol{x} = (\Delta x_1, \ldots, \Delta x_{n_{\text{bins}}})$ represents the difference between measurement and prediction in each measurement bin, with the element Δx_b defined for a given bin, b, as:

$$\Delta x_b(\boldsymbol{c},\boldsymbol{\theta}) = x_b^{\text{meas}} - x_b^{\text{pred}}(\boldsymbol{c},\boldsymbol{\theta}). \tag{6.13}$$

6.3.1 Maximum Likelihood and Likelihood ratio

From the likelihood function, a range of statistical methods can be applied to draw inferences about the SMEFT model parameters. One primary method is to identify the parameter values that make the observed data most probable, known as the Maximum Likelihood Estimation (MLE) [118]. This approach involves finding the parameter values $\hat{\alpha}$ that maximize the likelihood function $L(\alpha)$.

For complex measurements involving multiple observables, it is often necessary to condense the data into a single test statistic $q_\alpha(x)$. According to the Neyman-Pearson lemma, when comparing two hypotheses, the ratio of the likelihood functions is the most powerful test to reject or choose one hypothesis over the other. The test statistic is thus defined as:

$$q_\alpha = -2\log\left(\frac{L(\alpha)}{L(\hat{\alpha})}\right). \tag{6.14}$$

The original Neyman-Pearson approach does not consider nuisance parameters, which are used in the likelihood functions discussed. Since the profile likelihood depends on these nuisance parameters, a specific method must be used to determine their values. The LHC convention

[120] is to set these parameters to their best-fit values in both the numerator and denominator, which brings about the complete profile likelihood ratio test statistic:

$$q(c_i) = -2\log\left(\frac{L(\boldsymbol{x}|c_i,\hat{\hat{\theta}})}{L(\boldsymbol{x}|\hat{c}_i,\hat{\theta})}\right), \tag{6.15}$$

where $\hat{\hat{\theta}}(c_i)$ represents the maximum likelihood estimate of the nuisance parameters for a given fixed value of c_i, while $\hat{c}_i$ and $\hat{\theta}$ denote the unconditional maximum likelihood estimates of both c_i and the nuisance parameters.

To find these estimates, maximum likelihood fits are conducted for individual Wilson coefficients by setting all other coefficients to zero and optimizing the likelihood with respect to the nuisance parameters.

Confidence intervals for the Wilson coefficients are then derived using Wilks' theorem, under the assumption that the test statistic $q(c_i)$ follows a χ^2 distribution [121].

Wilks' theorem states that, in the asymptotic limit, the test statistic $q(c_i)$ is distributed according to a χ^2 distribution with degrees of freedom equal to the number of parameters being tested. This allows us to calculate confidence intervals or regions for the parameters. The specifics depend on the dimensionality of the parameter space:

- For a single parameter (1D case), the confidence intervals are:
  - 1σ (68% confidence level) interval corresponds to $q(c_i) = 1$,
  - 2σ (95% confidence level) interval corresponds to $q(c_i) = 3.84$,
- For two parameters (2D case), the confidence regions are:
  - 1σ (68% confidence level) region corresponds to $q(c_i) = 2.30$,
  - 2σ (95% confidence level) region corresponds to $q(c_i) = 5.99$.

These intervals or regions provide a measure of the statistical uncertainty in the parameter estimates, indicating the range within which the true parameter values are expected to lie with the specified confidence level.

The `EFTFun` (EFT Fitter for UNfolded data) package implements this likelihood function, using the `Roofit` toolkit [122].

6.4 Uncertainty on Wilson coefficients

Wilson coefficients are obtained by maximizing the profile likelihood function, Equation 6.12. A test statistic, Equation 6.15 is then calculated which determines a confidence interval for the fitted Wilson coefficient value. The uncertainty in the Wilson coefficient is described by this confidence interval.

Several elements in addition to the measured and predicted data are required to build the profile likelihood function, Equation 6.12, including the covariance matrix, C. This matrix accounts for all the experimental uncertainties attributed to the measured data. This includes the unfolding uncertainty, the particle reconstruction systematic uncertainty (electrons, muons, jets), the luminosity uncertainty and the uncertainty in the background (all of which are explained in Chapter 5.6). The statistical uncertainty as well as the correlations for all these experimental uncertainties are encoded within the covariance matrix C.

Another class of uncertainties that deal with the prediction (and the model) are not included in the correlation matrix, but rather introduced as nuisance parameters in the fit. These contribute to the second multiplier term of Equation 6.12, $\prod_{i=1}^{n_{\text{nuisance}}} f_i(\theta_i)$.

The following nuisance parameters deal with the prediction uncertainties:

- The PDF uncertainty, called (`diboson_pdf`), is a constant 1% across the bins.
- The QCD scale uncertainty, called (`wz_scale`), is a constant 2.3% across the bins.
- The EW correction uncertainty, called (`wz_ew_correction`), is calculated bin-by-bin. It represents the percent difference between the `MATRIX` prediction (see Chapter 6.2.1) when combining NNLO QCD with NLO EW using either the additive or multiplicative schemes.

Additionally, if the EFT MC prediction has a small sample size in a bin of an observable, i.e. the relative error on that bin is $> 20\%$, then another nuisance parameter is added for that bin. This applies to any bin in the differential cross-section distributions of observables under study.

All nuisance parameters are modelled by a normal distribution with $\mu = 0$, $\sigma = 1$.

Further details on the pull plots, including their interpretation and selected examples, are presented in Appendix E.

CHAPTER 7

SMEFT studies on the $WZ \to \ell\nu\ell\ell$ channel

7.1 Sensitivity of SMEFT operators

There are 275 independent CP-conserving dimension-6 operators defined in the Warsaw basis under the top flavour scheme, as is illustrated in Table 2.1.

Out of these operators, not all are useful in the $WZ \to \ell\nu\ell\ell$ process. A full scan is done to determine which operators the process is sensitive to. The study compares the relative cross-section of the EFT term to the nominal Standard Model process. The EFT effect is therefore defined as $\frac{\sigma_{EFT}}{\sigma_{SM}}$.

The study helps to coarsely identify which parameters affect our process and ought to be further studied. The comparison is done at Leading-Order with `MadGraph5_aMC@NLO version 2.9.9` and the `SMEFTsim 3.0` model. Minimum phase-space cuts are made to make the study as general as possible, and to see the pure physics effects, excluding detector and reconstruction efficiencies. For this reason, `Pythia` showering is excluded.

7.1.1 Interference term effect

The interference term of the EFT operator with the SM (also called the linear term) can be separately generated using `EFT_ORDER: NP^2==1`.

Out of the 275 independent CP-conserving parameters, only 53 parameters returned a non-zero cross-section for the interference term. The others were therefore not investigated further.

Table 7.1 shows the relative effect of the EFT operators when their Wilson coefficient is set to $c = 1$. Operators for which the magnitude of the effect is less than 1×10^{-4} are not listed in the table for brevity.

The cross-section for the interference term scales linearly with the value of c, meaning that the relative effect listed in Table 7.1 corresponds to $c = 1$ as a benchmark. For most operators, a value of $c = 1$ is considered large and may already be excluded by other experimental

constraints. The listed effect demonstrates how sensitive the WZ process is to each operator. Operators with a very small effect (e.g., less than 10^{-4}) even for $c = 1$ indicate that the WZ process is inherently insensitive to them. Such operators are unlikely to produce measurable effects in WZ events, even if c takes on values allowed by other constraints.

For the interference term, it is possible for the cross-section to be negative. This means that the EFT operator is destructively interfering with the SM operators, and thus reducing the cross-section.

Operator	EFT effect vs SM
cHj3	$3.68 \times 10^{-1} \pm 0.48\%$
cHl311	$-1.21 \times 10^{-1} \pm 0.42\%$
cHl322	$-1.20 \times 10^{-1} \pm 0.43\%$
cll1221	$1.18 \times 10^{-1} \pm 0.36\%$
cHl111	$5.43 \times 10^{-2} \pm 0.39\%$
cHl122	$5.42 \times 10^{-2} \pm 0.40\%$
cHe22	$-4.41 \times 10^{-2} \pm 0.38\%$
cHj1	$4.37 \times 10^{-2} \pm 1.06\%$
cHe11	$-4.34 \times 10^{-2} \pm 0.40\%$
clj322	$3.61 \times 10^{-2} \pm 0.42\%$
clj311	$3.59 \times 10^{-2} \pm 0.44\%$
ceHRe22	$-2.98 \times 10^{-2} \pm 0.43\%$
cHDD	$-1.94 \times 10^{-2} \pm 2.40\%$

Operator	EFT effect vs SM
cW	$-1.70 \times 10^{-2} \pm 3.71\%$
cHWB	$9.80 \times 10^{-3} \pm 6.18\%$
clj111	$-5.33 \times 10^{-3} \pm 1.18\%$
clj122	$-5.29 \times 10^{-3} \pm 1.16\%$
cje22	$-4.55 \times 10^{-3} \pm 0.62\%$
cje11	$-4.47 \times 10^{-3} \pm 0.75\%$
ceWRe22	$-2.28 \times 10^{-4} \pm 0.61\%$
cll1122	$1.54 \times 10^{-4} \pm 0.55\%$
ceHRe11	$-1.43 \times 10^{-4} \pm 0.41\%$
cHW	$1.30 \times 10^{-4} \pm 0.43\%$
cll1111	$1.23 \times 10^{-4} \pm 0.65\%$
cll2222	$1.23 \times 10^{-4} \pm 0.60\%$

Table 7.1: *Relative cross-section effect for the linear term of EFT operators when the Wilson coefficients is set to $c = 1$. Only operators whose |effect| $> 1 \times 10^{-4}$ are listed.*

7.1.2 Quadratic term effect

Similar to the linear term, the quadratic term of the EFT operator can also be separately generated using `EFT_ORDER: NP==1`.

Out of the 53 parameters that returned a non-zero cross-section for the interference term, only 26 parameters returned a non-zero cross-section for the quadratic term.

Table 7.2 shows the relative effect of the EFT operators when their Wilson coefficient for the operator is set to $c = 1$.

The cross-section for the quadratic term scales with the value of c^2, and so will the effect. Again, it should be noted that for most operators, a $c = 1$ value is considered quite large, and so the effect listed in the table serves as a benchmark to demonstrate how sensitive the WZ process is to each operator. Operators with a very small effect even when $c = 1$ can therefore be

considered insensitive, and are thus not pursued further.

Unlike the interference term, the effect of the quadratic term is always positive as the amplitude is squared in Equation 6.1.

Operator	EFT effect vs SM
cW	$2.02 \times 10^{-1} \pm 0.43\%$
cHj3	$2.01 \times 10^{-1} \pm 0.37\%$
cHWB	$1.99 \times 10^{-2} \pm 0.39\%$
cHj1	$1.30 \times 10^{-2} \pm 0.36\%$
ceWRe11	$1.03 \times 10^{-2} \pm 0.48\%$
ceWRe22	$1.02 \times 10^{-2} \pm 0.45\%$
cHDD	$9.36 \times 10^{-3} \pm 0.37\%$
cHl322	$7.17 \times 10^{-3} \pm 0.39\%$
cHl311	$7.16 \times 10^{-3} \pm 0.36\%$
cll1221	$3.66 \times 10^{-3} \pm 0.35\%$
cHe22	$3.07 \times 10^{-3} \pm 0.37\%$
cHl111	$3.07 \times 10^{-3} \pm 0.38\%$
cHe11	$3.07 \times 10^{-3} \pm 0.37\%$

Operator	EFT effect vs SM
cHl122	$3.06 \times 10^{-3} \pm 0.39\%$
ceBRe22	$1.48 \times 10^{-3} \pm 0.43\%$
ceBRe11	$1.48 \times 10^{-3} \pm 0.37\%$
cHW	$5.76 \times 10^{-5} \pm 0.51\%$
cHbox	$2.24 \times 10^{-6} \pm 0.39\%$
cuWRe	$8.25 \times 10^{-7} \pm 0.42\%$
cHu	$4.32 \times 10^{-7} \pm 0.42\%$
cuBRe	$2.11 \times 10^{-7} \pm 0.35\%$
cdWRe	$4.46 \times 10^{-9} \pm 0.44\%$
cHd	$2.75 \times 10^{-9} \pm 0.39\%$
cdBRe	$1.17 \times 10^{-9} \pm 0.35\%$
cuHRe	$3.25 \times 10^{-10} \pm 0.42\%$
cHudRe	$4.80 \times 10^{-14} \pm 0.48\%$

Table 7.2: *Relative cross-section effect for the quadratic term of EFT operators when the Wilson coefficients is set to $c = 1$. Only operators that returned a non-zero cross-section for the linear term are listed.*

7.1.3 Cumulative effect

Both linear and quadratic terms offer a higher order correction in the EFT Lagrangian. Out of all the 275 independent CP-conserving parameters, the ones affecting the $WZ \to \ell\nu\ell\ell$ channel the most are plotted in Figure 7.1. The linear and quadratic effects are plotted separately, for the Wilson coefficient value of $c = 1$.

For most parameters, the interference effect is more significant than the quadratic effect. This can be naively expected because the interference term is a factor of Λ^2 suppressed, while the quadratic term is a factor of Λ^4 suppressed. However, this is not always the pattern followed, most notably for the SMEFT parameter c_W which has a very large quadratic effect. This motivates having both linear and quadratic term corrections included in the MC predictions.

From the sensitivity study, a list of the EFT operators to which the physics process of interest was most sensitive is determined:

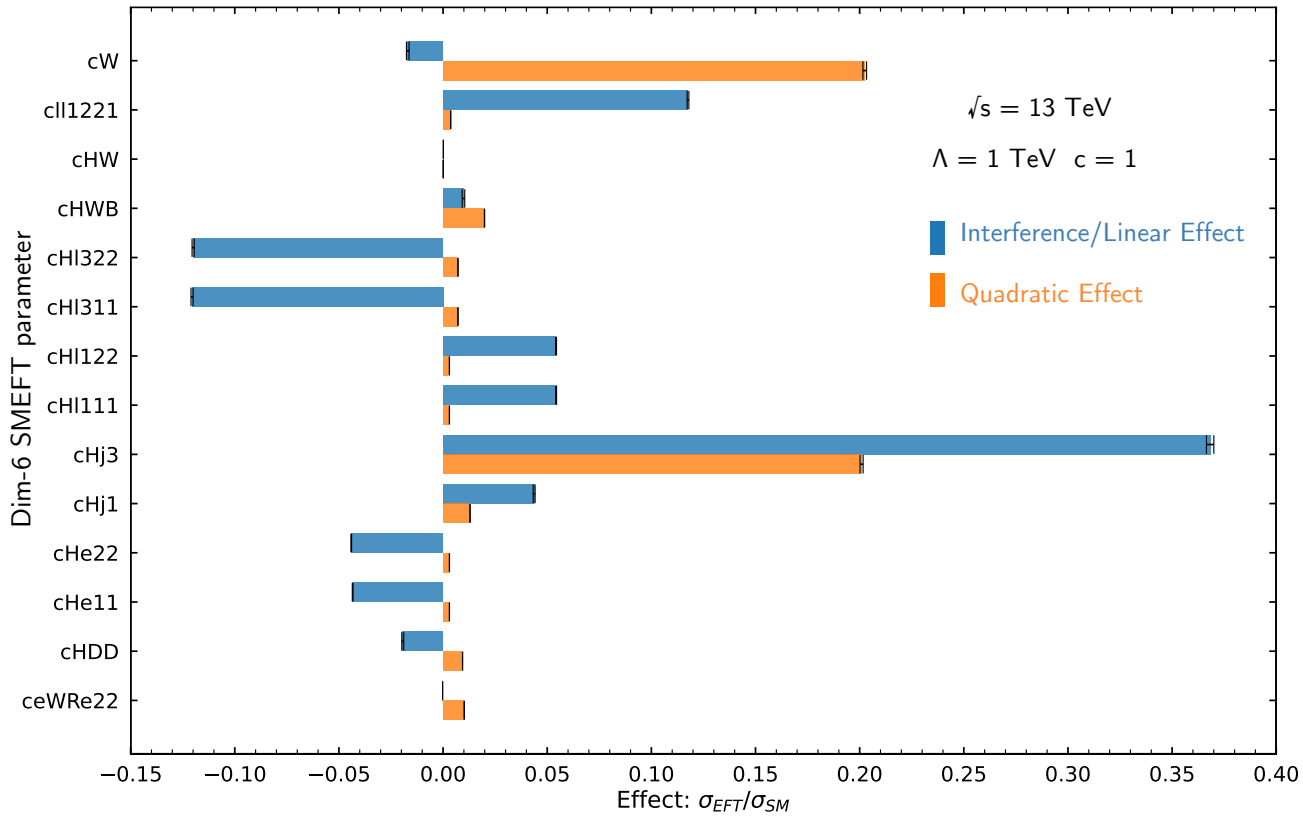

Figure 7.1: $\frac{\sigma_{EFT}}{\sigma_{SM}}$ *for interference (linear) and quadratic contributions of different dim-6 SMEFT parameters. Only the operators with the most prominent effect are shown. The Wilson-coefficient value is set to* $c = 1$.

- `cHDD`
- `cHl122`
- `cHl322`
- `cHj3`
- `cll1221`
- `cHl111`
- `cHl311`
- `cHj1`
- `cHWB`
- `cW`

7.1.4 Physics behind the sensitivity of these operators

The complete list of dimension-6 operators is shown in Appendix B. A brief description of the physical nature of each of the sensitive operators is given here:

`cHDD`

`cHDD` is the Wilson coefficient for the operator $Q_{HD} = (D^\mu H^\dagger H)(H^\dagger D_\mu H)$ where D_μ is defined in Equation 2.21. This operator changes the kinetic term for the Higgs field and its covariant derivatives, affecting all three EW vector bosons: γ, W, Z. Concerning WZ physics, it affects the triple gauge coupling WWZ vertex, and the $f\bar{f}$ coupling to a Z, where f is a fermion, as

shown in Figure 7.2.

Figure 7.2: *Feynman diagrams of vertices affected by the Q_{HD} operator that influences WZ physics.*

`cHl1`

`cHl111` and `cHl122` are Wilson coefficients of the diagonal matrix elements of the operator $Q_{H\ell}^{(1)} = \left(H^\dagger i\overleftrightarrow{D}_\mu H\right)\left(\bar{\ell}_p\gamma^\mu\ell_r\right)$, where the subscripts p, r are flavour indices. `cHl111` is the 11 element of the matrix while `cHl122` is the 22 element of the matrix. The operator modifies the interaction between the Higgs field and the lepton fields, and because of the derivative, it affects the EW bosons. It only affects couplings to the Z boson as it doesn't explicitly include the $SU(2)$ structure component, unlike in its counterpart operator $Q_{H\ell}^{(3)}$ (discussed below). Element 11 only concerns 1^{st} generation leptons (i.e. $e^\pm, v_e$) and Element 22 only concerns 2^{nd} generation leptons (i.e. $\mu^\pm, v_\mu$). Concerning WZ physics, the operator affects the $l\bar{l}$ coupling to a Z, where l is a lepton, as as shown in Figure 7.3. Quarks are unaffected by this operator.

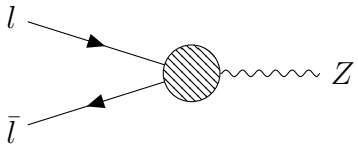

Figure 7.3: *Feynman diagram of the vertex affected by the $Q_{H\ell}^{(1)}$ operator that influences WZ physics. For $\left(Q_{H\ell}^{(1)}\right)_{11}$, l is of the first generation and for $\left(Q_{H\ell}^{(1)}\right)_{22}$, l is of the second generation.*

`cHl3`

`cHl311` and `cHl322` are Wilson coefficients of the diagonal matrix elements of the operator $Q_{H\ell}^{(3)} = \left(H^\dagger i\overleftrightarrow{D}^i_\mu H\right)\left(\bar{\ell}_p\sigma^i\gamma^\mu\ell_r\right)$ where the subscripts p, r are flavour indices. `cHl311` is the 11 element of the matrix while `cHl322` is the 22 element of the matrix. These operators affect the coupling between the Higgs field and lepton currents and include an $SU(2)$ structure that affects the interactions involving the $SU(2)$ gauge fields more directly. They affect all three EW vector

bosons: γ, W, Z, as well as all fermions. Concerning WZ physics, they affect the triple gauge coupling WWZ vertex, the $f\bar{f}$ coupling to a Z, and the $f\bar{f}$ coupling to a W, where f is a fermion, as shown in Figure 7.4.

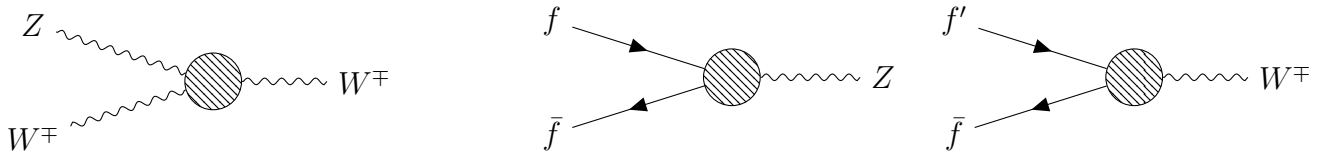

Figure 7.4: *Feynman diagrams of vertices affected by the $Q_{H\ell}^{(3)}$ operator that influences WZ physics. The Feynman diagram involving the W contains leptons f' and f of different flavours while that involving the Z contains the same flavour $f\bar{f}$ pair.*

`cHWB`

`cHWB` is the Wilson coefficient for the operator $Q_{HWB} = H^\dagger \sigma^i H W^i_{\mu\nu} B^{\mu\nu}$ where W and B are the field strength tensors of the $SU(2)$ and $U(1)$ gauge fields respectively, used in Equations 2.18 and 2.19. The operator modifies the couplings between the Higgs field and the electroweak gauge bosons and impacts the mixing between the $SU(2)$ and $U(1)$ gauge fields. Concerning WZ physics, it affects the triple gauge coupling WWZ vertex, and the $f^\pm f^\mp$ coupling to a Z, where f is a charged fermion, as shown in Figure 7.5. This operator doesn't affect the coupling to neutrinos.

Figure 7.5: *Feynman diagrams of vertices affected by the Q_{HWB} operator that influences WZ physics. f includes only charged leptons, excluding the coupling to neutrinos.*

`cW`

`cW` is the Wilson coefficient for the operator $Q_W = \epsilon^{ijk} W^{i\nu}_{\mu} W^{j\rho}_{\nu} W^{k\mu}_{\rho}$ where ϵ is the Levi-Civita symbol and W is the field strength tensor of the $SU(2)$ gauge field shown in Equation 2.18. It modifies the self-interactions of the $SU(2)$ gauge fields, which includes only the three EWK vector bosons: γ, W, Z. Concerning WZ physics it affects the triple gauge coupling WWZ vertex, as shown in Figure 7.6.

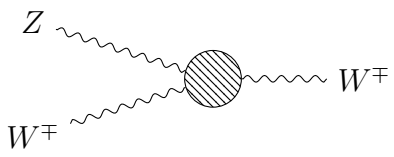

Figure 7.6: *Feynman diagram of the vertex affected by the Q_W operator that influences WZ physics.*

`cHj1`

`cHj1` is the Wilson coefficient for the operator $Q_{Hq}^{(1)} = \left(H^\dagger i\overleftrightarrow{D}_\mu H\right)(\bar{q}\gamma^\mu q)$ where q represents the quark field. It modifies the interactions between the Higgs field and the quarks, except for the 3rd generation quarks. Similarly to `cHl1`, this operator only affects the Z (and H) boson without affecting the couplings of the W and the γ. Concerning WZ physics, this operator modifies the $Zq\bar{q}$ vertex, as shown in Figure 7.7.

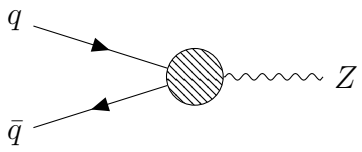

Figure 7.7: *Feynman diagrams of the vertex affected by the $Q_{Hq}^{(1)}$ operator that influences WZ physics. q includes only the first and second-generation quarks.*

`cHj3`

`cHj3` is the Wilson coefficient of the operator $Q_{Hq}^{(3)} = \left(H^\dagger i\overleftrightarrow{D}^i_\mu H\right)(\bar{q}_p\sigma^i\gamma^\mu q_r)$ where the subscripts p, r are flavour indices. This operator affects the coupling between the Higgs field and quark fields and includes an $SU(2)$ structure that affects the interactions involving the $SU(2)$ gauge fields more directly. It affects the W, Z, and the H couplings with the first and second quark generations. Concerning WZ physics, this operator affects the $Zq\bar{q}$ vertex and the $Wq\bar{q}$ vertex as shown in Figure 7.8.

`cll1221`

`cll1221` is a subset of the `cll` operator $Q_{\ell\ell} = (\bar{\ell}_p\gamma_\mu\ell_r)(\bar{\ell}_s\gamma^\mu\ell_t)$ where the subscripts are flavour indices and in this specific case, $p = 1, r = 2, s = 2, t = 1$. This operator modifies interactions between leptons by introducing a new four-fermion interactions that are not present in the

Figure 7.8: *Feynman diagrams of vertices affected by the $Q_{Hq}^{(3)}$ operator that influences WZ physics. The Feynman diagram involving the W contains quarks q, q' of different flavours while the one involving the Z contains the same flavour $q\bar{q}$ pair. q, q' includes only the first and second-generation quarks.*

Standard Model. Due to the flavour mixing in the 1221 element, modifications to the W, Z, and H coupling with leptons are possible. Concerning WZ physics, it affects the $f\bar{f}$ coupling to a Z, and the $f\bar{f}$ coupling to a W, where f is a fermion, as shown in Figure 7.9.

Figure 7.9: *Feynman diagrams of vertices affected by the $(Q_{\ell\ell})_{1221}$ operator that influences WZ physics. The Feynman diagram involving the W contains leptons f of different flavours while that involving the Z contains the same flavour $f\bar{f}$ pair.*

7.2 Sensitivity of EFT operators to physical observables

Of the observables listed in Section 5.4, some have been previously studied for Vector Boson polarisation in WZ production [57, 94] and have had their binning optimised. These observables provide a possible manifestation for new physics affecting the triple gauge WZ vertex.

The observables are presented as histograms indicating the differential cross-sectional distributions i.e. $\frac{d\sigma^{\text{fid.}}}{d\mathcal{X}}$, where $\mathcal{X}$ is the observable. In the above mentioned studies, the observables and their binning are listed in Table 7.3 below:

Observable	Number of Bins	Bin Edges
$\cos\theta^*_{W_\ell}$	5	[-1.0, -0.6, -0.2, 0.2, 0.6, 1.0]
$\cos\theta^*_{Z_\ell}$	7	[-1.0, -0.8, -0.5, -0.2, 0.2, 0.5, 0.8, 1.0]
$\lvert\cos\theta_V\rvert$	5	[0.0, 0.3, 0.5, 0.7, 0.9, 1.0]
$\phi^*_{W_\ell}$	6	[-3.14, -2.0, -1.15, 0.0, 1.15, 2.0, 3.14]
$\phi^*_{Z_\ell}$	10	[-3.14, -2.52, -1.89, -1.26, -0.63, 0.0, 0.63, 1.26, 1.89, 2.52, 3.14]
m_T^{WZ} (GeV)	12	[0, 140, 160, 180, 210, 250, 300, 400, 500, 600, 700, 900, 1000+]

Table 7.3: *Binning information for various observables. For $\lvert\cos\theta_V\rvert$, New Physics dominates in the $\lvert\cos\theta_V\rvert \sim 0.1$ regime [58]. For m_T^{WZ}, New Physics dominates in the high p_T bins, where EFT operators that grow with energy become more significant. The bin edges for m_T^{WZ} are in GeV.*

The effect of the EFT parameters on these observables compared to the SM predictions is studied individually for each of the parameters listed in Section 7.1.4.

Effect is once again defined bin-by-bin as:

$$\text{Effect} = \frac{\text{EFT prediction}}{\text{SM prediction}} = \frac{\left(\frac{d\sigma^{\text{fid.}}_{\text{EFT}}}{d\mathcal{X}}\right)}{\left(\frac{d\sigma^{\text{fid.}}_{\text{SM}}}{d\mathcal{X}}\right)} \tag{7.1}$$

A higher value means that the operator is more sensitive to EFT effects. For all of the studies, the EFT parameter $c = 1$.

All predictions are at leading order with `MadGraph5_aMC@NLO version 2.9.9` and the `SMEFTsim 3.0` model. The events are interfaced with `Pythia 8.244` for parton showering and hadronisation. Particle-level analysis is done using `Rivet 3.1.2`.

7.2.1 *Observable:* $q_W \cos\theta^*_{W_\ell}$

The effect of each EFT parameter compared to the SM prediction is shown in Figures 7.10 and 7.11 for the linear (interference) term and the quadratic term, respectively, for the $\cos\theta^*_{W_\ell}$ observable. The linear term can have a destructive effect, reducing the cross-section and the prediction in a particular bin.

The majority of the EFT parameters have an effect for their linear term, except for the `cW` parameter which has a small effect. The quadratic term is however largest for the `cHj3` and `cW` parameters.

7.2.2 *Observable:* $\cos\theta^*_{Z_\ell}$

Similarly, the effect of each EFT parameter compared to the SM prediction is shown in Figures 7.12 and 7.13 for the linear (interference) term and the quadratic term, respectively, for the $\cos\theta^*_{Z_\ell}$ observable.

Once again, the majority of the EFT parameters have an effect for their linear term, except for the `cW` parameter which has a small effect. The quadratic term is however largest for by the `cHj3` and `cW` parameters.

7.2.3 *Observable:* $|\cos\theta_V|$

The effect of each EFT parameter compared to the SM prediction is shown in Figures 7.14 and 7.15 for the linear (interference) term and the quadratic term, respectively, for the $|\cos\theta_V|$ observable.

The majority of the sensitivity comes in the first bins, slowly dropping off as the value of

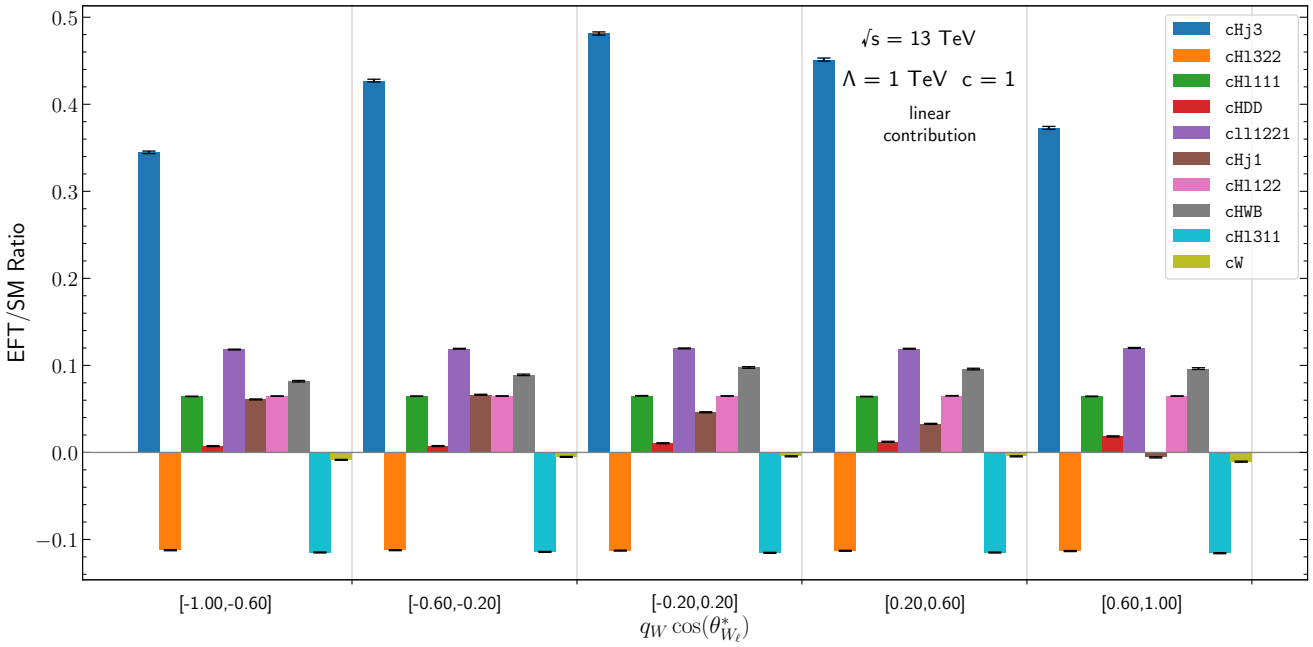

Figure 7.10: *Sensitivity for the linear (interference) contribution of different EFT parameters when* $c = 1$ *on the* $q_W \cos\theta^*_{W_\ell}$ *observable.*

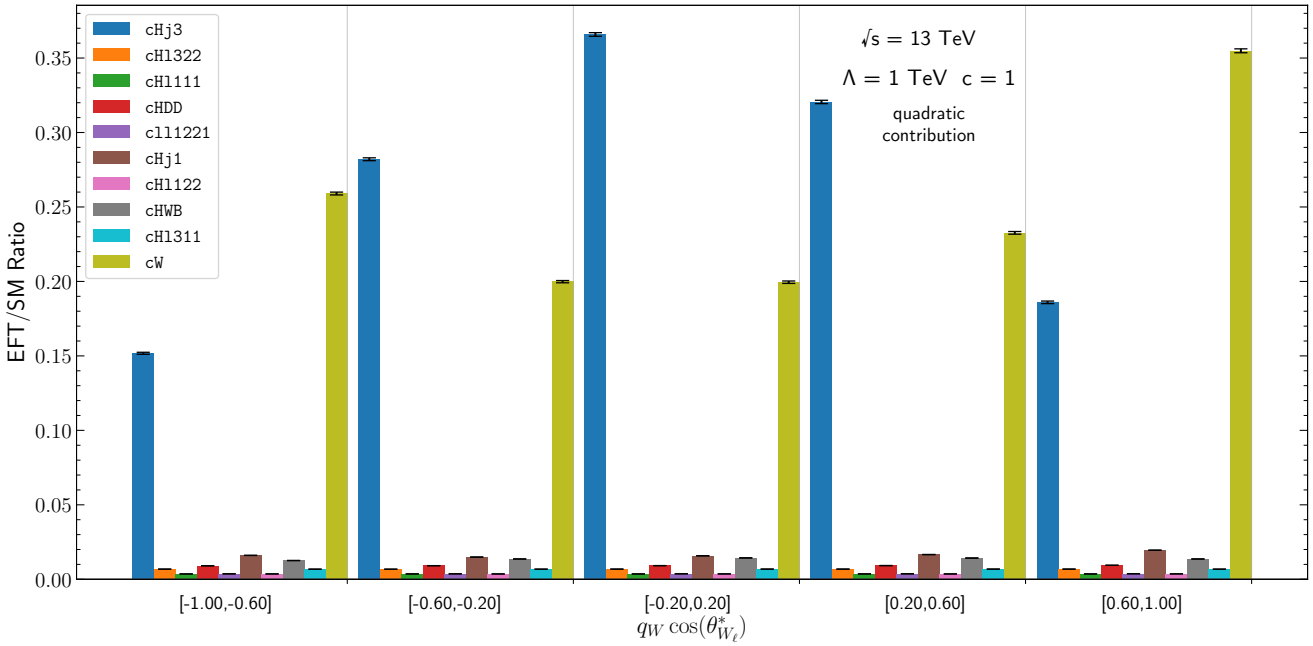

Figure 7.11: *Sensitivity for the quadratic contribution of different EFT parameters when* $c = 1$ *on the* $\cos\theta^*_{W_\ell}$ *observable.*

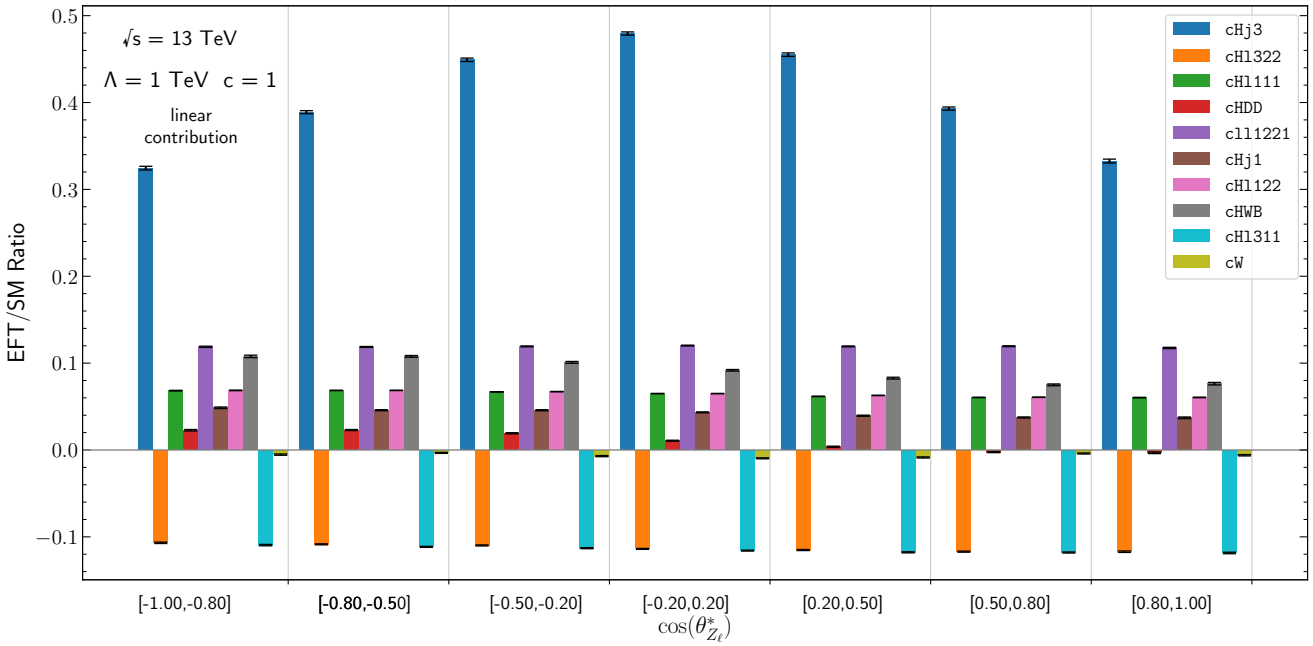

Figure 7.12: *Sensitivity for the linear (interference) contribution of different EFT parameters when $c = 1$ on the $\cos\theta^*_{Z_\ell}$ observable.*

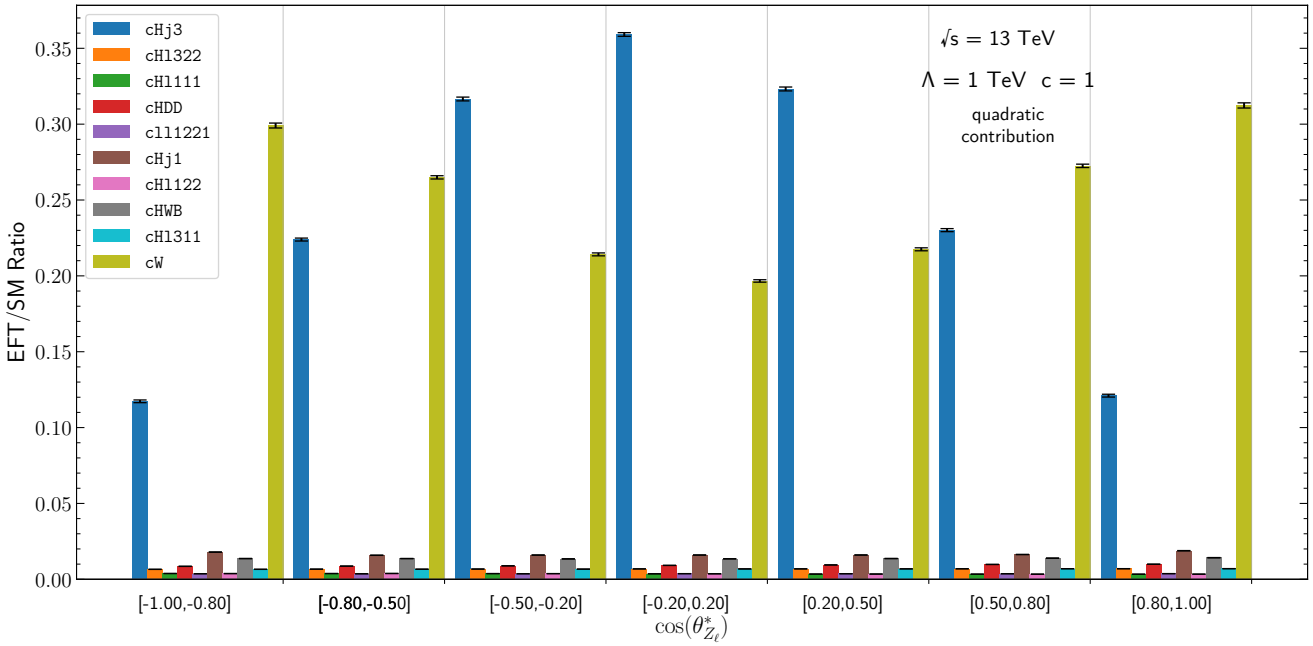

Figure 7.13: *Sensitivity for the quadratic contribution of different EFT parameters when $c = 1$ on the $\cos\theta^*_{Z_\ell}$ observable.*

$|\cos\theta_V|$ increases. This pattern is observed in both the linear and quadratic terms. Again, the majority of the EFT parameters show an effect for their linear term. The quadratic term is also once again largest for the `cHj3` and `cW` parameters.

7.2.4 *Observable:* $\phi^*_{W_\ell}$

The effect of each EFT parameter compared to the SM prediction is shown in Figures 7.16 and 7.17 for the linear (interference) term and the quadratic term, respectively, for the $\phi^*_{W_\ell}$ observable.

Similar observations to $\cos\theta^*_{W_\ell}$ can be made in the sense that the majority of the EFT parameters show an effect for their linear term. The quadratic term is once again largest for the `cHj3` and `cW` parameters.

7.2.5 *Observable:* $\phi^*_{Z_\ell}$

The effect of each EFT parameter compared to the SM prediction is shown in Figures 7.18 and 7.19 for the linear (interference) term and the quadratic term, respectively, for the $\phi^*_{Z_\ell}$ observable.

As with $\phi^*_{W_\ell}$, the majority of the EFT parameters show an effect for their linear term, although not as large for the `cW` term. The quadratic term is however again largest for the `cHj3` and `cW` parameters.

7.2.6 *Observable:* m_T^{WZ}

The effect of each EFT parameter compared to the SM prediction is shown in Figures 7.20 and 7.21 for the linear (interference) term and the quadratic term, respectively, for the m_T^{WZ} observable.

The majority of the sensitivity comes in the last bins, slowly dropping off as the value of m_T^{WZ} decreases. This pattern is observed in both the linear and quadratic terms. The majority of the EFT parameters show an effect for their linear term, although the `cHj3` has a remarkably strong impact. The quadratic term is outstandingly affected by the `cHj3` and `cW` parameters, with an effective ratio of ≥ 20 in the high m_T bin.

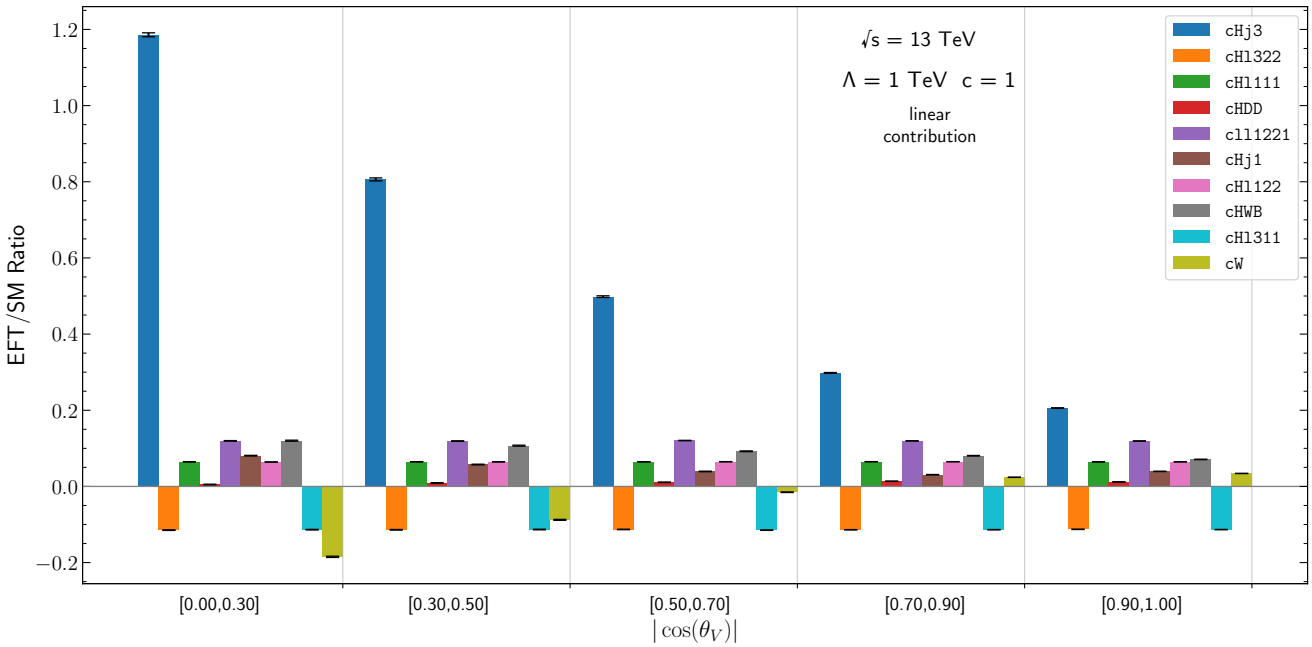

Figure 7.14: *Sensitivity for the linear (interference) contribution of different EFT parameters when $c = 1$ on the $|\cos\theta_V|$ observable.*

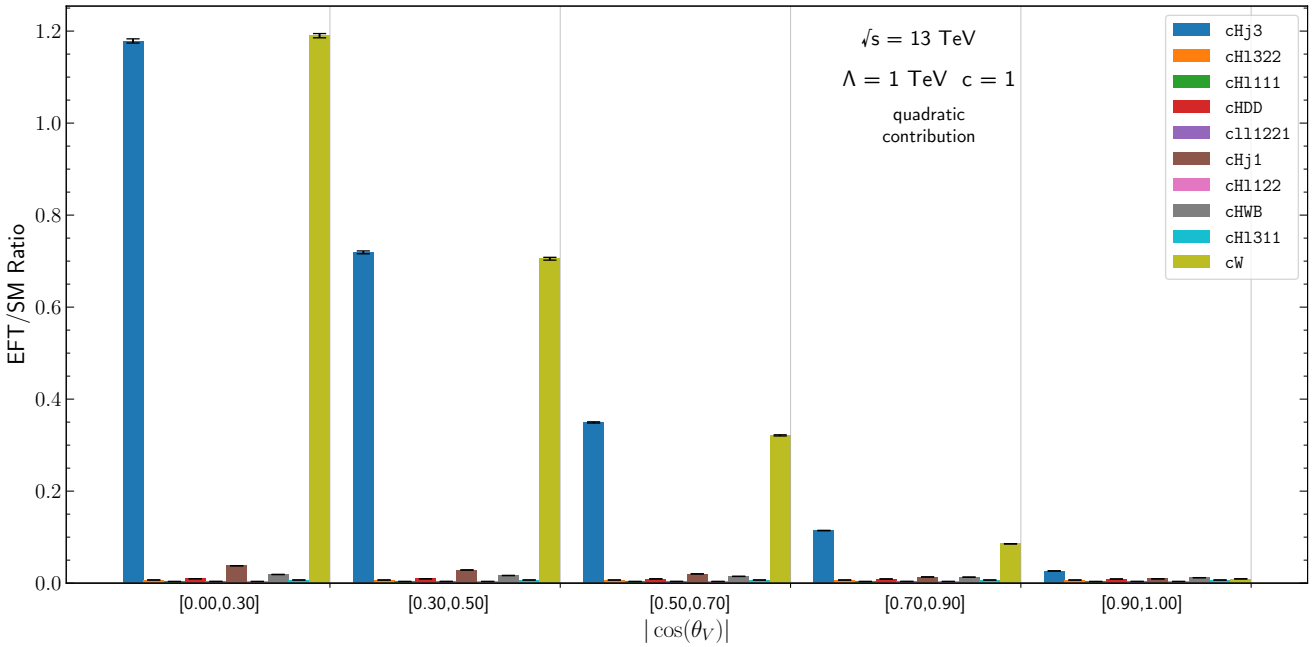

Figure 7.15: *Sensitivity for the quadratic contribution of different EFT parameters when $c = 1$ on the $|\cos\theta_V|$ observable.*

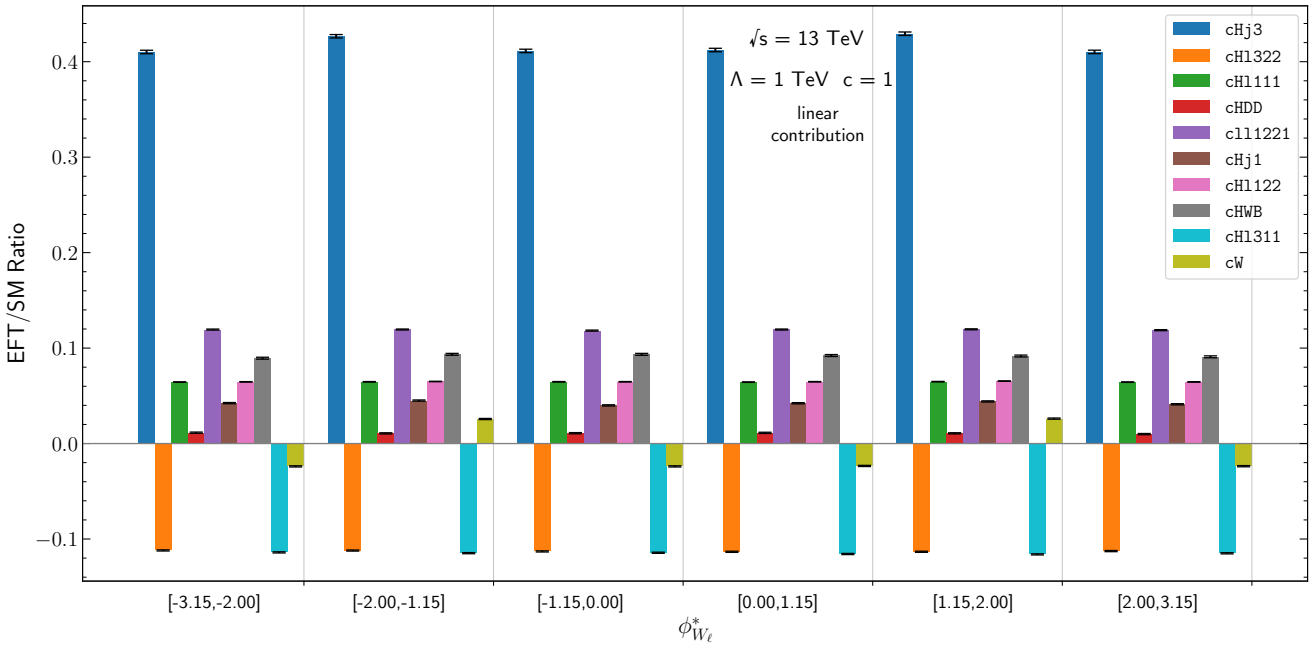

Figure 7.16: *Sensitivity for the linear (interference) contribution of different EFT parameters when $c = 1$ on the $\phi^*_{W_\ell}$ observable.*

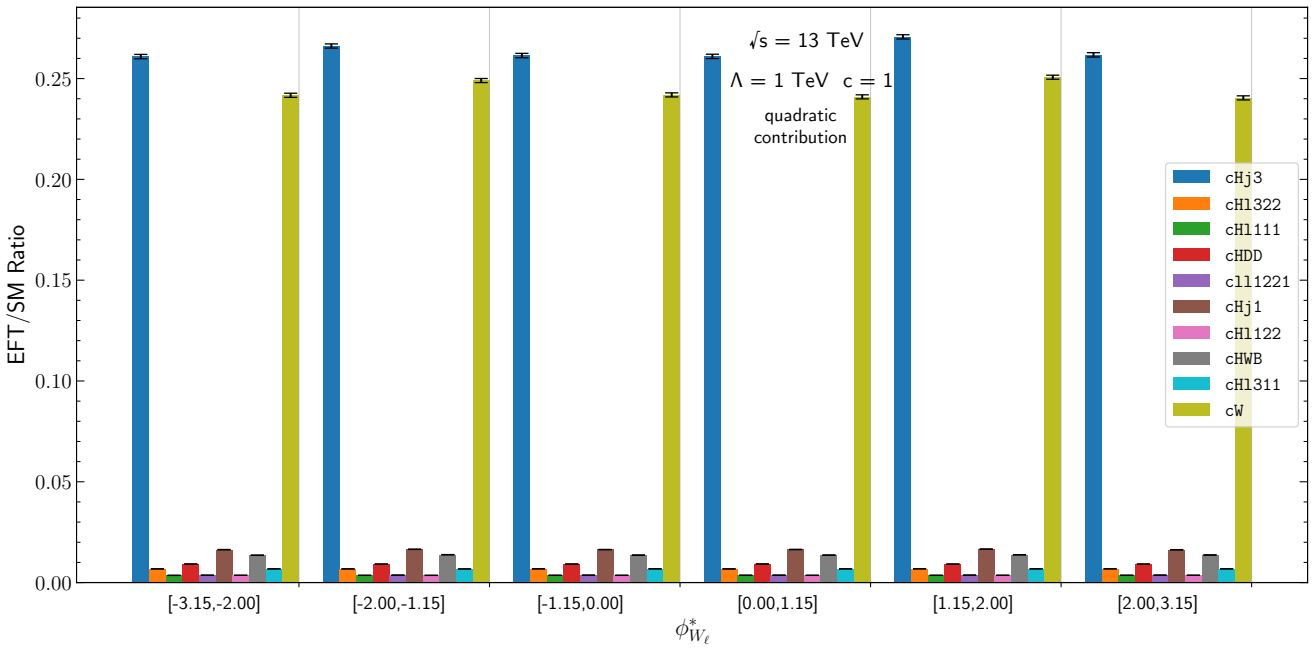

Figure 7.17: *Sensitivity for the quadratic contribution of different EFT parameters when $c = 1$ on the $\phi^*_{W_\ell}$ observable.*

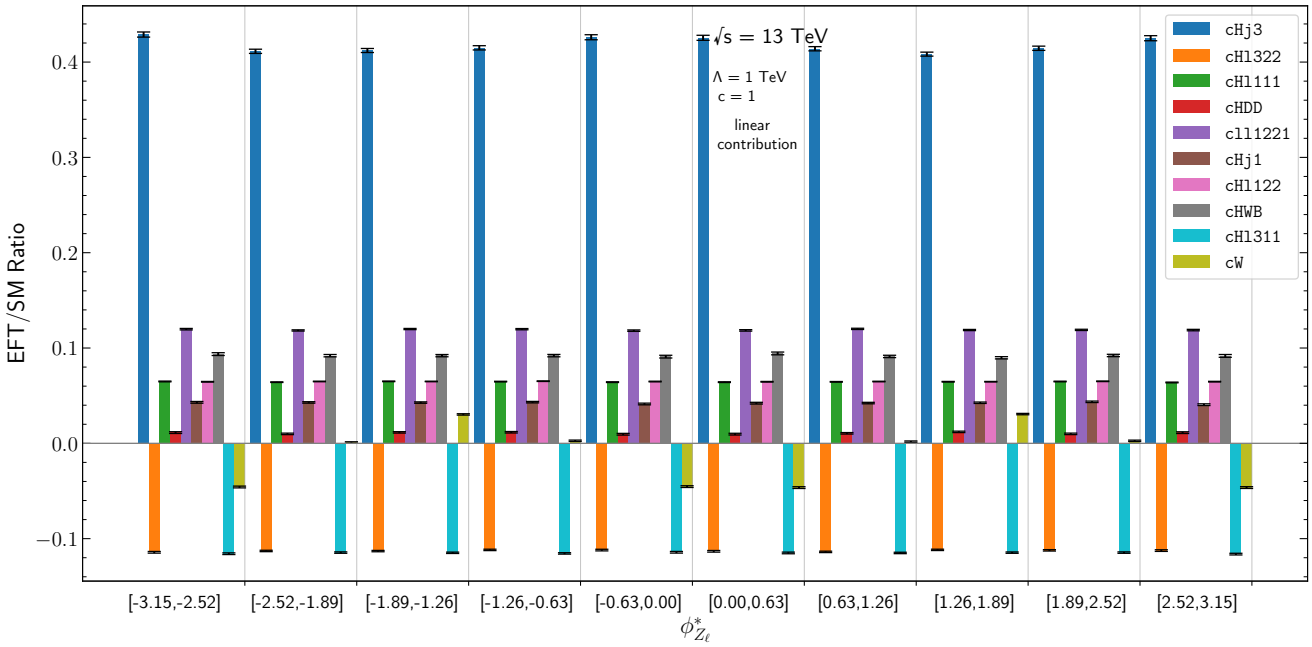

Figure 7.18: *Sensitivity for the linear (interference) contribution of different EFT parameters when $c = 1$ on the $\phi^*_{Z_\ell}$ observable.*

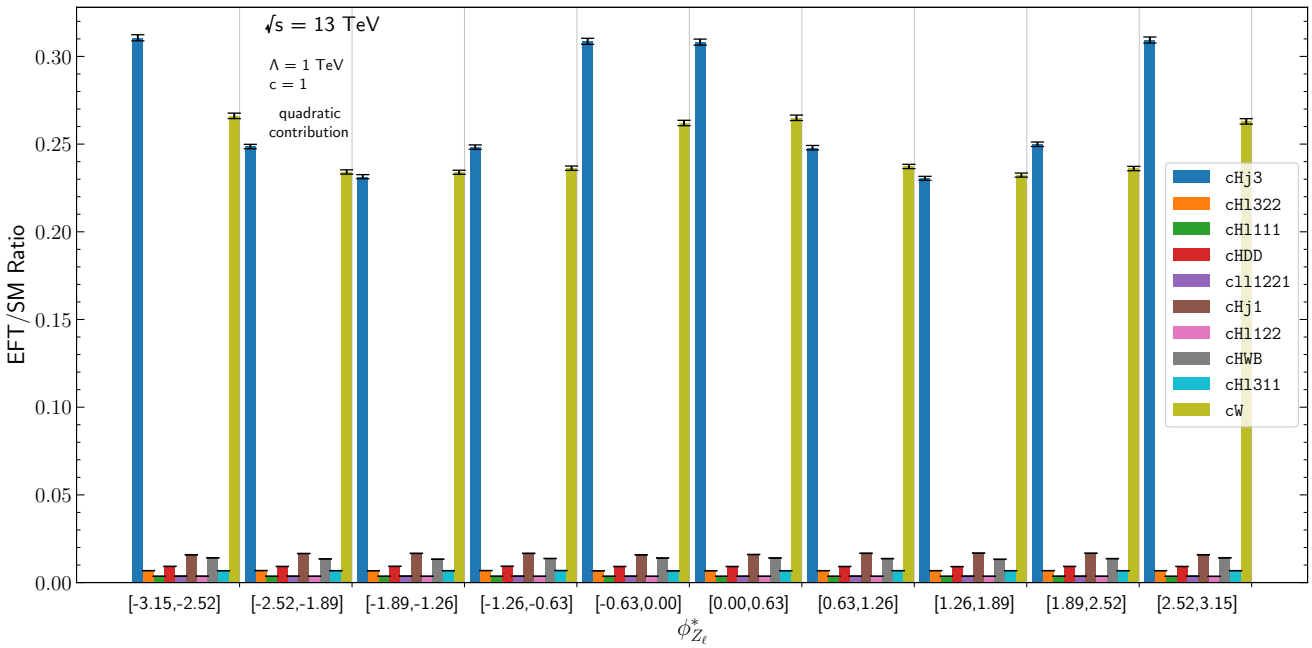

Figure 7.19: *Sensitivity for the quadratic contribution of different EFT parameters when $c = 1$ on the $\phi^*_{Z_\ell}$ observable.*

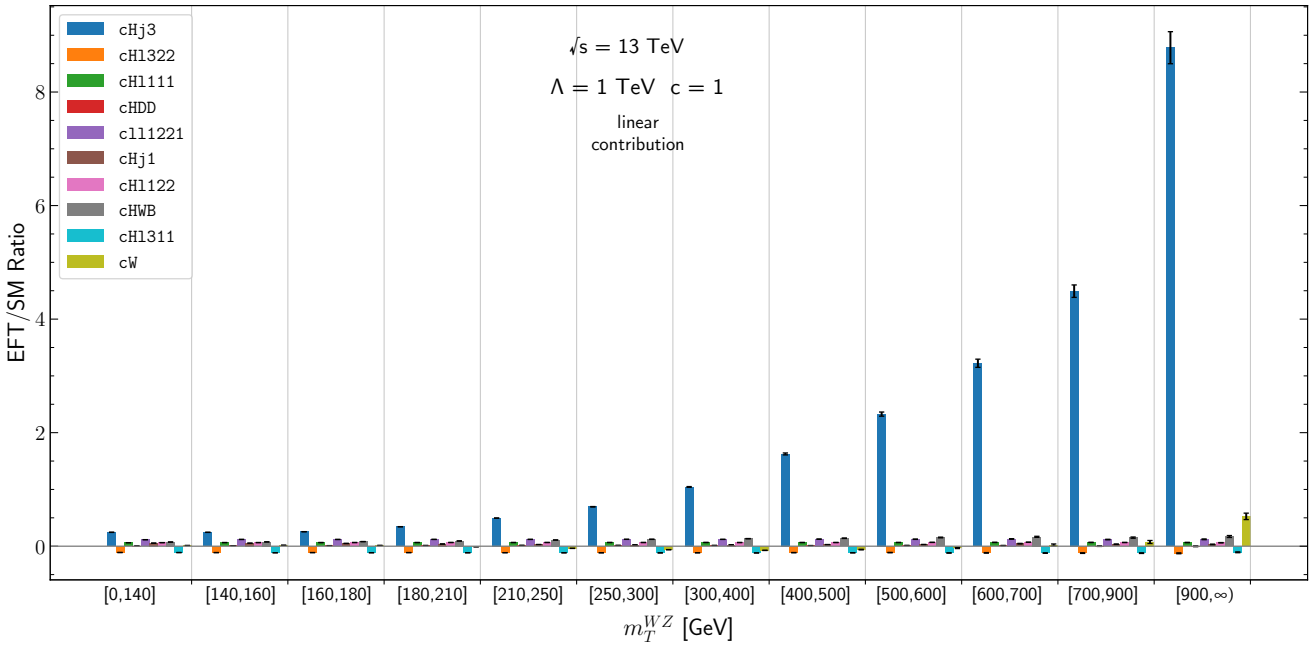

Figure 7.20: *Sensitivity for the linear (interference) contribution of different EFT parameters when $c = 1$ on the m_T^{WZ} observable.*

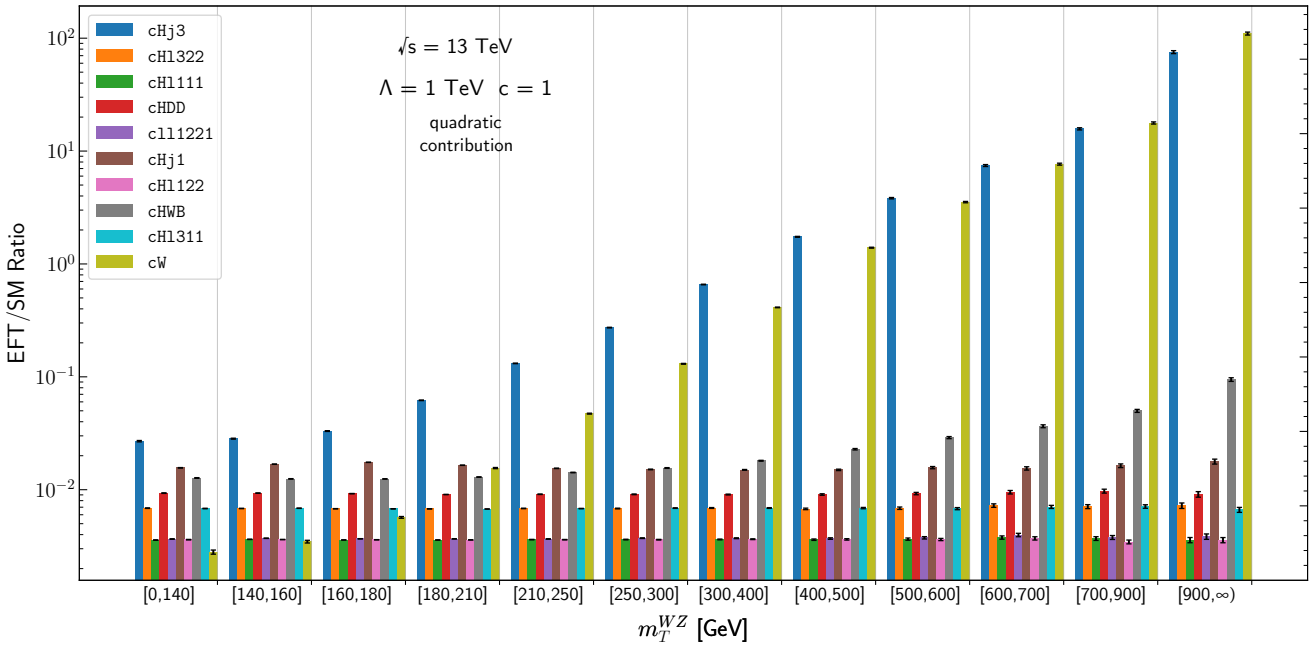

Figure 7.21: *Sensitivity for the quadratic contribution of different EFT parameters when $c = 1$ on the m_T^{WZ} observable. EFT/SM ratio is in log-scale to demonstrate the heightened effect produced by some parameters.*

7.2.7 Summary

Summing the absolute values of each bin for both the linear and quadratic terms for a particular EFT parameter provides insight into how strongly the parameter influences the observable. These summed values are presented in Table 7.4.

Among the observables, m_T^{WZ} stands out for its significant sensitivity to the `cHj3` and `cW` parameters. For other parameters, m_T^{WZ} offers increased sensitivity compared to other observables, reinforcing its importance in probing EFT effects. However, the larger uncertainties associated with m_T^{WZ} for some parameters (e.g., `cHj3`, `cW`) indicate a trade-off between sensitivity and precision.

The observable $\phi^*_{Z_\ell}$ emerges as particularly sensitive, with all parameters showing a large impact across its range. This highlights $\phi^*_{Z_\ell}$ as an excellent choice for studying EFT effects due to its broad sensitivity.

Similarly, $|\cos\theta_V|$ proves to be a sensitive observable, especially for `cHj3` and `cW`, demonstrating its utility in disentangling EFT contributions. Observables such as $\cos\theta^*_{W_\ell}$, $\cos\theta^*_{Z_\ell}$ and $\phi^*_{W_\ell}$ are also strongly influenced by `cHj3` and `cW`, but they retain sensitivity to other parameters as well.

	Sum of absolute ratios across all bins (linear + quad)					
Parameter	$\cos\theta^*_{W_\ell}$	$\cos\theta^*_{Z_\ell}$	$\lvert\cos\theta_V\rvert$	$\phi^*_{W_\ell}$	$\phi^*_{Z_\ell}$	m_T^{WZ}
`cHj3`	3.4 ± 0.13%	4.5 ± 0.13%	5.4 ± 0.17%	4.1 ± 0.13%	6.9 ± 0.13%	130 ± 1.8%
`cHl322`	0.60 ± 0.21%	0.84 ± 0.21%	0.60 ± 0.24%	0.72 ± 0.20%	1.2 ± 0.22%	1.5 ± 0.79%
`cHl111`	0.34 ± 0.16%	0.48 ± 0.17%	0.34 ± 0.20%	0.41 ± 0.16%	0.68 ± 0.17%	0.83 ± 0.64%
`cHDD`	0.15 ± 1.3%	0.20 ± 1.3%	0.094 ± 1.6%	0.12 ± 1.3%	0.20 ± 1.3%	0.22 ± 11.0%
`cll1221`	0.61 ± 0.18%	0.86 ± 0.18%	0.61 ± 0.21%	0.74 ± 0.17%	1.2 ± 0.18%	1.5 ± 0.70%
`cHj1`	0.29 ± 0.44%	0.41 ± 0.46%	0.36 ± 0.44%	0.35 ± 0.44%	0.59 ± 0.44%	0.63 ± 1.9%
`cHl122`	0.34 ± 0.15%	0.48 ± 0.15%	0.34 ± 0.17%	0.41 ± 0.15%	0.68 ± 0.15%	0.83 ± 0.56%
`cHWB`	0.53 ± 0.39%	0.74 ± 0.41%	0.59 ± 0.43%	0.63 ± 0.39%	1.1 ± 0.38%	1.8 ± 1.4%
`cHl311`	0.61 ± 0.20%	0.85 ± 0.21%	0.61 ± 0.24%	0.73 ± 0.20%	1.2 ± 0.22%	1.5 ± 0.78%
`cW`	1.3 ± 0.20%	1.8 ± 0.19%	2.7 ± 0.22%	1.6 ± 0.18%	2.7 ± 0.18%	140 ± 2.4%

Table 7.4: *Sum of absolute ratios across all bins for different observables ($\cos\theta^*_{W_\ell}$, $\cos\theta^*_{Z_\ell}$, $|\cos\theta_V|$, $\phi^*_{W_\ell}$, $\phi^*_{Z_\ell}$, and m_T^{WZ}) for both linear + quadratic terms. In all cases, the EFT parameter, $c = 1$. The uncertainties are statistical and are given as percentages of the absolute ratios.*

In summary, $\phi^*_{Z_\ell}$ and m_T^{WZ} are the most broadly sensitive observables across all parameters, with $|\cos\theta_V|$, $\phi^*_{W_\ell}$, $\cos\theta^*_{W_\ell}$, and $\cos\theta^*_{Z_\ell}$ offering complementary sensitivity patterns.

EFT modifications usually grow with energy, becoming more prominent at high p_T [123] (or high m_T), which is why kinematic variables like m_T^{WZ} are particularly sensitive.

Angular variables like $|\cos\theta_V|$ exploit the fact that EFT modification affecting the triple-gauge coupling would cause a removal of the radiation-zero effect [58]. Thus sensitivity is gained in

such observables by observing an absence of a SM predicted phenomenon.

7.3 Cross-terms

Thus far only the linear (interference) and quadratic terms from Equation 6.1 have been studied. However, EFT operators interfere with each other giving rise to cross-terms.

Cross-terms are often neglected in studies as there are many ways to combine the sensitive parameters in pairs, making analyses more complex. In many cases, the cross-terms are assumed to be smaller than the linear and quadratic terms, to justify why they are neglected.

However, when multiple operators contribute significantly to a process, their interference (cross-term) can become non-negligible, and valuable for study. In analyses of linear and quadratic predictions without cross-terms, all EFT parameters are set to 0, except for the one being considered. Including cross-terms allows for the consideration of linear and quadratic terms for multiple operators simultaneously, rather than in isolation. This approach increases the potential impact of the EFT operators on the overall process. Considering cross-terms leads to more robust constraints on EFT Wilson coefficients, compared to the simple approximation of considering only one EFT operator at a time.

This study is unique as it incorporates the cross-terms for 2 operators at a time. This way, an measurement of 2 EFT operators can be made simultaneously. This is a novel analysis made in the $WZ \to \ell\nu\ell\ell$ channel.

The following sections highlight the impact of different cross-terms. Later the significance of adding the cross-terms to the linear and quadratic terms is also examined.

7.3.1 Effect of cross-terms

"Effect" is once again defined as in Equation 7.1. As a first study, pair-wise combinations for all operators listed in Section 7.1.4 are generated to gauge which combinations are sensitive to the observed distributions in the $WZ \to \ell\nu\ell\ell$ channel. This results in $\binom{10}{2} = 45$ different combinations.

Figures 7.22 - 7.27 show the effect of the cross-terms, when both Wilson coefficients are set to $c = 1$, with respect to the SM prediction for the observables of interest. The same result occurs when $c = -1$ for both operators. If $c = -1$ for one operator and $c = +1$ for the other operator, the result is multiplied by -1.

Several cross-term combinations have somewhat small sensitivity $\mathcal{O}(5\%)$ for $\cos\theta^*_{W_\ell}$, $\cos\theta^*_{Z_\ell}$ $\phi^*_{W_\ell}$ and $\phi^*_{Z_\ell}$. In contrast the very sensitive bins in the $|\cos\theta_V|$ and m_T^{WZ} observables show that

some cross-terms have a very large effect: $\mathcal{O}(25\%)$ and $\mathcal{O}(200\%+)$, respectively. It should be noted that the value of $c = 1$ has already been excluded by other analyses and is unreasonably large for some parameters, which is why the effect can be exaggerated. Nonetheless, the effect of some cross-terms within these observables motivates the need and opportunity for these contributions to be studied.

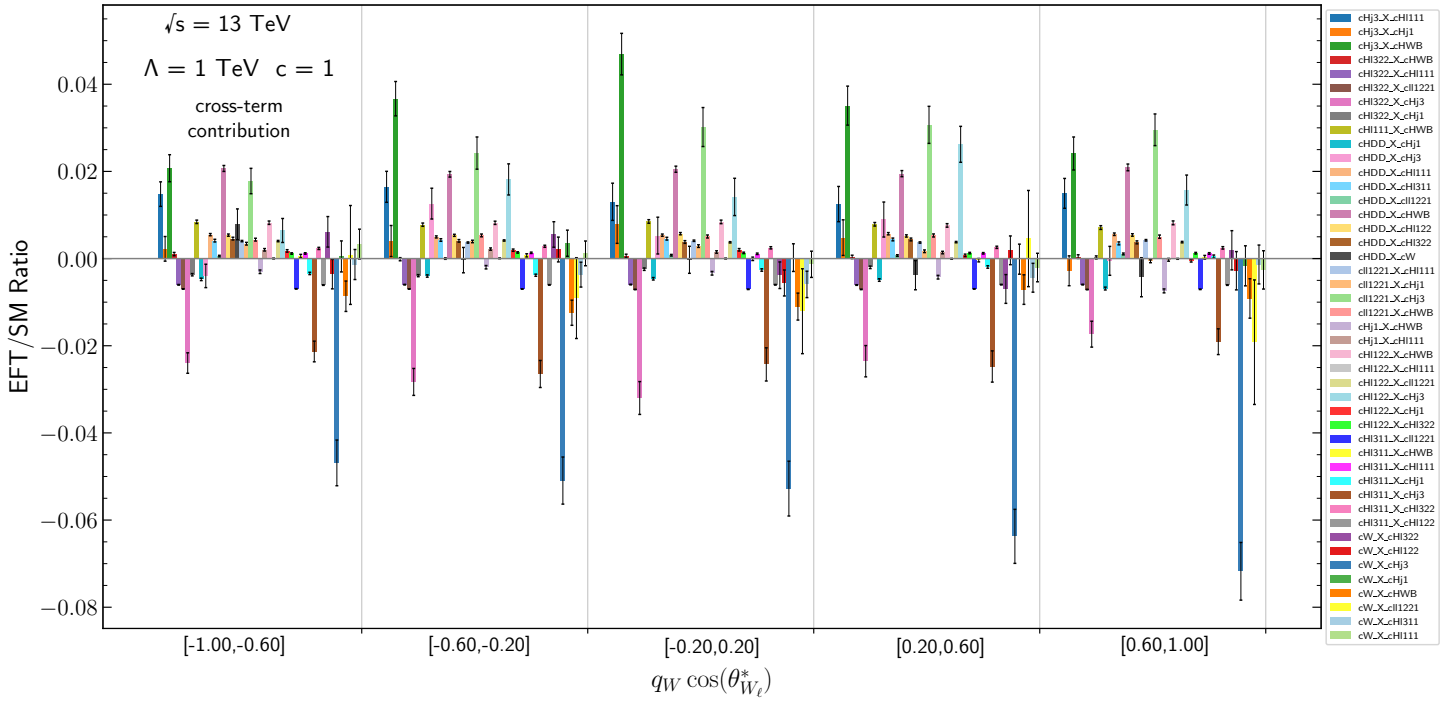

Figure 7.22: *Sensitivity for the cross-term contribution of different pairs of EFT parameters when all $c_i = 1$ on the $\cos\theta^*_{W_\ell}$ observable.*

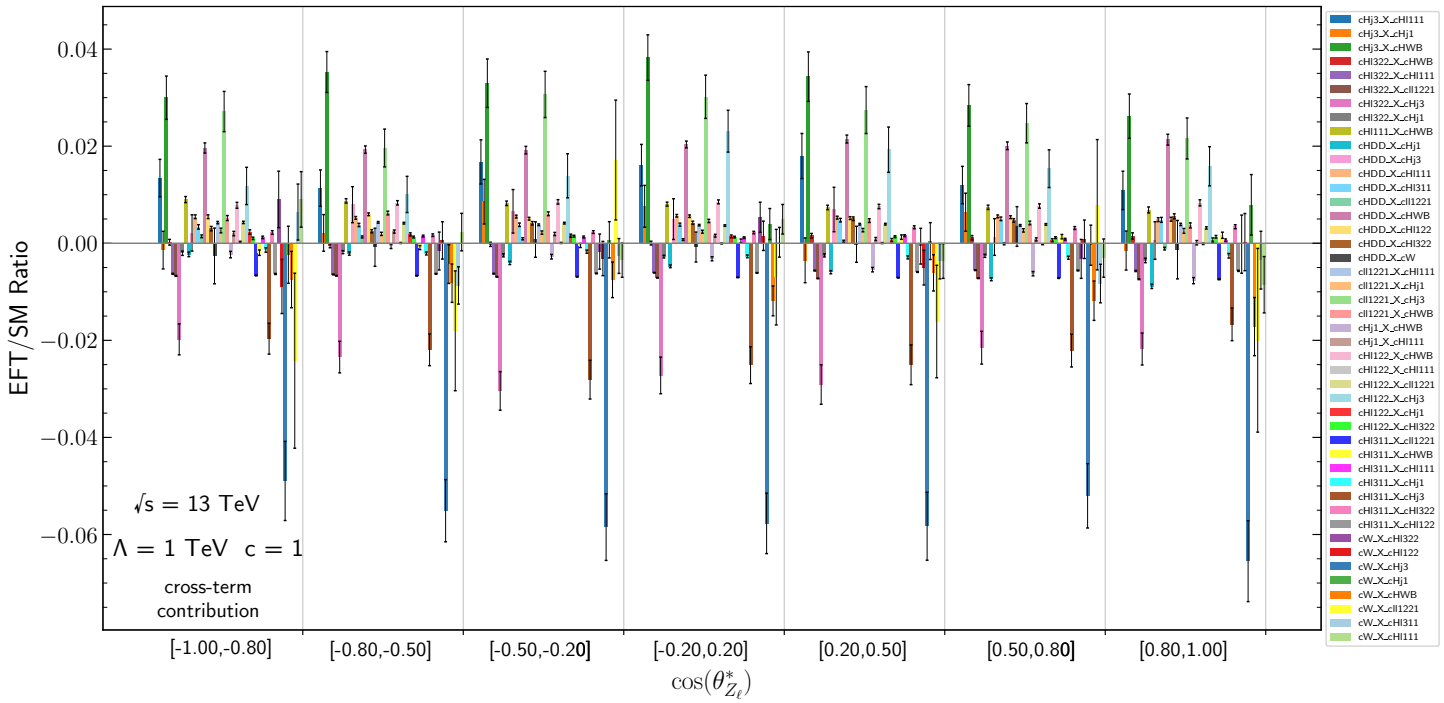

Figure 7.23: *Sensitivity for the cross-term contribution of different pairs of EFT parameters when all $c_i = 1$ on the $\cos\theta^*_{Z_\ell}$ observable.*

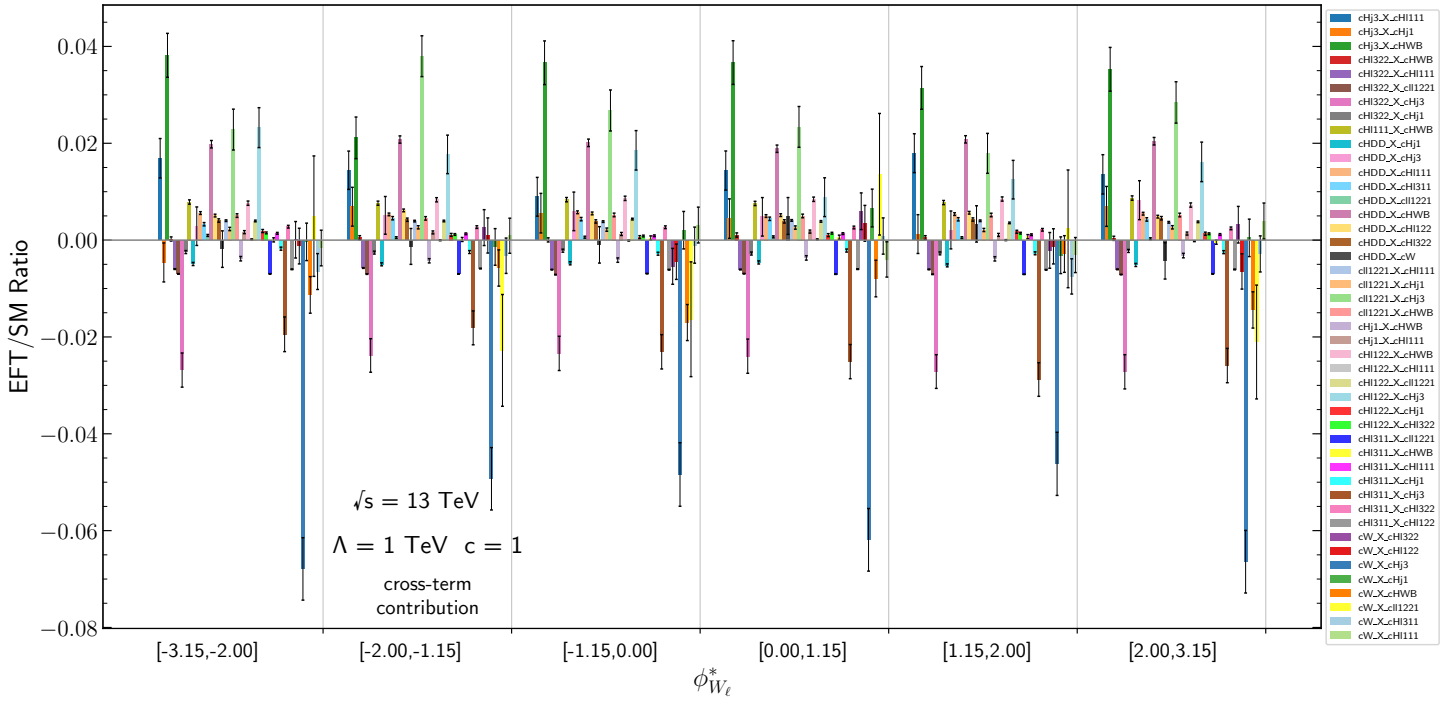

Figure 7.24: *Sensitivity for the cross-term contribution of different pairs of EFT parameters when all $c_i = 1$ on the $\phi^*_{W_\ell}$ observable.*

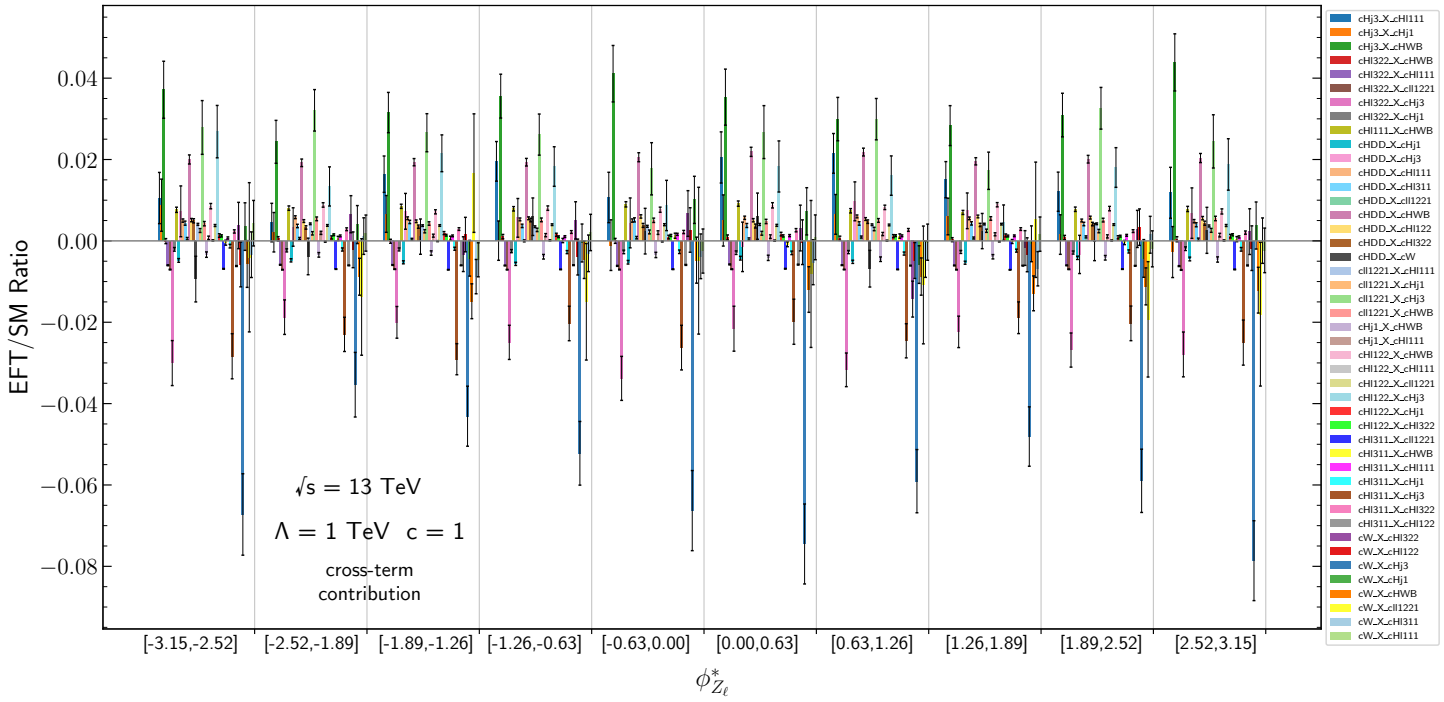

Figure 7.25: *Sensitivity for the cross-term contribution of different pairs of EFT parameters when all $c_i = 1$ on the $\phi^*_{Z_\ell}$ observable.*

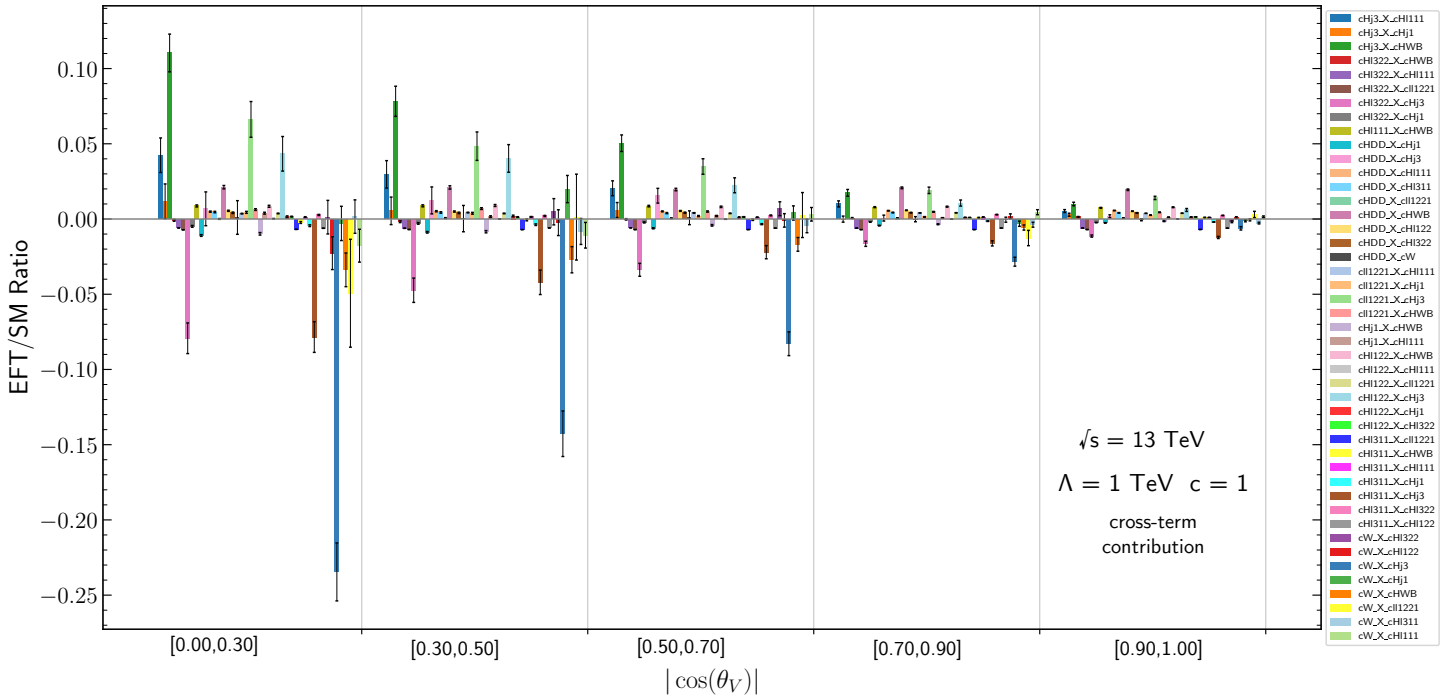

Figure 7.26: *Sensitivity for the cross-term contribution of different pairs of EFT parameters when all $c_i = 1$ on the $|\cos\theta_V|$ observable.*

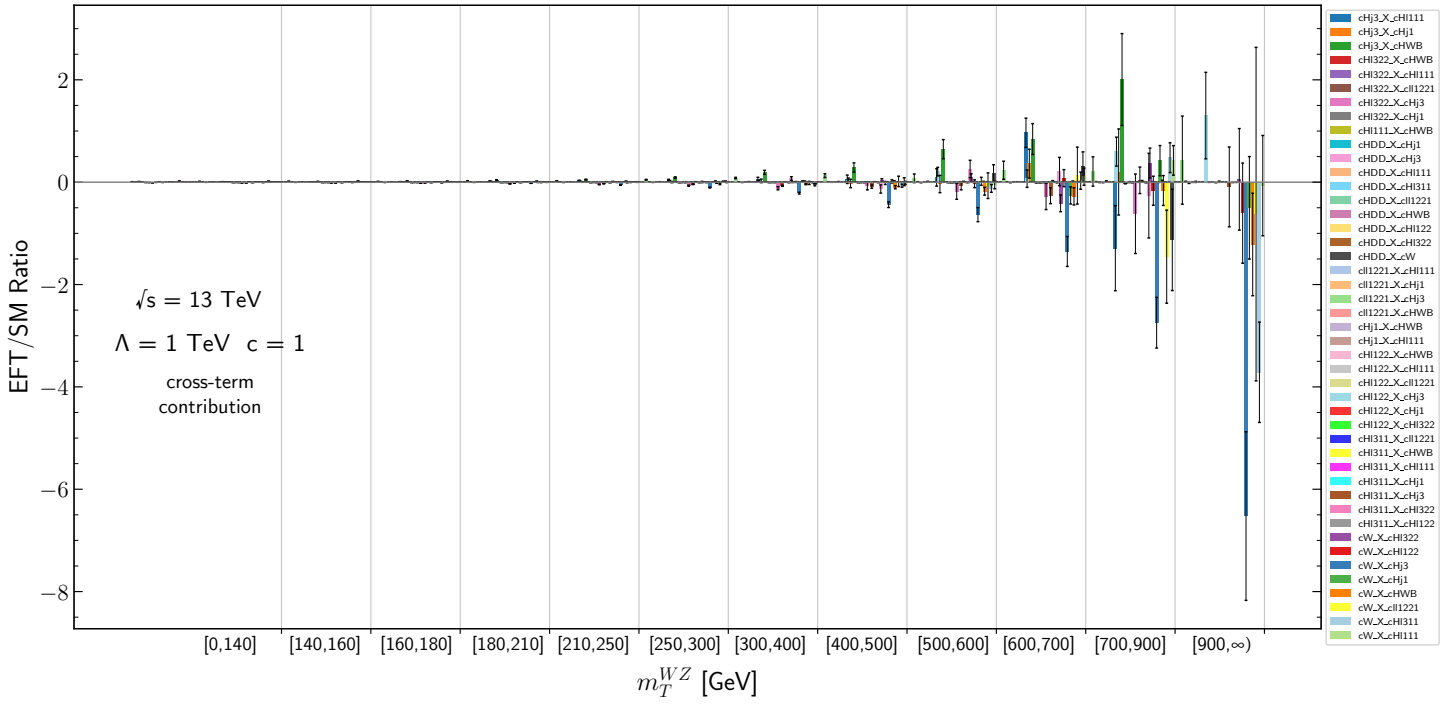

Figure 7.27: *Sensitivity for the cross-term contribution of different pairs of EFT parameters when all $c_i = 1$ on the m_T^{WZ} observable.*

As was done in the linear and quadratic cases, the absolute values of the ”effect” in each bin can be summed for every observable. This aids in quantifying and identifying which cross-term combinations have a large effect across all observables, and are thus worth further studying. Figures 7.28 and 7.29 visually demonstrate the combinatorial effect each pair of parameters has. The former considers only the 5 angular observables, while the latter incorporates the sum of all 5 angular observables and the kinematic m_T^{WZ} observable.

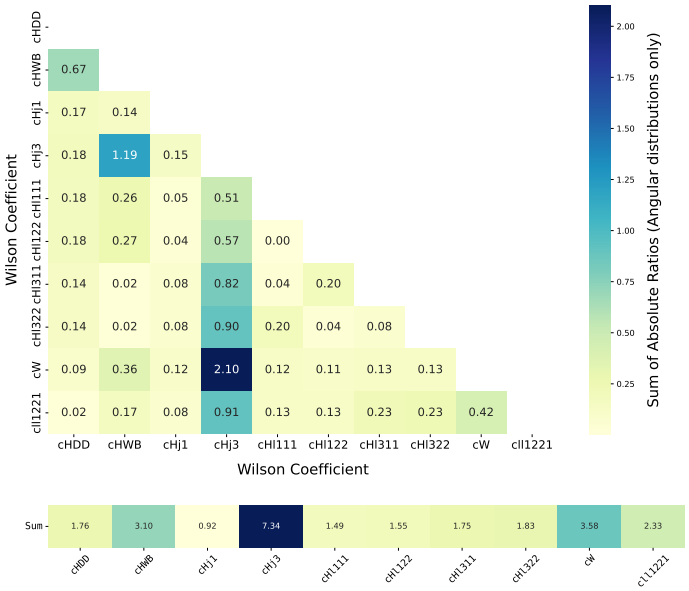

Figure 7.28: *Sum of the absolute values of each bin across all* $\cos\theta^*_{W_\ell}$, $\cos\theta^*_{Z_\ell}$, $|\cos\theta_V|$, $\phi^*_{W_\ell}$ *and* $\phi^*_{Z_\ell}$ *observables. EFT parameters are* $c = 1$.

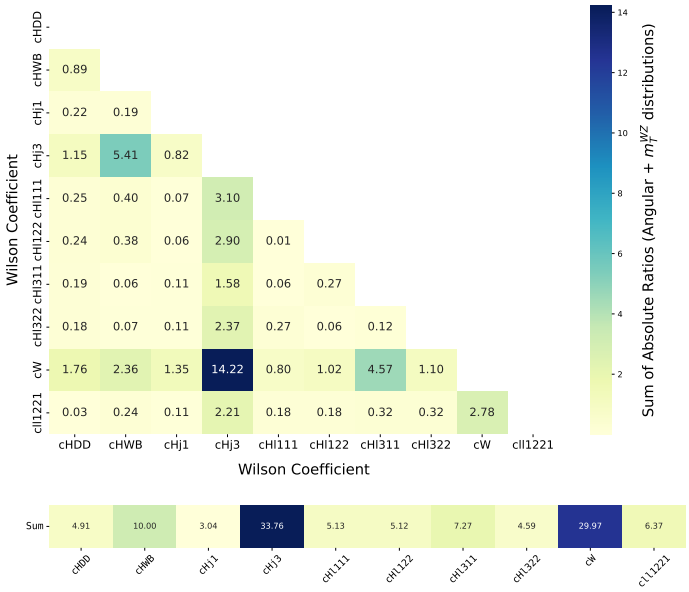

Figure 7.29: *Sum of the absolute values of each bin across all* $\cos\theta^*_{W_\ell}$, $\cos\theta^*_{Z_\ell}$, $|\cos\theta_V|$, $\phi^*_{W_\ell}$ *and* $\phi^*_{Z_\ell}$ + m_T^{WZ} *observables. EFT parameters are* $c = 1$.

Cross-terms of some parameters appear to be very sensitive, as shown in Figures 7.28 and 7.29. As a result, the cross-terms for the following 4 Wilson coefficients were selected as having an effect on the physics process concerned, and were therefore studied further:

- `cHj3`
- `cW`
- `cHWB`
- `cll1221`

7.3.2 Total EFT deviation in observable distributions

The motivation for considering the cross-terms is further realised because Wilson coefficients are simultaneously allowed to be non-zero (with respect to the study in this thesis, two Wilson coefficients are allowed to be non-zero). This means that in Equation 6.1, linear and quadratic terms from both Wilson operators are summed, together with their cross-term. For very sensitive

operators, as we have studied in the previous sections, summing them pair-wise would result in an even larger deviation from the Standard Model.

To illustrate this, we can consider an example of the cHj3 and cW parameters which from the previous sections were found to be the most sensitive. Figure 7.30 shows the total effect of the linear, quadratic and cross-terms for both cHj3 and cW parameters, when $c = 1$. The grey filled histogram shows the SM contribution. The green and blue solid lines show the full SM + BSM contribution if cHj3 or cW parameters are considered one at a time. However, both parameters could be considered simultaneously by summing their individual contributions and the cross-term contribution. The black solid line represents this total BSM contribution.

It can be seen that a larger inclusive cross-section can be achieved when considering the two parameters together. This translates in improved sensitivity as is shown in the ratio plots (bottom panel of each subplot in Figure 7.30). The full SM + cHj3 + cW contribution consistently has the largest BSM/SM ratio, across all bins and across all observables.

Hence, adding the extra cross-term contribution and considering two Wilson coefficients at a time can provide enhanced sensitivity, allowing to better constrain the parameters.

7.4 SMEFT with 0+1j

Thus far, all sensitivity studies shown above deal with Leading-order diagrams, calculated and generated with SMEFTsim 3.0 and MADGRAPH5_AMC@NLO using the 0j scheme. i.e. no additional jets are required in the process. This helps to focus directly on the contributions of the SMEFT operators without the added complication of NLO QCD.

However, to accurately mimic the conditions in proton colliders, NLO QCD effects must be taken into account. Section 6.2 introduces the idea of using a 'merged' Monte Carlo generation strategy, which includes the generation of an additional process with the signal plus one jet together with the signal process in the final state. i.e. the so called "0+1j" strategy. Section 6.2.1 validates this strategy for the purely SM case. In this section, we further validate this for the BSM cases where SMEFT operators are present.

SMEFTsim 3.0 uses FeynRules to generate an input model for MADGRAPH5_AMC@NLO to calculate the additional EFT produced diagrams for a particular physics process. SMEFTsim 3.0 has the benefit of parameterisation/decomposition: the individual linear, quadratic and cross-terms can be generated separately [40]. However, this package works at the LO in both QCD and EW.

Another widely adopted input model is SMEFTatNLO [105] which has the advantage of using loop induced and next-to-leading-order computations in QCD, along with simulating the SMEFT effects. (EW interactions are still at LO). A current theoretical limitation is its inability to use

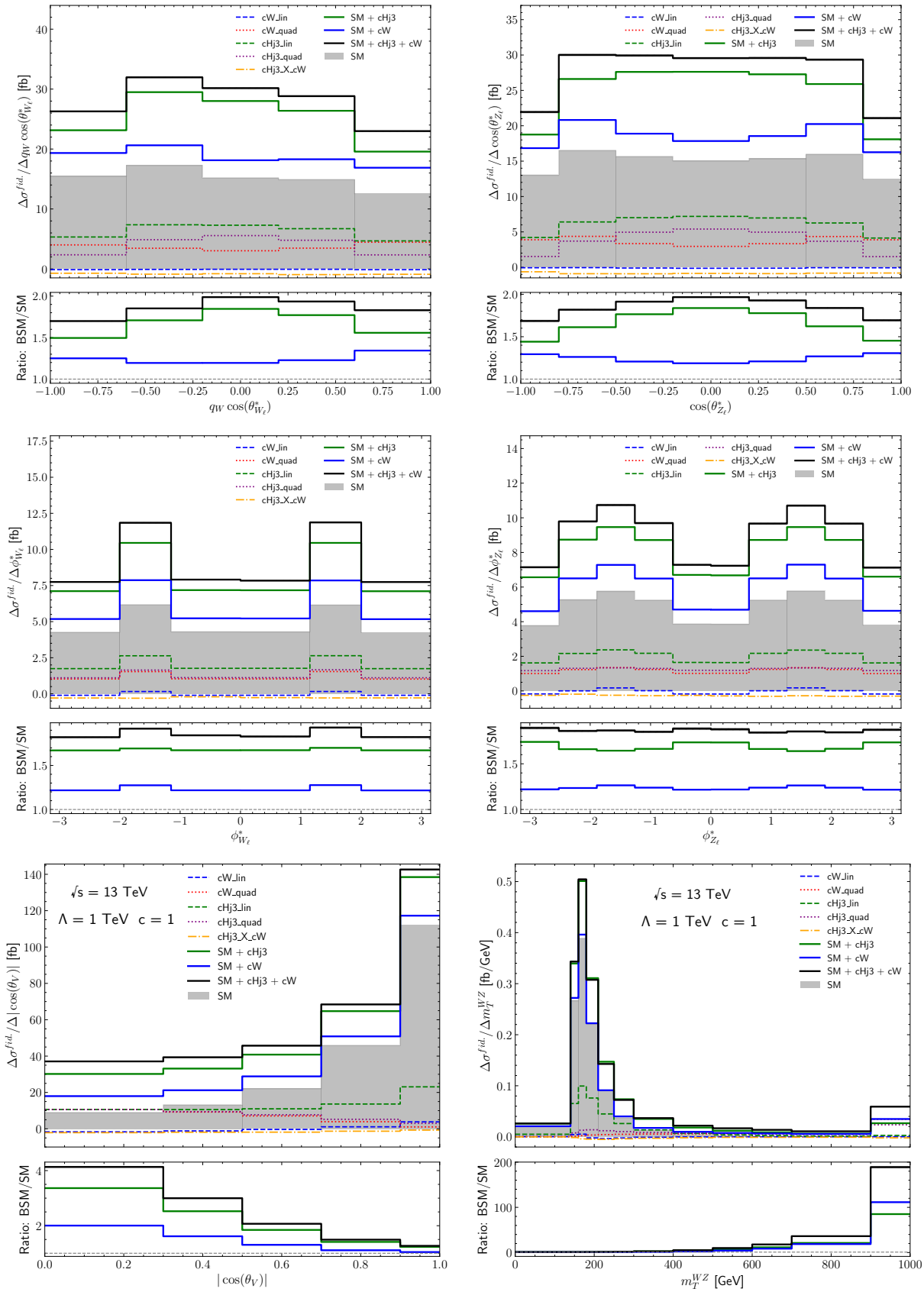

Figure 7.30: *SM (grey filled histograms) and BSM (coloured lines) differential distributions for the $WZ \to \ell\nu\ell\ell$ process. BSM predictions considering one Wilson coefficient at a time are shown for `cHj3` (solid green line) and `cW` (solid blue line). Adding both contributions and the cross-term gives the full BSM prediction (solid black line). Pure linear, quadratic and cross EFT components are shown as dashed lines. All values of the parameters are set to $c = 1$.*

the decomposition method when interfacing working at NLO: It becomes increasingly difficult to separate the diagrams cleanly into “SM-only”, “linear in EFT”, “quadratic in EFT” when NLO loops on the propagators and vertices are involved.

SMEFTatNLO generates the sum of SM + BSM effects, accounting for NLO QCD. This can be used to validate the “0+1j” strategy using the SMEFTsim 3.0 setup to simulate BSM effects. The validation is done for the Wilson coefficients of interest listed in Section 7.1.4.

SMEFTatNLO assumes the same flavour symmetry as in the SMEFTsim-top model, except for the treatment of down quarks [40]. Since both models have their Wilson coefficients in the Warsaw basis, a one-to-one mapping of Wilson coefficients between the two packages exists. An exception to this is the cHj1 and cHj3 parameters which are defined as a combination of parameters in the SMEFTatNLO package.

7.4.1 Inclusive cross-section comparison

The predictions of the inclusive cross-section calculated by SMEFTatNLO and SMEFTsim 3.0 LO can be compared to quantify the magnitude of change in going from LO to NLO. As described in Section 6.2, LO generations can be enhanced to add some NLO contribution by using the 0+1j scheme, which adds a jet in the final state.

Table 7.5 shows the SMEFTatNLO inclusive cross-section for the SM prediction and the SM + EFT prediction, for various Wilson coefficients of interest. The same is reported for the LO generation using SMEFTsim, for both 0j and the 0+1j strategy.

It is quite evident that the 0+1j scheme at LO gives a much better approximation to the SMEFTatNLO prediction than the 0j scheme. A percentage difference of $\leq 10\%$ is noted from SMEFTatNLO to the SMEFTsim 0+1j LO scheme.

7.4.2 Observable distribution comparison

The distributions for each observable of interest can be compared for the state-of-the-art SMEFTatNLO generation and the 0+1j SMEFTsim 3.0 LO generation. It should be noted that the SMEFTatNLO data sample has a smaller sample size, compared to the SMEFTsim 3.0 LO generation.

The SMEFTatNLO data sample consists of the SM prediction + the EFT linear and quadratic prediction for the particular Wilson coefficient.
The SMEFTsim LO generation also consists of the sum of the SM prediction, the EFT linear, and the EFT quadratic prediction for the particular Wilson coefficient. All coefficients are set to the value $c = 1$. The predictions used for this comparison do not include the cross-terms.

The figures compare the differential distributions of the observables of interest for the pa-

Parameter	SMEFTatNLO σ_{incl} (fb)	0j σ_{incl} (fb)	0+1j σ_{incl} (fb)	% diff SMEFTatNLO vs 0j	% diff SMEFTatNLO vs 0+1j
SM	48.7 (52.06 in POWHEG)	30.1	45.9	47.1	6.2
SM +					
cHDD	49.0	30.8	46.9	45.7	4.4
cHWB	52.6	33.3	50.6	44.9	3.9
cHj3	77.3	50.6	70.5	41.6	9.2
cHl111	51.9	32.2	49.1	46.8	5.5
cHl122	51.5	32.2	49.1	46.1	4.8
cHl311	43.2	26.9	40.9	46.6	5.4
cHl322	43.4	26.9	40.9	46.8	5.8
cW	55.6	37.3	54.4	39.4	2.2
cll1221	54.5	33.9	51.7	46.7	5.2

Table 7.5: *Inclusive cross-section comparison of SMEFTatNLO SM and EFT production with LO SMEFTsim production for both 0j and the 0+1j strategy. All EFT parts contain the linear and quadratic contribution, with* $c = 1$.

rameters for SM (Figure 7.31) cHDD (Figure 7.32), cHl111 (Figure 7.33), cHl122 (Figure 7.34), cHl311 (Figure 7.35), cHl322 (Figure 7.36), cHj3 (Figure 7.37), cHWB (Figure 7.38), cll1221 (Figure 7.39), and cW (Figure 7.40) respectively.

In general, the ratios of 0+1j/SMEFTatNLO exhibit are flat across the kinematic ranges, suggesting that the NLO and LO predictions do not differ drastically in shape, and a common multiplicative factor could be used for LO calculations to arrive at at NLO prediction. The largest difference usually occurs in the high energy m_T^{WZ} bins, which is where EFT operators have a larger effect, and in the $|cos\theta_V| > 0.9$ region, where the boson momentum is largely in the longitudinal direction. Other angular observables, in general, seem to have a relatively flat ratio when going from LO to NLO.

For the Standard Model distributions, the three angular variable distributions are relatively flat, with the per-bin ratios typically lying between 0.92 and 1.0. The largest deviation occurs in the $|cos\theta_V|$ observable, where the ratio dips to 0.87 in the kinematic region corresponding to smaller boson transverse momentum. In this region, higher-order corrections, particularly initial-state radiation (which alters the longitudinal momentum of the system), are significant. These effects are not modelled at the LO 0+1j level. There is also slight deviation in the ratio for the the m_T^{WZ} variable, especially in the highest m_T bins, but this is accounted for in the statistical

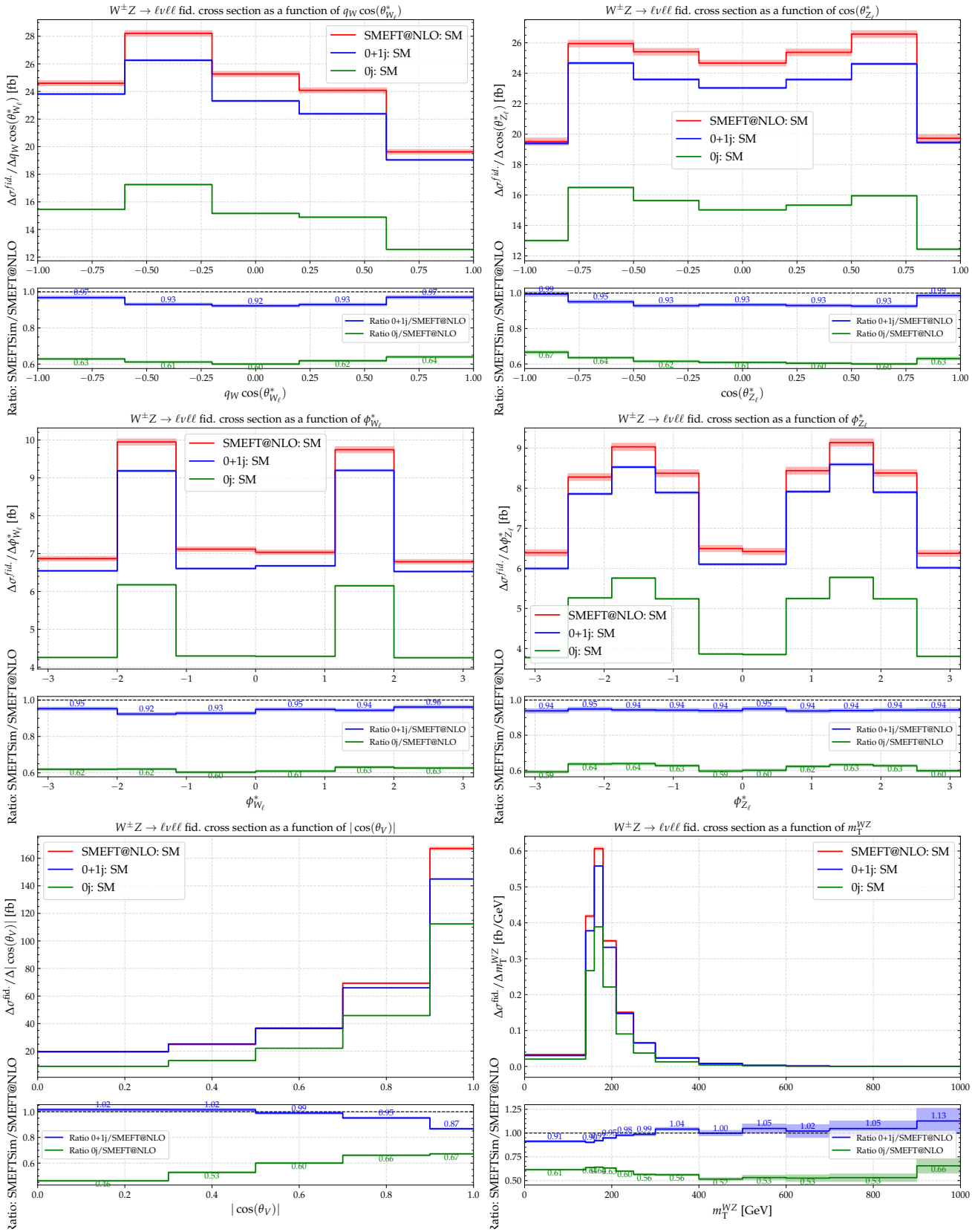

Figure 7.31: *Comparison of the differential distributions of the observables of interest for* `SMEFTatNLO` *and 0+1j* `SMEFTsim 3.0` *LO for SM ($c = 0$). The ratio plot shows a bin-by-bin ratio between* `SMEFTatNLO` *and* `SMEFTsim` *LO. All uncertainty bands are statistical.*

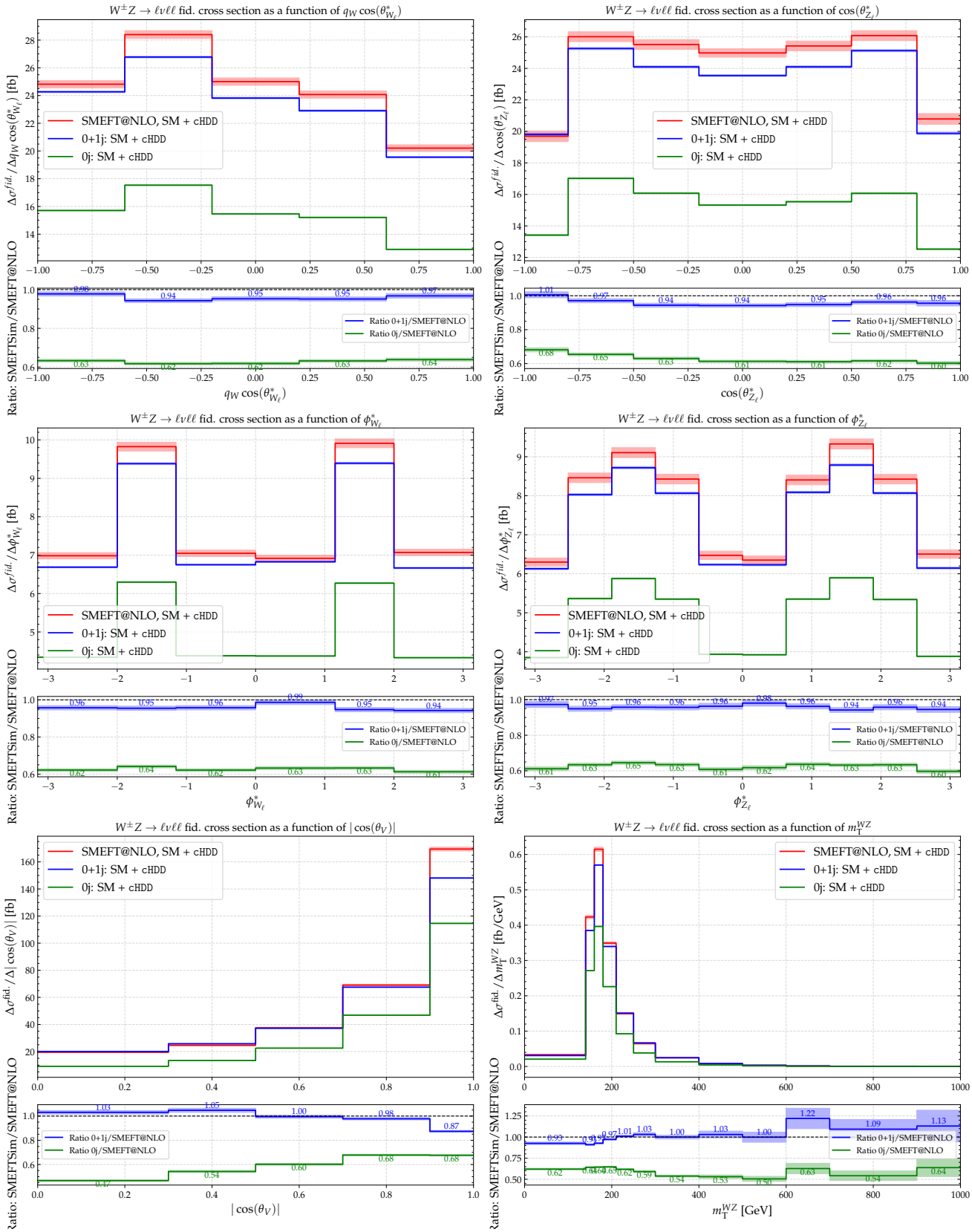

Figure 7.32: *Comparison of the differential distributions of the observables of interest for* `SMEFTatNLO` *and 0+1j* `SMEFTsim 3.0` *LO, with* `cHDD=1`*. The ratio plot shows a bin-by-bin ratio between* `SMEFTatNLO` *and* `SMEFTsim` *LO. All uncertainty bands are statistical.*

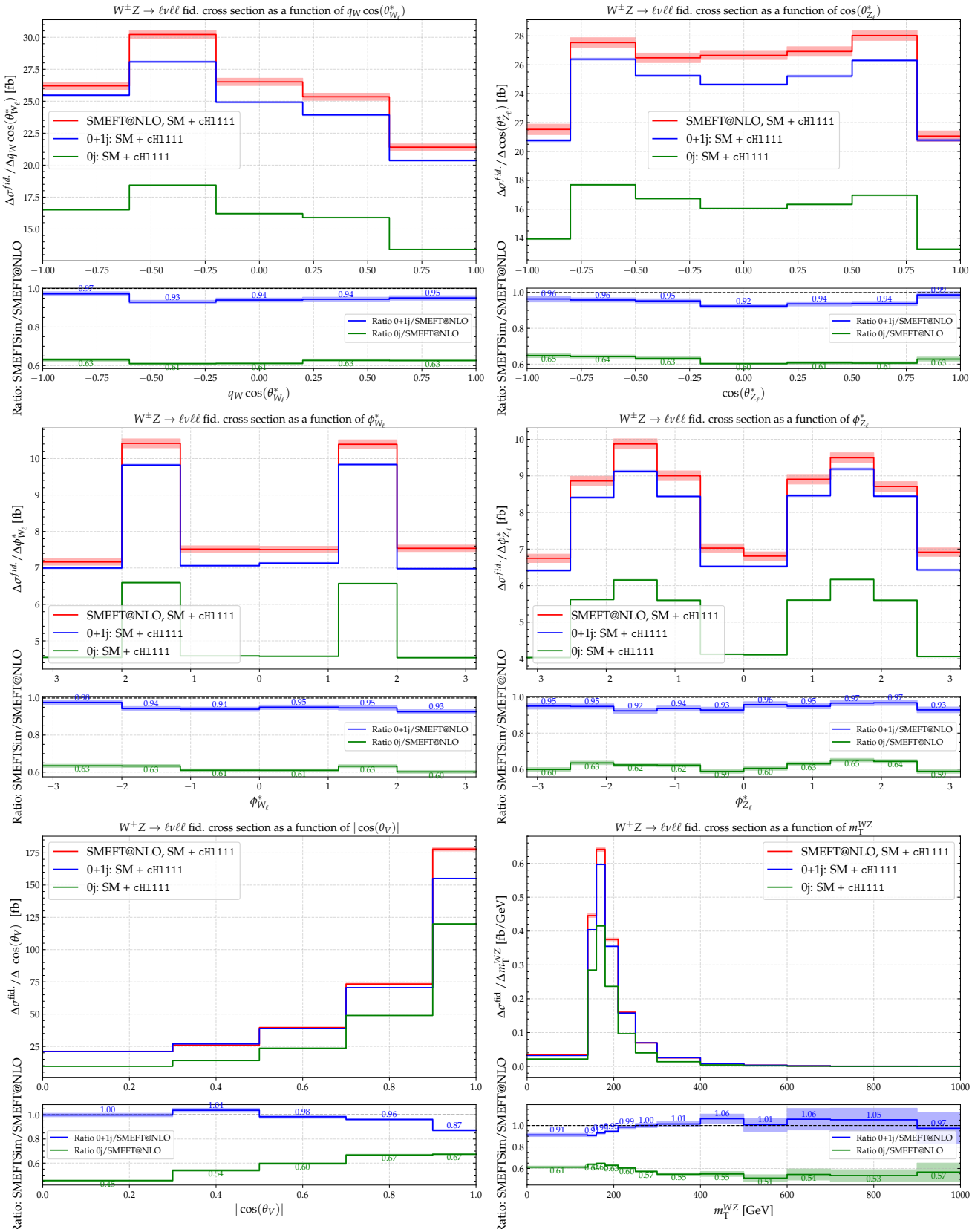

Figure 7.33: *Comparison of the differential distributions of the observables of interest for* `SMEFTatNLO` *and 0+1j* `SMEFTsim 3.0` *LO, with* `cHl111=1`*. The ratio plot shows a bin-by-bin ratio between* `SMEFTatNLO` *and* `SMEFTsim` *LO. All uncertainty bands are statistical.*

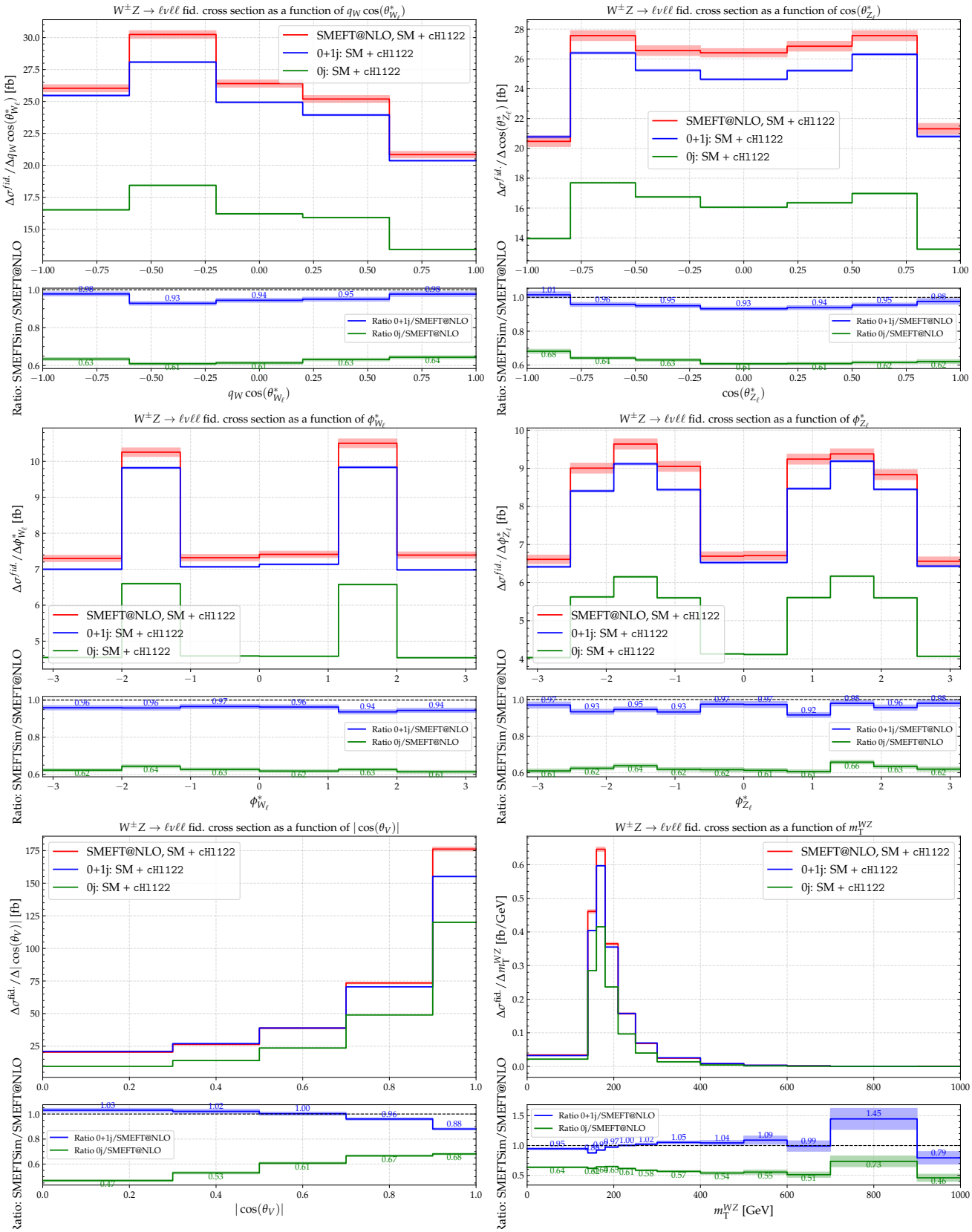

Figure 7.34: *Comparison of the differential distributions of the observables of interest for* `SMEFTatNLO` *and 0+1j* `SMEFTsim 3.0` *LO, with* `cHl122=1`*. The ratio plot shows a bin-by-bin ratio between* `SMEFTatNLO` *and* `SMEFTsim` *LO. All uncertainty bands are statistical.*

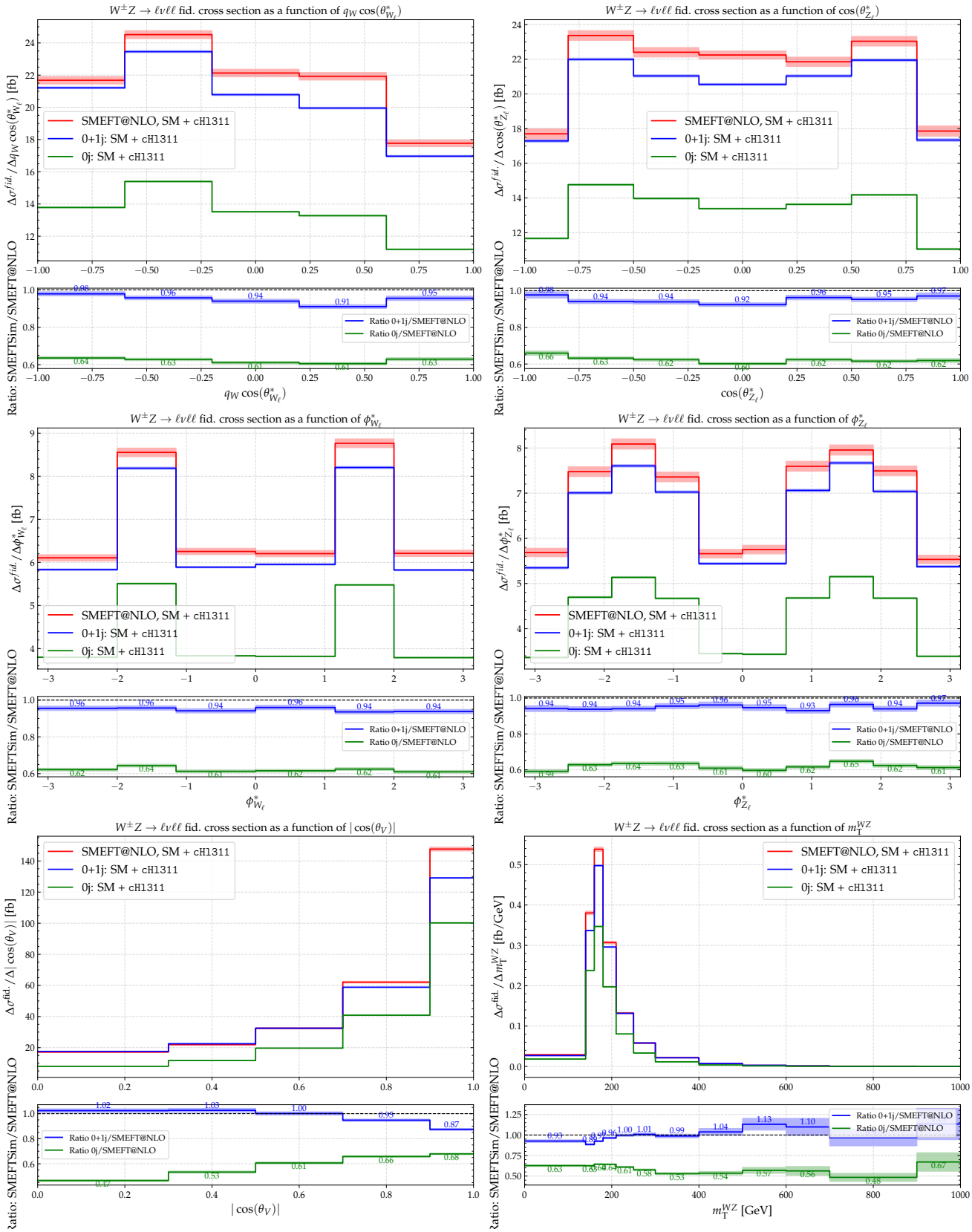

Figure 7.35: *Comparison of the differential distributions of the observables of interest for* `SMEFTatNLO` *and 0+1j* `SMEFTsim 3.0` *LO, with* `cHl311=1`*. The ratio plot shows a bin-by-bin ratio between* `SMEFTatNLO` *and* `SMEFTsim` *LO. All uncertainty bands are statistical.*

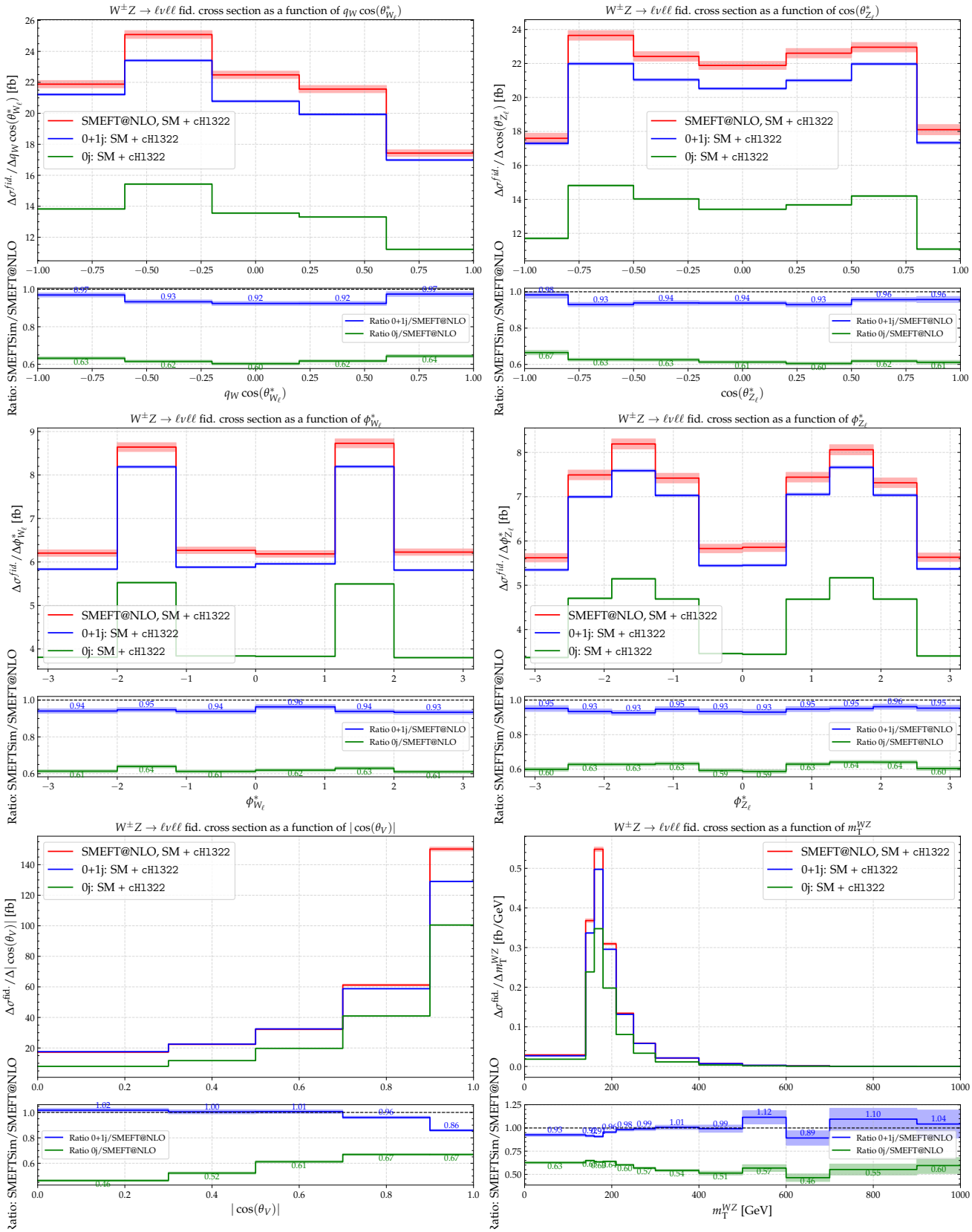

Figure 7.36: *Comparison of the differential distributions of the observables of interest for* `SMEFTatNLO` *and 0+1j* `SMEFTsim 3.0` *LO, with* `cHl322=1`*. The ratio plot shows a bin-by-bin ratio between* `SMEFTatNLO` *and* `SMEFTsim` *LO. All uncertainty bands are statistical.*

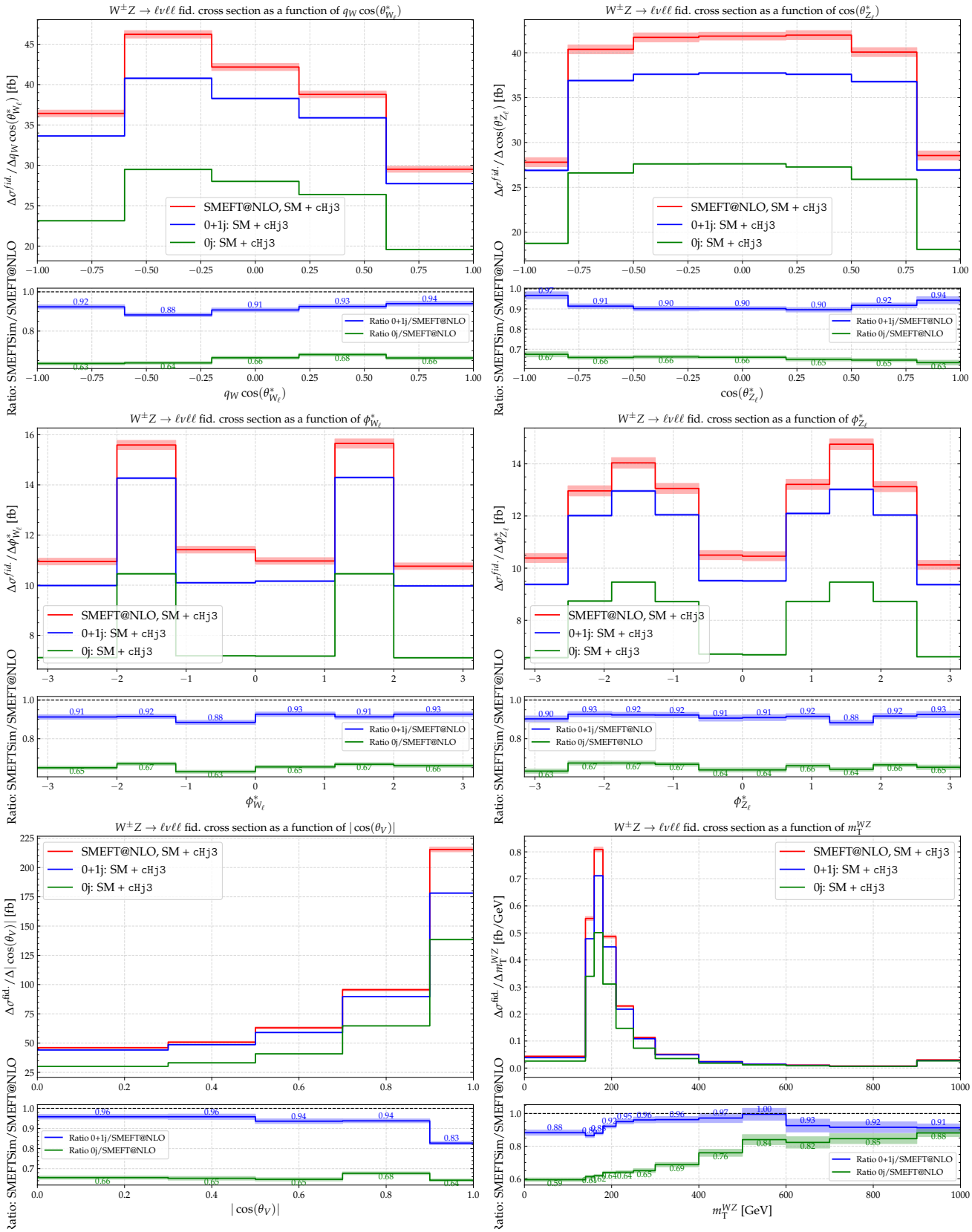

Figure 7.37: *Comparison of the differential distributions of the observables of interest for* `SMEFTatNLO` *and 0+1j* `SMEFTsim 3.0` *LO, with* `cHj3=1`*. The ratio plot shows a bin-by-bin ratio between* `SMEFTatNLO` *and* `SMEFTsim` *LO. All uncertainty bands are statistical.*

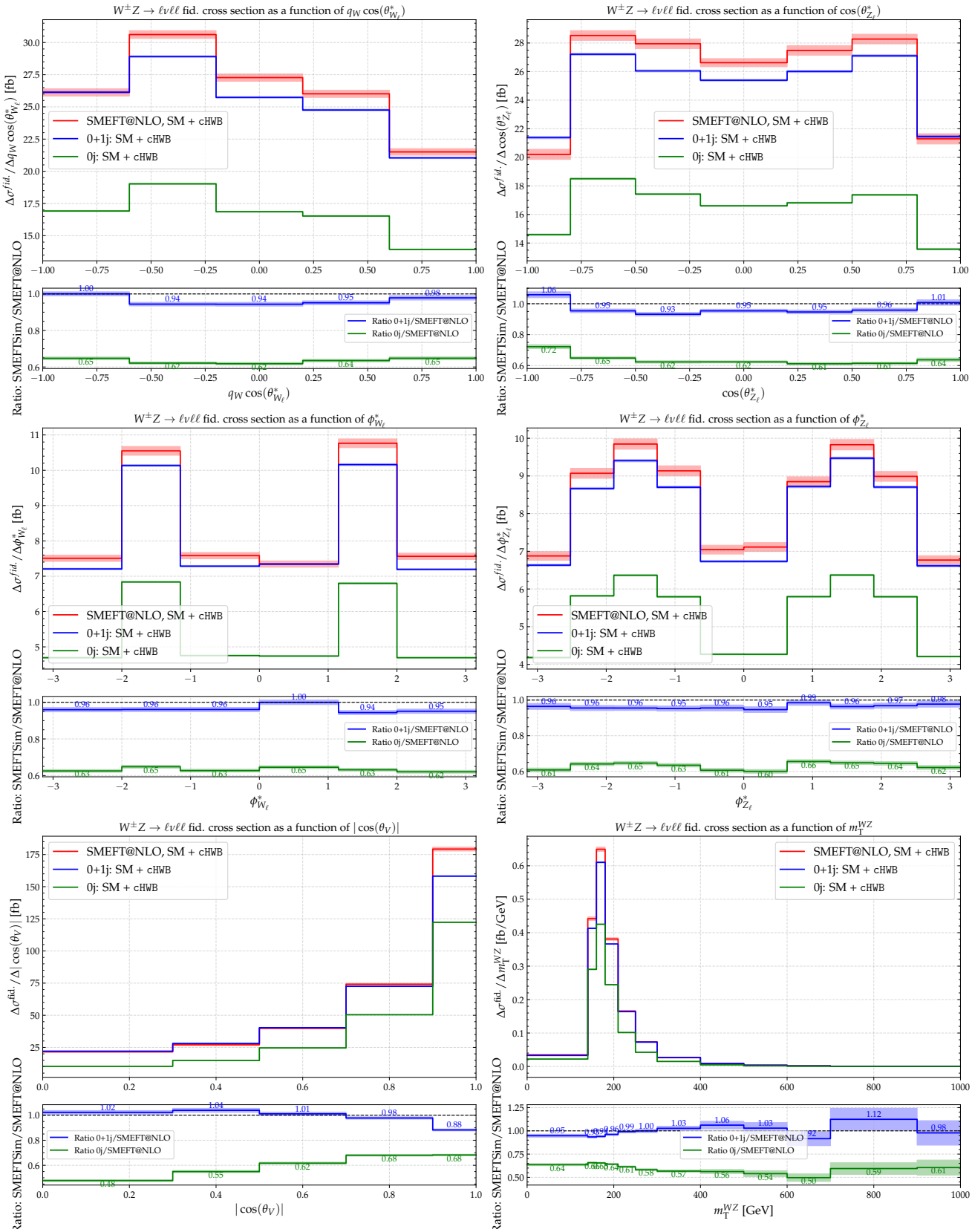

Figure 7.38: *Comparison of the differential distributions of the observables of interest for* `SMEFTatNLO` *and 0+1j* `SMEFTsim 3.0` *LO, with* `cHWB=1`*. The ratio plot shows a bin-by-bin ratio between* `SMEFTatNLO` *and* `SMEFTsim` *LO. All uncertainty bands are statistical.*

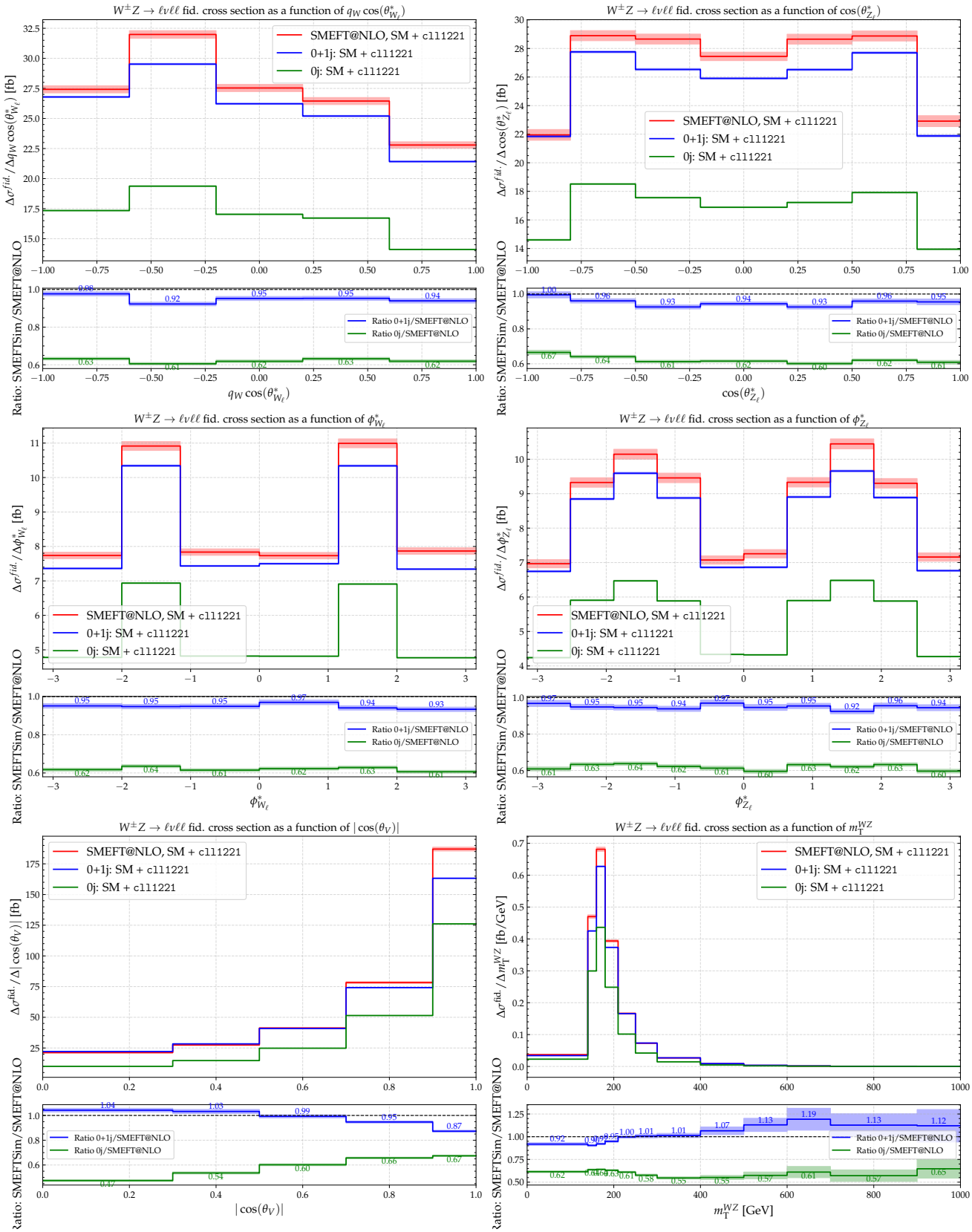

Figure 7.39: *Comparison of the differential distributions of the observables of interest for* `SMEFTatNLO` *and 0+1j* `SMEFTsim 3.0` *LO, with* `cll1221=1`*. The ratio plot shows a bin-by-bin ratio between* `SMEFTatNLO` *and* `SMEFTsim` *LO. All uncertainty bands are statistical.*

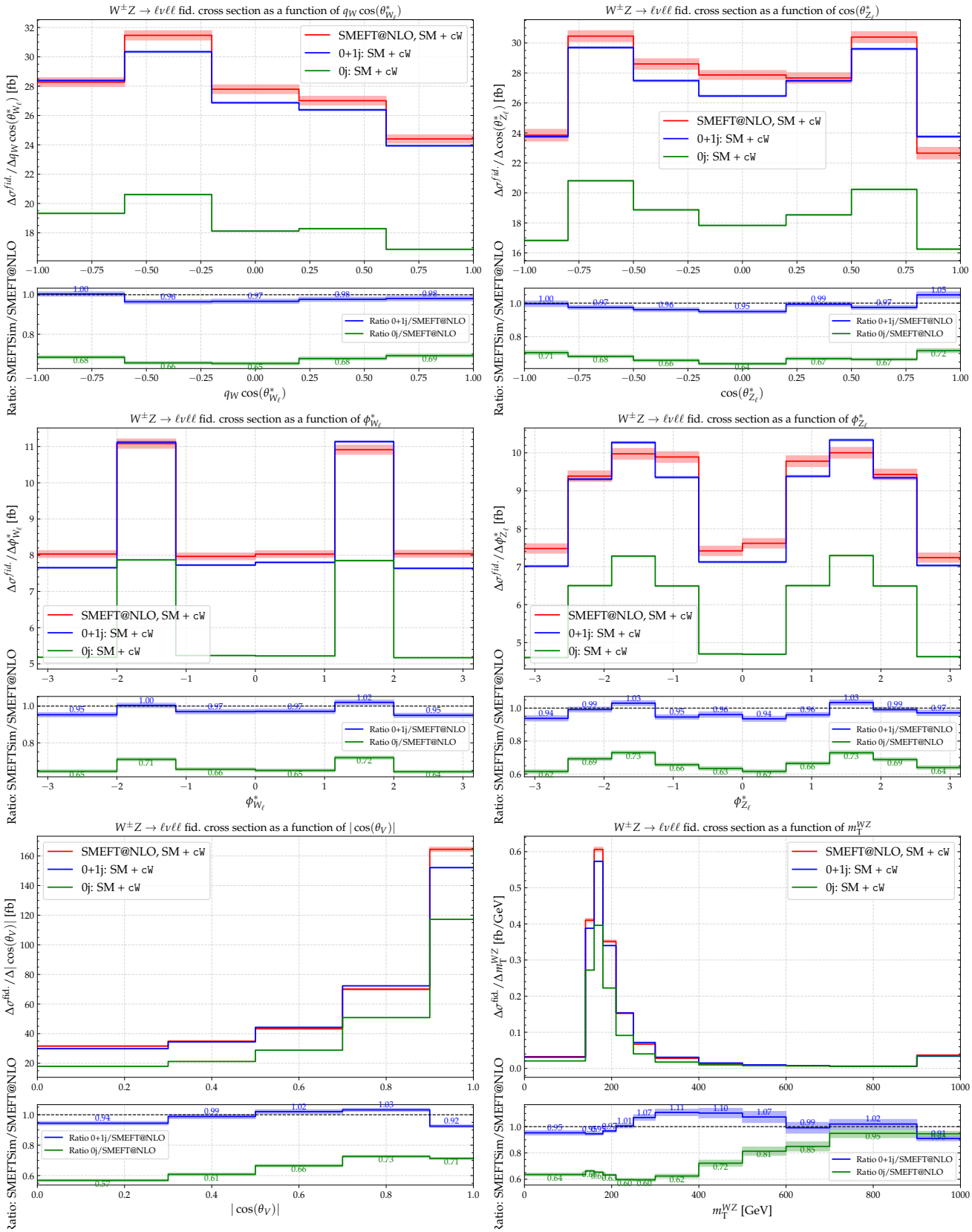

Figure 7.40: *Comparison of the differential distributions of the observables of interest for* `SMEFTatNLO` *and 0+1j* `SMEFTsim 3.0` *LO, with* `cW=1`*. The ratio plot shows a bin-by-bin ratio between* `SMEFTatNLO` *and* `SMEFTsim` *LO. All uncertainty bands are statistical.*

error bars.

For cHDD distributions, the ratio remains relatively flat, with values typically lying between 0.9 and 1.15. The higher bins of the m_T^{WZ} variable do experience some deviation between the higher order MCs.

In the cHl111, cHl122, cHl311 and cHl322 distributions, the ratio also remains fairly flat, generally fluctuating between 0.87 and 1.01. Of note is a large deviation of 1.45 in the higher m_T^{WZ} bins for cHl122.

The cHj3 distribution also shows a somewhat flat behaviour, with the ratio values typically lying between 0.9 and 1.0.

For the cHWB distribution, the ratio is flat within the range 0.9 to 1.00.

For the cll1221 distribution, the ratio also remains flat, fluctuating between 0.87 and 1.15.

For the cW distribution, the ratios are mostly flat, lying between 0.89 and 1.1. For this Wilson coefficient in particular, the 0+1j predictions are in strong agreement with the SMEFTatNLO predictions.

The difference in magnitude between the EFT distributions is dominated by the difference in SM predictions from LO to NLO. The EFT effects are relatively unchanged from the increase in order in QCD, thus showing that the 0+1j samples predict the EFT effects just as well as SMEFTatNLO generation.

Given the bin-by-bin ratio results as well as the results from the integrated inclusive cross-section predictions, the SMEFTsim LO prediction is considerably improved using the 0+1j scheme, and the description of the SMEFT effects are closer to state-of-the-art SMEFTatNLO predictions. The use of 0+1j MC samples is therefore justified, as they produce predictions comparable to the state-of-the-art SMEFTatNLO results.

With this result, the SMEFT prediction (x_b^{pred} in Equation 6.13), derived from the SM + EFT predictions (Equation 6.1), demonstrates that the 0+1j method provides a satisfactory EFT prediction at NLO. Thus, in this analysis, only the SM prediction is scaled to higher orders, while the EFT contribution is directly obtained from the 0+1j generation.

Further plots in which the SM contribution is neglected, and only the EFT contribution is compared are presented in Appendix F.

CHAPTER 8

SMEFT interpretation of the $WZ \to \ell\nu\ell\ell$ channel in the ATLAS Run-2 dataset

This chapter presents the results and SMEFT interpretation of the $WZ \to \ell\nu\ell\ell$ channel using the full Run-2 ATLAS dataset of 139 fb^{-1} collected at $\sqrt{s} = 13$ TeV (2015–2018).

Reconstruction-level histograms (after event selection and background subtraction) are unfolded with the response matrix (Section 5.5) to the fiducial particle level (dressed leptons). The unfolded distributions are then compared to particle level MC (truth) predictions shown in Figure 6.1. This thesis presents an interpretation of the data at the dressed particle level.

For each measured result, an expected CI is also provided. The expected CI is obtained by performing the fit to an Asimov data sample [124, 125] i.e. in this case, a Standard Model data sample, with all nuisance parameters set to their central value. Although by construction, a fit to this data set will extract the input central values (which is the SM, i.e. $c = 0$), it can be used to study the Nuisance Parameters constraints and correlations and can provide a range for the expected significances.

8.1 Particle Level results

8.1.1 1D EFT limits

The Likelihood function of Equation 6.12 is maximised for one Wilson coefficient of interest and one observable of interest at a time. The profile likelihood ratio test statistic defined in Equation 6.15 is then used to measure Wilson coefficients and either observe non-zero values or exclude them in a 95% confidence interval.

The measured 95% confidence intervals obtained by fitting the linear and quadratic EFT contributions for the Wilson coefficients of interest are listed in Table 8.1. Scans of the profile likelihood ratio statistic for each coefficient are shown in Appendix C. The expected 1D limits,

as well as the profile likelihood scans are also shown in Appendix C.

EFT parameter	Observable					
	$\cos(\theta^*_{W_\ell})$	$\cos(\theta^*_{Z_\ell})$	$\lvert\cos(\theta_V)\rvert$	m_T^{WZ}	$\phi^*_{W_\ell}$	$\phi^*_{Z_\ell}$
cHDD	[-4.27, 2.59]	[-3.99, 2.88]	[-3.50, 2.33]	[-3.99, 1.72]	[-4.91, 3.28]	[-4.00, 2.74]
cHl111	[-2.85, 1.50]	[-2.83, 1.49]	[-3.33, 1.01]	[-2.91, 0.89]	[-1.53, 2.09]	[-2.29, 1.40]
cHl122	[-2.88, 1.46]	[-2.88, 1.45]	[-3.34, 0.98]	[-2.90, 0.88]	[-1.59, 2.05]	[-2.30, 1.38]
cHl311	[-0.85, 1.56]	[-0.87, 1.50]	[-0.57, 1.75]	[-0.54, 1.52]	[-1.23, 0.87]	[-0.82, 1.23]
cHl322	[-0.86, 1.52]	[-0.86, 1.49]	[-0.57, 1.74]	[-0.51, 1.54]	[-1.21, 0.87]	[-0.83, 1.21]
cHj1	[-1.42, 1.76]	[-3.74, 1.68]	[-2.03, 1.03]	[-2.61, 1.79]	[-5.03, 2.46]	[-4.69, 1.88]
cHj3	[-0.61, 0.16]	[-1.28, 0.32]	[-0.76, -0.02]	[-0.18, 0.02]	[-2.24, -1.84] ∪ [-0.10,0.37]	[-0.45, 0.24]
cW	[-0.91, 0.80]	[-0.73, 0.63]	[-0.23, 0.32]	[-0.11, 0.09]	[-0.96, 0.92]	[-0.53, 0.78]
cll1221	[-1.38, 0.83]	[-1.36, 0.84]	[-1.57, 0.55]	[-1.38, 0.51]	[-0.80, 1.21]	[-1.13, 0.79]
cHWB	[-7.31, 0.92]	[-7.42, -4.49] ∪ [-2.86,1.03]	[-7.35, 0.05]	[-2.38, 0.34]	[-8.28, -6.55] ∪ [-0.44, 1.40]	[-7.29, -5.46] ∪ [-2.00, 0.96]

Table 8.1: *Measured 95% confidence intervals for EFT parameters, determined by fitting the weighted sum of the linear and quadratic terms for each of the listed observables. The ∪ symbol indicates disjoint ranges included by the measurement.*

Figure 8.1 shows the confidence intervals (CIs) of the different EFT coefficients for each observable studied. Together with the measured CI, an expected CI is also provided.

All but one of the limits obtained includes the SM value within at least the 95% CI.

Within the 95% CI range for $|\cos(\theta_V)|$, cHj3 has a very small value that does not include the $c = 0$ SM point. The cHj3 parameter only just includes the SM point within the 95% CI for m_T^{WZ}.

It should be noted that by definition, the 95% CI would not include the true parameter value 5% of the time. This would mean, statistically it is likely that the SM point could be excluded in these fits 5% of the time. Therefore this result is statistically expected.

Also noteworthy is the cHWB parameter whose profile likelihood ratio test statistic contains multiple minima, some of which dip in and out of the 1σ and 2σ thresholds (shown in Appendix C). For this reason, a discontinuous 95% CI is reported for this parameter. cHj3 for $\phi^*_{W_\ell}$ also has a similar profile likelihood ratio test statistic, causing a discontinuous 95% CI. The "second" 95% interval in these cases suggests a rather large value of c, so while this is mathematically possible, it is physically quite unlikely as the effect of such a large c would have already been seen in other measurements [126].

Different observables offer different insight into the strength of each EFT parameter. In par-

ticular, the most sensitive observables, $|\cos(\theta_V)|$ and m_T^{WZ}, offer very tight constraints for `cW` and `cHj3`. All observables suggest that `cHj3` is skewed more in the negative direction, suggesting a negative value for this parameter, should it be non-zero.

On the other hand, some parameters such as `cHj1` and `cHDD` are not constrained very effectively, suggesting that other analyses may be better suited to see the effects of these parameters.

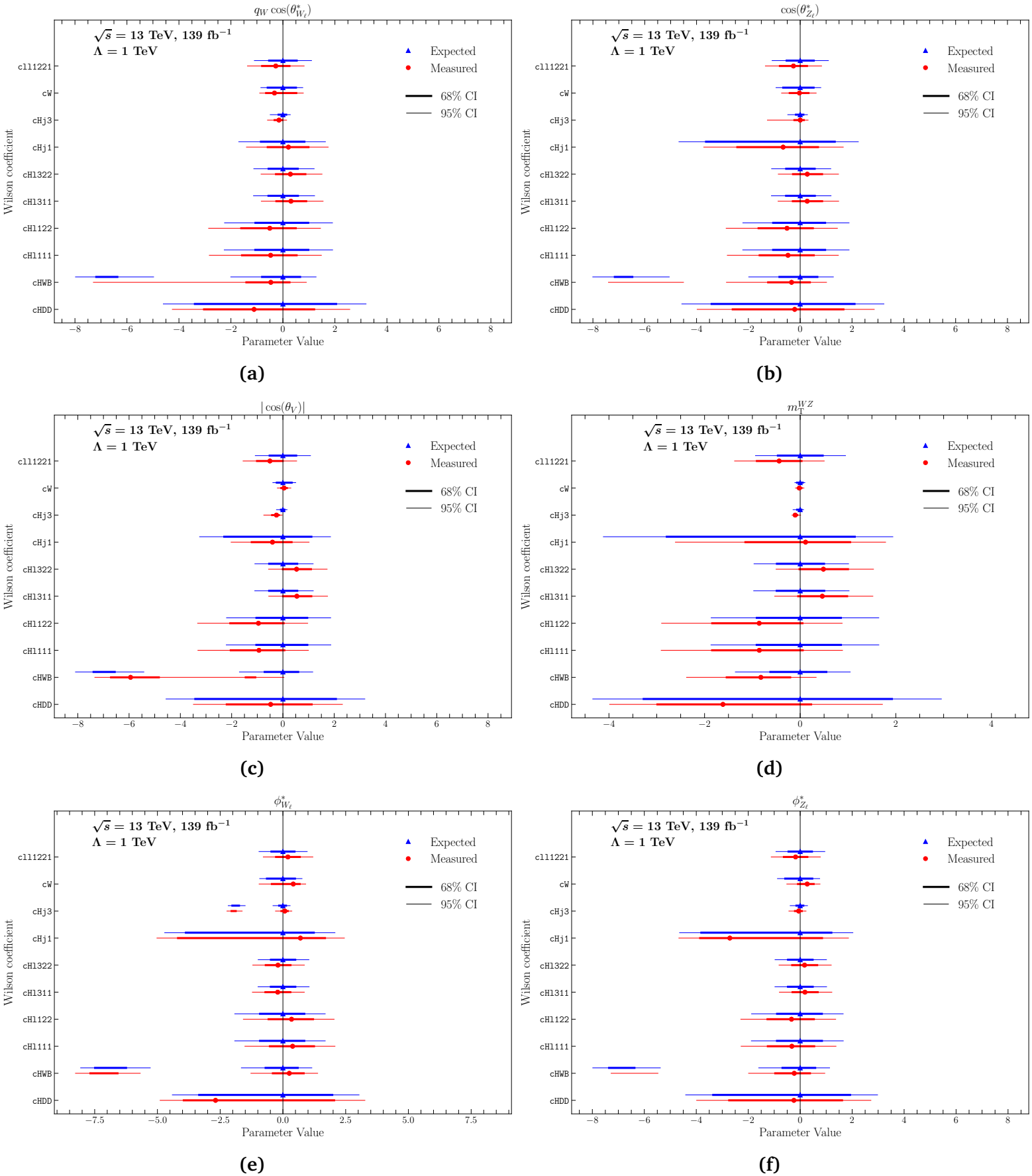

Figure 8.1: *Expected (blue) and measured (red) 95% CIs for each Wilson coefficient of interest, and for each observable studied. Results are quoted for fits that take into account both linear + quadratic contributions. Expected distributions are obtained when fitting an Asimov Standard Model data sample.*

8.1.2 2D EFT limits

By including the cross-terms, the predictions that go into the fit of Equation 6.12 are now a function of two Wilson coefficients. The unfolded data can thus be fit to this prediction to provide 2D scans of the likelihood surface. Using the profile likelihood ratio test statistic defined in Equation 6.15, confidence intervals for allowed ranges of Wilson coefficients are obtained.

The interpretation focuses on the combination of the previously studied 4 most sensitive cross-terms in Section 7.3.1.

The 2D scans provide insight into correlations between the two EFT parameters. If the contours are elongated along a diagonal axis, the two parameters are correlated, while if the contours are more circular, the parameters are independent.

Observable: $q_W \cos\theta^*_{W_\ell}$

Figure 8.2 illustrates the profile likelihood ratio test statistic scan for the measurement of the $q_W \cos\theta^*_{W_\ell}$ observable. The expected profile likelihood ratio using both the Asimov data and real data is shown in Appendix D.1.

The black solid line corresponds to the borders of the 68% CI when varying both parameters. The black dashed line represents the 95% CI when varying both parameters. The white solid horizontal and vertical lines correspond to the 95% CI of the 1D fit for the individual parameter.

The SM point (0,0) as illustrated by a white filled circle, is inside the 68% boundary of all scans. However, the parameter space of plausible values for each coefficient pair is wide, suggesting that while the data is not strongly rejecting the Standard Model, certain parameter combinations may leave room for possible deviations.

For some parameter scans, namely `cHj3 x cHWB`, `cHj3 x cW`, multiple minima are present in the profile likelihood statistic surface. For the case of `cHj3 x cHWB`, two separate distinct regions lie in the 68% CI, and they are all commonly enclosed in the 95% CI.

The contours for `cHj3 x cll1221` and `cHj3 x cW` (Figures 8.2 (b) and (d)), show elongation either diagonally or horizontally, which suggests that these coefficients are quite correlated. `cW x cll1221` (Figure 8.2 (f)) also shows a tilt, which could suggest some correlation. All other plots are somewhat circular, suggesting minimal correlation between parameters.

`cll1221` consistently shows the largest allowed ranges, while `cW` and `cHj3` are the most tightly constrained coefficients in this observable.

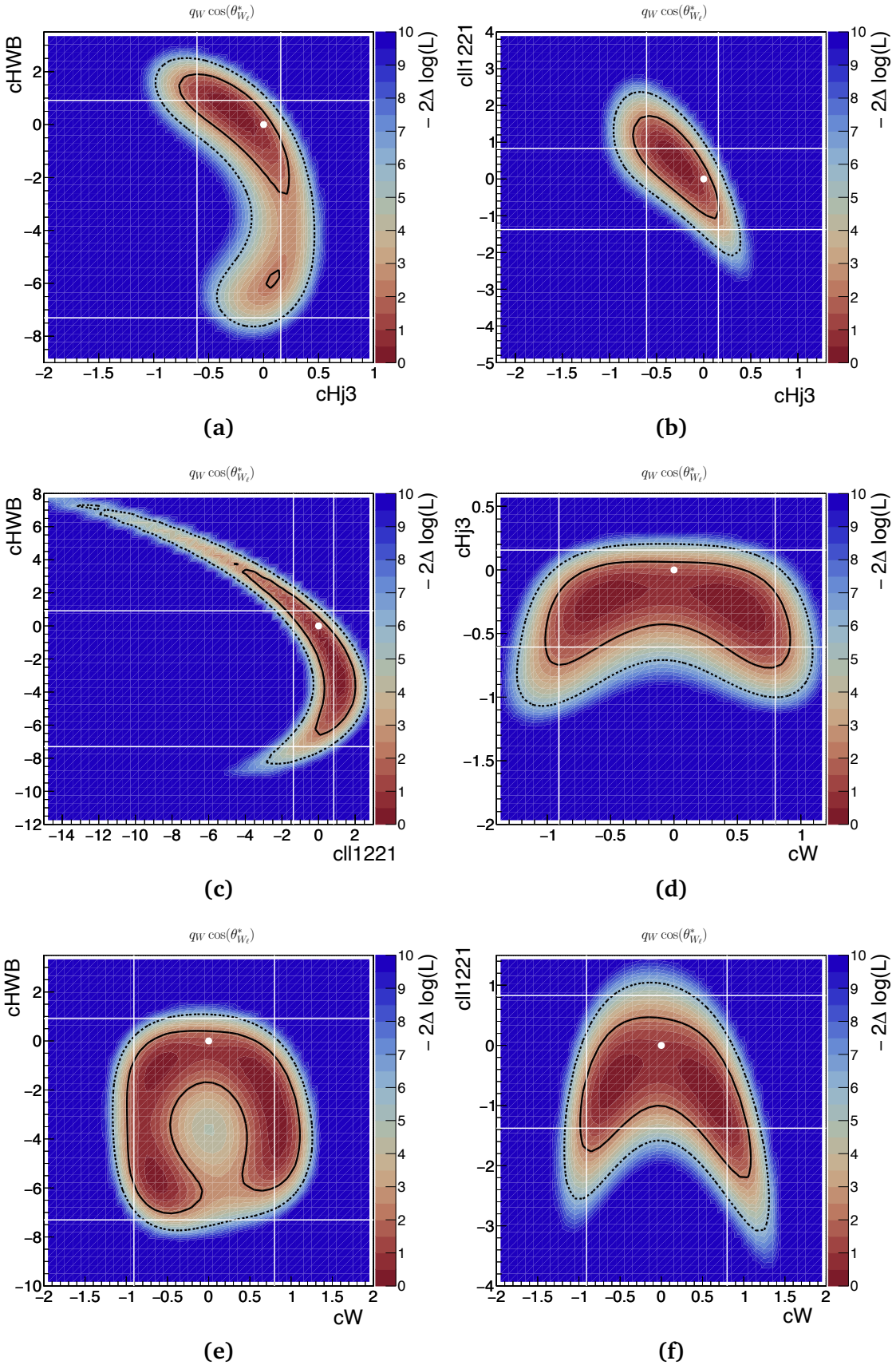

Figure 8.2: *2D scans of the profile likelihood ratio test statistic (Equation 6.15) for the $q_W \cos\theta^*_{W_\ell}$ observable. The white dot represents the SM point (0,0). The black solid (dashed) lines correspond to the borders of 68% (95%) CI when varying both parameters. The white solid line corresponds to the 95% CI of the 1D fit for the individual parameter. Expected results are shown in Appendix D.1.*

Observable: $\cos\theta^*_{Z_\ell}$

Figure 8.3 shows the profile likelihood ratio test statistic scan for the measurement of the $\cos\theta^*_{Z_\ell}$ observable. The expected profile likelihood ratio using Asimov data is shown in Appendix D.2.

The SM point (0,0) as illustrated by a filled white circle, is included in all the 68% CI for all parameter combinations studied. Again, the parameter space of plausible values for each coefficient pair is wide, suggesting that while the data is not strongly rejecting the Standard Model, certain parameter combinations may leave the possibility of deviations. Nonetheless, some minima in the plots occur at high c values, which make it physically unlikely as these effects would already have been discovered [126, 127].

Such an example is in the `cHj3 x cW` plot (Figure 8.3 (d)), where 3 minima are found, all enclosed within the 68% CI. The other two minima have values of `cHj3` ≈ -1.2, which is significantly different from the `cHj3` $= 0$ i.e. SM point. `cHj3 x cHWB`, `cHj3 x cll1221` and `cW x cHWB` (Figures 8.3 (a), (b) and (e)) all share such a feature.

The scan for `cll1221 x cHWB` (Figure 8.3 (c)), shows the elongated region, but with an abrupt jagged drop off on the left and top ends. This happens when the fit fails to minimize for that parameter space. The range was still kept in the plot to show the elongation and the shape of the diagonal ellipse.

The expected 2D plots shown in Appendix D.2 also have similar shapes to the measured plots, with a key difference being the multiple minima in the measured plots now become one smooth large minimum of the expected surface contours.

All other diagrams show the SM point within the 68% CI, except for the scan of `cHj3 × cHWB`, where the SM point is enclosed within the 95% CI. The shape for this likelihood surface is also quite different to the expected shape.

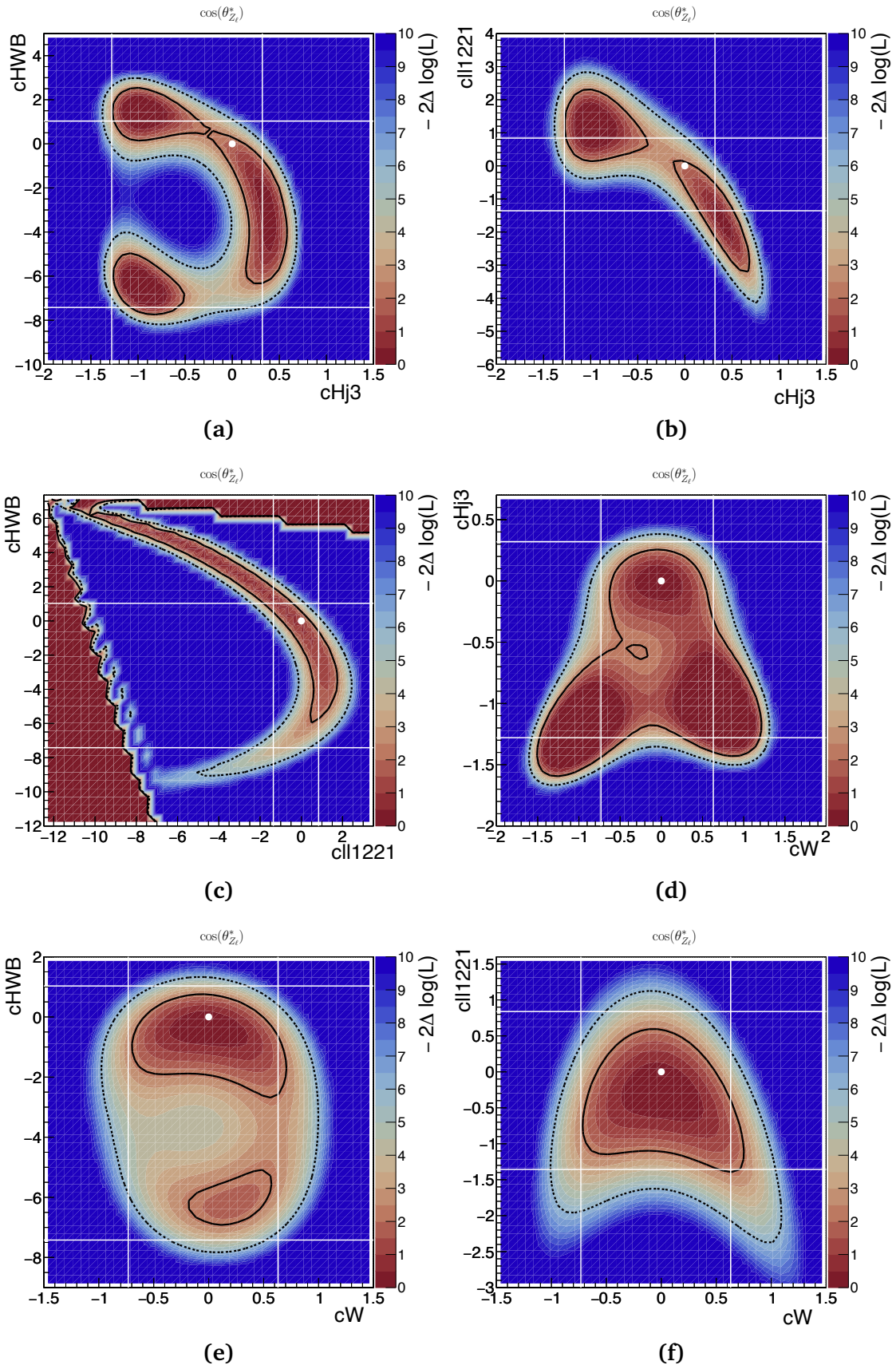

Figure 8.3: *2D scans of the profile likelihood ratio test statistic (Equation 6.15) for the* $\cos\theta^*_{Z_\ell}$ *observable. The white dot represents the SM point (0,0). The black solid (dashed) lines correspond to the borders of 68% (95%) CI when varying both parameters. The white solid line corresponds to the 95% CI of the 1D fit for the individual parameter. Expected results are shown in Appendix D.2.*

Observable: $|\cos\theta_V|$

Figure 8.4 illustrates the profile likelihood ratio test statistic scan for the measurement of the $|\cos\theta_V|$ observable. The expected profile likelihood ratio using Asimov data is shown in Appendix D.3.

In this observable, the SM point (0,0) as illustrated by a filled white circle, is included at the 68% CI, in only one combination: `cW x cll1221` (Figure 8.4 (f)). All others include the SM at the 95 %CI.

As reported in 8.1, the 95% CI for `cHj3` did not include the `cHj3` $= 0$ point (albeit only just). Therefore the 2D plots involving `cHj3` $= 0$ could offer valuable insight.

Combinations `cHj3 x cHWB`, `cHj3 x cll1221` and `cHj3 x cW` (Figures 8.4 (a), (b), (d)) all show the SM point close to the boundary of the 95% interval. Notably, `cHj3 x cll1221` Figure (b), a rather diagonal surface, is seen to have a shape distinctly different from the expected one in Appendix D.3. This suggests that the measured data is shifting the likelihood of the parameter values considerably. Also noteworthy is all 3 combinations of `cHj3` favour a slightly negative value for this parameter.

It should also be mentioned that `cll1221 x cHWB` (Figure 8.4 (c)) also has the SM point at the edge of the 95% interval, and with a much less exaggerated ellipse shape than the 2D plot of the expected data (in Appendix D.3.)

Observable: m_T^{WZ}

Figure 8.5 illustrates the profile likelihood ratio test statistic scan for the measurement of the m_T^{WZ} observable. The expected profile likelihood ratio using Asimov data is shown in Appendix D.4.

In this observable, the SM point (0,0) as illustrated by a filled white circle, is included in the 68% CI for 3 combinations: `cll1221 x cHWB`, `cW x cHWB` and `cW x cll1221`. The remaining three, `cHj3 x cHWB`, `cHj3 x cll1221` and `cHj3 x cW`, include the SM at the 95%CI.

This observable is unique due to the absence of multiple minima in the log-likelihood surfaces. Additionally, all plots exhibit some degree of correlation between the coefficient pairs. This is not very surprising as the last few bins of m_T^{WZ} which are the most sensitive to New Physics effects, also suffer from having little shape information. Without shape discrimination, the observable cannot distinguish which Wilson coefficient drives an excess in the final bin.

m_T^{WZ} has much tighter constraints for the parameters, especially for `cHj3 x cW` (Figure 8.5 (d)). For example, for m_T^{WZ}, `cHj3` approximately spans the range (-0.2,0.05) while for $|\cos\theta_V|$, `cHj3` approximately spans the range (-0.9,0.5). This is behaviour also seen in the 1D limits.

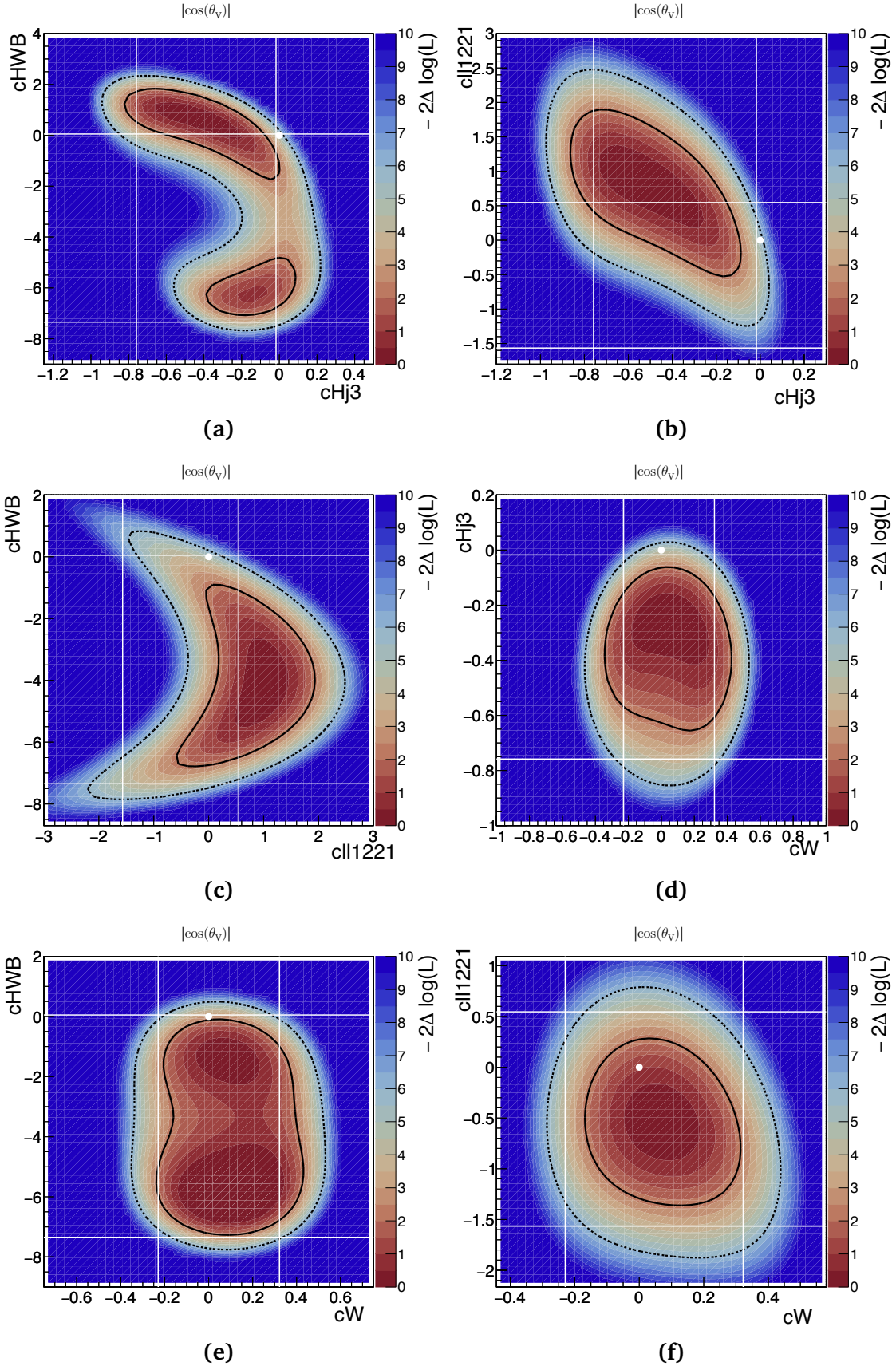

Figure 8.4: *2D scans of the profile likelihood ratio test statistic (Equation 6.15) for the* $|\cos\theta_V|$ *observable. The white dot represents the SM point (0,0). The black solid (dashed) lines correspond to the borders of 68% (95%) CI when varying both parameters. The white solid line corresponds to the 95% CI of the 1D fit for the individual parameter. Expected results are shown in Appendix D.3.*

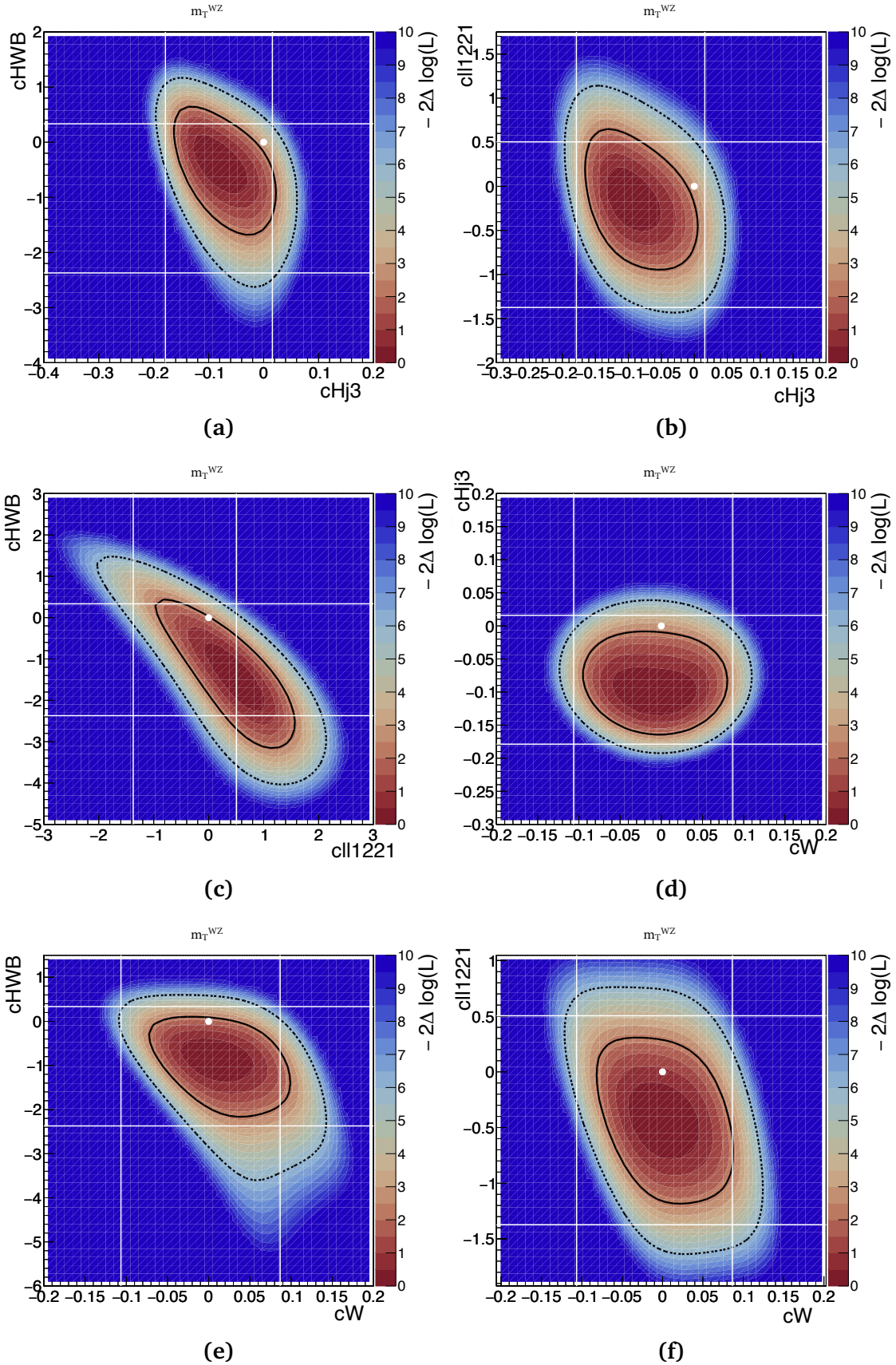

Figure 8.5: *2D scans of the profile likelihood ratio test statistic (Equation 6.15) for the m_T^{WZ} observable. The white dot represents the SM point (0,0). The black solid (dashed) lines correspond to the borders of 68% (95%) CI when varying both parameters. The white solid line corresponds to the 95% CI of the 1D fit for the individual parameter. Expected results are shown in Appendix D.4*

Observable: $\phi^*_{W\ell}$

Figure 8.6 illustrates the profile likelihood ratio test statistic scan for the measurement of the $\phi^*_{W\ell}$ observable. The expected profile likelihood ratio using Asimov data is shown in Appendix D.5.

The SM point (0,0) as illustrated by a filled white circle, is inside the 68% boundary of all scans. However, the broad parameter space hints at potential deviations. So while the data doesn't reject the SM, certain parameter combinations leave the possibility of new physics.

Combinations including `cHj3` and `cHWB` parameters exhibit circular likelihood shapes. This is due to the fact that in the 1D scenario, both of these parameters have two distinct 95% CI ranges (Table 8.1).

Shapes of the measured data are very similar to the expected shapes shown in Appendix D.5. However, importantly, the circular diagrams, `cHj3 x cHWB`, `cHj3 x cW` and `cHWB x cW` (Figures 8.4 (a), (b), (e)) all have a uniform minimum surface in the Asimov plot i.e. the concentric circles are rather symmetrical. In the data plots, there is a slight asymmetry. The asymmetry favours more negative values of `cHj3`, more negative values of `cHWB` and more positive values of `cW`. The allowed ranges for `cHWB` and `cll1221` are generally quite large for this observable.

Observable: $\phi^*_{Z\ell}$

Figure 8.7 illustrates the profile likelihood ratio test statistic scan for the measurement of the $\phi^*_{Z\ell}$ observable. The expected profile likelihood ratio using Asimov data is shown in Appendix D.6.

The SM point (0,0) as illustrated by a filled white circle, is inside the 68% boundary of all scans. However once again, the parameter space has a wide area of possible ranges within the 1σ band, so while the data doesn't reject the SM, certain parameter combinations leave the possibility of new physics.

Strong correlations are seen for many of the parameter scans, most notably, `cHj3 x cll1221`, `cHj3 x cW` and `cW x cll1221` (Figures 8.4 (b), (d), (f)).

When comparing to the expected scan for `cW x cHWB`, a significant change of shape is seen i.e. from a circular profile in the expected scan to a banana-shape profile for the measured scan. This highlights that the data strongly excludes a region of the parameter space ($\texttt{cW} \approx 1 \cup \texttt{cHWB} \approx [-6, -2]$).

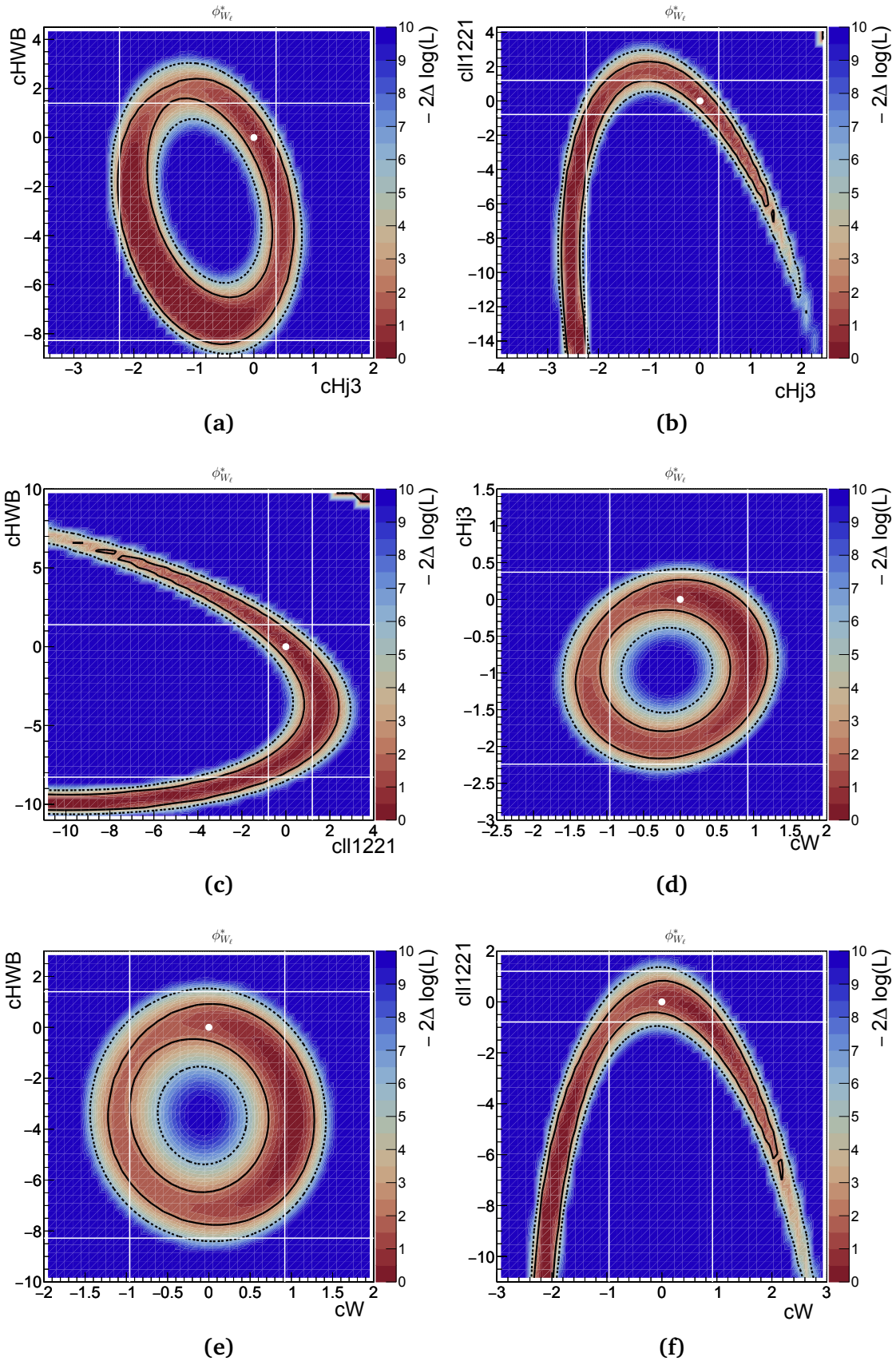

Figure 8.6: *2D scans of the profile likelihood ratio test statistic (Equation 6.15) for the $\phi^*_{W_\ell}$ observable. The white dot represents the SM point (0,0). The black solid (dashed) lines correspond to the borders of 68% (95%) CI when varying both parameters. The white solid line corresponds to the 95% CI of the 1D fit for the individual parameter. Expected results are shown in Appendix D.5.*

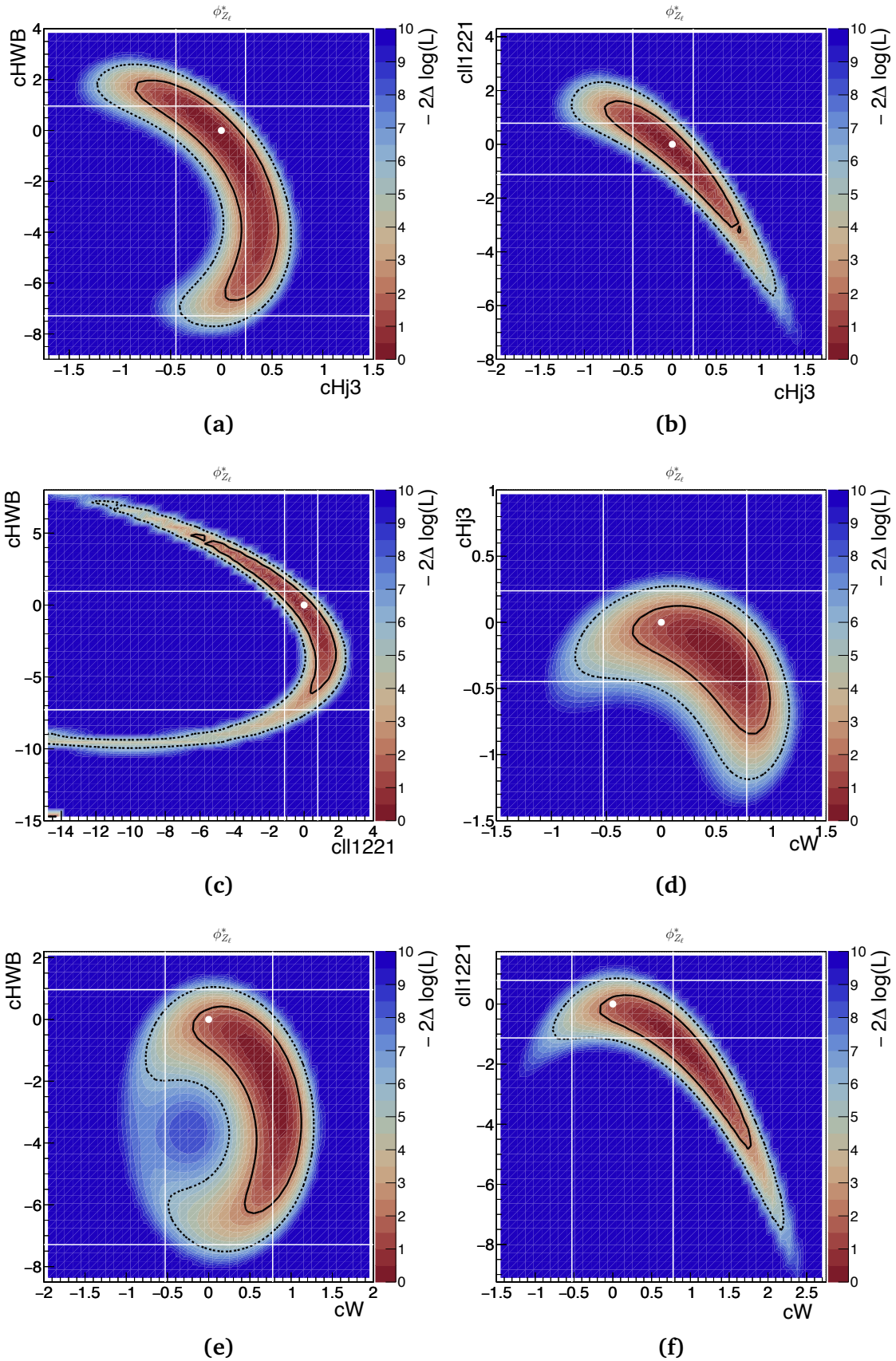

Figure 8.7: *2D scans of the profile likelihood ratio test statistic (Equation 6.15) for the $\phi^*_{Z_\ell}$ observable. The white dot represents the SM point (0,0). The black solid (dashed) lines correspond to the borders of 68% (95%) CI when varying both parameters. The white solid line corresponds to the 95% CI of the 1D fit for the individual parameter. Expected results are shown in Appendix D.6.*

8.1.3 Summary

Limits on one-dimensional EFT coefficients have been established at the particle level, and for the first time in this channel, two-dimensional limits on EFT coefficients have also been obtained using the complete Run-2 dataset. These limits have been determined for all six observables.

For the one-dimensional (1D) limits, the SM point, i.e., $c_{EFT} = 0$, falls within the 95% CI for all measurements. The cHj3 parameter in the $|\cos\theta_V|$ observable only just excludes the SM point where the 95% CI is [-0.760, -0.018]. Other observables indicate that the 1D limit on cHj3 includes the SM point within at least the 95% CI. The two-dimensional (2D) limits for cHj3 in combination with other parameters for the $|\cos\theta_V|$ observable generally show the SM point located near the boundary of the 95% CI, suggesting that this observable is sensitive to the cHj3 parameter and hints at potentially non-zero values for cHj3. Both the 1D and the 2D limits for cHj3 strongly suggest a negative value for the Wilson coefficient, if non-zero.

For the two-dimensional (2D) limits, the SM point, i.e., $c_{EFT_1} = c_{EFT_2} = 0$, is included within the 95% CI for all combinations and observables studied.

Strong constraints are given both in the 1D and 2D limits for the cW parameter. cHj3 is also well constrained in 1D and 2D for all observables, especially in m_T^{WZ}. cHWB generally allows the largest parameter space, showing poor constraints on this parameter, in both the 1D and the 2D cases. However, in both the 1D and the 2D cases, the observable m_T^{WZ} constraints this parameter much more effectively than all the other observables. For the parameter cHj3, the 1D 95% CI is roughly 3.5 times smaller in m_T^{WZ} then in the next best observable (which in this case is $\phi^*_{Z_\ell}$). For the parameter cW, the 1D 95% CI is roughly 2.75 times smaller in m_T^{WZ} then in the next best observable (which in this case is $|\cos\theta_V|$).

Much poorer constraints in all observables appear for cll1221 when combined with cHWB, than when combined with the other parameters. This could highlight significant correlations that may be introduced with this cross term.

In terms of observables, m_T^{WZ} and $|\cos\theta_V|$ offer the strongest overall constraints. The other angular observables show varying constraint strengths.

Pull plots, which evaluate the quality of the fits and assess potential biases are examined for all 1D and 2D results. A selection of these are shown in Appendix E, with the nuisance parameters defined in Chapter 6.4.

For the 1D expected (Asimov) fits, all nuisance parameters are contained within the 1σ band. However, for the measured fits for cHj3, the error on the nuisance parameter diboson_pdf (see Section 6.4) pull is usually larger than the 2σ band in m_T^{WZ} and $|\cos\theta_V|$. Here, diboson_pdf is the nuisance parameter representing the PDF uncertainty, which we assume to be a constant 1%

across all bins. m_T^{WZ} also has significantly larger errors on the pulls for the `diboson_pdf` nuisance parameter. A possible reason for the larger pulls is the lack of statistics in the very high m_T^{WZ} bins. m_T^{WZ} is also the only kinematic variable where the momentum of the initial state particles could have a real impact on the distribution, and the highest bins represent the most extreme case. All other 1D measured fits have a more constrained pull plot as the nuisance parameter pulls are within 1σ.

For the 2D fits, most nuisance parameters in are contained within the 1σ band, and all are contained within the 2σ band. Most are centred around 0, although a few exceptions do occur. No systematic bias in the fits is noted.

The 2D constraints highlight the correlations between the parameters, underscoring the impact of the cross-terms in obtaining a full picture of the parameter constraints.

8.2 Results in the context of other measurements

Both the 1D and 2D results for different physics channels (Higgs, Top, Electroweak) feed into a global combination machinery, where limits for similar operators but in individual channels are statistically combined. This allows for increased reach by probing operators sensitive to particular processes. The combination is done at the level of ATLAS, which these results will feed into, and at the level of the LHC [128], where ATLAS, CMS and LHCb interpretations are combined. The results from this thesis will provide the particle level limits for ATLAS WZ in the global combination.

The results indicate that the data does not reject the Standard Model hypothesis (i.e. Wilson coefficients $c = 0$) for the operators studied with the observables used here. The exception seen in the 1D limit `cHj3` parameter in the $|\cos\theta_V|$ observable is consistent with statistical expectation (by definition, the 95% CI would not include the true parameter value 5% of the time), or could also be consistent with a potential slight deviation from the SM. Other observables do not rule out this possibility, although they do include the SM in their 1σ range.

Nonetheless, it is clear that the constraints for `cHj3` and `cW` are very stringent, showing the importance of this analysis.

`cHj3` is the Wilson coefficient for the $Q_{Hq}^{(3)}$ operator. Using the `top` flavour scheme and in the Warsaw basis, Figure 8.8 summarizes the measured 1D limits at the particle level for all observables.

The most stringent 95% CI obtained is from the m_{T}^{WZ} observable:

$$\frac{\texttt{cHj3}}{\Lambda^2} \in [-0.18, 0.02] \text{ TeV}^{-2} \quad \text{at the 95\% confidence level, assuming } \Lambda = 1 \text{ TeV}.$$

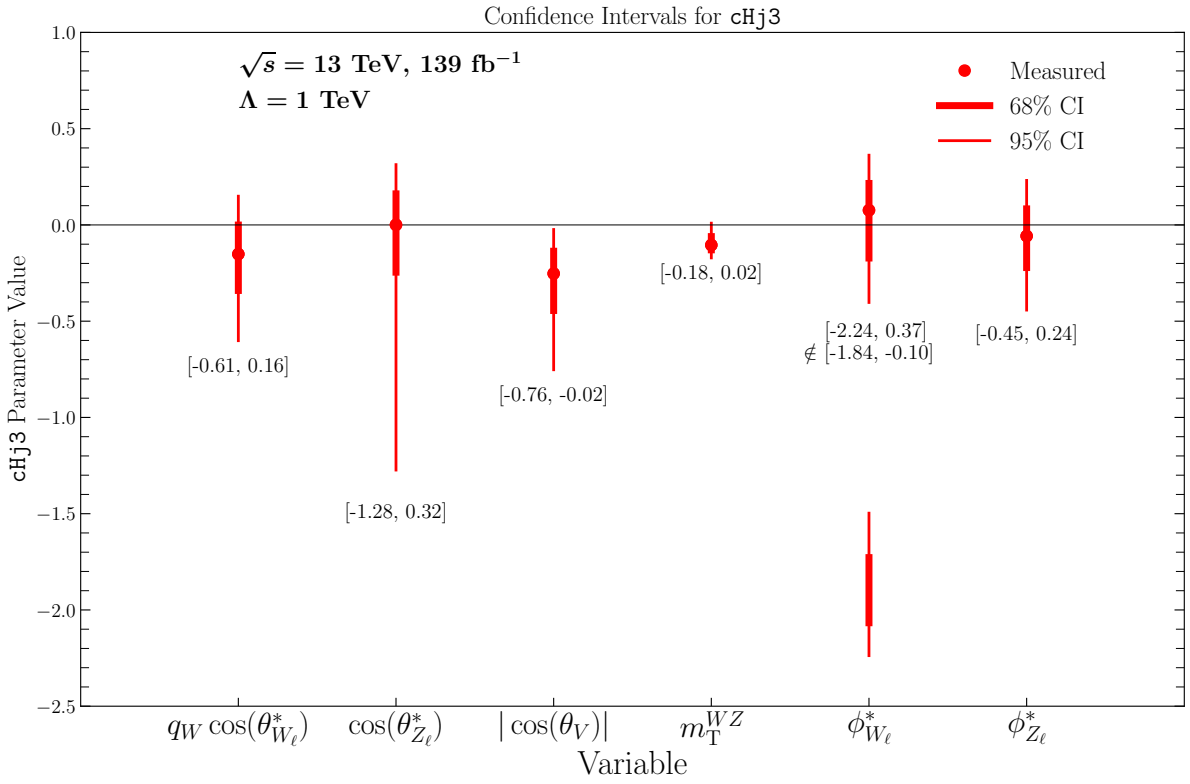

Figure 8.8: *Measured 1D limits on* `cHj3` *for all observables studied. Values at the bottom of the bar indicate the 95%CI for the respective observable.*

Table 8.2 compares this with other current published limits.

	This Study: Observable m_{T}^{WZ} (95% CI)	**Reference Limits (95% CI)**	**Notes on Reference**
`cHj3`	$[-0.179, 0.016]$	$[-0.164, 0.039]$	**Individual analysis measurement**: ATLAS Higgs boson decaying into b quarks with a vector boson [127].
		$[-0.39, 0.34]$	**Global Combination**: Global SMEFT analysis using Higgs-Top processes at ATLAS and CMS Run-2 [129].
		$[-0.166, -0.010]$	**Global Combination**: Global SMEFT analysis using LEP, SLD data, and ATLAS/CMS Run-2 [126]. Considered the latest and strongest global fit.

Table 8.2: *Comparison of* `cHj3` *limits from this study and reference analyses. CMS has not published any 1D limits on* `cHj3` *for the WZ leptonic channel yet.*

cHj3 can be probed quite well in Higgs related channels where observed limits form a benchmark single analysis measurement in [127]. The power from the WZ over other channels is that it is essentially only sensitive to cHj3 and not strongly sensitive to other Higgs related operators like cHj1, cHu, and cHd that are strongly correlated with cHj3 in Higgs analyses. Similar limits are obtained with this single analysis measurement $H \rightarrow bV$. Limits reported in this thesis are better than the global combination analysis that uses Higgs-Top processes at ATLAS and CMS Run-2 [129], which indicates the value of including EW processes such as the WZ in constraining this parameter. The strongest global combination limit [126], widely regarded as the reference, includes high-precision measurements of the W and Z boson branching ratios and electroweak couplings from LEP and SLD, as well as W mass determinations from LEP and the Tevatron colliders. The limits reported here (single measurement) are slightly less stringent than the global combination, but are still quite competitive. With the new limits presented in this thesis, additional input is provided for the global combination that will make an even stronger limit.

The analysis is also sensitive to cW, and stringent 1D limits have also been obtained for this Wilson coefficient. cW is the Wilson coefficient for the operator $Q_W = \epsilon^{ijk} W_\mu^{i\nu} W_\nu^{j\rho} W_\rho^{k\mu}$. Using the top flavour scheme and in the Warsaw basis, Figure 8.9 summarizes the measured 1D limits at the particle level for all observables.

The best 95% CI obtained is once again from the m_{T}^{WZ} observable:

$$\frac{\mathtt{cW}}{\Lambda^2} \in [-0.11, 0.09] \text{ TeV}^{-2} \quad \text{at the 95\% confidence level, assuming } \Lambda = 1 \text{ TeV}.$$

Table 8.3 compares this with other current published limits.

The CMS WZ reference limit uses a data sample of similar size and a similar approach for the same run period as the results presented in this thesis. Our limits are extremely close to this result, which is expected. The CMS $W\gamma$ analysis [132] shows that the limits depend on the cutoff value p_T^γ. The limits in this thesis are comparable to the $p_T^\gamma = 800$ GeV cut-off value, and become less competitive when the highest cut-off value of 1500 GeV is used. The limits in this thesis offer a large improvement over those established by the ATLAS Run-2 Vector Boson Fusion Zjj analysis [133].

The EFT 2D constraints are novel for the WZ channel, and are particularly important as for the first time, correlations from the effect of cross-terms between EW sensitive operators are studied and seen.

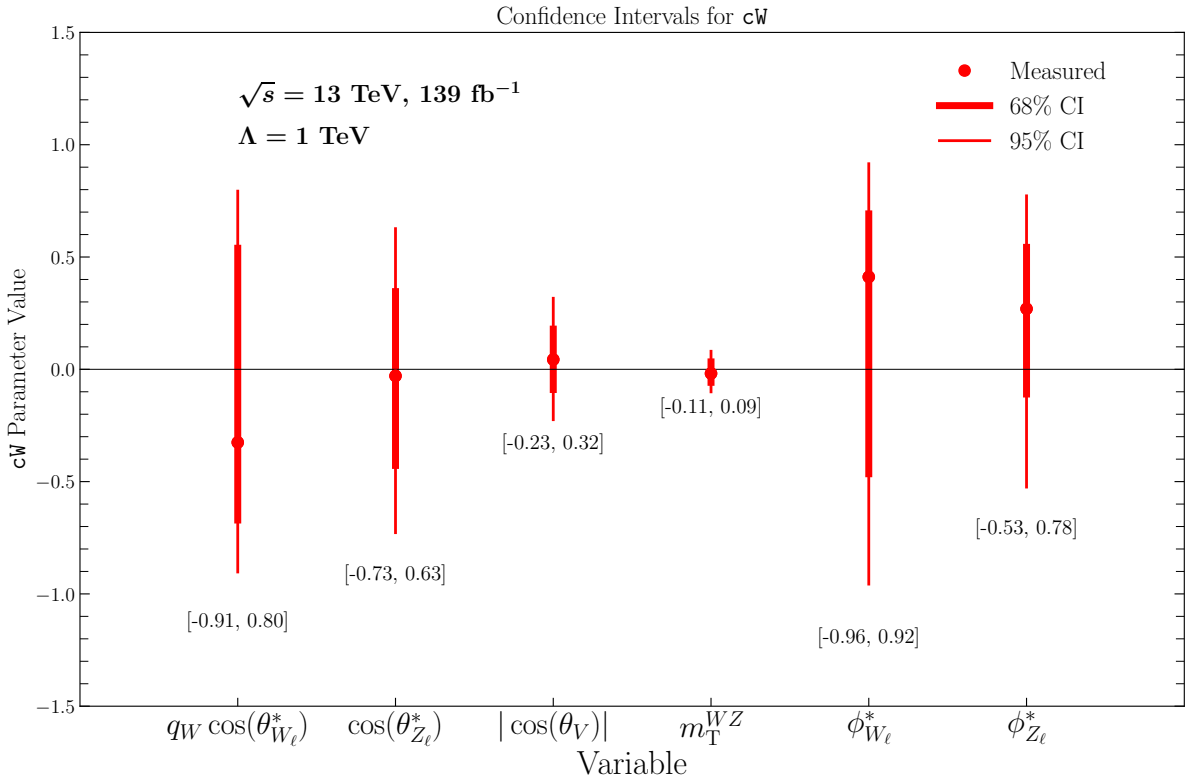

Figure 8.9: *Measured 1D limits on* `cW` *for all observables studied. Values at the bottom of the bar indicate the 95%CI for the respective observable.*

	This Study: Observable m_{T}^{WZ} (95% CI)	**Reference Limits (95% CI)**	**Notes on Reference**
`cW`	$[-0.107, 0.087]$	$[-0.070, 0.085]$	**Individual analysis measurement**: CMS WZ Run-2 [130]. Uses HISZ basis [131] instead of the Warsaw basis.
		$[-0.062, 0.052]$	**Individual analysis measurement**: CMS $W\gamma$ Run-2 [132]. p_T^γ cutoff at 1500 GeV.
		$[-0.19, 0.41]$	**Individual analysis measurement**: ATLAS VBF Zjj Run-2 [133].

Table 8.3: *Comparison of* `cW` *limits from this study and reference analyses.*

The parameter space of possible Wilson coefficient values is quite wide within the 1σ band, so while the data doesn't reject the SM, certain parameter combinations still leave room for the possibility of new physics.

The 2D plots, especially for `cHj3 x cW` are valuable to the physics community as stringent limits can be made on the simultaneous constraining of these parameters. In particular, as seen in the 1D case as well, the m_{T}^{WZ} observable offers remarkable limits, just slightly outside the 1D CIs.

Ideally, a global analysis would involve an n-dimensional likelihood fit spanning both a large set of observables and multiple simultaneously non-zero Wilson coefficients. Such an approach would maximize sensitivity to subtle correlations and interdependencies in SMEFT parameter space. However, this is limited not only by computational resources, but also by the amount of data— binning across several variables quickly exhausts the available events.

Currently, 2D constraints offer the most insight to New Physics parameters in physics processes at the current energy scale. The results presented here constrain six unique combinations of Wilson coefficients, some of which have never been explored before.

An alternative method of simultaneously constraining multiple Wilson coefficients uses Principal component analysis where a modified basis that consists of linear combinations of the Warsaw basis operators are created and fed into the likelihood fit. An example of this is done in [107].

In the context of the bigger picture, both the 1D and 2D limits will feed into the Global combination efforts of ATLAS and the LHC. The 1D limits provide improved sensitivity for certain parameters, while for others they offer complementary information when compared with results from other analyses and sensitive processes. The novel 2D limits also offer insight into unique correlations sensitive only to the WZ channel, which is valuable for the global combination [126].

CHAPTER 9

Conclusions and outlook

The properties of the triple-gauge coupling, when measured with high precision, provide a means of identifying any potential deviations from Standard Model predictions. The ATLAS detector at the LHC collected 139 fb^{-1} of proton–proton collision data during Run 2, creating an unparalleled opportunity to explore and probe this rare coupling in the Electroweak sector. This thesis examines the full $WZ \to \ell\nu\ell\ell$ data sample to provide insights to possible physics Beyond the Standard Model.

Deviations from the SM can be quantified using a model-independent framework called Effective Field Theory, where higher dimension operators are added to the SM Lagrangian. The work done in this thesis focuses on a subset of relevant dimension-6 operators that affect the Electroweak sector and the $WZ \to \ell\nu\ell\ell$ channel. This work sets limits on the most sensitive Wilson coefficients, which are scalar quantities that regulate the strength of each EFT operator.

An area of special interest in this study is the examination of differential variables, such as the transverse mass distribution of the WZ system, $\frac{d\sigma}{dm_T^{WZ}}$. Although the LHC's collision energy may be too low to directly observe new physics, several models beyond the SM predict deviations that may become more apparent at high values of m_T^{WZ}. In this region of high transverse mass, even though cross-sections are low, significant deviations could potentially appear without conflicting with prior experimental observations. Other angular observables, such as $\cos(\theta^*_{W_\ell})$ and $\cos(\theta^*_{Z_\ell})$, which represent the angle that the W (or Z) lepton makes with the parent boson direction in the W (or Z) rest frame, are also studied. Additionally, the angle that either boson makes with the incident proton direction in the WZ rest frame, $\cos(\theta_V)$, as well as the azimuthal angles of the decay leptons around the parent bosons, $\phi^*_{W_\ell}$ and $\phi^*_{Z_\ell}$, are analysed. These angles offer an alternative way to probe the triple-gauge coupling as they are measured from the centre of mass of the colliding system, rather than the lab frame, which makes them independent of boosts. Studies conducted in this thesis show that all 5 angular observables and the kinematic observable m_T^{WZ} would be sensitive to EFT effects.

Out of the 2499 dimension-6 operators that exist, many of them have a minimal effect on this

channel. This thesis presents studies of the CP-even Wilson coefficients with the most impact: cHDD, cHl111, cHl122, cHl311, cHl322, cHj1, cHj3, cHWB, cll1221, cW.

Special work was done to ensure accurate and state-of-the-art SM and EFT predictions were obtained and generated. The cross section for WZ production is measured across several angular and kinematic variables and compared to predictions from the SM, utilising MATRIX calculations at NNLO and the Monte Carlo event generators Powheg+Pythia at NLO. The MATRIX calculations exhibit the closest agreement with the observed data.

The contributions of the dimension-6 EFT parameters were simulated with the MadGraph+Pythia event generators using the SMEFTsim model at LO. NLO effects were partially incorporated by including events with an additional jet in the matrix element. This is referred to as the 0+1j merged scheme. This prediction was validated against the SMEFTatNLO generator which is able to generate predictions at NLO QCD, but the SMEFT contributions cannot be parameterised.

EFT constraints using all six observables were made on each of the 10 Wilson coefficients based on the Run-2 dataset. By considering both the linear (interference) and the quadratic contributions of each of these coefficients, no significant deviation from the Standard Model is observed at the 95% CI for most of the 1D particle-level fits. The only exception to this is the cHj3 parameter in the $|\cos\theta_V|$ observable which only just excludes the SM point where the 95% CI is [-0.760, -0.018]. It is also worth noting that due to statistical fluctuations, approximately 1 out of every 20 1D or 2D limits is expected to exclude the SM point. cHj3 for all other observables includes the SM point in the 95% CI.

For the first time, cross-terms, which quantify the interference of different EFT operators with each other are also included in the EFT predictions for this channel. This allows for constraining 2 Wilson-coefficients at a time. Because the number of combinations are large, only the most sensitive cross-terms are studied, namely: cHj3, cW, cHWB and cll1221. This resulted in six new 2D limits where pairs of EFT coefficients were constrained using the data for each observable.

In the 2D particle-level fits, no significant deviation from the Standard Model is observed at the 95% CI. Strong constraints on cW and cHj3 have been obtained using all observables. Constraints tend to be symmetrical around 0 for cW. For cHj3, constraints show that a negative value is more likely.

Different observables make it possible to examine the physics from various perspectives, and as a result, some observables are more sensitive than others. The m_T^{WZ} and $|\cos\theta_V|$ provide the highest sensitivity and the most stringent constraints. The polar angles and the azimuthal angles provide less strict constraints, but complementary information.

The reinterpretation could be significantly improved if several observables could be combined to obtain one result in a statistically consistent manner. One way that the field is trying to do this

currently is to use multivariate boosted decision trees or Neural Network (NN) implementations. An investigation into the feasibility of using a Neural Network implementation was conducted by the author of this thesis using the `ML4EFT` framework [134]. In this approach, each observable is provided as a feature to the NN input, where it is weighted based on its sensitivity as determined during the NN training process. The challenge with this approach, as experienced during the feasibility study, was teaching the NN about the scalability of the Wilson coefficient c i.e. the NN is trained at a particular value of c but then has to infer the value of c of a new data sample, which would need an interpolation or an extrapolation from its trained value. Self-consistency studies showed bias with this method and so it was not further pursued. However, the EFT community strongly believes in the potential of this approach of solving the multivariate problem, and it is actively being pursued.

Stringent limits are set on the most sensitive operators, `cHj3` and `cW`. This thesis presents a strong first individual analysis measurement for the `cHj3` parameter on the WZ leptonic channel, with no complementary information on this parameter by CMS yet. The limits are complemented closely by the global combination limits [126], that use several data samples from different experiments. This result also presents strong limits on `cW`, comparable to that reported by CMS for the same channel. Limits for these two parameters would be especially critical for more stringent global combination limits.

Another limiting factor is the data sample size obtained from the detector itself. Since BSM processes observable at the LHC are extremely rare - due to their weak coupling to the Standard Model, or the very high masses of the new particles involved— a larger amount of data would increase sensitivity to statistically rare processes, thereby greatly informing the EFT fit results. The upgrade of the LHC to the High-Luminosity LHC will try to address this problem: a higher luminosity is projected to reduce the total uncertainty of several coupling modifiers (κ parameters) [135], which collectively quantify Beyond the Standard Model (BSM) physics. The higher luminosity requires an upgrade to the current detector systems to be able to handle and process the new event rate. Appendix G documents work developed for the Liquid Argon sub-detector, where a tool that acts as a test-bench to the LAr Processor was developed. Further, integration efforts of combining and interfacing with several different LAr upgrade boards are shown in Appendix G.

The larger statistics of rare physics processes collected during the LHC's Run-3 and HL-LHC programs, coupled with machine learning techniques that enable multivariate observables and the simultaneous fitting of multiple Wilson coefficients in n-dimensional parameter spaces, will significantly improve the constraints on Beyond the Standard Model (BSM) physics measured in this thesis.

Bibliography

[1] A. Einstein. *The Field Equations of Gravitation*. Sitzungsber. Preuss. Akad. Wiss. Berlin (Math. Phys.), 1915:844–847, 1915.

[2] F. Englert and R. Brout. *Broken Symmetry and the Mass of Gauge Vector Mesons*. Physical Review Letters, 13:321–323, Aug 1964. URL https://doi.org/10.1103/PhysRevLett.13.321.

[3] S. Weinberg. *A Model of Leptons*. Physical Review Letters, 19:1264–1266, Nov 1967. URL https://doi.org/10.1103/PhysRevLett.19.1264.

[4] P. Higgs. *Broken Symmetries and the Masses of Gauge Bosons*. Physical Review Letters, 13: 508–509, 1964. URL https://doi.org/10.1103/PhysRevLett.13.508.

[5] D. J. Gross and F. Wilczek. *Asymptotically Free Gauge Theories. I*. Physical Review D, 8: 3633–3652, Nov 1973. URL https://doi.org/10.1103/PhysRevD.8.3633.

[6] ATLAS Collaboration. *Observation of a new particle in the search for the Standard Model Higgs boson with the ATLAS detector at the LHC*. Physics Letters B, 716(1):1–29, September 2012. ISSN 0370-2693. URL http://doi.org/10.1016/j.physletb.2012.08.020.

[7] CMS Collaboration. *Observation of a new boson at a mass of 125 GeV with the CMS experiment at the LHC*. Physics Letters B, 716(1):30–61, September 2012. ISSN 0370-2693. URL http://doi.org/10.1016/j.physletb.2012.08.021.

[8] T. Cohen. *As Scales Become Separated: Lectures on Effective Field Theory*, 2020. URL https://arxiv.org/abs/1903.03622.

[9] I. Brivio and M. Trott. *The standard model as an effective field theory*. Physics Reports, 793:1–98, 2019. ISSN 0370-1573. URL https://www.sciencedirect.com/science/article/pii/S0370157318303223.

[10] P. Gaete, J. A. Helayël-Neto, and L. P. R. Ospedal. *Remarks on an anomalous triple gauge boson couplings*, 2020. URL https://arxiv.org/abs/2008.04908.

[11] ALEPH Collaboration, DELPHI Collaboration, L3 Collaboration, OPAL Collaborationn, and LEP Electroweak Working Group. *Electroweak measurements in electron–positron collisions at W-boson-pair energies at LEP*. Physics Reports, 532(4):119–244, November 2013. ISSN 0370-1573. URL http://doi.org/10.1016/j.physrep.2013.07.004.

[12] C. N. Yang and R. L. Mills. *Conservation of Isotopic Spin and Isotopic Gauge Invariance*. Physical Review, 96:191–195, Oct 1954. URL https://doi.org/10.1103/PhysRev.96.191.

[13] H. David Politzer. *Reliable Perturbative Results for Strong Interactions?* Physical Review Letters, 30:1346–1349, Jun 1973. URL https://doi.org/10.1103/PhysRevLett.30.1346.

[14] I. Neutelings. *Standard Model Particles*, 2016. URL https://tikz.net/sm_particles/.

[15] R. P. Feynman. *Mathematical Formulation of the Quantum Theory of Electromagnetic Interaction*. Physical Review, 80:440–457, Nov 1950. URL https://doi.org/10.1103/PhysRev.80.440.

[16] S. Tomonaga. *On a Relativistically Invariant Formulation of the Quantum Theory of Wave Fields**. Progress of Theoretical Physics, 1(2):27–42, 08 1946. ISSN 0033-068X. URL https://doi.org/10.1143/PTP.1.27.

[17] S. Weinberg. *Non-Abelian Gauge Theories of the Strong Interactions*. Physical Review Letters, 31:494–497, Aug 1973. URL https://doi.org/10.1103/PhysRevLett.31.494.

[18] S. L. Glashow. *Partial Symmetries of Weak Interactions*. Nuclear Physics, 22:579–588, 1961. URL https://doi.org/10.1016/0029-5582(61)90469-2.

[19] C. S. Wu, E. Ambler, R. W. Hayward, D. D. Hoppes, and R. P. Hudson. *Experimental Test of Parity Conservation in β Decay*. Physical Review, 105:1413–1414, 1957. URL https://doi.org/10.1103/PhysRev.105.1413.

[20] N. Cabibbo. *Unitary Symmetry and Leptonic Decays*. Physical Review Letters, 10:531–533, Jun 1963. URL https://doi.org/10.1103/PhysRevLett.10.531.

[21] M. Kobayashi and T. Maskawa. *CP-Violation in the Renormalizable Theory of Weak Interaction*. Progress of Theoretical Physics, 49(2):652–657, 02 1973. ISSN 0033-068X. URL https://doi.org/10.1143/PTP.49.652.

[22] P. W. Higgs. *Spontaneous Symmetry Breakdown without Massless Bosons*. Physical Review, 145:1156–1163, May 1966. URL https://doi.org/10.1103/PhysRev.145.1156.

[23] M. Thomson. *Modern Particle Physics*. Cambridge University Press, 2013. ISBN 9781107034266.

[24] A. Pich. *The Standard Model of Electroweak Interactions*. In 2010 European School of High Energy Physics, number IFIC-11-73, FTUV-12-0102, pages 1–50, 1 2012. URL https://arxiv.org/abs/1201.0537.

[25] P. van Nieuwenhuizen. *Supergravity*. Physics Reports, 68(4):189–398, 1981. ISSN 0370-1573. URL https://www.sciencedirect.com/science/article/pii/0370157381901575.

[26] Y. Fukuda et al. *Evidence for Oscillation of Atmospheric Neutrinos*. Physical Review Letters, 81:1562–1567, Aug 1998. URL https://doi.org/10.1103/PhysRevLett.81.1562.

[27] SNO Collaboration. *Direct Evidence for Neutrino Flavor Transformation from Neutral-Current Interactions in the Sudbury Neutrino Observatory*. Physical Review Letters, 89: 011301, Jun 2002. URL https://link.aps.org/doi/10.1103/PhysRevLett.89.011301.

[28] V. C. Rubin, Jr. Ford, W. K., and N. Thonnard. *Rotational properties of 21 SC galaxies with a large range of luminosities and radii, from NGC 4605 (R=4kpc) to UGC 2885 (R=122kpc)*. Astrophysical Journal, 238:471–487, June 1980. URL https://doi.org/10.1086/158003.

[29] M. B. Gavela, P. Hernández, J. Orloff, and O. Pène. *Standard model CP-violation and baryon asymmetry*. Modern Physics Letters A, 09(09):795–809, 1994. URL https://doi.org/10.1142/S0217732394000629.

[30] A. G. Riess et al. *Observational Evidence from Supernovae for an Accelerating Universe and a Cosmological Constant*. The Astronomical Journal, 116(3):1009–1038, September 1998. ISSN 0004-6256. URL http://doi.org/10.1086/300499.

[31] N. Arkani–Hamed, S. Dimopoulos, and G. Dvali. *The hierarchy problem and new dimensions at a millimeter*. Physics Letters B, 429(3):263–272, 1998. ISSN 0370-2693. URL https://www.sciencedirect.com/science/article/pii/S0370269398004663.

[32] A. Falkowski. *Lectures on Effective Field Theories*, September 2020. URL https://indico.in2p3.fr/event/22195/contributions/86017/attachments/59873/81148/eftlectures.pdf.

[33] T. Appelquist and J. Carazzone. *Infrared singularities and massive fields*. Physical Review D, 11:2856–2861, May 1975. URL https://doi.org/10.1103/PhysRevD.11.2856.

[34] E. Fermi. *Tentativo di una Teoria Dei Raggi* . Il Nuovo Cimento (1924-1942), 11(1):1–19, 1934. URL https://doi.org/10.1007/BF02959820.

[35] G. Altarelli. *The Higgs and the Excessive Success of the Standard Model*, 2014. URL https://arxiv.org/abs/1407.2122.

[36] W. Buchmüller and D. Wyler. *Effective lagrangian analysis of new interactions and flavour conservation*. Nuclear Physics B, 268(3):621–653, 1986. ISSN 0550-3213. URL https://www.sciencedirect.com/science/article/pii/0550321386902622.

[37] S. Weinberg. *Baryon- and Lepton-Nonconserving Processes*. Physical Review Letters, 43:1566–1570, Nov 1979. URL https://doi.org/10.1103/PhysRevLett.43.1566.

[38] E. E. Jenkins, A. V. Manohar, and P. Stoffer. *Low-energy effective field theory below the electroweak scale: operators and matching*. Journal of High Energy Physics, 2018(3):16, 2018. ISSN 1029-8479. URL https://doi.org/10.1007/JHEP03(2018)016.

[39] B. Grzadkowski, M. Iskrzyński, M. Misiak, and J. Rosiek. *Dimension-six terms in the Standard Model Lagrangian*. Journal of High Energy Physics, 2010(10):85, 2010. ISSN 1029-8479. URL https://doi.org/10.1007/JHEP10(2010)085.

[40] I. Brivio. *SMEFTsim 3.0 — a practical guide*. Journal of High Energy Physics, 2021(4), April 2021. ISSN 1029-8479. URL http://doi.org/10.1007/JHEP04(2021)073.

[41] G. Boldrini. *SM and EFT interpretation of Vector Boson Scattering measurements at CMS and development of the DAQ system for the Barrel Timing Layer for HL-LHC*. PhD thesis, INFN, Milan Bicocca, 2024. URL https://cds.cern.ch/record/2887923.

[42] S. Navas et al. *Review of particle physics*. Physical Review D, 110(3):030001, 2024. URL https://doi.org/10.1103/PhysRevD.110.030001.

[43] R. D. Ball et al. *Parton distributions from high-precision collider data*. The European Physical Journal C, 77(10):663, 2017. URL https://doi.org/10.1140/epjc/s10052-017-5199-5.

[44] J. C. Collins and D. E. Soper. *Parton distribution and decay functions*. Nuclear Physics B, 194(3):445–492, 1982. ISSN 0550-3213. URL https://www.sciencedirect.com/science/article/pii/0550321382900219.

[45] M. Schott and M. Dunford. *Review of single vector boson production in pp collisions at* $\sqrt{s} = 7$ *TeV*. The European Physical Journal C, 74(7), July 2014. ISSN 1434-6052. URL http://doi.org/10.1140/epjc/s10052-014-2916-1.

[46] S. Höche. *Introduction to parton-shower event generators*. In Theoretical Advanced Study Institute in Elementary Particle Physics: Journeys Through the Precision Frontier: Amplitudes for Colliders, pages 235–295, 2015. URL http://doi.org/10.1142/9789814678766_0005.

[47] Z. Nagy and D. E. Soper. *What is a parton shower?* Physical Review D, 98(1), July 2018. ISSN 2470-0029. URL http://doi.org/10.1103/PhysRevD.98.014034.

[48] B. Andersson, G. Gustafson, G. Ingelman, and T. Sjostrand. *Parton Fragmentation and String Dynamics*. Physics Reports, 97(LU-TP-83-10):31–145, 1983. URL https://doi.org/10.1016/0370-1573(83)90080-7.

[49] D. J. Lange. *The EvtGen particle decay simulation package*. Nuclear Instruments and Methods in Physics Research Section A: Accelerators, Spectrometers, Detectors and Associated Equipment, 462(1):152–155, 2001. ISSN 0168-9002. URL https://www.sciencedirect.com/science/article/pii/S0168900201000894.

[50] T. Sjostrand and M. van Zijl. *A Multiple Interaction Model for the Event Structure in Hadron Collisions*. Physical Review D, 36(LU-TP-87-5):2019, 1987. URL https://doi.org/10.1103/PhysRevD.36.2019.

[51] T. Sjöstrand, S. Ask, J. R. Christiansen, R. Corke, N. Desai, P. Ilten, S. Mrenna, S. Prestel, C. O. Rasmussen, and P. Z. Skands. *An introduction to PYTHIA 8.2*. Computer Physics Communications, 191:159–177, Jun 2015. ISSN 0010-4655. URL http://doi.org/10.1016/j.cpc.2015.01.024.

[52] E. Bothmann, Singh G., S. Höche, J. Krause, F. Krauss, S. Kuttimalai, S. Liebschner, D. Napoletano, M. Schönherr, H. Schulz, S. Schumann, and F. Siegert. *Event generation with Sherpa 2.2*. SciPost Physics, 7(3), September 2019. ISSN 2542-4653. URL http://doi.org/10.21468/SciPostPhys.7.3.034.

[53] J. Alwall, R. Frederix, S. Frixione, V. Hirschi, F. Maltoni, O. Mattelaer, H.-S. Shao, T. Stelzer, P. Torrielli, and M. Zaro. *The automated computation of tree-level and next-to-leading order differential cross sections, and their matching to parton shower simulations*. Journal of High Energy Physics, 2014(7), July 2014. ISSN 1029-8479. URL http://doi.org/10.1007/JHEP07(2014)079.

[54] P. Nason. *A New method for combining NLO QCD with shower Monte Carlo algorithms*. Journal of High Energy Physics, 11(BICOCCA-FT-04-11):040, 2004. URL https://doi.org/10.1088/1126-6708/2004/11/040.

[55] S. Frixione, P. Nason, and C. Oleari. *Matching NLO QCD computations with Parton Shower simulations: the POWHEG method*. Journal of High Energy Physics, 11(BICOCCA-FT-07-9, GEF-TH-21-2007):070, 2007. URL https://doi.org/10.1088/1126-6708/2007/11/070.

[56] S. Alioli, P. Nason, C. Oleari, and E. Re. *A general framework for implementing NLO calculations in shower Monte Carlo programs: the POWHEG BOX*. Journal of High Energy Physics, 06(DESY-10-018, SFB-CPP-10-22, IPPP-10-11, DCPT-10-22):043, 2010.

[57] A. M. Burger. *Measurement of vector Boson polarisation in WZ production at the LHC with the ATLAS detector*. Theses, Université Grenoble Alpes, July 2018. URL https://tel.archives-ouvertes.fr/tel-02132816.

[58] U. Baur, T. Han, and J. Ohnemus. *Amplitude zeros in WZ production*. Physical Review Letters, 72(25):3941–3944, June 1994. ISSN 0031-9007. URL http://doi.org/10.1103/PhysRevLett.72.3941.

[59] M. Kagan. *Measurement of the WZ production cross section and limits on anomalous triple gauge couplings at $\sqrt{s}$=7 TeV using the ATLAS detector*. PhD thesis, Harvard U., 2012. URL https://cds.cern.ch/record/1455843.

[60] L. Evans and P. Bryant. *LHC Machine*. Journal of Instrumentation, 3(08):S08001–S08001, Aug 2008. URL https://doi.org/10.1088/1748-0221/3/08/S08001.

[61] ATLAS Collaboration. *The ATLAS Experiment at the CERN Large Hadron Collider*. Journal of Instrumentation, 3(08):S08003, Aug 2008. URL https://doi.org/10.1088/1748-0221/3/08/S08003.

[62] CMS Collaboration. *The CMS experiment at the CERN LHC*. Journal of Instrumentation, 3: S08004, 2008. URL https://doi.org/10.1088/1748-0221/3/08/S08004.

[63] ALICE Collaboration. *The ALICE experiment at the CERN LHC*. Journal of Instrumentation, 3:S08002, 2008. URL https://doi.org/10.1088/1748-0221/3/08/S08002.

[64] LHCb Collaboration. *The LHCb Detector at the LHC*. Journal of Instrumentation, 3:S08005, 2008. URL https://doi.org/10.1088/1748-0221/3/08/S08005.

[65] E. Mobs. *The CERN accelerator complex - 2019. Complexe des accélérateurs du CERN - 2019*. (CERN-GRAPHICS-2019-002), Jul 2019. URL https://cds.cern.ch/record/2684277.

[66] Z. Marshall and the ATLAS Collaboration. *Simulation of Pile-up in the ATLAS Experiment*. Journal of Physics: Conference Series, 513(2):022024, jun 2014. URL https://doi.org/10.1088/1742-6596/513/2/022024.

[67] ATLAS Collaboration. *Luminosity Public Results: Run 2*. https://twiki.cern.ch/twiki/bin/view/AtlasPublic/LuminosityPublicResultsRun2, .

[68] ATLAS Collaboration. *Approved Plots DAQ*. https://twiki.cern.ch/twiki/bin/view/AtlasPublic/ApprovedPlotsDAQ, .

[69] A. Elliot. *Implementation of the ATLAS trigger within the ATLAS Multi-Threaded AthenaMT Framework*. PoS, LeptonPhoton2019:139, 2019. URL https://doi.org/10.22323/1.367.0139.

[70] ATLAS Collaboration. *ATLAS Computing: technical design report*. CERN, Geneva, 2005. URL https://cds.cern.ch/record/837738.

[71] J. Pequenao and P. Schaffner. *How ATLAS detects particles: diagram of particle paths in the detector*. 2013. URL https://cds.cern.ch/record/1505342.

[72] ATLAS Collaboration. *Electron and Photon Reconstruction in ATLAS*. https://opendata.atlas.cern/docs/documentation/physic_objects/electronphoton_reco.

[73] ATLAS Collaboration. *Performance of the ATLAS track reconstruction algorithms in dense environments in LHC Run 2*. The European Physical Journal C, 77(10), October 2017. ISSN 1434-6052. URL http://doi.org/10.1140/epjc/s10052-017-5225-7.

[74] T. Cornelissen, M. Elsing, I. Gavrilenko, W. Liebig, E. Moyse, and A. Salzburger. *The new ATLAS track reconstruction (NEWT)*. Journal of Physics: Conference Series, 119:032014, 2008. URL https://cds.cern.ch/record/1176900.

[75] ATLAS Collaboration. *Vertex Reconstruction Performance of the ATLAS Detector at* $\sqrt{s} = 13$ *TeV*. ATL-PHYS-PUB-2015-026, CERN, Geneva, 2015. URL https://cds.cern.ch/record/2037717.

[76] ATLAS Collaboration. *Electron reconstruction and identification in the ATLAS experiment using the 2015 and 2016 LHC proton–proton collision data at* $\sqrt{s} = 13$*TeV*. The European Physical Journal C, 79(8), August 2019. ISSN 1434-6052. URL http://doi.org/10.1140/epjc/s10052-019-7140-6.

[77] ATLAS Collaboration. *Electron and photon performance measurements with the ATLAS detector using the 2015–2017 LHC proton-proton collision data*. Journal of Instrumentation, 14(12):P12006–P12006, December 2019. ISSN 1748-0221. URL http://doi.org/10.1088/1748-0221/14/12/P12006.

[78] ATLAS Collaboration. *Electron efficiency measurements with the ATLAS detector using the 2015 LHC proton-proton collision data*. ATLAS-CONF-2016-024, CERN, Geneva, 2016. URL https://cds.cern.ch/record/2157687.

[79] ATLAS Collaboration. *Electron and photon reconstruction and performance in ATLAS using a dynamical, topological cell clustering-based approach*. ATL-PHYS-PUB-2017-022, CERN, Geneva, 2017. URL https://cds.cern.ch/record/2298955.

[80] ATLAS Collaboration. *Improved electron reconstruction in ATLAS using the Gaussian Sum Filter-based model for bremsstrahlung*. ATLAS-CONF-2012-047, CERN, Geneva, 2012. URL https://cds.cern.ch/record/1449796.

[81] G. Tarna and ATLAS Collaboration. *Electron identification with the ATLAS detector*. PoS, EPS-HEP2017(ATL-PHYS-PROC-2017-173):769, 2017. URL https://doi.org/10.22323/1.314.0769.

[82] ATLAS Collaboration. *Muon reconstruction performance of the ATLAS detector in proton–proton collision data at* $\sqrt{s}$ *=13 TeV*. The European Physical Journal C, 76(5), May 2016. ISSN 1434-6052. URL http://doi.org/10.1140/epjc/s10052-016-4120-y.

[83] M. Cacciari, G. P. Salam, and G. Soyez. *The anti-*k_t*jet clustering algorithm*. Journal of High Energy Physics, 2008(04):063–063, April 2008. ISSN 1029-8479. URL http://doi.org/10.1088/1126-6708/2008/04/063.

[84] ATLAS Collaboration. *Improving jet substructure performance in ATLAS using Track-CaloClusters*. ATL-PHYS-PUB-2017-015, CERN, Geneva, 2017. URL https://cds.cern.ch/record/2275636.

[85] ATLAS Collaboration. *E_T^{miss} performance in the ATLAS detector using 2015-2016 LHC p-p collisions*. ATLAS-CONF-2018-023, CERN, Geneva, 2018. URL https://cds.cern.ch/record/2625233.

[86] ATLAS Collaboration. *Performance of missing transverse momentum reconstruction for the ATLAS detector in the first proton-proton collisions at at $\sqrt{s}$= 13 TeV*. ATL-PHYS-PUB-2015-027, CERN, Geneva, 2015. URL https://cds.cern.ch/record/2037904.

[87] The ATLAS Collaboration. *Measurement of $W^{\pm}Z$ production cross sections in pp collisions at $\sqrt{s} = 8$ TeV with the ATLAS detector and limits on anomalous gauge boson self-couplings*. Physical Review D, 93(9), May 2016. ISSN 2470-0029. URL http://doi.org/10.1103/PhysRevD.93.092004.

[88] L. Boudet, F. Costanza, L. Di Ciaccio, D. Iliadis, E. Kasimi, R. Keeler, I. Koletsou, J. E. Lambert, R. Mcpherson, C. Petridou, J. Pretel, J. C. Rivera Vergara, E. Sauvan, L. Selem, M. J. Shroff, and I. Trigger. *Measurements and interpretations of $W^{\pm}Z$ production cross-sections in pp collisions at $\sqrt{s} = 13$ TeV with the ATLAS detector*. ATL-COM-PHYS-2025-019, July 2025. URL https://arxiv.org/abs/2507.03500. ATLAS internal document submitted to the Journal of High Energy Physics (reference ID: JHEP_092P_0725). The author is a contributor to this work.

[89] ATLAS collaboration. *Muon reconstruction and identification efficiency in ATLAS using the full Run 2 pp collision data set at $\sqrt{s} = 13$ TeV*. Eur. Phys. J. C, 81(7):578, 2021. URL https://doi.org/10.1140/epjc/s10052-021-09233-2.

[90] ATLAS Collaboration. *TruthClassification Directory in ATLAS Athena (Release 21.2)*, 2023. URL https://gitlab.cern.ch/atlas/athena/-/tree/21.2/PhysicsAnalysis/AnalysisCommon/TruthClassification.

[91] A. Ballestrero, E. Maina, and G. Pelliccioli. *Polarized vector boson scattering in the fully leptonic WZ and ZZ channels at the LHC*. Journal of High Energy Physics, 2019(9), September 2019. ISSN 1029-8479. URL http://doi.org/10.1007/JHEP09(2019)087.

[92] M. Abadi et al. *TensorFlow: Large-Scale Machine Learning on Heterogeneous Systems*. https://www.tensorflow.org/, 2015.

[93] F. Chollet et al. *Keras*. https://github.com/fchollet/keras, 2015.

[94] The ATLAS Collaboration. *Measurement of $W^{\pm}Z$ production cross sections and gauge boson polarisation in pp collisions at $\sqrt{s} = 13$ TeV with the ATLAS detector*. The European Physical Journal C, 79(6), June 2019. ISSN 1434-6052. URL http://doi.org/10.1140/epjc/s10052-019-7027-6.

[95] ATLAS Collaboration. *Measurements of differential cross-sections in four-lepton events in 13 TeV proton-proton collisions with the ATLAS detector*. Journal of High Energy Physics, 2021 (7), July 2021. ISSN 1029-8479. URL http://dx.doi.org/10.1007/JHEP07(2021)005.

[96] The ATLAS Collaboration. *Measurements of b-jet tagging efficiency with the ATLAS detector using $t\bar{t}$ events at $\sqrt{s} = 13$TeV*. Journal of High Energy Physics, 2018(8), August 2018. ISSN 1029-8479. URL http://doi.org/10.1007/JHEP08(2018)089.

[97] ATLAS Collaboration. *Observation of the associated production of a top quark and a Z boson in pp collisions at $\sqrt{s}$= 13 TeV with the ATLAS detector*. Journal of High Energy Physics, 2020(7), July 2020. ISSN 1029-8479. URL http://dx.doi.org/10.1007/JHEP07(2020)124.

[98] Biondi, S. *Experience with using unfolding procedures in ATLAS*. EPJ Web Conference, 137: 11002, 2017. URL https://doi.org/10.1051/epjconf/201713711002. 12th Conference on Quark Confinement and the Hadron Spectrum (Confinement XII), Thessaloniki, Greece, 29 Aug - 2 Sep 2016.

[99] G. D'Agostini. *A multidimensional unfolding method based on Bayes Theorem*. DESY-94-099, DESY, Hamburg, 1994. URL https://cds.cern.ch/record/265717.

[100] Tim Adye. *Unfolding algorithms and tests using RooUnfold*. In PHYSTAT 2011, pages 313–318, Geneva, 2011. CERN. URL https://doi.org/10.5170/CERN-2011-006.313.

[101] ATLAS Collaboration. *Luminosity determination in pp collisions at $\sqrt{s} = 13$ TeV using the ATLAS detector at the LHC*. ATLAS-CONF-2019-021, CERN, Geneva, 2019. URL https://cds.cern.ch/record/2677054.

[102] G. Avoni, M. Bruschi, G. Cabras, D. Caforio, N. Dehghanian, A. Floderus, B. Giacobbe, F. Giannuzzi, F. Giorgi, P. Grafström, V. Hedberg, F. Lasagni Manghi, S. Meneghini, J. Pinfold, E. Richards, C. Sbarra, N. Semprini Cesari, A. Sbrizzi, R. Soluk, G. Ucchielli, S. Valentinetti, O. Viazlo, M. Villa, C. Vittori, R. Vuillermet, and A. Zoccoli. *The new LUCID-2 detector for luminosity measurement and monitoring in ATLAS*. Journal of Instrumentation, 13(07):P07017, 2018. URL https://cds.cern.ch/record/2633501.

[103] J. Butterworth, S. Carrazza, A. Cooper-Sarkar, A. De Roeck, J. Feltesse, S. Forte, J. Gao, S. Glazov, J. Huston, Z. Kassabov, R. McNulty, A. Morsch, P. Nadolsky, V. Radescu, J. Rojo, and R. Thorne. *PDF4LHC recommendations for LHC Run II*. Journal of Physics G: Nuclear and Particle Physics, 43(2):023001, January 2016. ISSN 1361-6471. URL http://doi.org/10.1088/0954-3899/43/2/023001.

[104] A. Alloul, N. Christensen, C. Degrande, C. Duhr, and B. Fuks. *FeynRules 2.0— A complete toolbox for tree-level phenomenology*. Computer Physics Communications, 185(8): 2250–2300, August 2014. ISSN 0010-4655. URL http://doi.org/10.1016/j.cpc.2014.04.012.

[105] C. Degrande, G. Durieux, F. Maltoni, K. Mimasu, E. Vryonidou, and C. Zhang. *Automated one-loop computations in the standard model effective field theory*. Physical Review D, 103 (9), May 2021. ISSN 2470-0029. URL http://doi.org/10.1103/PhysRevD.103.096024.

[106] A. Buckley, J. Butterworth, D. Grellscheid, H. Hoeth, L. Lönnblad, J. Monk, H. Schulz, and F. Siegert. *Rivet user manual*. Computer Physics Communications, 184(12):2803–2819, December 2013. ISSN 0010-4655. URL http://doi.org/10.1016/j.cpc.2013.05.021.

[107] ATLAS Collaboration. *Combined effective field theory interpretation of differential cross-sections measurements of WW, WZ, 4l, and Z-plus-two-jets production using ATLAS data*. ATL-PHYS-PUB-2021-022, CERN, Geneva, 2021. URL https://cds.cern.ch/record/2776648.

[108] G. Durieux and SMEFT@NLO package developers. *Personal communication*, July 2024.

[109] P. Nason. *A new method for combining NLO QCD with shower Monte Carlo algorithms*. Journal of High Energy Physics, 11:040, 2004. URL https://doi.org/10.1088/1126-6708/2004/11/040.

[110] S. Frixione, P. Nason, and C. Oleari. *Matching NLO QCD computations with parton shower simulations: the POWHEG method*. Journal of High Energy Physics, 11:070, 2007. URL https://doi.org/10.1088/1126-6708/2007/11/070.

[111] S. Alioli, P. Nason, C. Oleari, and E. Re. *A general framework for implementing NLO calculations in shower Monte Carlo programs: the POWHEG BOX*. Journal of High Energy Physics, 06:043, 2010. URL https://doi.org/10.1007/JHEP06(2010)043.

[112] P. Nason and G. Zanderighi. *W^+W^-, WZ and ZZ production in the POWHEG-BOX-V2*. The European Physical Journal C, 74:2702, January 2014. URL https://doi.org/10.1140/epjc/s10052-013-2702-5.

[113] ATLAS Collaboration. *Measurement of the Z/γ^* boson transverse momentum distribution in pp collisions at $s = 7$ TeV with the ATLAS detector*. Journal of High Energy Physics, 09: 145, 2014. URL https://doi.org/10.1007/JHEP09(2014)145.

[114] H.-L. Lai et al. *New parton distributions for collider physics*. Physical Review D, 82:074024, 2010. URL https://doi.org/10.1103/PhysRevD.82.074024.

[115] J. Pumplin et al. *New Generation of Parton Distributions with Uncertainties from Global QCD Analysis*. Journal of High Energy Physics, 07:012, 2002. URL https://doi.org/10.1088/1126-6708/2002/07/012.

[116] M. Grazzini, S. Kallweit, and M. Wiesemann. *Fully differential NNLO computations with MATRIX*. The European Physical Journal C, 78(7), June 2018. ISSN 1434-6052. URL http://doi.org/10.1140/epjc/s10052-018-5771-7.

[117] V. Bertone, S. Carrazza, N. Hartland, and J. Rojo. *Illuminating the photon content of the proton within a global PDF analysis*. SciPost Physics, 5(1), July 2018. ISSN 2542-4653. URL http://doi.org/10.21468/SciPostPhys.5.1.008.

[118] G. Cowan. *Statistical Data Analysis*. Oxford science publications. Clarendon Press, 1998. ISBN 9780198501558.

[119] D. C. Montgomery and G. C. Runger. *Applied Statistics and Probability for Engineers*. John Wiley & Sons, 2010. ISBN 9780470053041.

[120] W. Verkerke. *Lecture Notes on Advanced Methods in Statistical Data Analysis: Practical Statistics – Part II: Composite Hypothesis, Nuisance Parameters*, 2014. URL https://indico.cern.ch/event/305391/contributions/701304/

attachments/580262/798889/Verkerke_Statistics_L2.pdf. Presented at the Advanced Methods in Statistical Data Analysis workshop, October 6–10, Rockefeller University.

[121] S. S. Wilks. *The Large-Sample Distribution of the Likelihood Ratio for Testing Composite Hypotheses*. Annals Math. Statist., 9(1):60–62, 1938. URL https://doi.org/10.1214/aoms/1177732360.

[122] W. Verkerke and D. Kirkby. *The RooFit toolkit for data modeling*. eConf, C0303241: MOLT007, 2003. URL https://arxiv.org/abs/physics/0306116.

[123] S. Grossi and R. Torre. *More variables or more bins? Impact on the EFT interpretation of Drell–Yan measurements*. The European Physical Journal C, 84(7):713, 2024. URL https://doi.org/10.1140/epjc/s10052-024-13086-w.

[124] G. Cowan, K. Cranmer, E. Gross, and O. Vitells. *Asymptotic formulae for likelihood-based tests of new physics*. The European Physical Journal C, 71(2), February 2011. ISSN 1434-6052. URL http://doi.org/10.1140/epjc/s10052-011-1554-0.

[125] I. Asimov. *Franchise*. In Isaac Asimov: The Complete Stories, Vol. 1. Broadway Books, 1990.

[126] E. Celada, T. Giani, J. ter Hoeve, L. Mantani, J. Rojo, A. N. Rossia, M. O. A. Thomas, and E. Vryonidou. *Mapping the SMEFT at high-energy colliders: from LEP and the (HL-)LHC to the FCC-ee*. Journal of High Energy Physics, 09:091, 2024. URL https://doi.org/10.1007/JHEP09(2024)091.

[127] ATLAS Collaboration. *Measurement of the associated production of a Higgs boson decaying into b-quarks with a vector boson at high transverse momentum in pp collisions at $\sqrt{s}$ = 13 with the ATLAS detector*. Physics Letters B, 816:136204, 2021. ISSN 0370-2693. URL https://www.sciencedirect.com/science/article/pii/S0370269321001441.

[128] LPCC Subgroup. *LHC Effective Field Theory Working Group*, 2024. URL https://lpcc.web.cern.ch/lhc-eft-wg.

[129] F. Garosi, D. Marzocca, A. Rodríguez Sánchez, and A. Stanzione. *Indirect constraints on top quark operators from a global SMEFT analysis*. Journal of High Energy Physics, 12: 129, 2023. URL https://doi.org/10.1007/JHEP12(2023)129.

[130] CMS Collaboration. *Measurement of the inclusive and differential WZ production cross sections, polarization angles, and triple gauge couplings in pp collisions at $\sqrt{s}$ = 13 TeV*.

Journal of High Energy Physics, 2022(7), July 2022. ISSN 1029-8479. URL http://doi.org/10.1007/JHEP07(2022)032.

[131] K. Hagiwara, S. Ishihara, R. Szalapski, and D. Zeppenfeld. *Low-energy effects of new interactions in the electroweak boson sector*. Physical Review D, 48:2182–2203, 1993. URL https://doi.org/10.1103/PhysRevD.48.2182.

[132] CMS Collaboration. *Measurement of $W^{\pm}\gamma$ differential cross sections in proton-proton collisions at $\sqrt{s}$ = 13 TeV and effective field theory constraints*. Physical Review D, 105(5), March 2022. ISSN 2470-0029. URL http://doi.org/10.1103/PhysRevD.105.052003.

[133] ATLAS Collaboration. *Differential cross-section measurements for the electroweak production of dijets in association with a Z boson in proton–proton collisions at ATLAS*. The European Physical Journal C, 81(2), February 2021. ISSN 1434-6052. URL http://doi.org/10.1140/epjc/s10052-020-08734-w.

[134] R. G. Ambrosio, J. ter Hoeve, M. Madigan, J. Rojo, and V. Sanz. *Unbinned multivariate observables for global SMEFT analyses from machine learning*. Journal of High Energy Physics, 2023(3), March 2023. ISSN 1029-8479. URL http://doi.org/10.1007/JHEP03(2023)033.

[135] ATLAS Collaboration. *Snowmass White Paper Contribution: Physics with the Phase-2 ATLAS and CMS Detectors*. ATL-PHYS-PUB-2022-018, CERN, Geneva, 2022. URL https://cds.cern.ch/record/2805993.

[136] O. Aberle et al. *High-Luminosity Large Hadron Collider (HL-LHC): Technical design report*. CERN Yellow Reports: Monographs. CERN, Geneva, 2020. URL https://cds.cern.ch/record/2749422.

[137] ATLAS Collaboration. *Technical Design Report for the Phase-II Upgrade of the ATLAS LAr Calorimeter*. CERN-LHCC-2017-018. ATLAS-TDR-027, CERN, Geneva, Sep 2017. URL http://cds.cern.ch/record/2285582.

[138] P. Moreira et al. *lpGBT: Low-Power Radiation-Hard Multipurpose High-Speed Transceiver ASIC for High-Energy Physics Experiments*. IEEE Transactions on Nuclear Science, 72(1): 24–37, 2025. URL https://doi.org/10.1109/TNS.2024.3506753.

[139] M. Shroff. *A data injector for the High Luminosity LHC ATLAS Liquid Argon Signal Processor*. Master's thesis, University of Victoria, 2020. URL https://cds.cern.ch/record/2753823.

[140] M. Shroff and ATLAS Collaboration. *Development of the ATLAS Liquid Argon Calorimeter Readout Electronics for the HL-LHC*. PoS, EPS-HEP2023:528, 2024. URL https://doi.org/10.22323/1.449.0528.

APPENDIX A

Effective Field Theories in Action - An example

A.1 Fermi-theory

A classical example of Effective Field Theories in action is the Fermi theory describing β- decay [34]. At the time it was proposed in 1934, Fermi had no prior knowledge of the W Boson, which mediates this interaction.

Considering a smaller subset of Fermi theory and looking at the muon decay process in the SM, the Feynman diagram for this is shown in Figure A.1 .

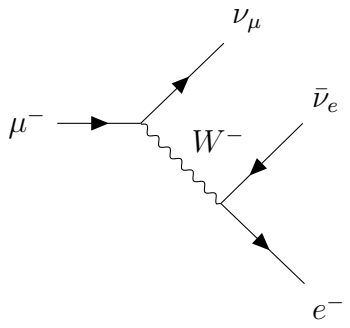

Figure A.1: *SM Feynman diagram for muon decay*

The muon decay amplitude is then:

$$-i\mathcal{M} = \left[\frac{g_W}{\sqrt{2}}\bar{u}(k_{\nu_\mu})\frac{1}{2}\gamma^\alpha(1-\gamma^5)u(k_\mu)\right]\frac{g_{\alpha\sigma}-\frac{k_\alpha k_\sigma}{m_W^2}}{k^2-m_W^2}\left[\frac{g_W}{\sqrt{2}}\bar{u}(k_e)\frac{1}{2}\gamma^\sigma(1-\gamma^5)v(k_{\nu_e})\right]. \tag{A.1}$$

In the physical processes, assuming that the electron and neutrinos are massless, the magnitude of the exchanged 4-momentum is limited by the mass of the muon: $0 \leq k^2 \leq m_\mu^2$.

This would mean that k^2 is much smaller than m_W^2 and the propagator can be written in an expansion of orders of mass as

$$-\frac{ig_{\alpha\sigma} - \frac{k_\alpha k_\sigma}{m_W^2}}{k^2 - m_W^2} \xrightarrow{|k|^2 \ll m_W^2} \frac{ig_{\alpha\sigma}}{m_W^2}\left(1 + \frac{k^2}{m_W^2} + \frac{k^4}{m_W^6} + ...\right) , \tag{A.2}$$

$$\Rightarrow i\mathcal{M} = \frac{g_W^2}{8m_W^2}\left[\bar{u}(k_{\nu_\mu})\gamma^\alpha(1-\gamma^5)u(k_\mu)\right] g_{\alpha\sigma}\left[\bar{u}(k_e)\gamma^\sigma(1-\gamma^5)v(k_{\nu_e})\right] + \mathcal{O}\left(\frac{1}{m_W^4}\right). \tag{A.3}$$

This is the same matrix element as that produced by a four-point interaction Lagrangian, which can be written as the Feynman diagram drawn below:

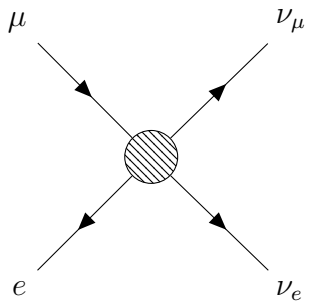

Figure A.2: *Four point interaction Feynman diagram for muon decay, valid for when* $|k|^2 \ll m_W^2$.

In this low energy limit, Equation A.3 shows that it is possible to construct an Effective theory where the W boson is absent. The Lagrangian for this theory simply needs to include the muon, electron and neutrino fields, and their interaction term.

$$\mathcal{L}_{\text{EFT}} = \frac{c}{\Lambda^2}(\bar{\nu}_\mu\bar{\gamma}_\rho\mu)(\bar{e}\bar{\gamma}_\rho\nu_e) , \tag{A.4}$$

where in this construction Λ^2 is the expansion scale and c is a factor called the Wilson coefficient.

$$\Lambda = m_W, \quad c = \frac{g_W^2}{8}. \tag{A.5}$$

The effect of the W exchange has now been included in the four-fermion operators; with the heavier W boson being "integrated out".

The effective Lagrangian adequately describes all processes including the muons, electrons and the neutrinos, in the strict regime that the energy scale is below $\Lambda = m_W$.

It should also be noted that the Effective Lagrangian is not renormalizable, which means that it needs to break down at a new energy scale. And indeed, the Effective Lagrangian does not describe muon decay at energy scales close to m_W.

APPENDIX B

Dimension-6 operators (in the Warsaw Basis)

X^3		$\psi^2 XH$		$(\bar{R}R)(\bar{R}R)$	
Q_G	$f^{abc}G^{a\nu}_{\mu}G^{b}_{\nu\rho}G^{\rho}_{c\mu}$	Q_{eW}	$(\bar{l}_p\sigma^{\mu\nu}e_r)^j HW^i_{\mu\nu}$	Q_{ee}	$(\bar{e}_p\gamma_\mu e_r)(\bar{e}_s\gamma^\mu e_t)$
$Q_{\tilde{G}}$	$f^{abc}\tilde{G}^{a\nu}_{\mu}\tilde{G}^{b}_{\nu\rho}G^{\rho}_{c\mu}$	Q_{eB}	$(\bar{l}_p\sigma^{\mu\nu}e_r)HB_{\mu\nu}$	Q_{uu}	$(\bar{u}_p\gamma_\mu u_r)(\bar{u}_s\gamma^\mu u_t)$
Q_W	$\epsilon^{ijk}W^{i\nu}_{\mu}W^{j}_{\nu\rho}W^{\rho}_{k\mu}$	Q_{uG}	$(\bar{q}_p\sigma^{\mu\nu}T^a u_r)\tilde{H}G^a_{\mu\nu}$	Q_{dd}	$(\bar{d}_p\gamma_\mu d_r)(\bar{d}_s\gamma^\mu d_t)$
$Q_{\tilde{W}}$	$\epsilon^{ijk}\tilde{W}^{i\nu}_{\mu}\tilde{W}^{j}_{\nu\rho}W^{\rho}_{k\mu}$	Q_{uW}	$(\bar{q}_p\sigma^{\mu\nu}u_r)\tilde{H}W^i_{\mu\nu}$	Q_{eu}	$(\bar{e}_p\gamma_\mu e_r)(\bar{u}_s\gamma^\mu u_t)$
H^6		Q_{uB}	$(\bar{q}_p\sigma^{\mu\nu}u_r)\tilde{H}B_{\mu\nu}$	Q_{ed}	$(\bar{e}_p\gamma_\mu e_r)(\bar{d}_s\gamma^\mu d_t)$
Q_H	$(H^\dagger H)^3$	Q_{dG}	$(\bar{q}_p\sigma^{\mu\nu}T^a d_r)HG^a_{\mu\nu}$	$Q^{(1)}_{ud}$	$(\bar{u}_p\gamma_\mu u_r)(\bar{d}_s\gamma^\mu d_t)$
H^4D^2		Q_{dW}	$(\bar{q}_p\sigma^{\mu\nu}d_r)HW^i_{\mu\nu}$	$Q^{(8)}_{ud}$	$(\bar{u}_p\gamma_\mu T^a u_r)(\bar{d}_s\gamma^\mu T^a d_t)$
$Q_{H\Box}$	$(H^\dagger H)\Box(H^\dagger H)$	Q_{dB}	$(\bar{q}_p\sigma^{\mu\nu}d_r)HB_{\mu\nu}$		
Q_{HD}	$(D^\mu H^\dagger D_\mu H)(H^\dagger H)$				
X^2H^2		ψ^2H^2D		$(\bar{L}L)(\bar{R}R)$	
Q_{HG}	$H^\dagger HG^a_{\mu\nu}G^{a\mu\nu}$	$Q^{(1)}_{Hl}$	$(H^\dagger i\overleftrightarrow{D}_\mu H)(\bar{l}_p\gamma^\mu l_r)$	Q_{le}	$(\bar{l}_p\gamma_\mu l_r)(\bar{e}_s\gamma^\mu e_t)$
$Q_{H\tilde{G}}$	$H^\dagger H\tilde{G}^a_{\mu\nu}G^{a\mu\nu}$	$Q^{(3)}_{Hl}$	$(H^\dagger i\overleftrightarrow{D}^I_\mu H)(\bar{l}_p\tau^I\gamma^\mu l_r)$	Q_{lu}	$(\bar{l}_p\gamma_\mu l_r)(\bar{u}_s\gamma^\mu u_t)$
Q_{HW}	$H^\dagger HW^I_{\mu\nu}W^{I\mu\nu}$	Q_{He}	$(H^\dagger i\overleftrightarrow{D}_\mu H)(\bar{e}_p\gamma^\mu e_r)$	Q_{ld}	$(\bar{l}_p\gamma_\mu l_r)(\bar{d}_s\gamma^\mu d_t)$
$Q_{H\tilde{W}}$	$H^\dagger H\tilde{W}^I_{\mu\nu}W^{I\mu\nu}$	$Q^{(1)}_{Hq}$	$(H^\dagger i\overleftrightarrow{D}_\mu H)(\bar{q}_p\gamma^\mu q_r)$	Q_{qe}	$(\bar{q}_p\gamma_\mu q_r)(\bar{e}_s\gamma^\mu e_t)$
Q_{HB}	$H^\dagger HB_{\mu\nu}B^{\mu\nu}$	$Q^{(3)}_{Hq}$	$(H^\dagger i\overleftrightarrow{D}^I_\mu H)(\bar{q}_p\tau^I\gamma^\mu q_r)$	$Q^{(1)}_{qu}$	$(\bar{q}_p\gamma_\mu q_r)(\bar{u}_s\gamma^\mu u_t)$
$Q_{H\tilde{B}}$	$H^\dagger H\tilde{B}_{\mu\nu}B^{\mu\nu}$	Q_{Hu}	$(H^\dagger i\overleftrightarrow{D}_\mu H)(\bar{u}_p\gamma^\mu u_r)$	$Q^{(8)}_{qu}$	$(\bar{q}_p\gamma_\mu T^a q_r)(\bar{u}_s\gamma^\mu T^a u_t)$
Q_{HWB}	$H^\dagger\sigma^I HW^I_{\mu\nu}B^{\mu\nu}$	Q_{Hd}	$(H^\dagger i\overleftrightarrow{D}_\mu H)(\bar{d}_p\gamma^\mu d_r)$	$Q^{(1)}_{qd}$	$(\bar{q}_p\gamma_\mu q_r)(\bar{d}_s\gamma^\mu d_t)$
$Q_{H\tilde{W}B}$	$H^\dagger\sigma^I H\tilde{W}^I_{\mu\nu}B^{\mu\nu}$	Q_{Hud}	$i(\tilde{H}^\dagger D_\mu H)(\bar{u}_p\gamma^\mu d_r)$	$Q^{(8)}_{qd}$	$(\bar{q}_p\gamma_\mu T^a q_r)(\bar{d}_s\gamma^\mu T^a d_t)$
ψ^2H^3		$(\bar{L}L)(\bar{L}L)$		$(\bar{L}R)(\bar{L}R)$, $(\bar{L}R)(LR)$	
Q_{eH}	$(H^\dagger H)(\bar{l}_p e_r H)$	Q_{ll}	$(\bar{l}_p\gamma_\mu l_r)(\bar{l}_s\gamma^\mu l_t)$	Q_{leqd}	$(\bar{l}^j_p e_r)(\bar{d}_s q^j_t)$
Q_{uH}	$(H^\dagger H)(\bar{q}_p u_r\tilde{H})$	$Q^{(1)}_{qq}$	$(\bar{q}_p\gamma_\mu q_r)(\bar{q}_s\gamma^\mu q_t)$	$Q^{(1)}_{quqd}$	$(\bar{q}^j_p u_r)\epsilon_{jk}(\bar{q}^k_s d_t)$
Q_{dH}	$(H^\dagger H)(\bar{q}_p d_r H)$	$Q^{(3)}_{qq}$	$(\bar{q}_p\gamma_\mu\tau^i q_r)(\bar{q}_s\gamma^\mu\tau^i q_t)$	$Q^{(8)}_{quqd}$	$(\bar{q}^j_p T^a u_r)\epsilon_{jk}(\bar{q}^k_s T^a d_t)$
		$Q^{(1)}_{lq}$	$(\bar{l}_p\gamma_\mu l_r)(\bar{q}_s\gamma^\mu q_t)$	$Q^{(1)}_{lequ}$	$(\bar{l}^j_p e_r)\epsilon_{jk}(\bar{q}^k_s u_t)$
		$Q^{(3)}_{lq}$	$(\bar{l}_p\gamma_\mu\tau^i l_r)(\bar{q}_s\gamma^\mu\tau^i q_t)$	$Q^{(3)}_{lequ}$	$(\bar{l}_p\sigma_{\mu\nu}e_r)\epsilon_{jk}(\bar{q}^j_s\sigma^{\mu\nu}u_t)$

Table B.1: *$\mathcal{L}^{(6)}$ baryon number-conserving operators in the Warsaw basis. Taken from [40].*

APPENDIX C

Likelihood scans for 1D fits

In this appendix, the profile likelihood ratio test statistic defined in Equation 6.15, is shown as a function of varying the EFT parameter.

Both measured and expected (Asimov) scans are shown for all parameters of interest. The likelihood ratios at 1σ and 2σ which form the 68% and 95% CI, respectively are also shown. The interpretation of these scans results in the limits presented in Section 8.1.1.

C.1 Observable: $q_W \cos\theta^*_{W_\ell}$

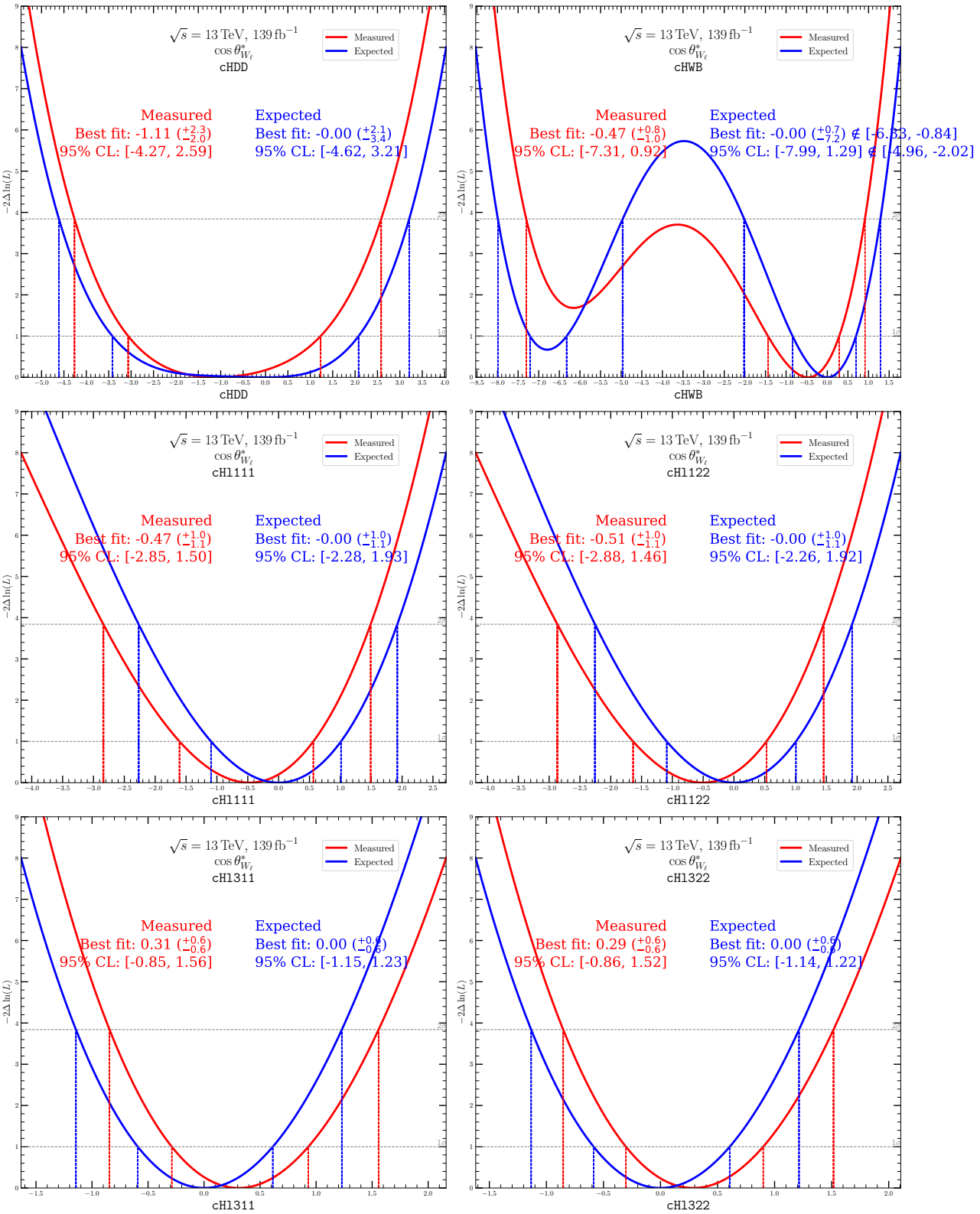

Figure C.1: *Profile likelihood scans for EFT parameters using the* $\cos\theta^*_{W_\ell}$ *distribution.*

Observable: $q_W \cos\theta^*_{W_\ell}$ (continued)

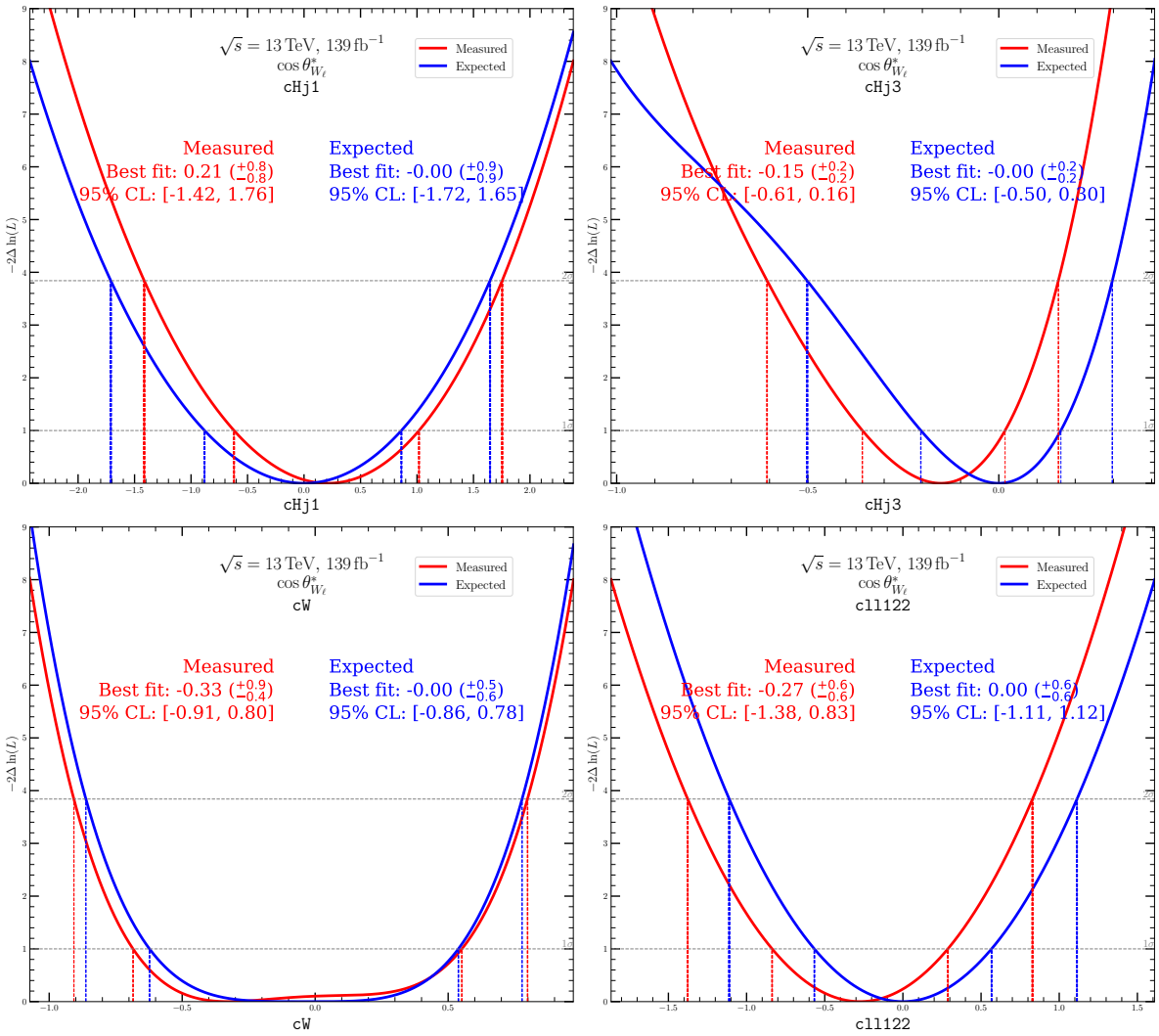

Figure C.2: *Profile likelihood scans for EFT parameters using the* $\cos\theta^*_{W_\ell}$ *distribution (continued).*

C.2 Observable: $\cos\theta^*_{Z_\ell}$

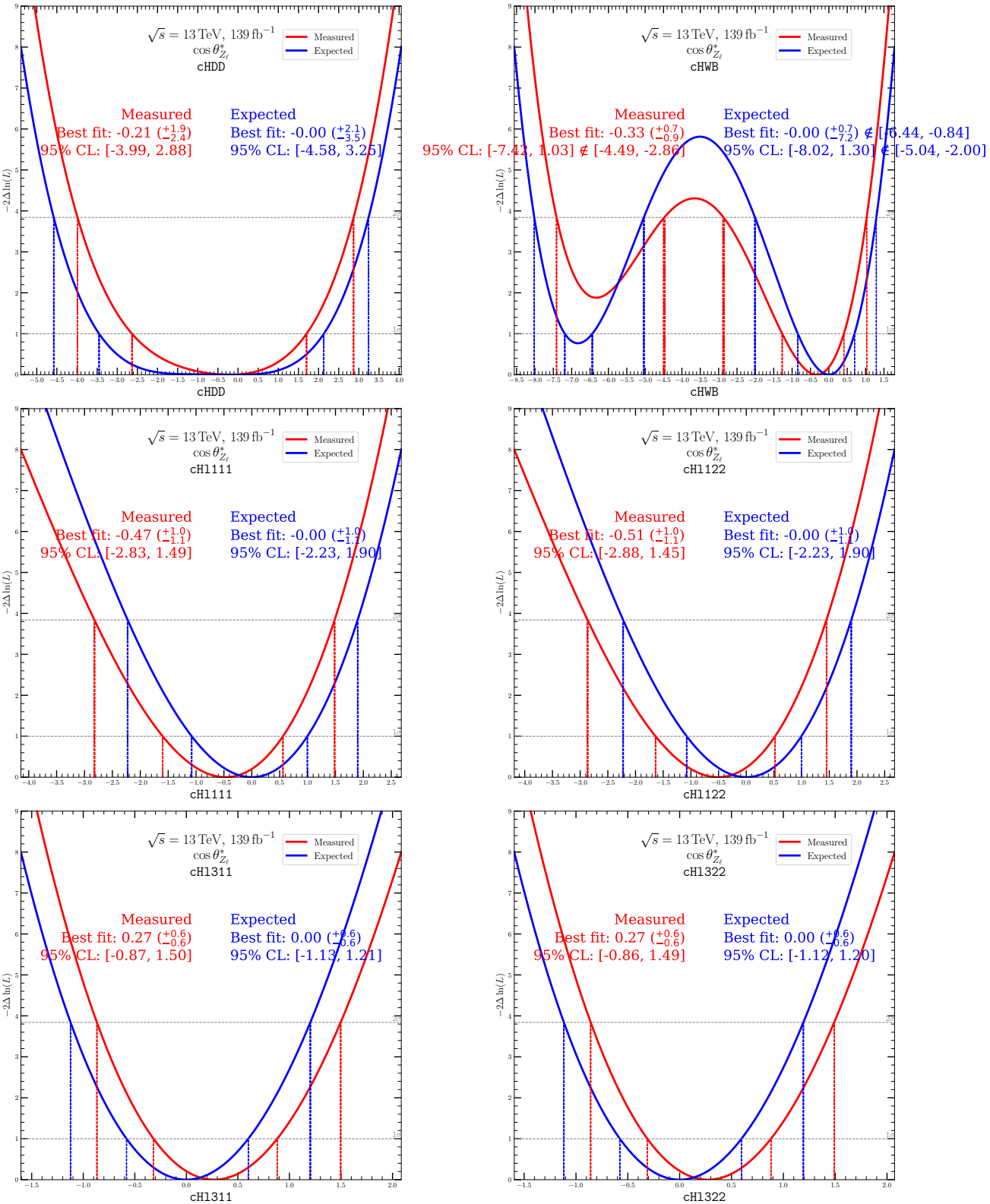

Figure C.3: *Profile likelihood scans for EFT parameters using the* $\cos\theta^*_{Z_\ell}$ *distribution.*

Observable: $\cos\theta^*_{Z_\ell}$ (continued)

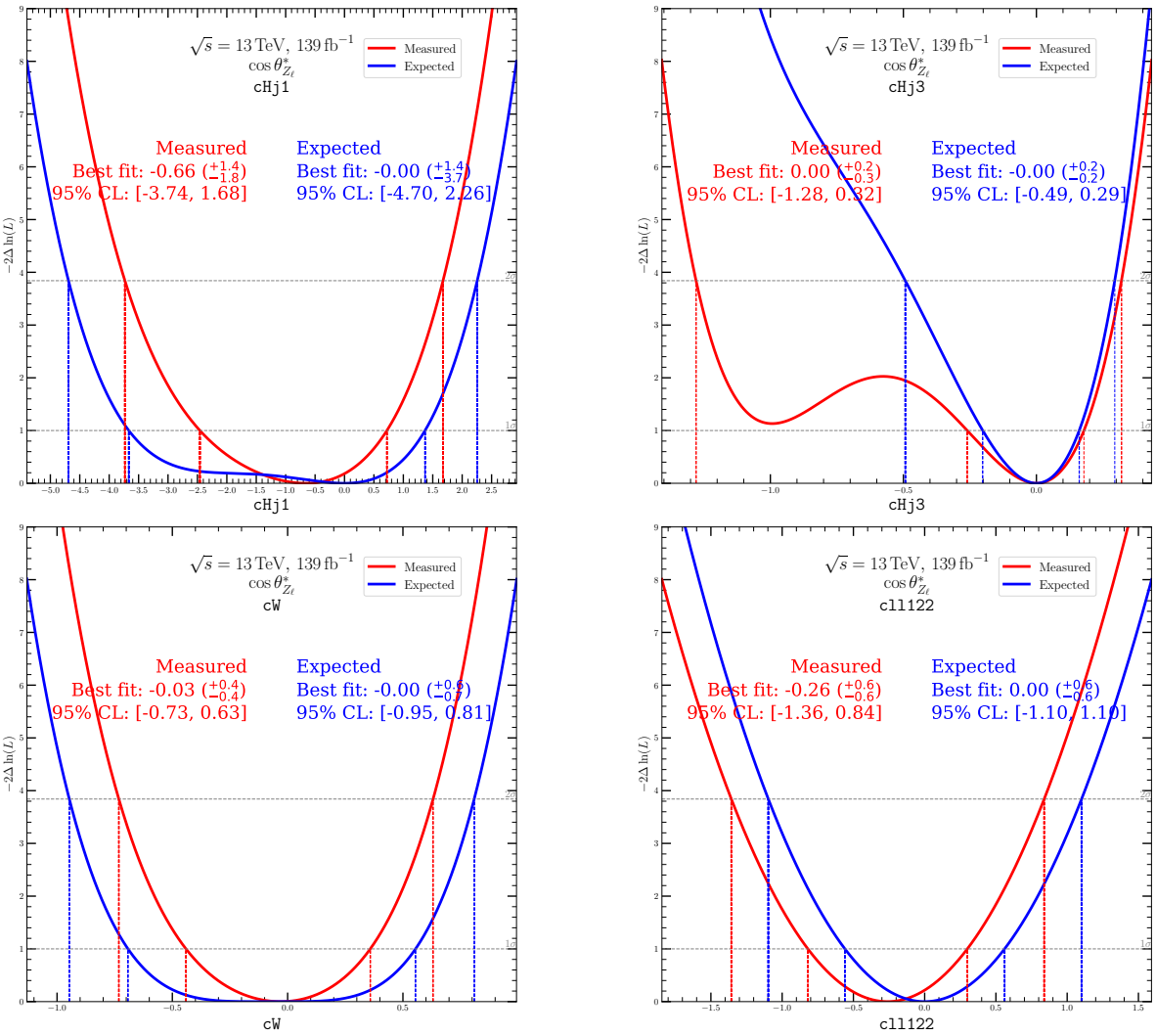

Figure C.4: *Profile likelihood scans for EFT parameters using the* $\cos\theta^*_{Z_\ell}$ *distribution (continued).*

C.3 Observable: $|\cos\theta_V|$

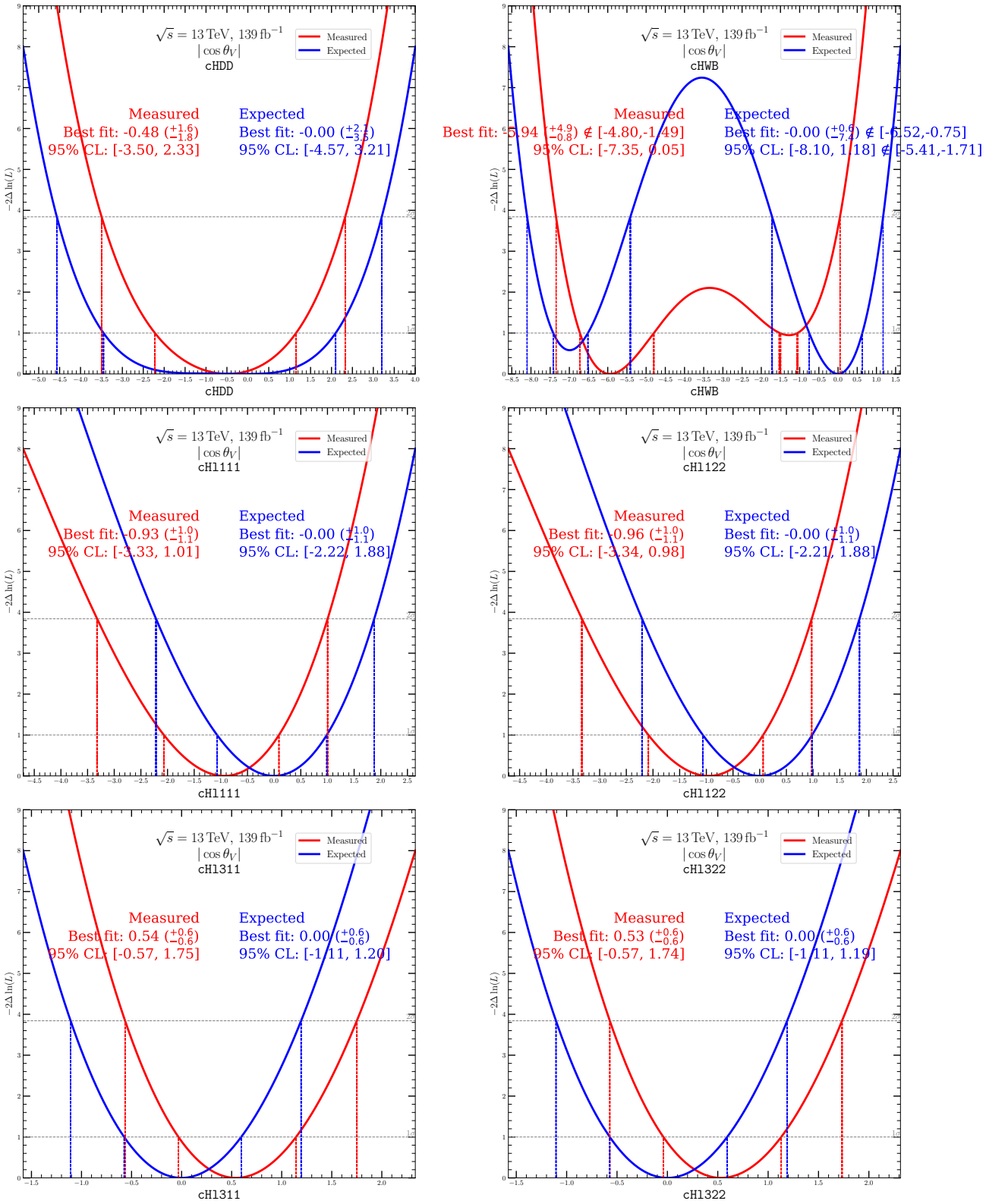

Figure C.5: *Profile likelihood scans for EFT parameters using the* $|\cos\theta_V|$ *distribution.*

Observable: $|\cos\theta_V|$ (continued)

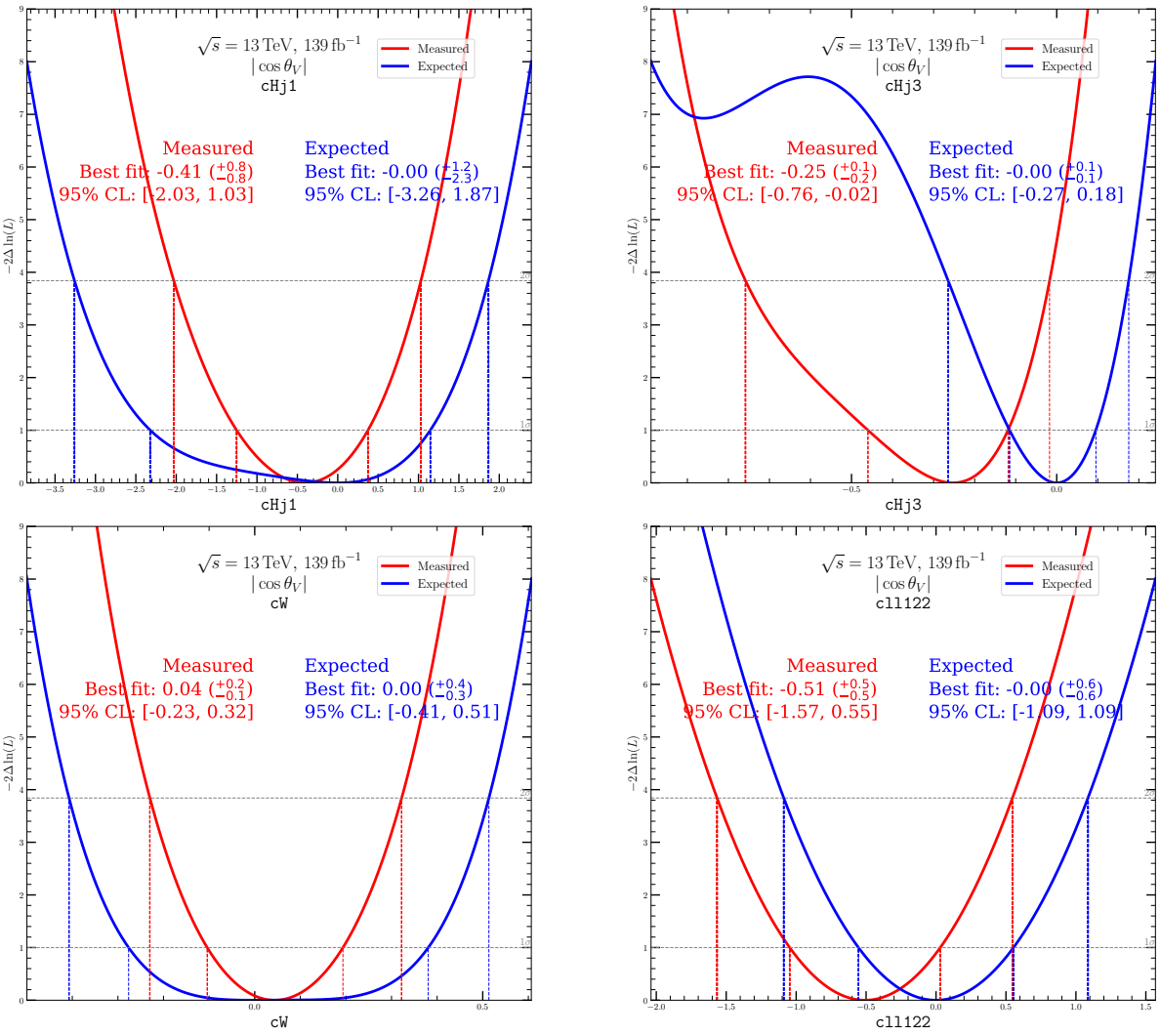

Figure C.6: *Profile likelihood scans for EFT parameters using the $|\cos\theta_V|$ distribution (continued).*

C.4 Observable: m_T^{WZ}

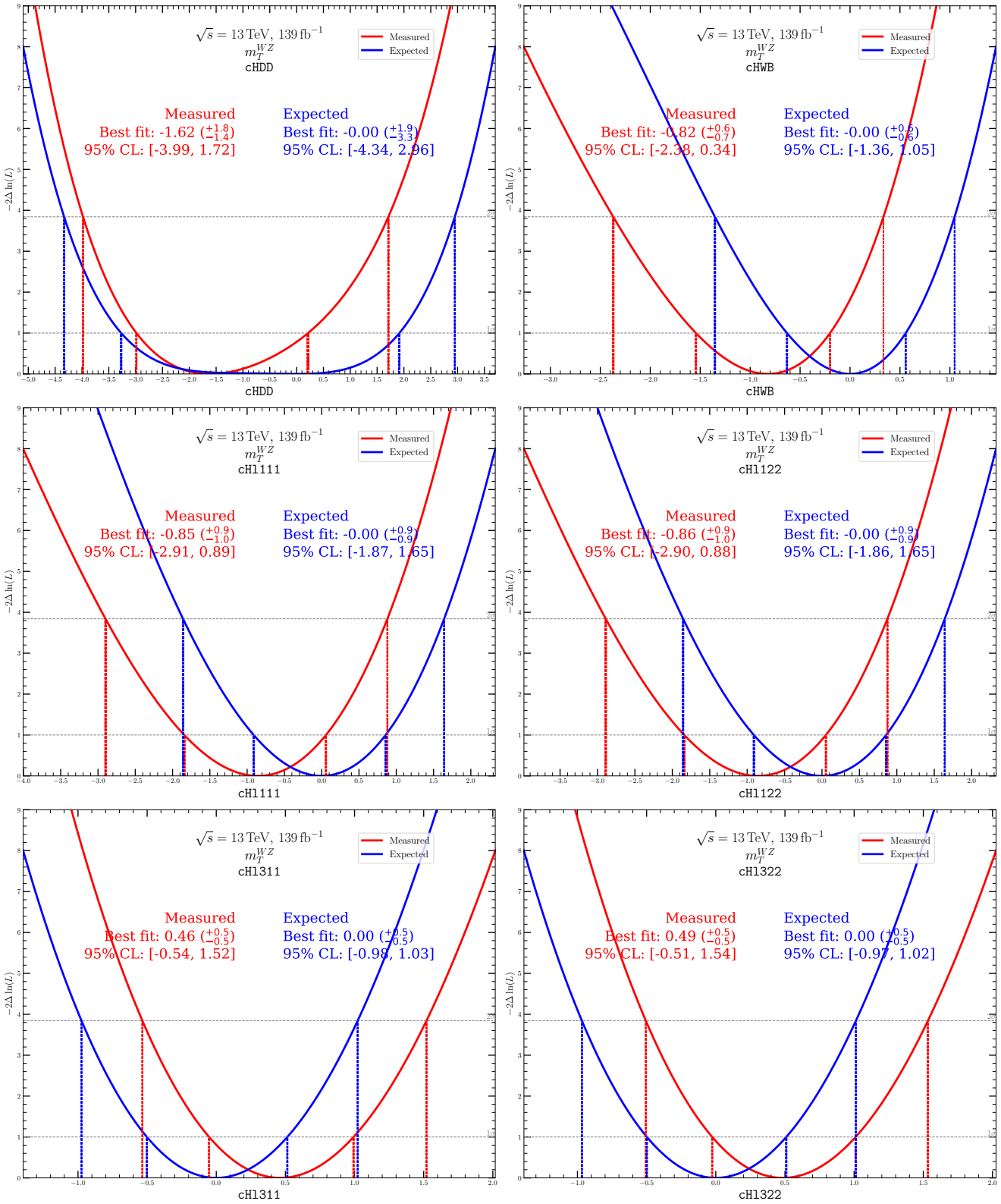

Figure C.7: *Profile likelihood scans for EFT parameters using the m_T^{WZ} distribution.*

Observable: m_T^{WZ} (continued)

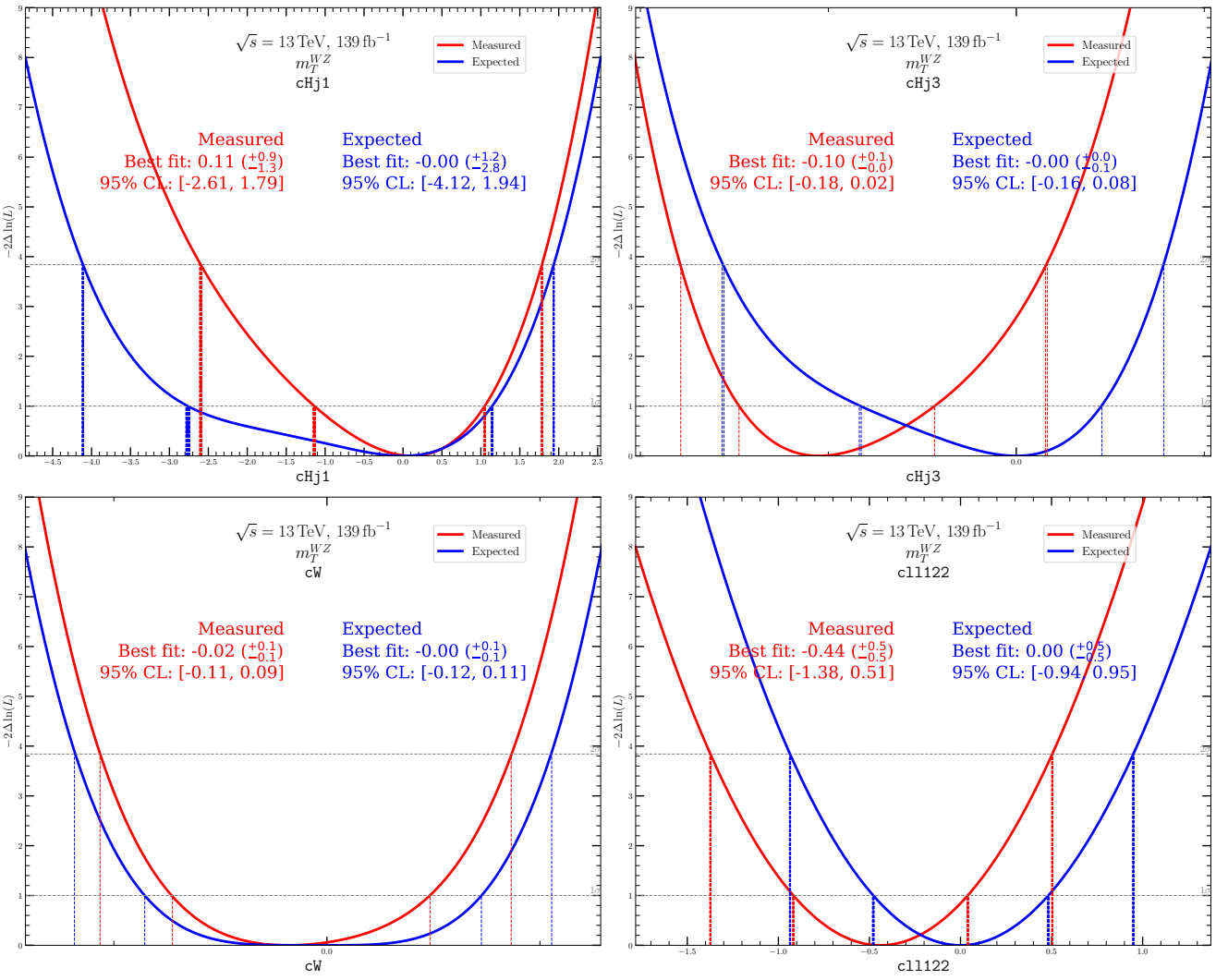

Figure C.8: *Profile likelihood scans for EFT parameters using the m_T^{WZ} distribution (continued).*

C.5 Observable: $\phi^*_{W_\ell}$

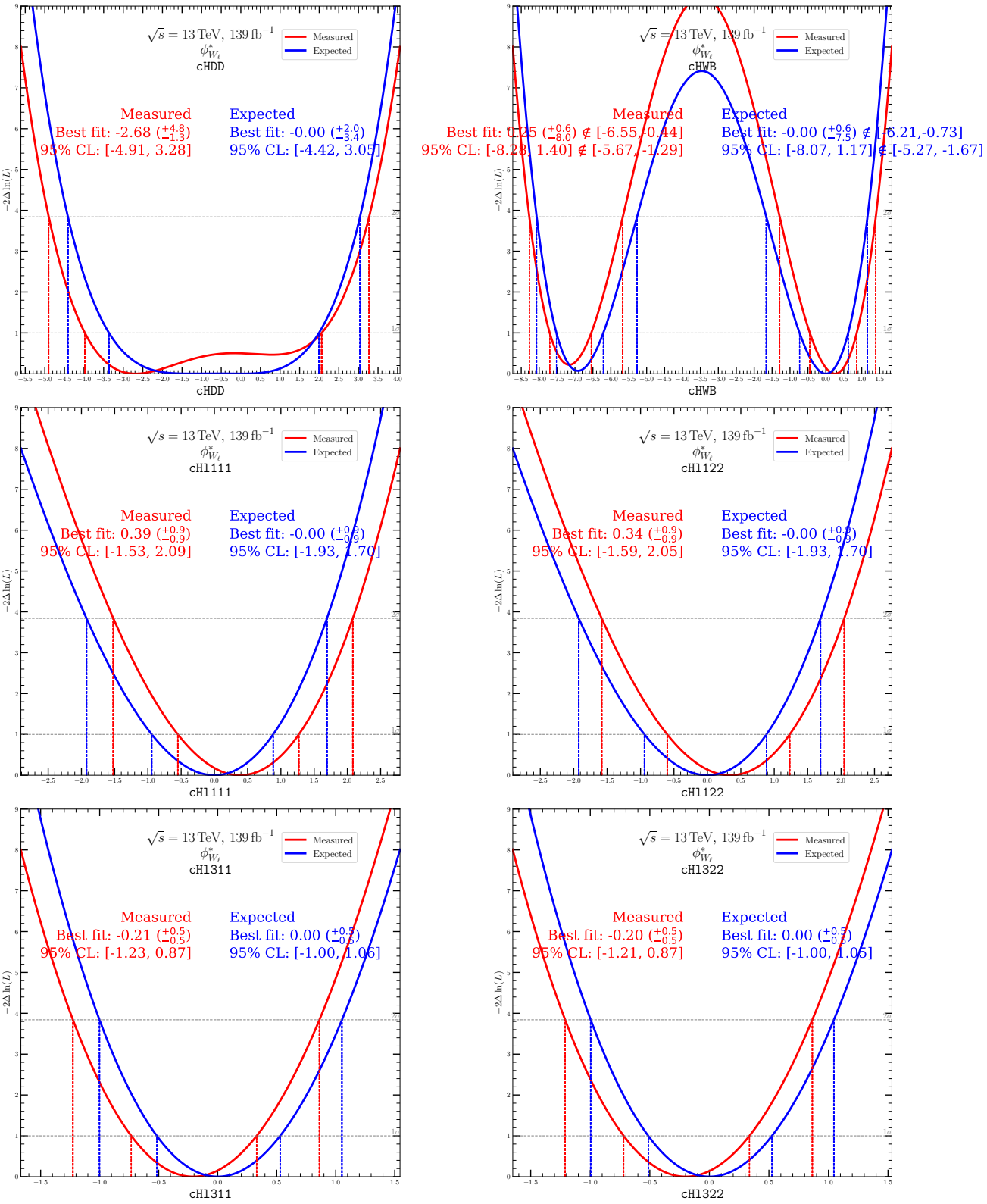

Figure C.9: *Profile likelihood scans for EFT parameters using the $\phi^*_{W_\ell}$ distribution.*

Observable: $\phi^*_{W_\ell}$ (continued)

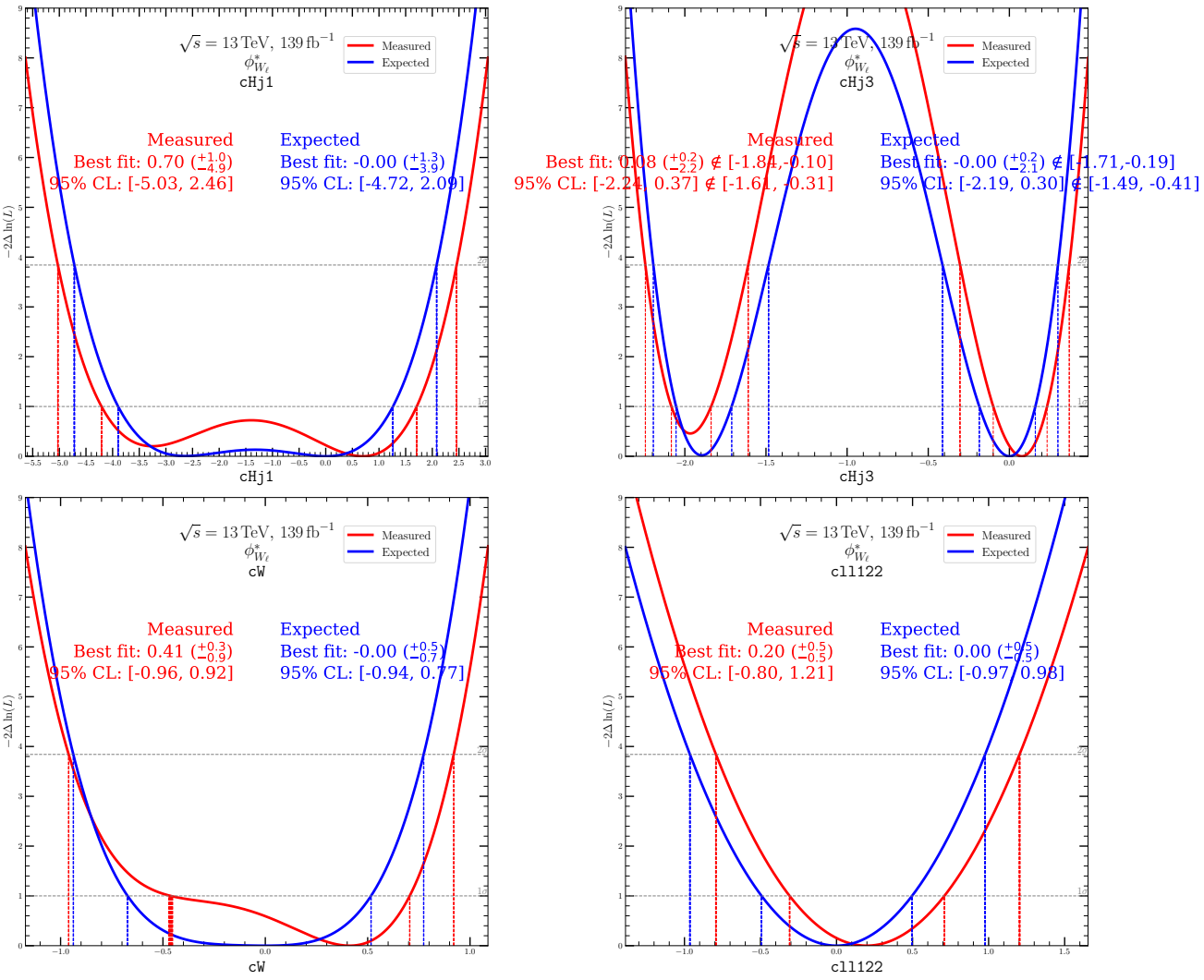

Figure C.10: *Profile likelihood scans for EFT parameters using the $\phi^*_{W_\ell}$ distribution (continued).*

C.6 Observable: $\phi^*_{Z_\ell}$

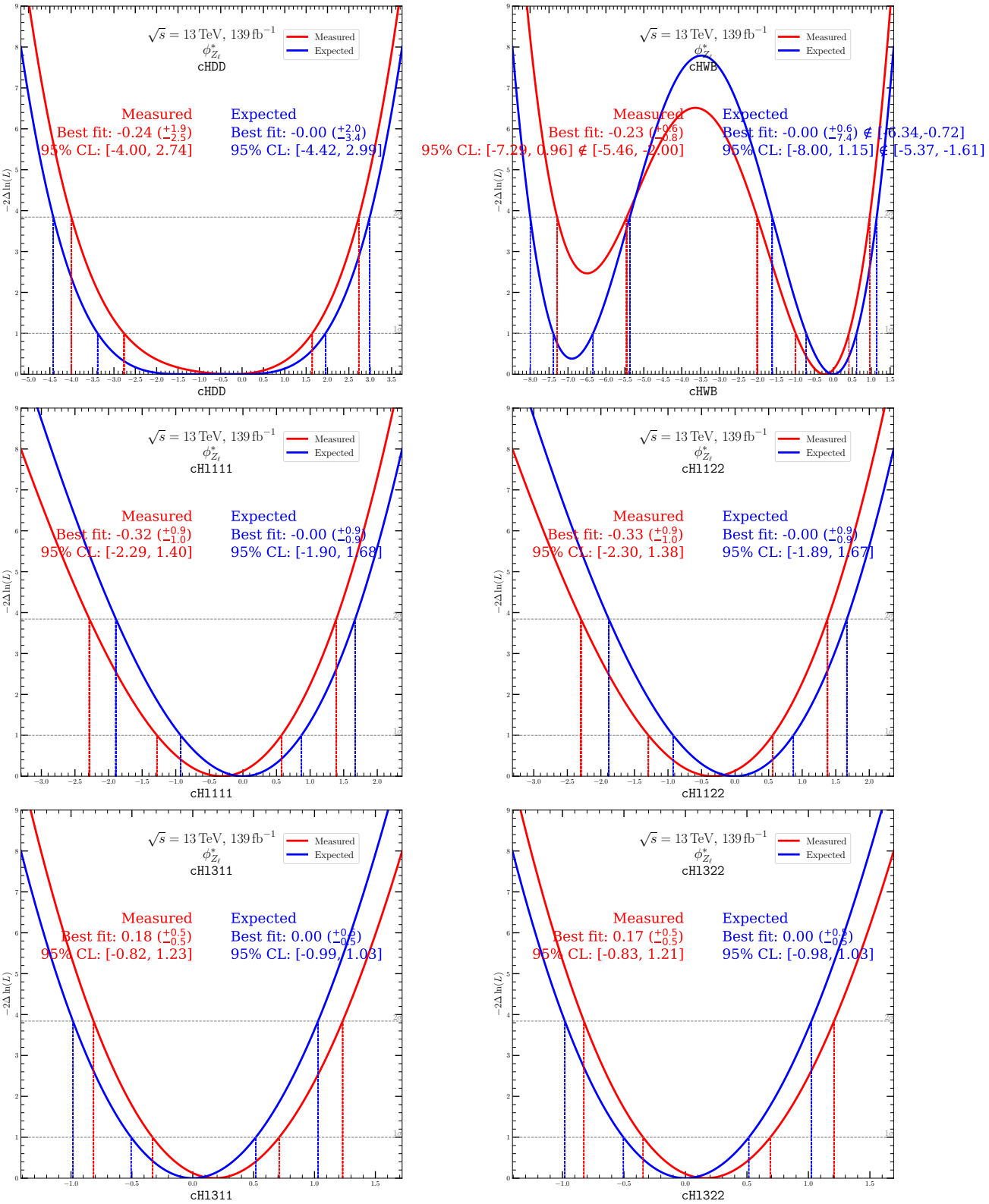

Figure C.11: *Profile likelihood scans for EFT parameters using the $\phi^*_{Z_\ell}$ distribution.*

Observable: $\phi^*_{Z_\ell}$ (continued)

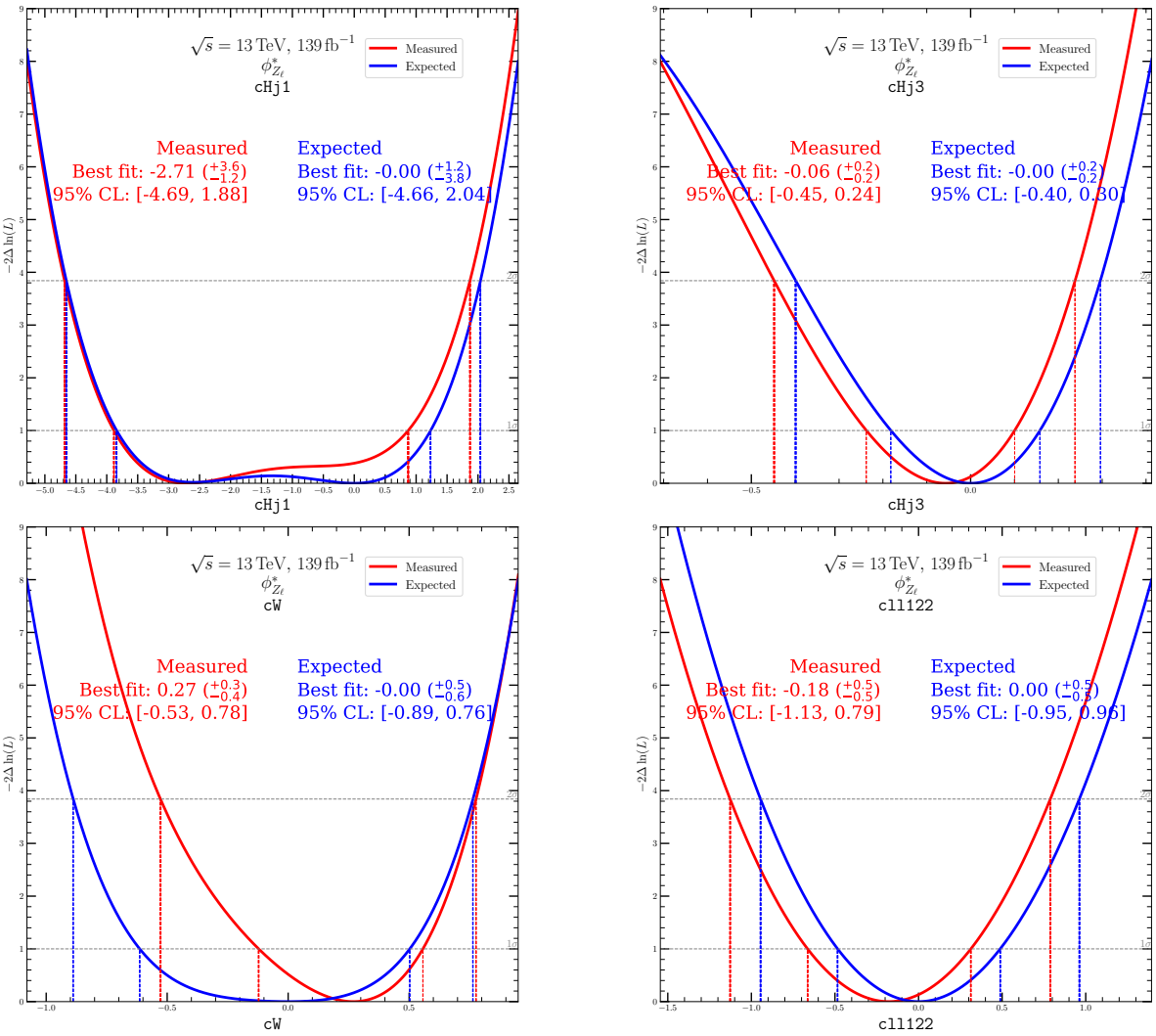

Figure C.12: *Profile likelihood scans for EFT parameters using the $\phi^*_{Z_\ell}$ distribution (continued).*

APPENDIX D

Expected (Asimov) and Measured likelihood scans for 2D fits

The figures in this appendix present the 2D profile likelihood ratio test statistic for both the Asimov dataset, where the measured data is replaced by the Gaussian mean values derived from Monte Carlo Standard Model predictions, and the actual measured data. This comparison provides the expected results and highlights key features, particularly the structure of the likelihood surface from the fits. The fits using the measured data (as shown in Chapter 8.1.2) are displayed on the left side of each page, while the expected fits using the Asimov samples/values appear on the right. By comparing the two plots within the same panel, one can assess how the measured data influences the profile likelihood across the parameter space.

D.1 Observable: $q_W \cos\theta^*_{W_\ell}$

$q_W \cos\theta^*_{W_\ell}$ - Measured

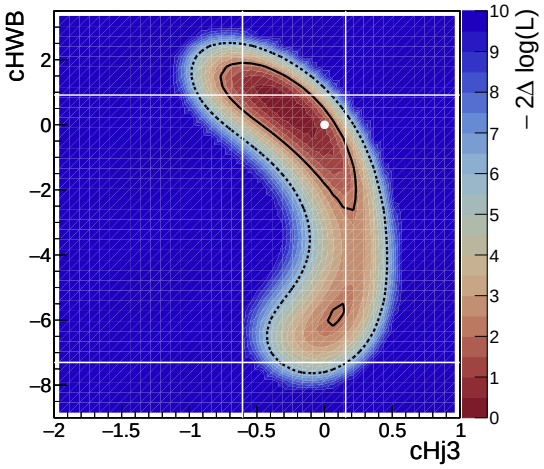

$q_W \cos\theta^*_{W_\ell}$ - Expected (Asimov)

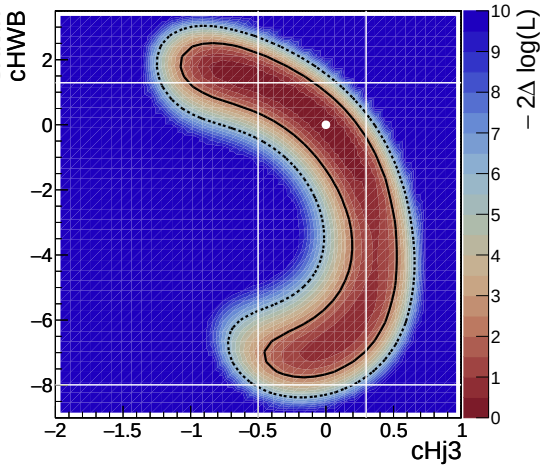

$q_W \cos\theta^*_{W_\ell}$ - Measured

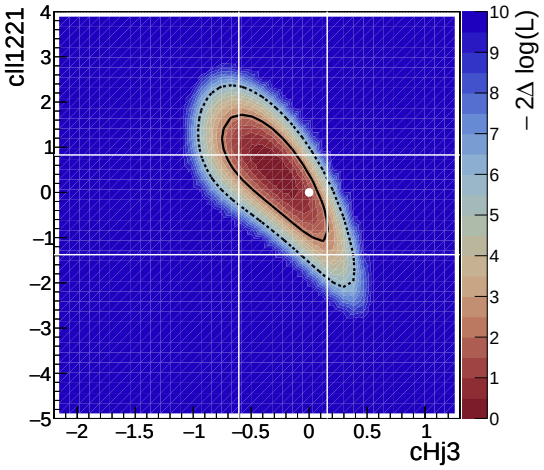

$q_W \cos\theta^*_{W_\ell}$ - Expected (Asimov)

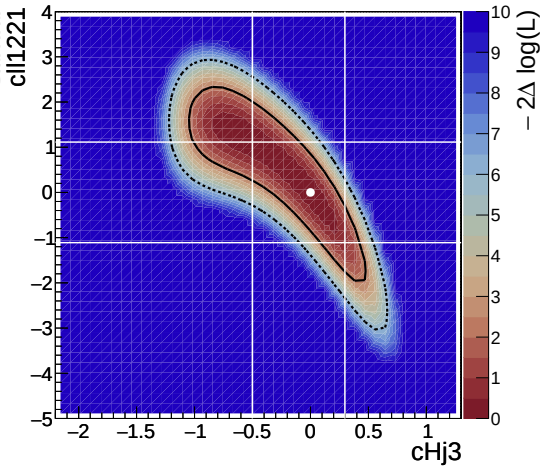

$q_W \cos\theta^*_{W_\ell}$ - Measured

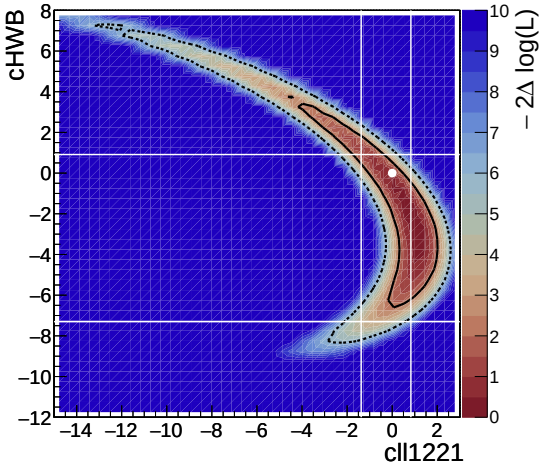

$q_W \cos\theta^*_{W_\ell}$ - Expected (Asimov)

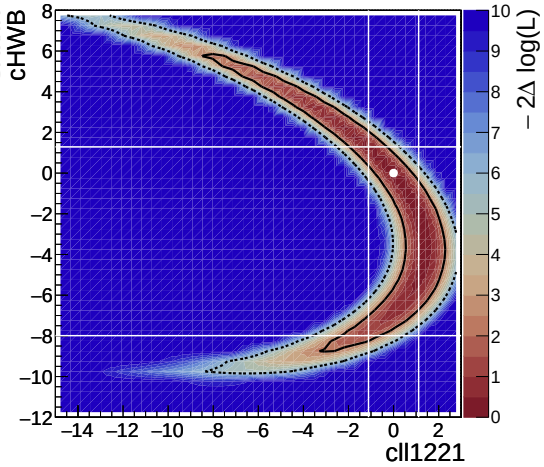

$q_W \cos\theta^*_{W_\ell}$ - Measured

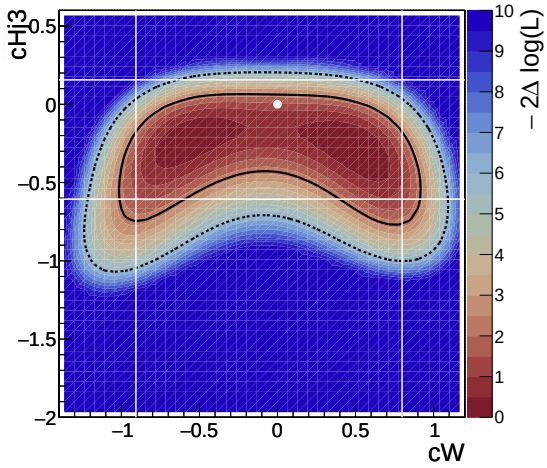

$q_W \cos\theta^*_{W_\ell}$ - Expected (Asimov)

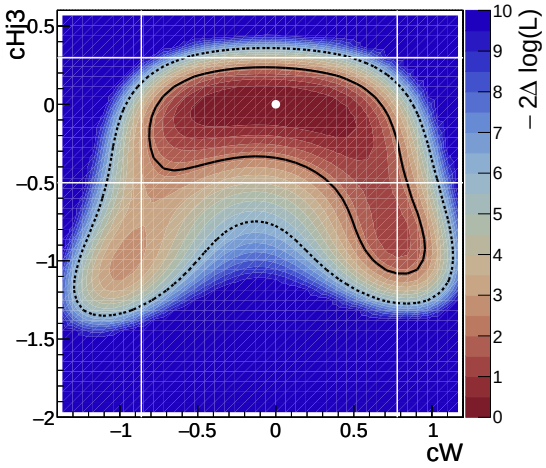

$q_W \cos\theta^*_{W_\ell}$ - Measured

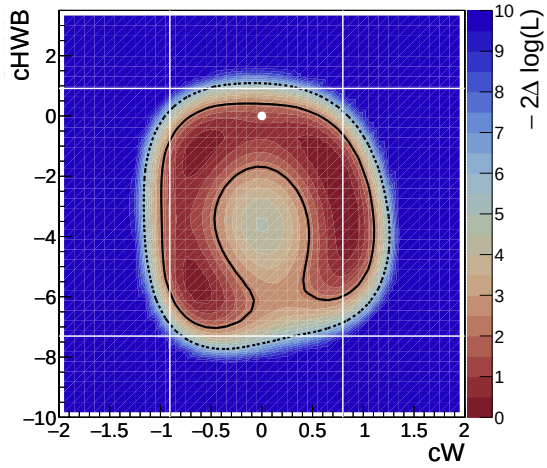

$q_W \cos\theta^*_{W_\ell}$ - Expected (Asimov)

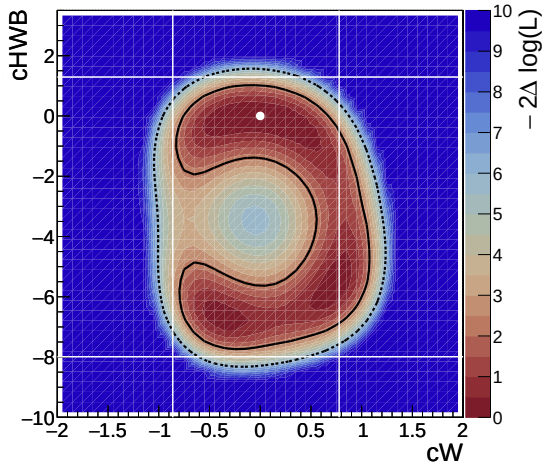

$q_W \cos\theta^*_{W_\ell}$ - Measured

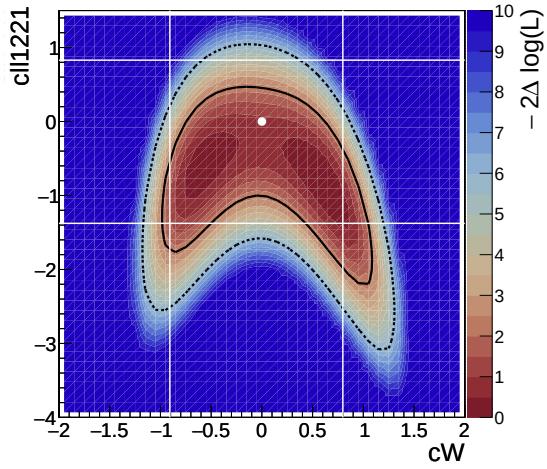

$q_W \cos\theta^*_{W_\ell}$ - Expected (Asimov)

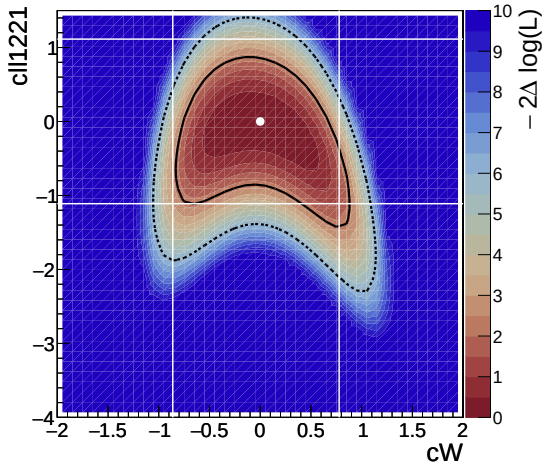

D.2 Observable: $\cos\theta^*_{Z_\ell}$

$\cos\theta^*_{Z_\ell}$ - Measured

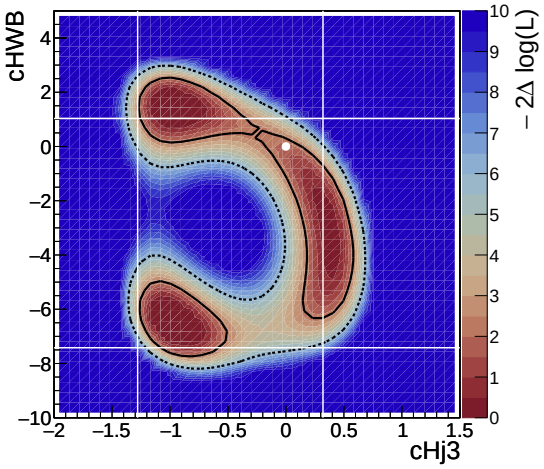

$\cos\theta^*_{Z_\ell}$ - Expected (Asimov)

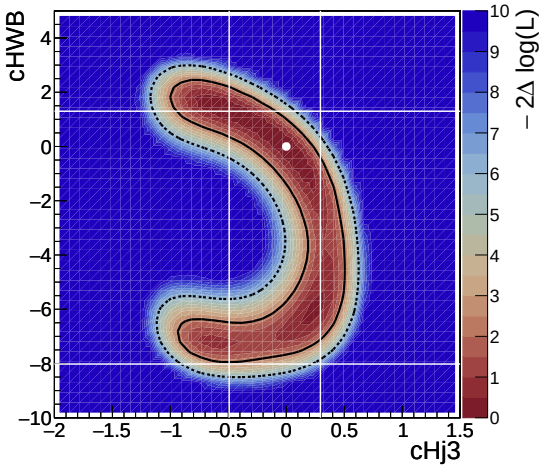

$\cos\theta^*_{Z_\ell}$ - Measured

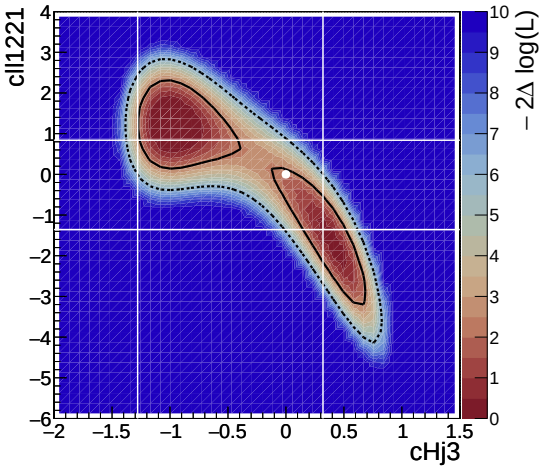

$\cos\theta^*_{Z_\ell}$ - Expected (Asimov)

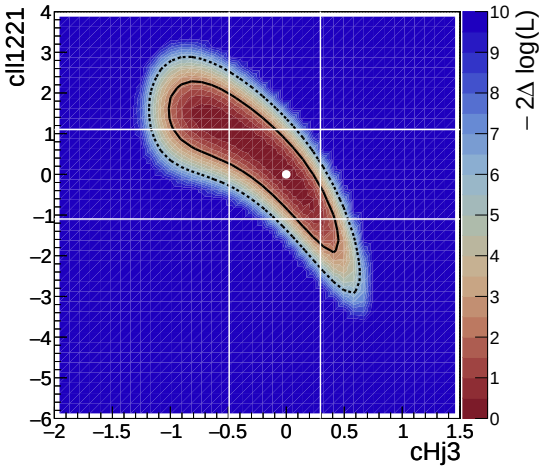

$\cos\theta^*_{Z_\ell}$ - Measured

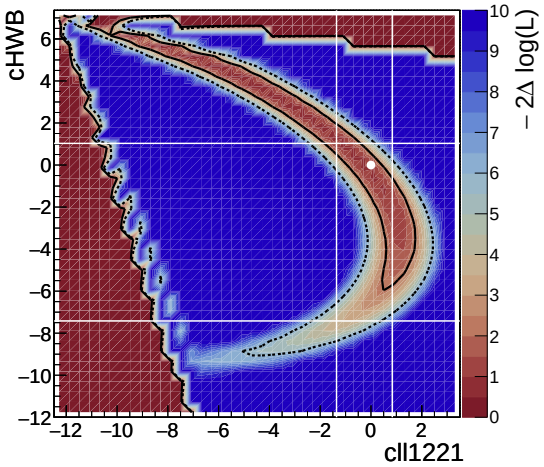

$\cos\theta^*_{Z_\ell}$ - Expected (Asimov)

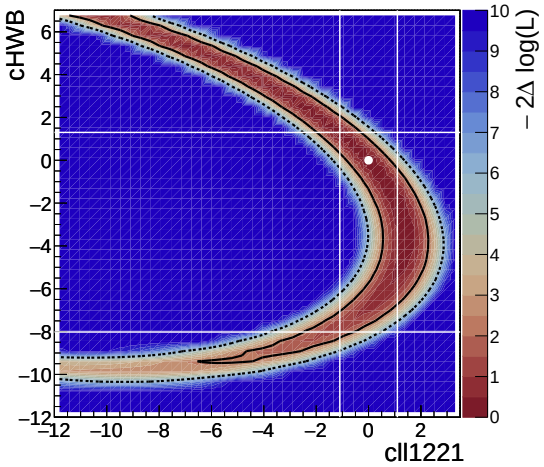

$\cos\theta^*_{Z_\ell}$ - Measured

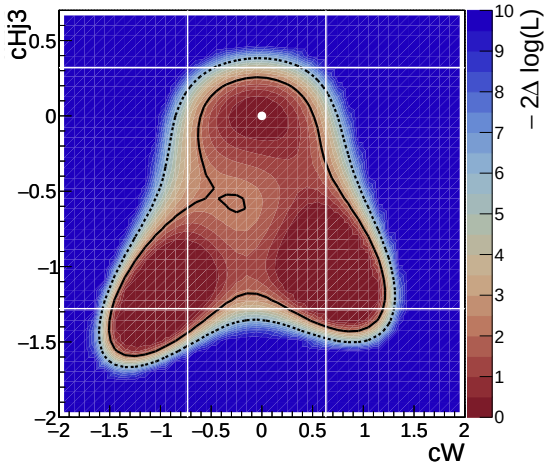

$\cos\theta^*_{Z_\ell}$ - Expected (Asimov)

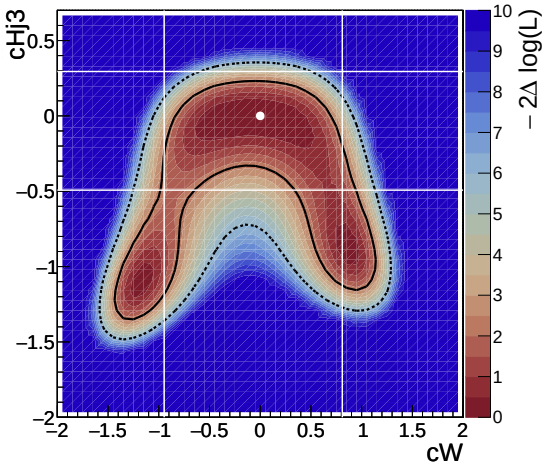

$\cos\theta^*_{Z_\ell}$ - Measured

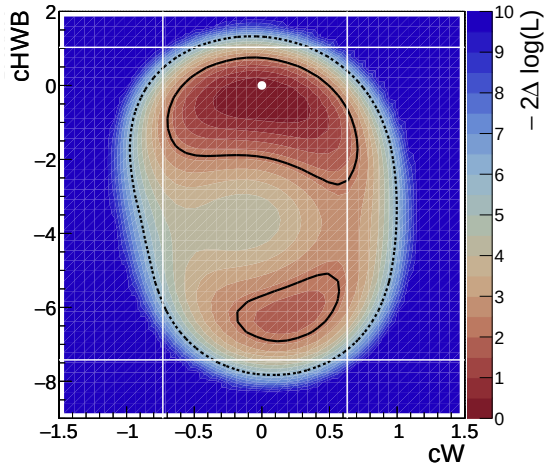

$\cos\theta^*_{Z_\ell}$ - Expected (Asimov)

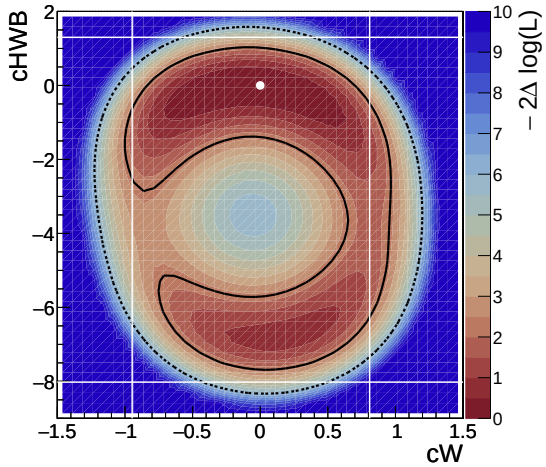

$\cos\theta^*_{Z_\ell}$ - Measured

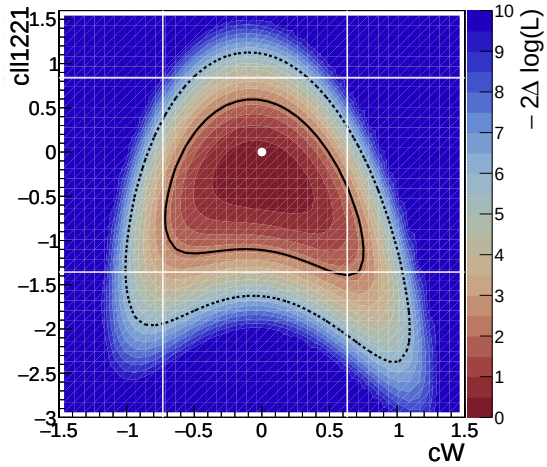

$\cos\theta^*_{Z_\ell}$ - Expected (Asimov)

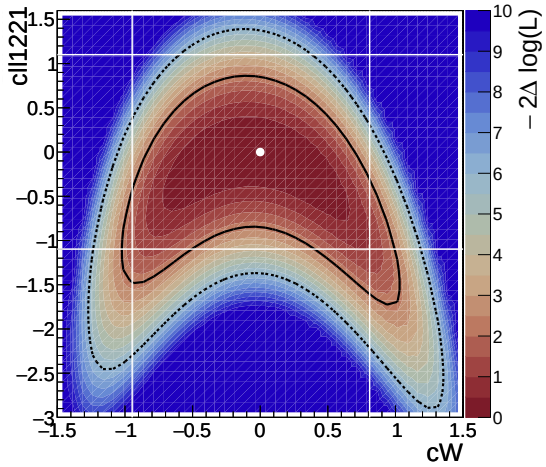

D.3 Observable: $|\cos\theta_V|$

$|\cos\theta_V|$ - Measured

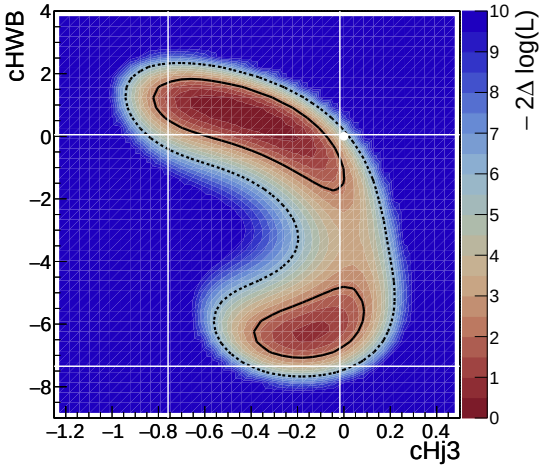

$|\cos\theta_V|$ - Expected (Asimov)

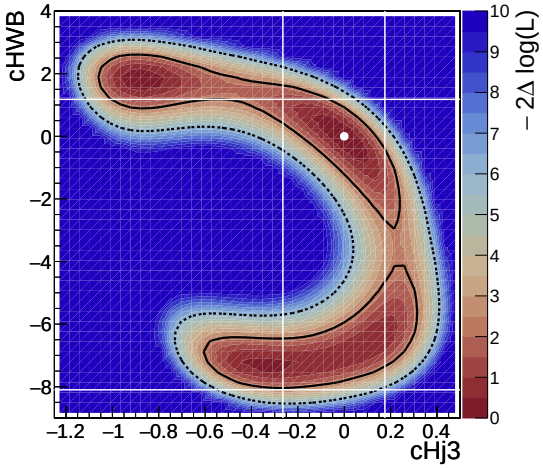

$|\cos\theta_V|$ - Measured

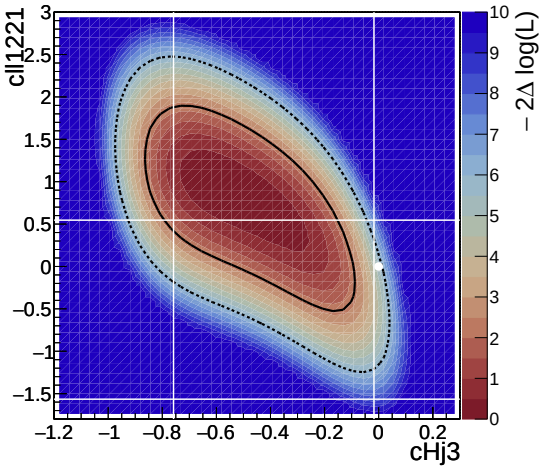

$|\cos\theta_V|$ - Expected (Asimov)

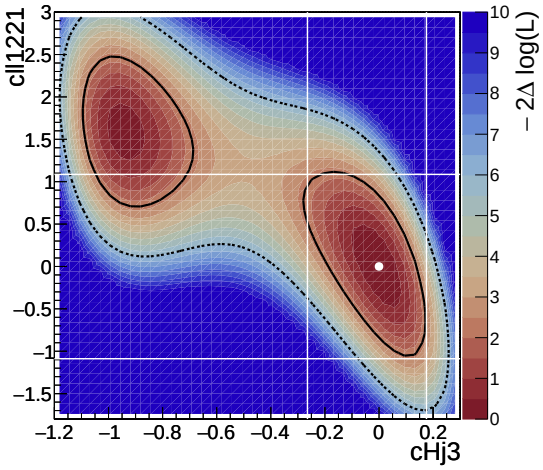

$|\cos\theta_V|$ - Measured

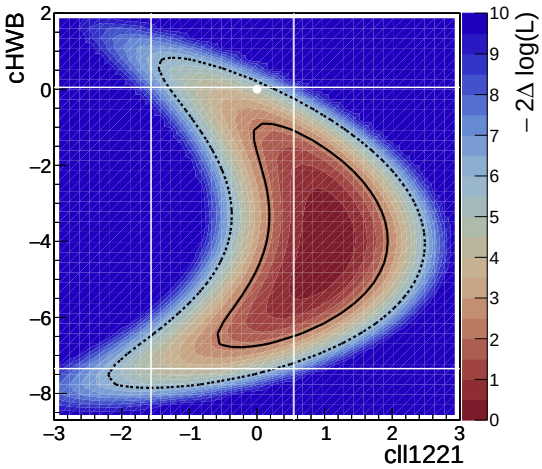

$|\cos\theta_V|$ - Expected (Asimov)

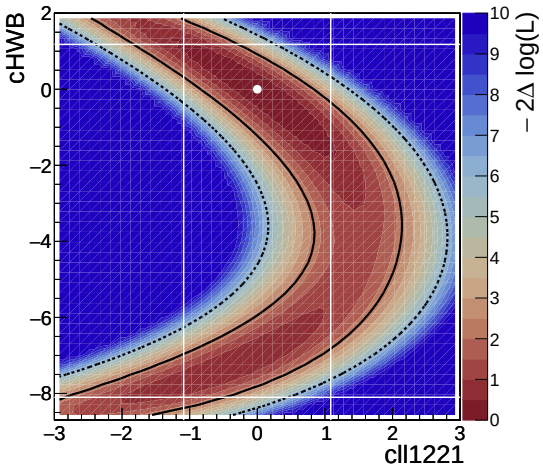

$|\cos\theta_V|$ - Measured

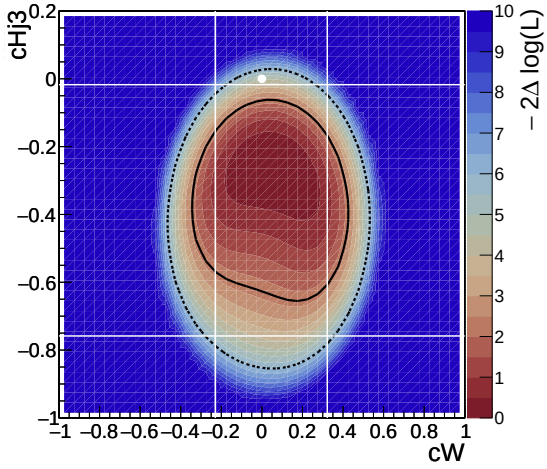

$|\cos\theta_V|$ - Expected (Asimov)

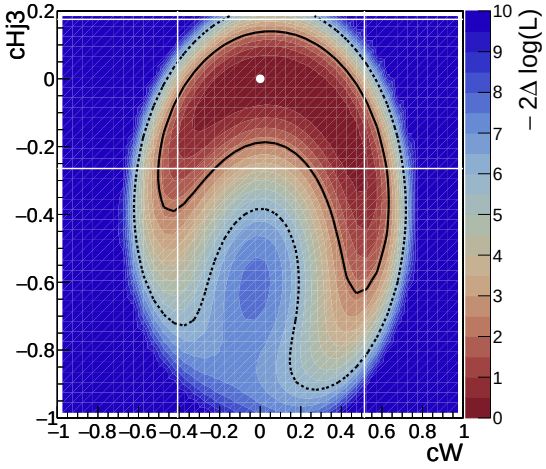

$|\cos\theta_V|$ - Measured

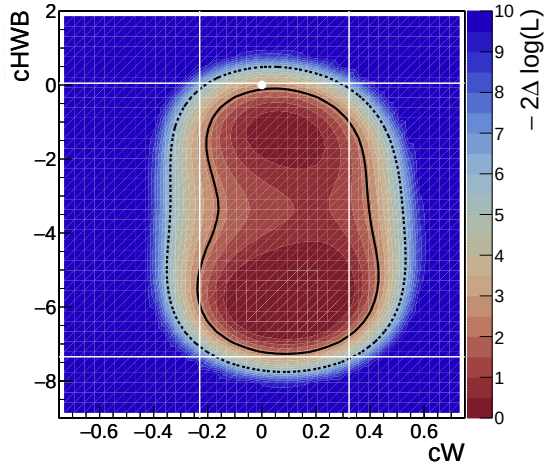

$|\cos\theta_V|$ - Expected (Asimov)

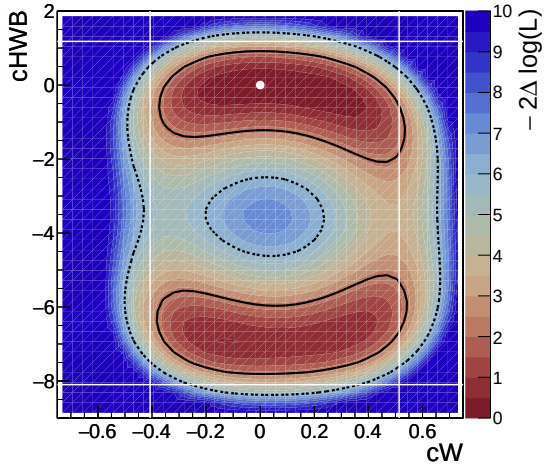

$|\cos\theta_V|$ - Measured

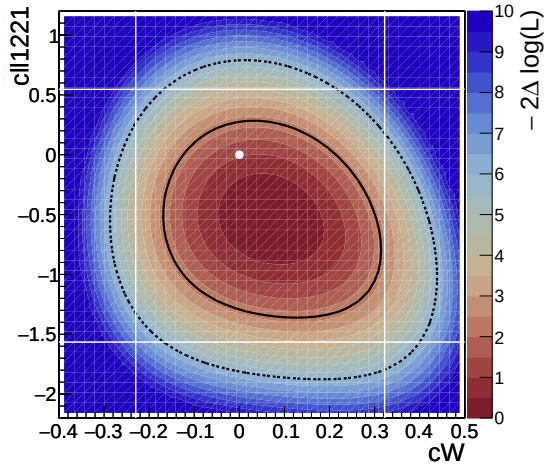

$|\cos\theta_V|$ - Expected (Asimov)

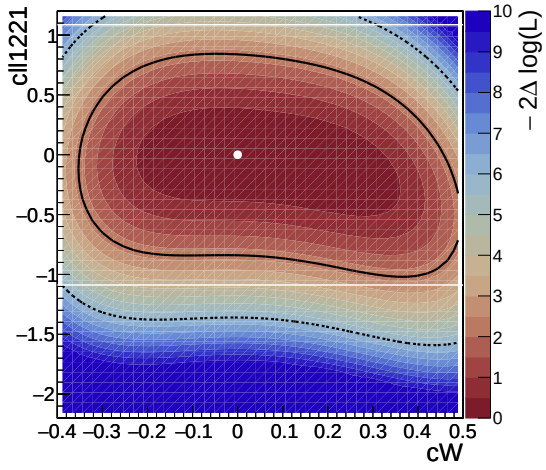

D.4 Observable: m_T^{WZ}

m_T^{WZ} - Measured

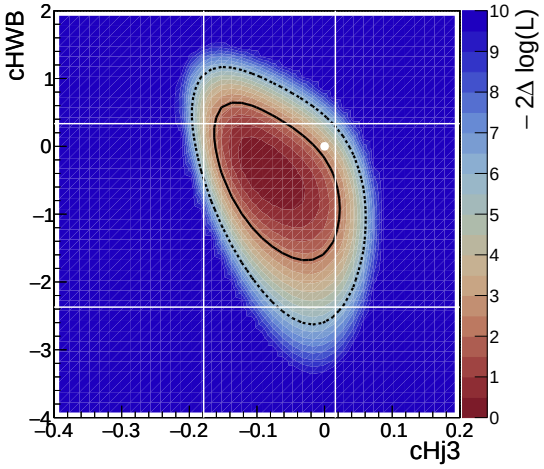

m_T^{WZ} - Expected (Asimov)

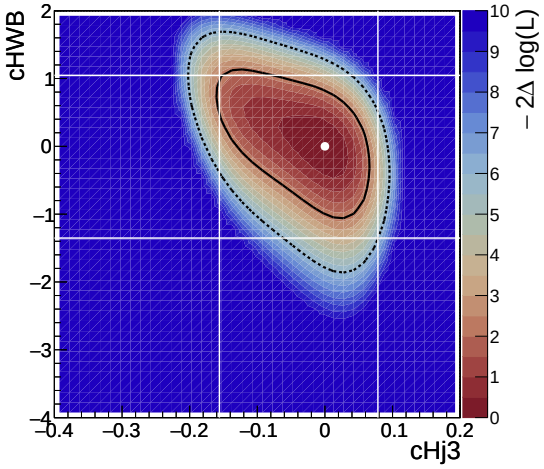

m_T^{WZ} - Measured

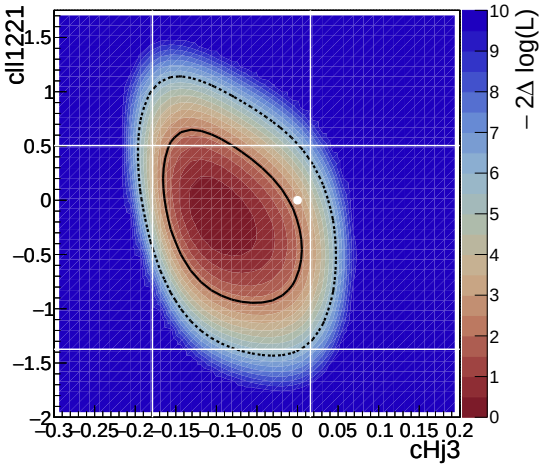

m_T^{WZ} - Expected (Asimov)

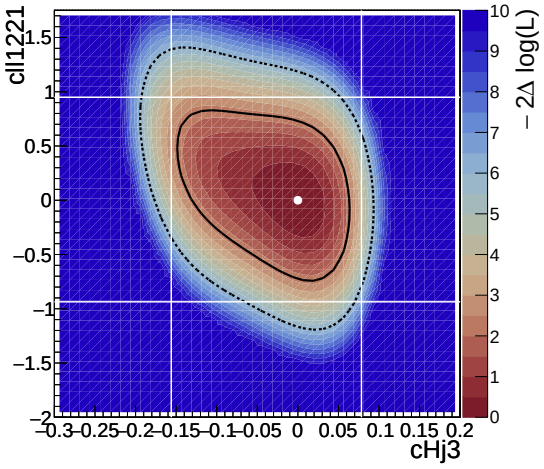

m_T^{WZ} - Measured

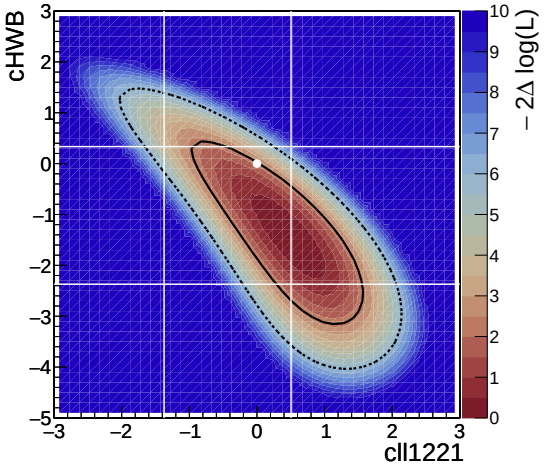

m_T^{WZ} - Expected (Asimov)

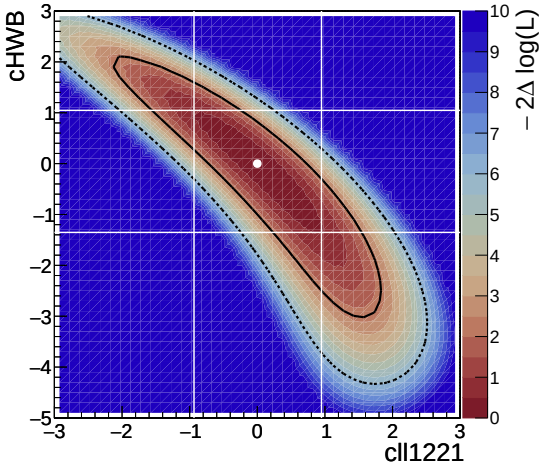

m_T^{WZ} - Measured

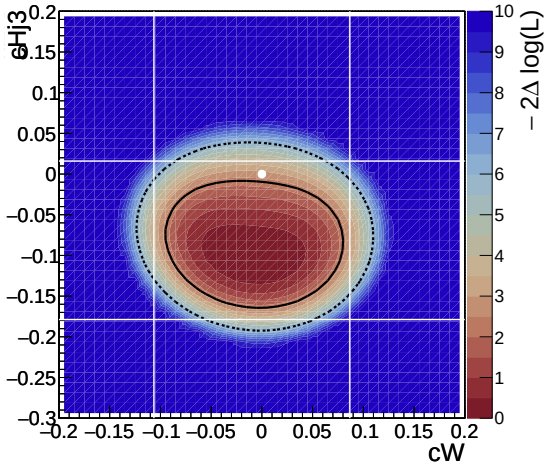

m_T^{WZ} - Expected (Asimov)

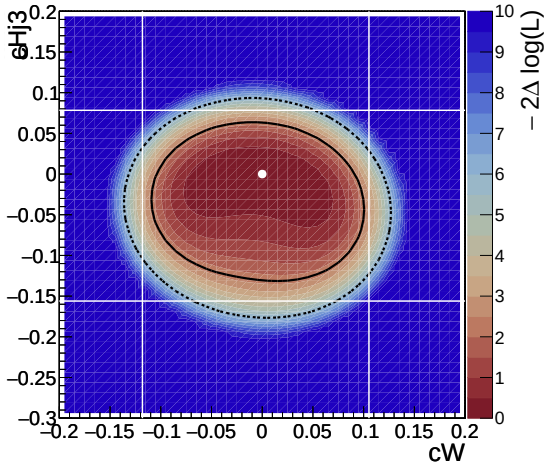

m_T^{WZ} - Measured

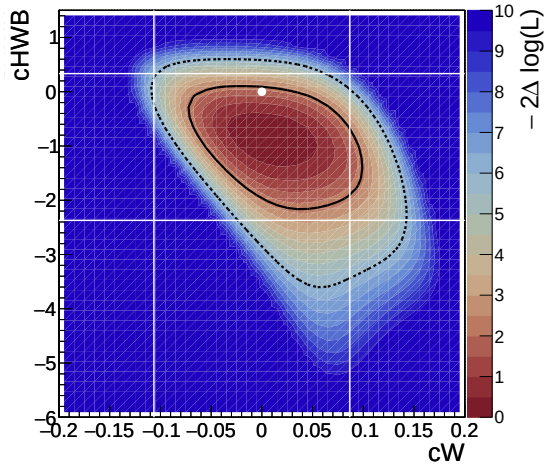

m_T^{WZ} - Expected (Asimov)

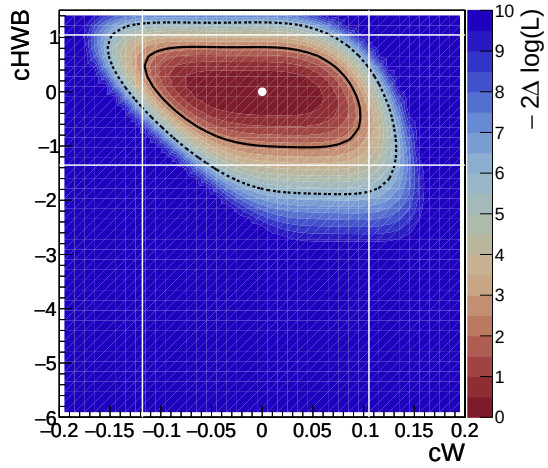

m_T^{WZ} - Measured

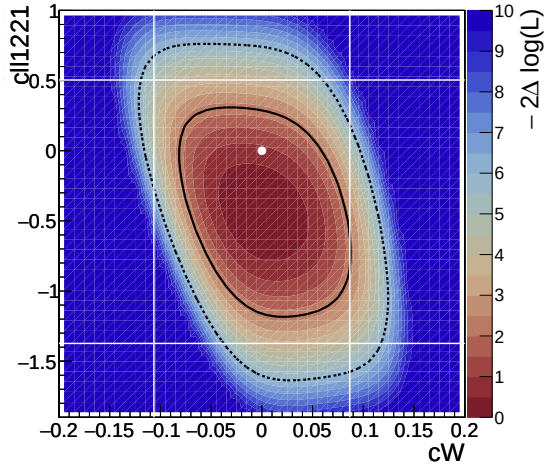

m_T^{WZ} - Expected (Asimov)

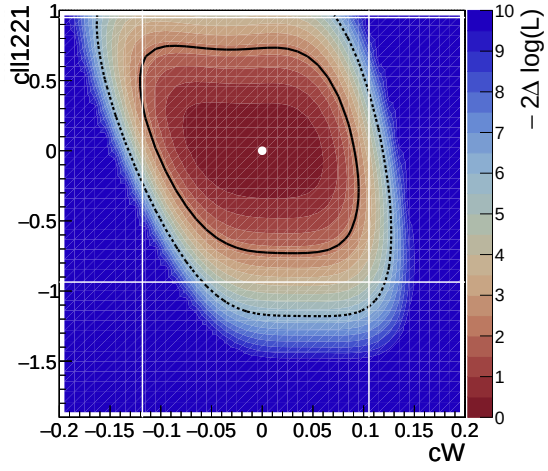

D.5 Observable: ϕ_{W_l}

$\phi^*_{W_\ell}$ - Measured

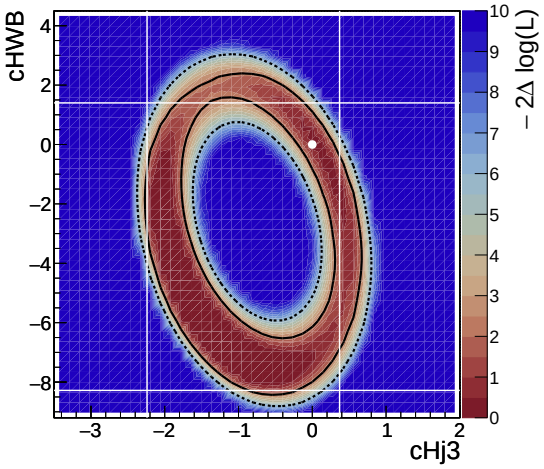

$\phi^*_{W_\ell}$ - Expected (Asimov)

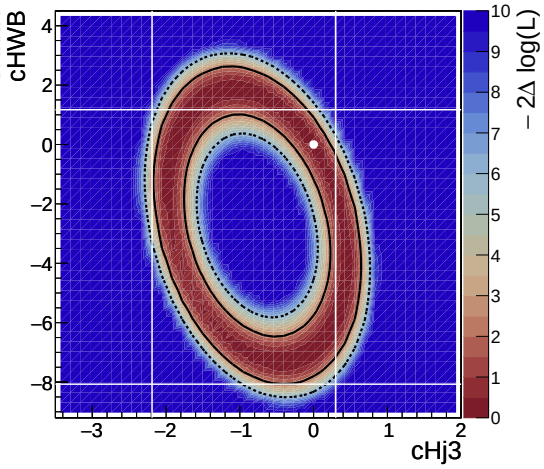

$\phi^*_{W_\ell}$ - Measured

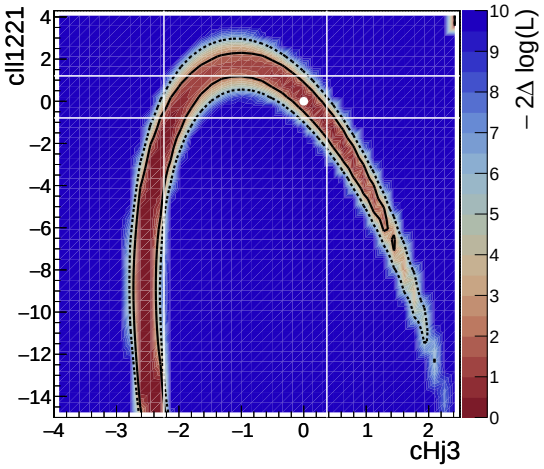

$\phi^*_{W_\ell}$ - Expected (Asimov)

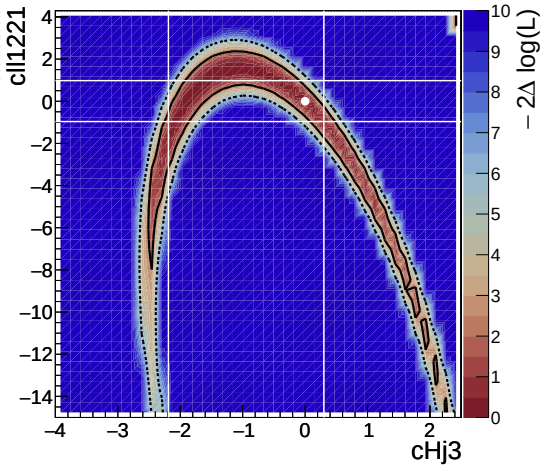

$\phi^*_{W_\ell}$ - Measured

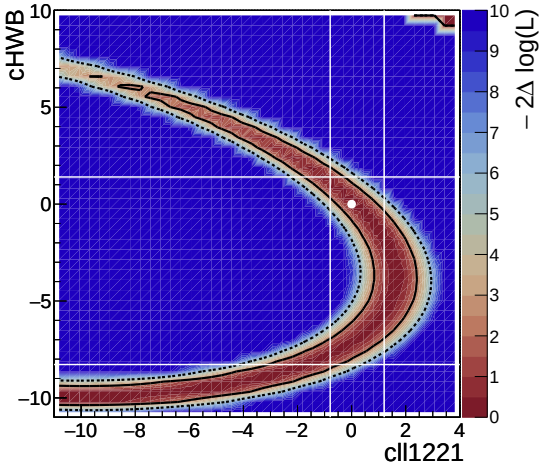

$\phi^*_{W_\ell}$ - Expected (Asimov)

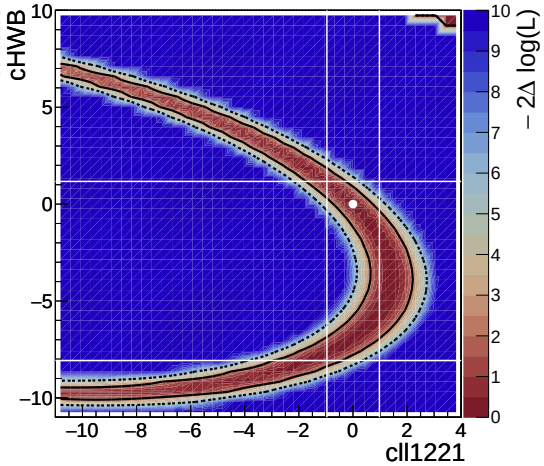

$\phi^*_{W_\ell}$ - Measured

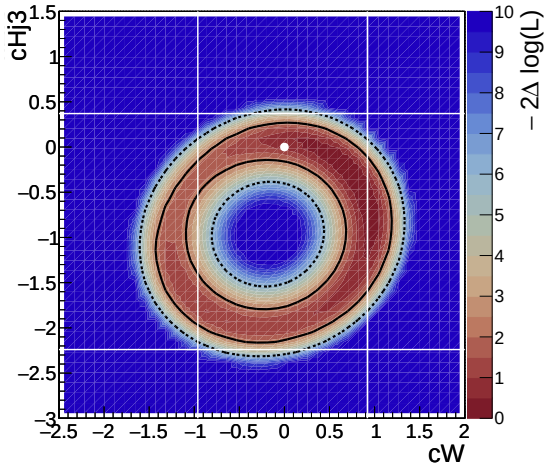

$\phi^*_{W_\ell}$ - Expected (Asimov)

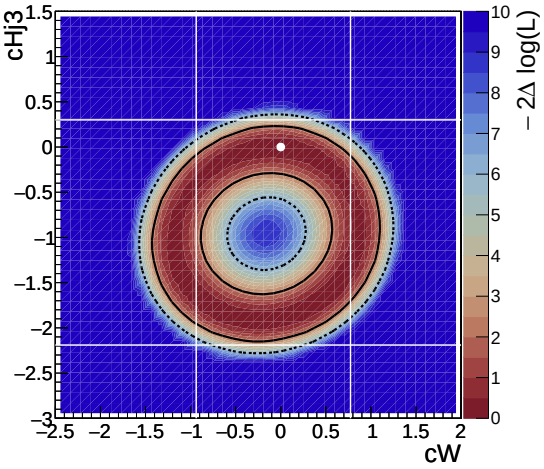

$\phi^*_{W_\ell}$ - Measured

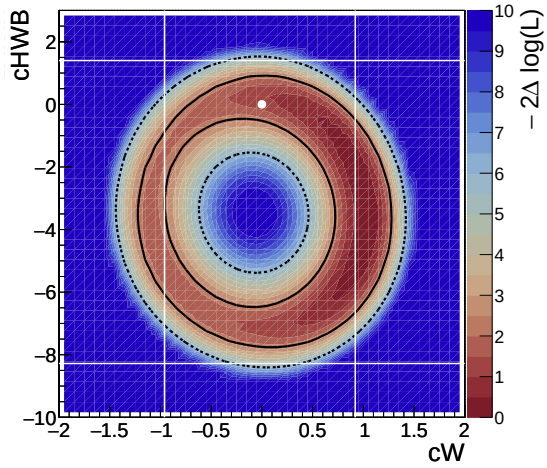

$\phi^*_{W_\ell}$ - Expected (Asimov)

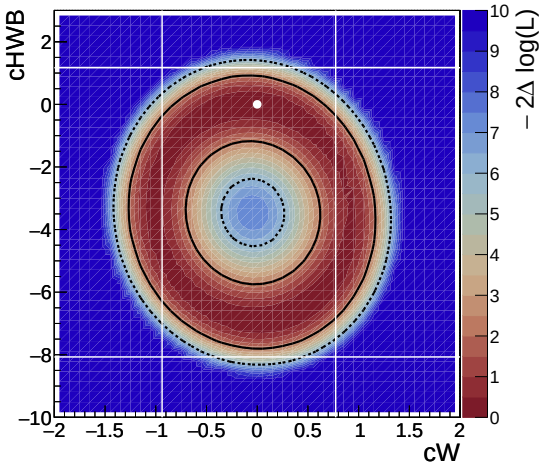

$\phi^*_{W_\ell}$ - Measured

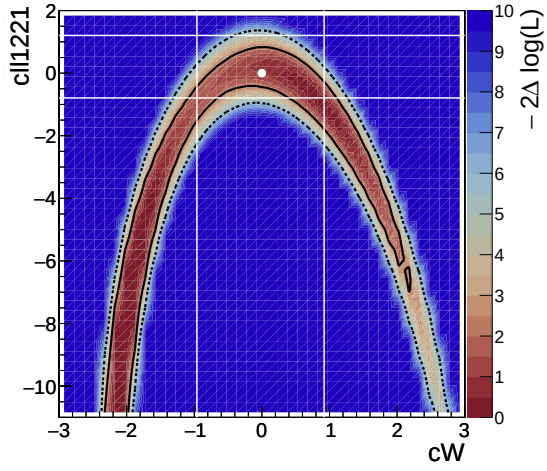

$\phi^*_{W_\ell}$ - Expected (Asimov)

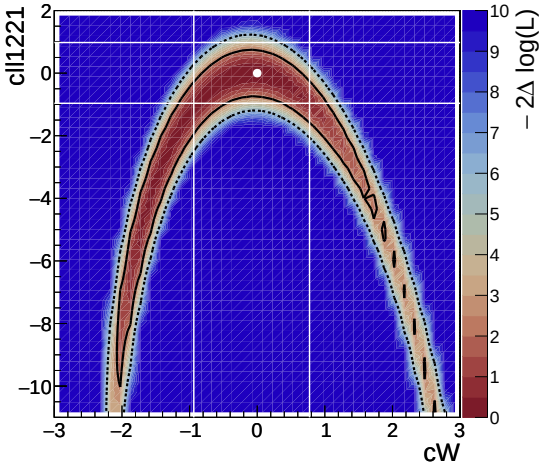

D.6 Observable: ϕ_{Z_l}

$\phi^*_{Z_\ell}$ - Measured

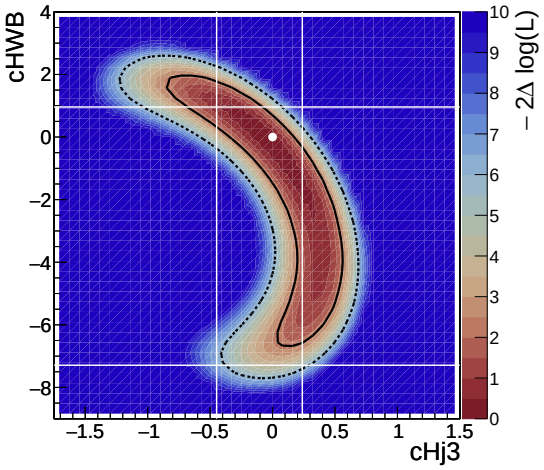

$\phi^*_{Z_\ell}$ - Expected (Asimov)

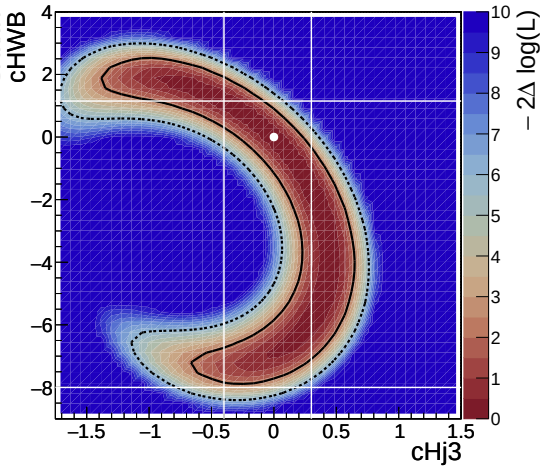

$\phi^*_{Z_\ell}$ - Measured

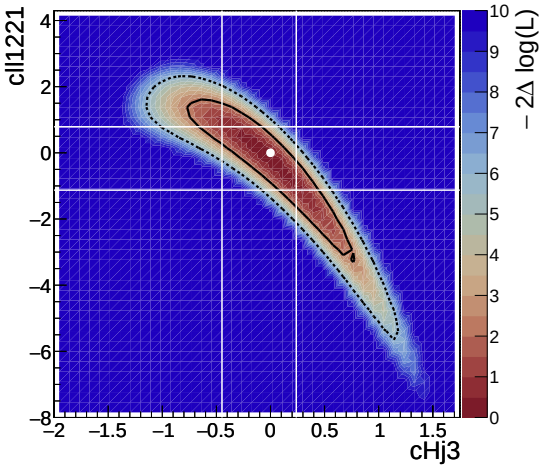

$\phi^*_{Z_\ell}$ - Expected (Asimov)

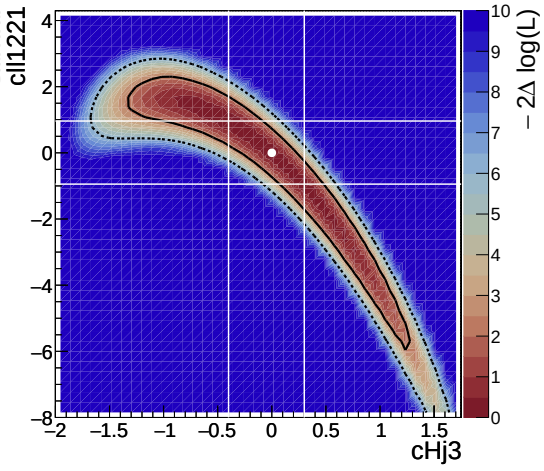

$\phi^*_{Z_\ell}$ - Measured

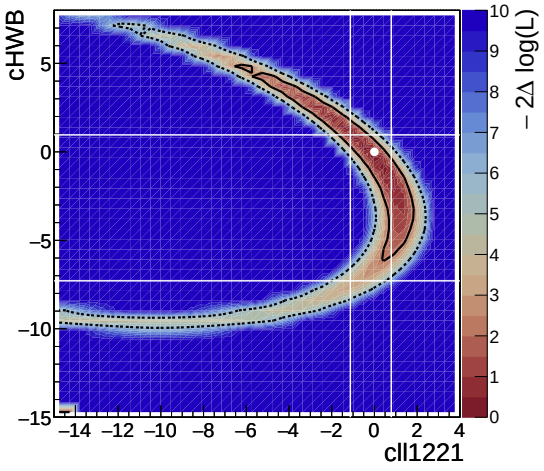

$\phi^*_{Z_\ell}$ - Expected (Asimov)

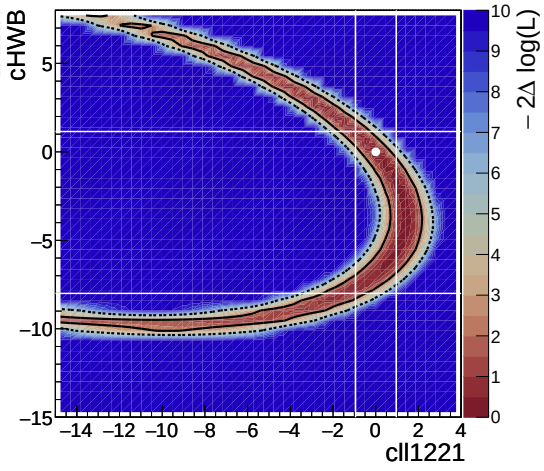

$\phi^*_{Z_\ell}$ - Measured

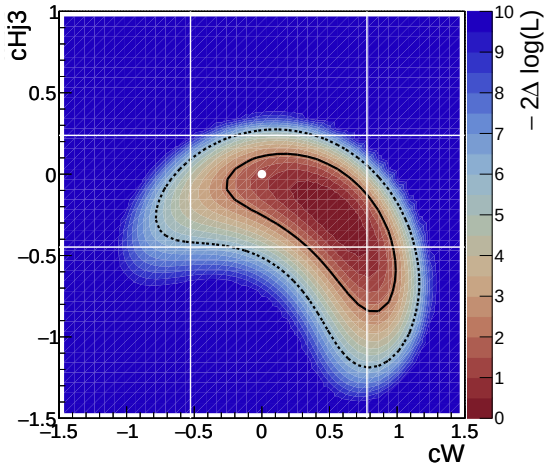

$\phi^*_{Z_\ell}$ - Expected (Asimov)

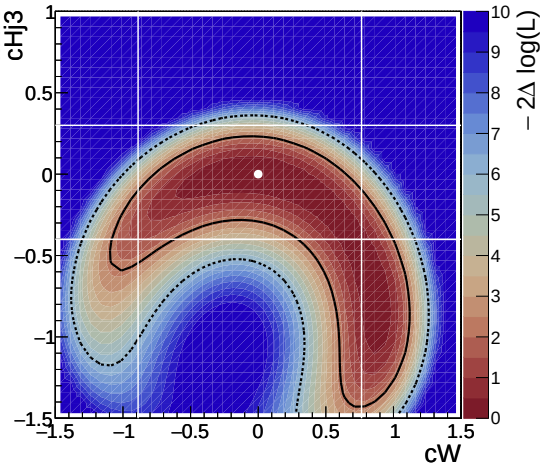

$\phi^*_{Z_\ell}$ - Measured

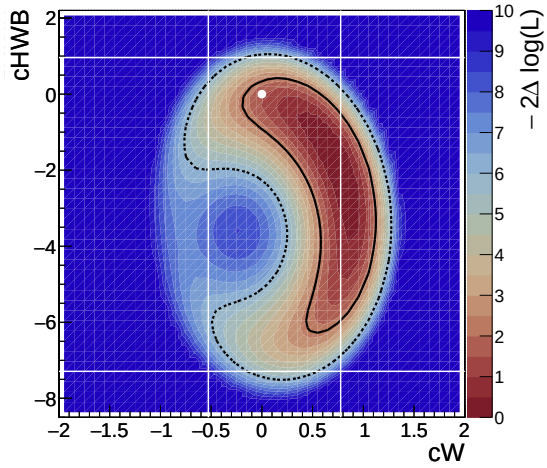

$\phi^*_{Z_\ell}$ - Expected (Asimov)

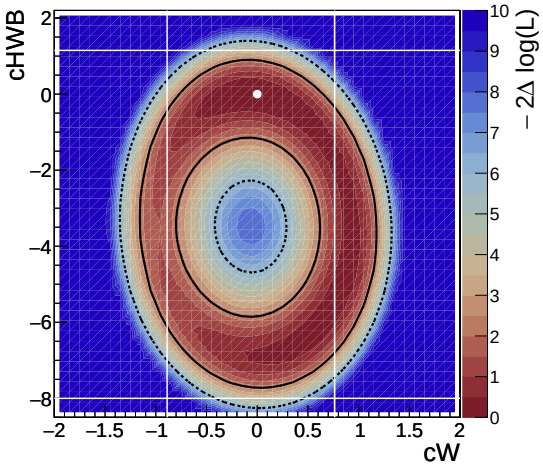

$\phi^*_{Z_\ell}$ - Measured

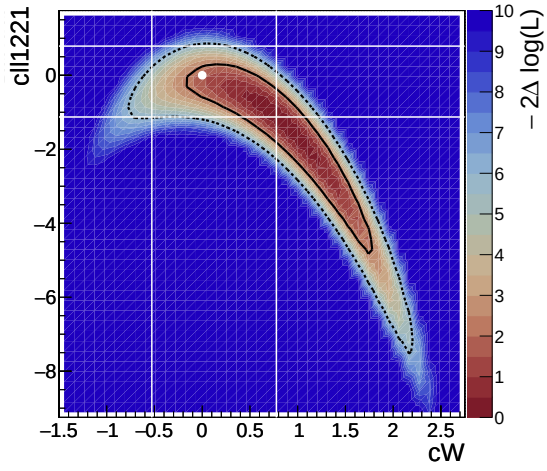

$\phi^*_{Z_\ell}$ - Expected (Asimov)

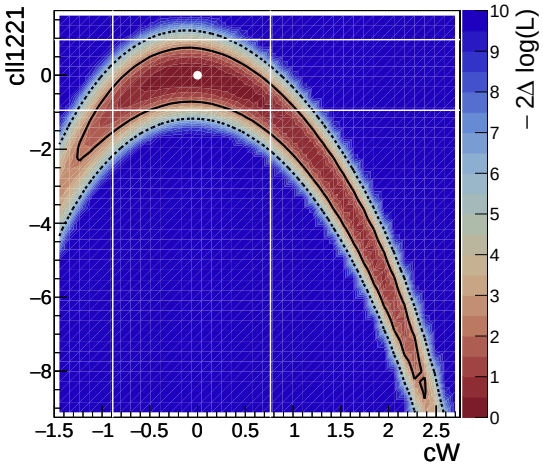

APPENDIX E

Pull plots for measured and expected fits

A pull plot is a diagnostic tool used to evaluate the behaviour of nuisance parameters. The pull plot provides insight into whether these parameters behave as expected and helps identify biases or systematic deviations in the fit.

Mathematically, the pull of a nuisance parameter θ_i is defined as:

$$P_i = \frac{\hat{\theta}_i - \theta_i^{\text{nominal}}}{\sigma_i} \tag{E.1}$$

where:

- $\hat{\theta}_i$ is the best-fit value of the nuisance parameter obtained from the fit.
- $\theta_i^{\text{nominal}}$ is the expected or prior value of the parameter (e.g., from theoretical predictions or external constraints).
- σ_i is the estimated uncertainty (standard deviation) of $\hat{\theta}_i$, obtained from the fit's covariance matrix.

A pull plot displays the values of P_i for multiple nuisance parameters. Ideally, the pull values should be centred around zero with a standard deviation of one.

Pull plots for a selection of 1D and 2D fits are presented in this Appendix. Plots that show a larger pull on the nuisance parameters are presented.

The following nuisance parameters are used in all fits, and further information on them can be found in Section 6.4:

- The PDF uncertainty called `diboson_pdf`
- The QCD scale uncertainty called `wz_scale`
- The EWK correction uncertainty called `wz_ew_correction`

Additionally, if the EFT MC prediction has small sample size in a particular bin, i.e. the relative error on that bin is $> 20\%$, then another nuisance parameter `mcstat_*` is added for that bin.

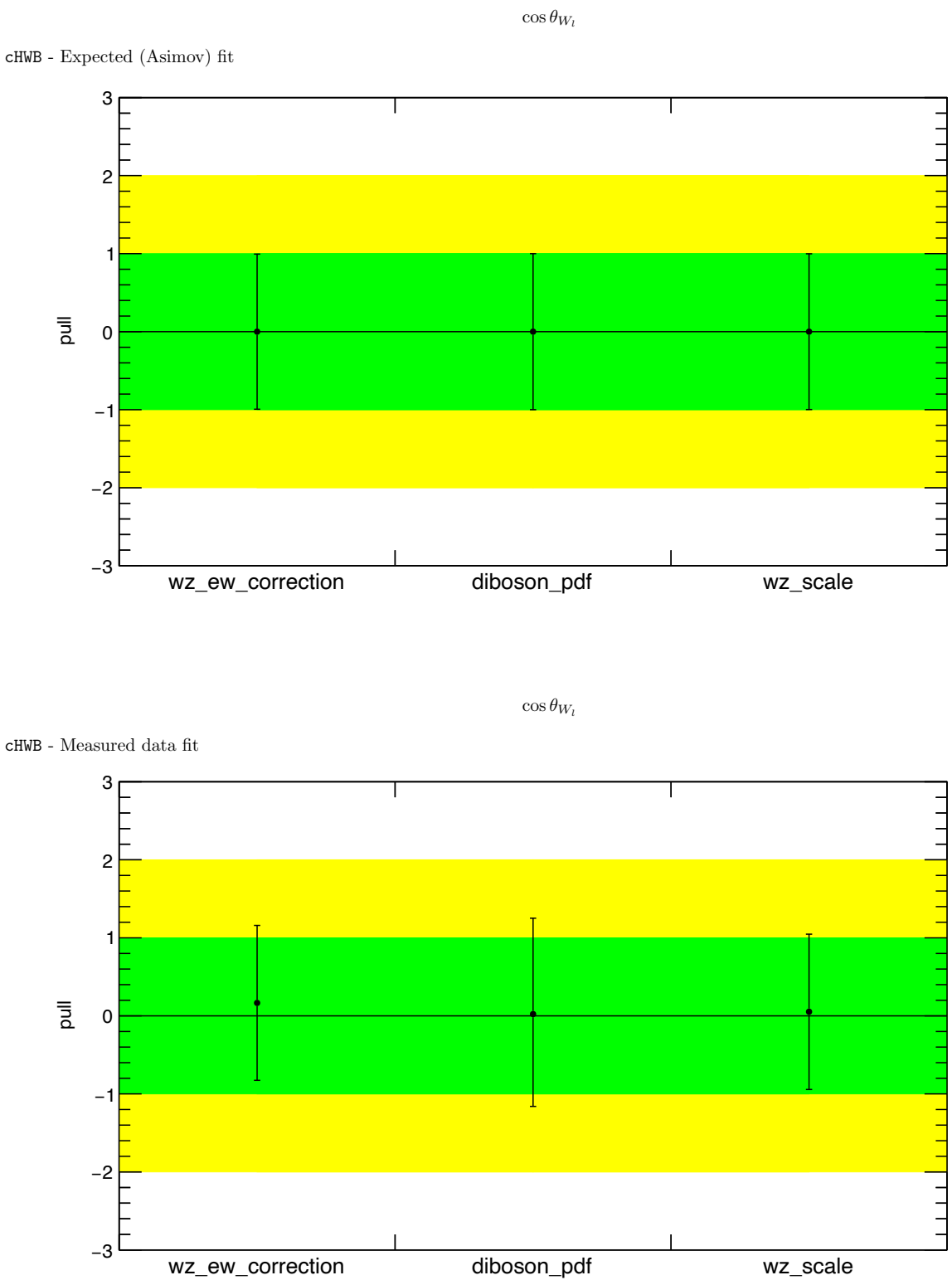

Figure E.1: *Pull plots of 1D fits for cHWB using the* $\cos\theta^*_{W_\ell}$ *observable. Both Expected pulls (upper panel) and Measured pulls (lower panel) are shown.*

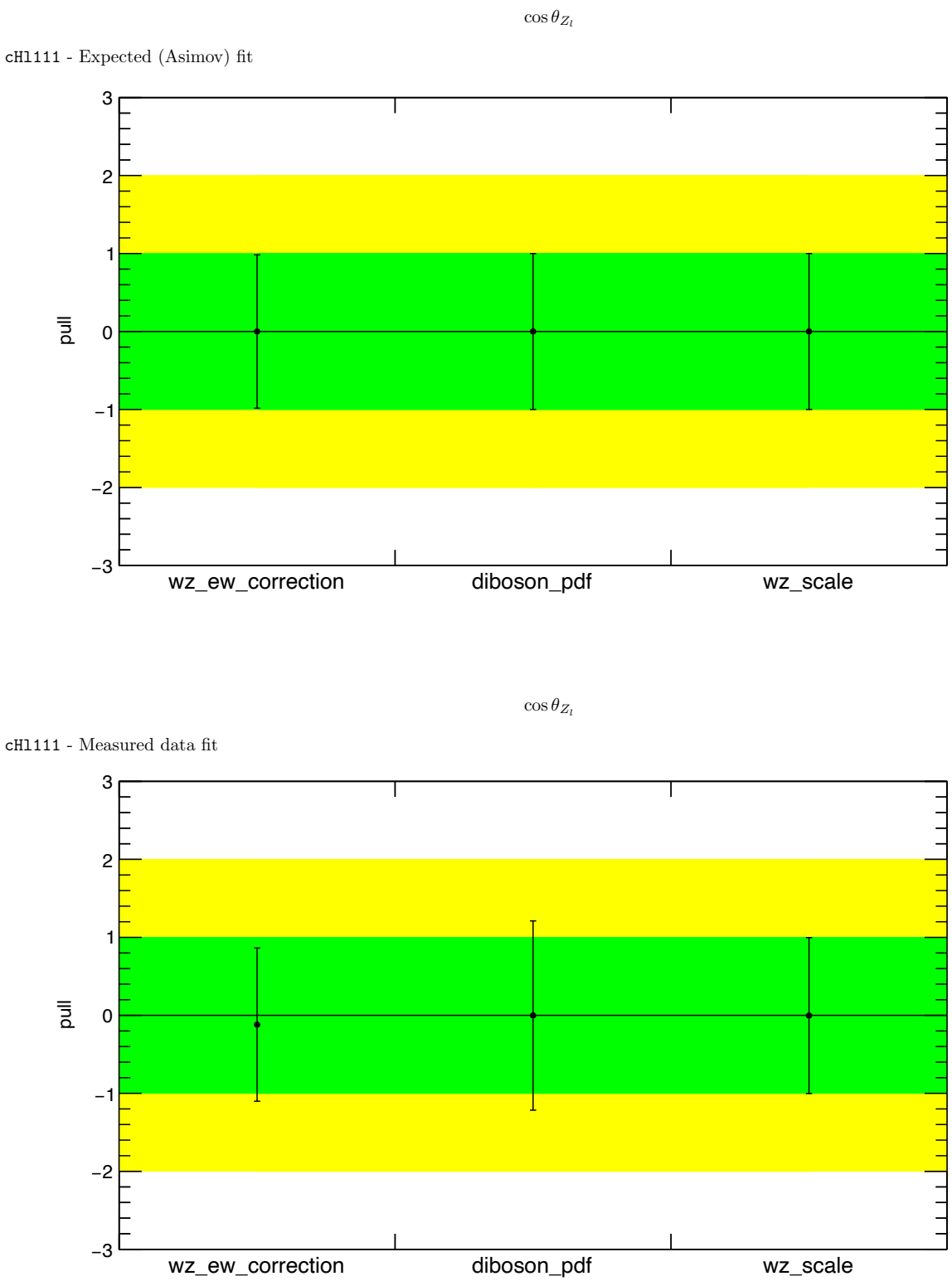

Figure E.2: *Pull plots of 1D fits for* `cHl111` *using the* $\cos\theta^*_{Z_\ell}$ *observable. Both Expected pulls (upper panel) and Measured pulls (lower panel) are shown.*

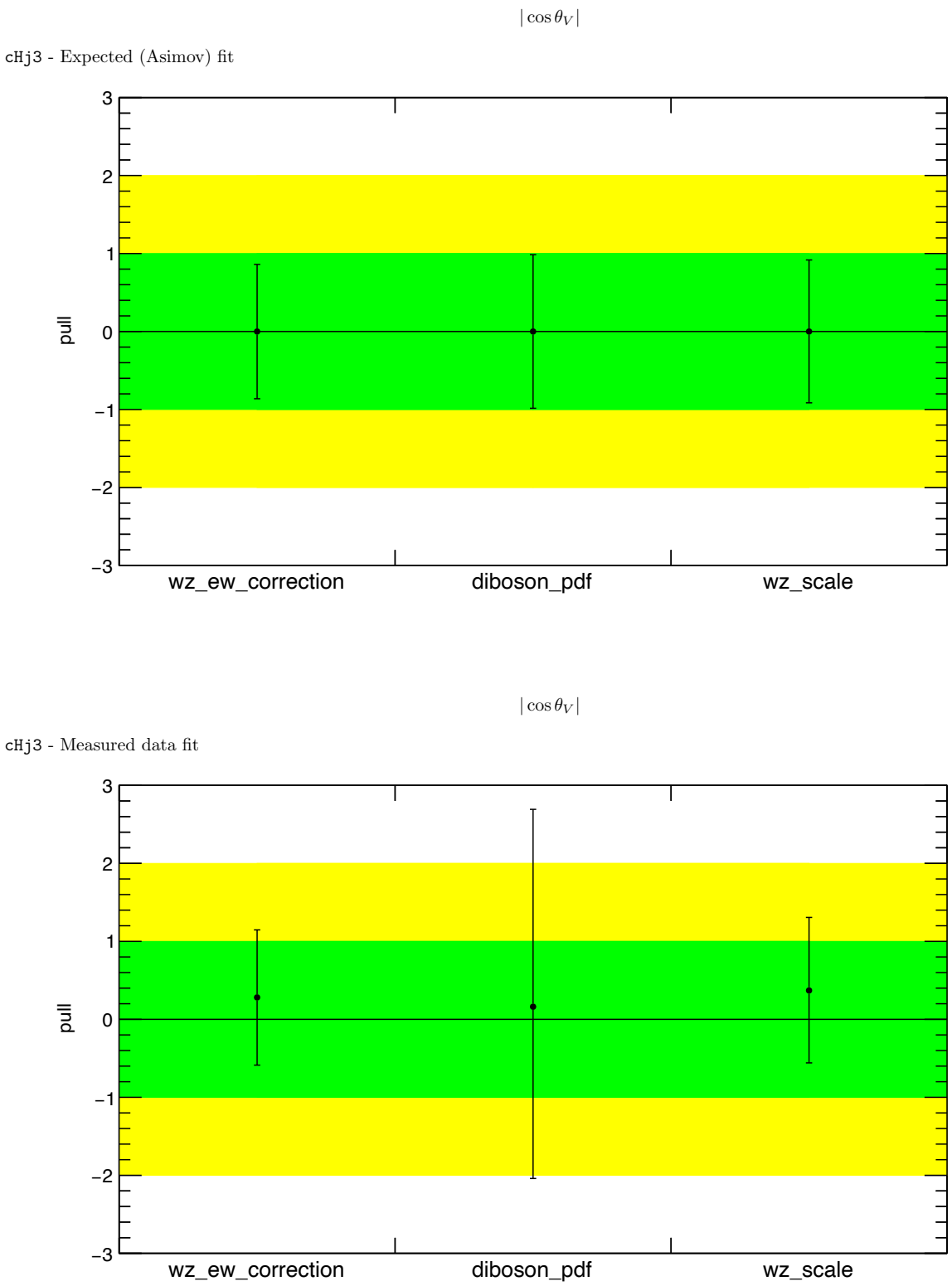

Figure E.3: *Pull plots of 1D fits for* `cHj3` *using the* $|\cos\theta_V|$ *observable. Both Expected pulls (upper panel) and Measured pulls (lower panel) are shown.*

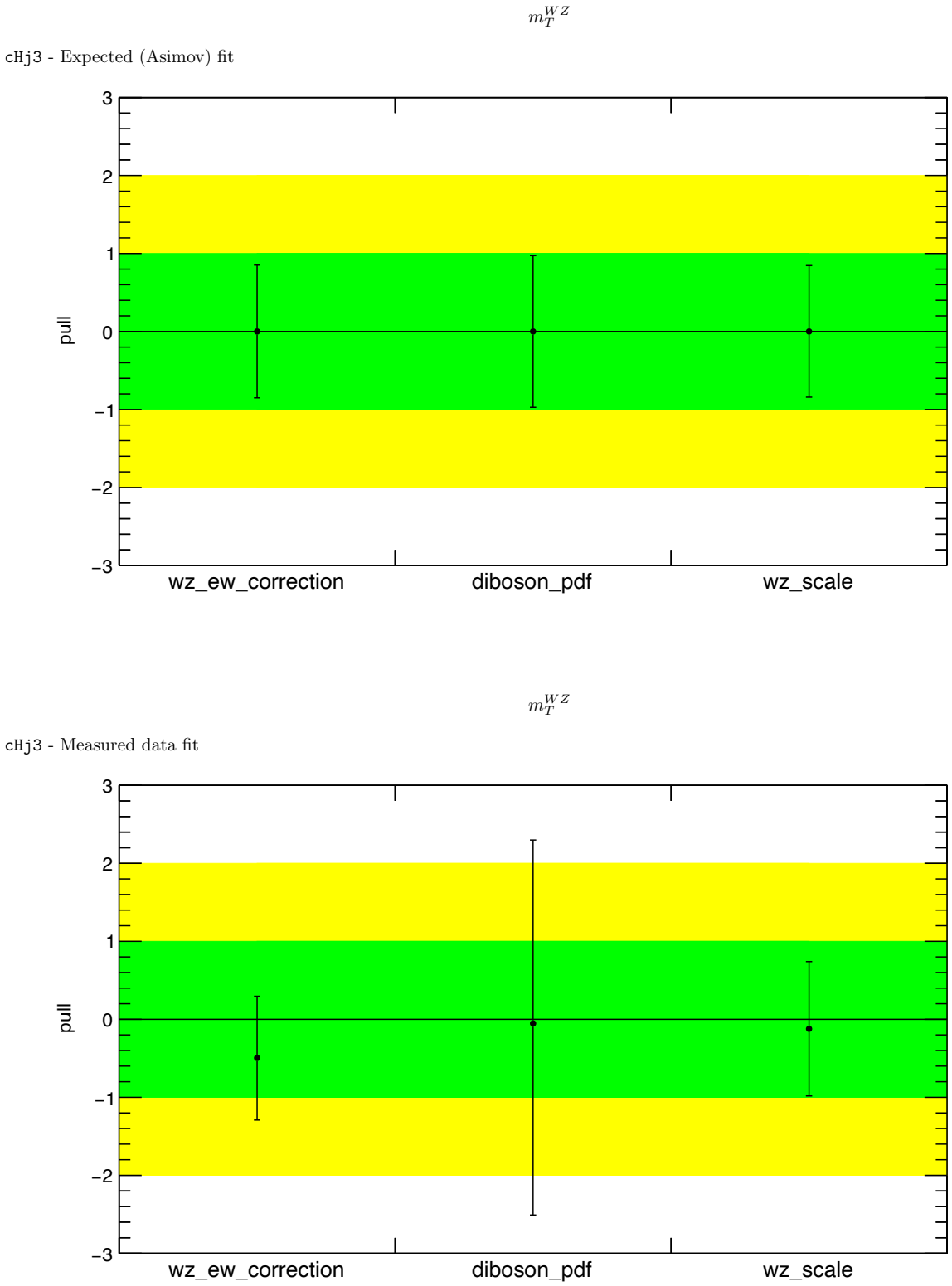

Figure E.4: *Pull plots of 1D fits for* `cHj3` *using the* m_T^{WZ} *observable. Both Expected pulls (upper panel) and Measured pulls (lower panel) are shown.*

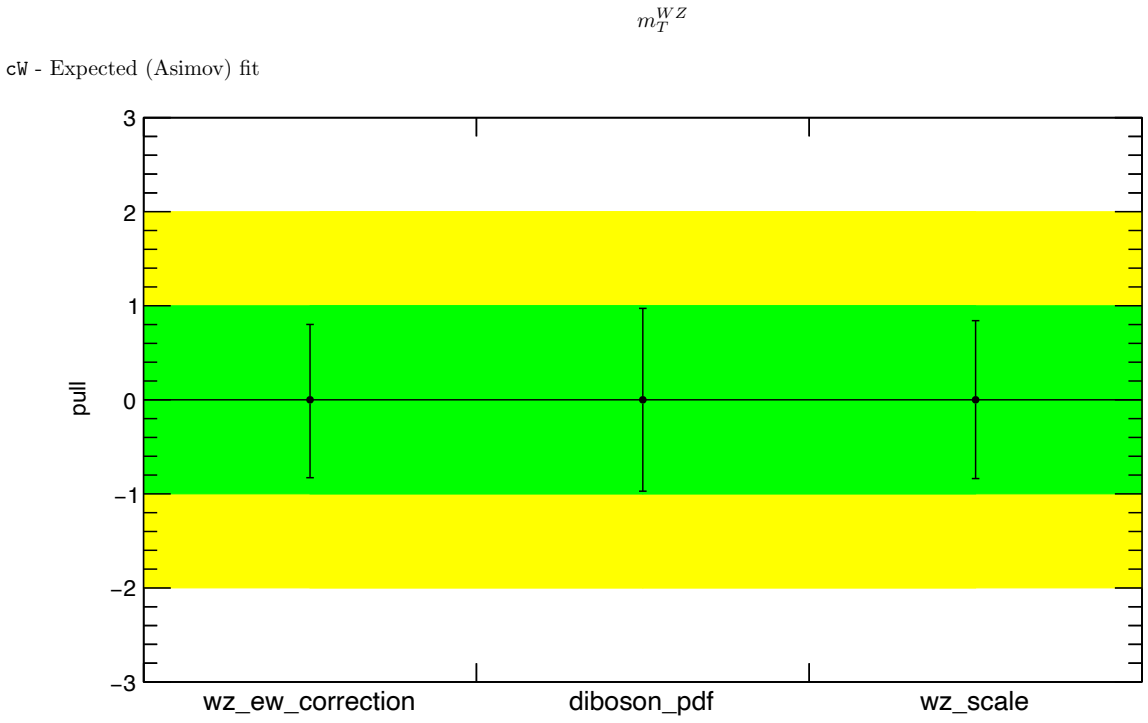

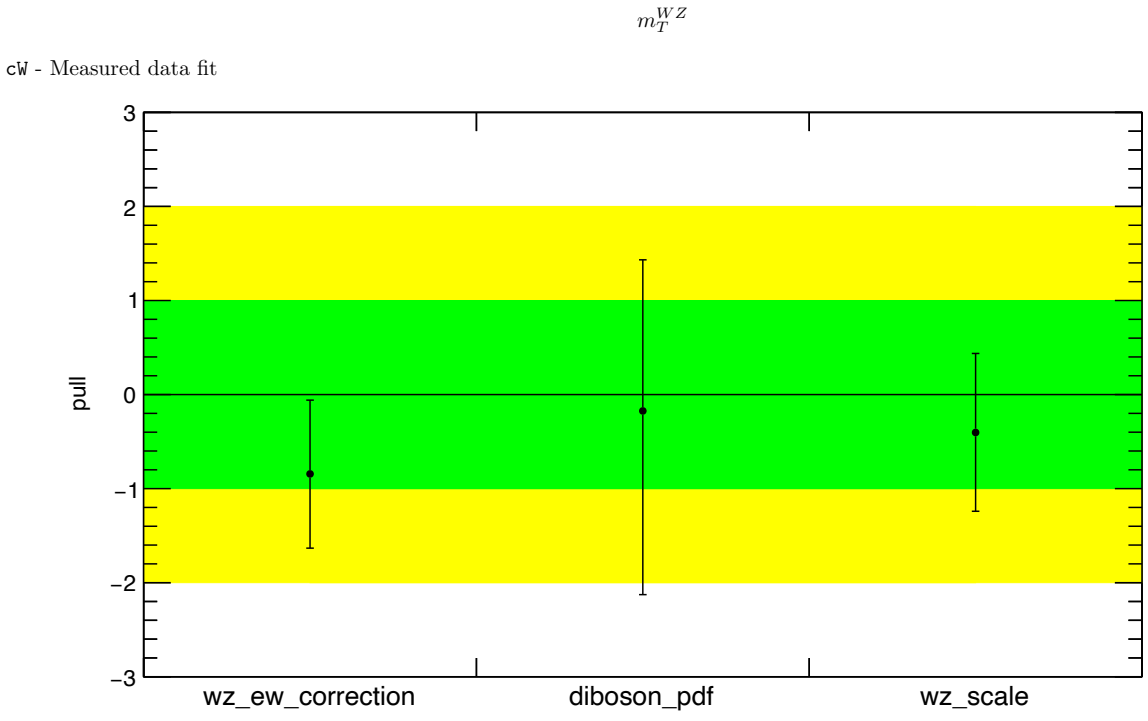

Figure E.5: *Pull plots of 1D fits for* `cW` *using the* m_T^{WZ} *observable. Both Expected pulls (upper panel) and Measured pulls (lower panel) are shown.*

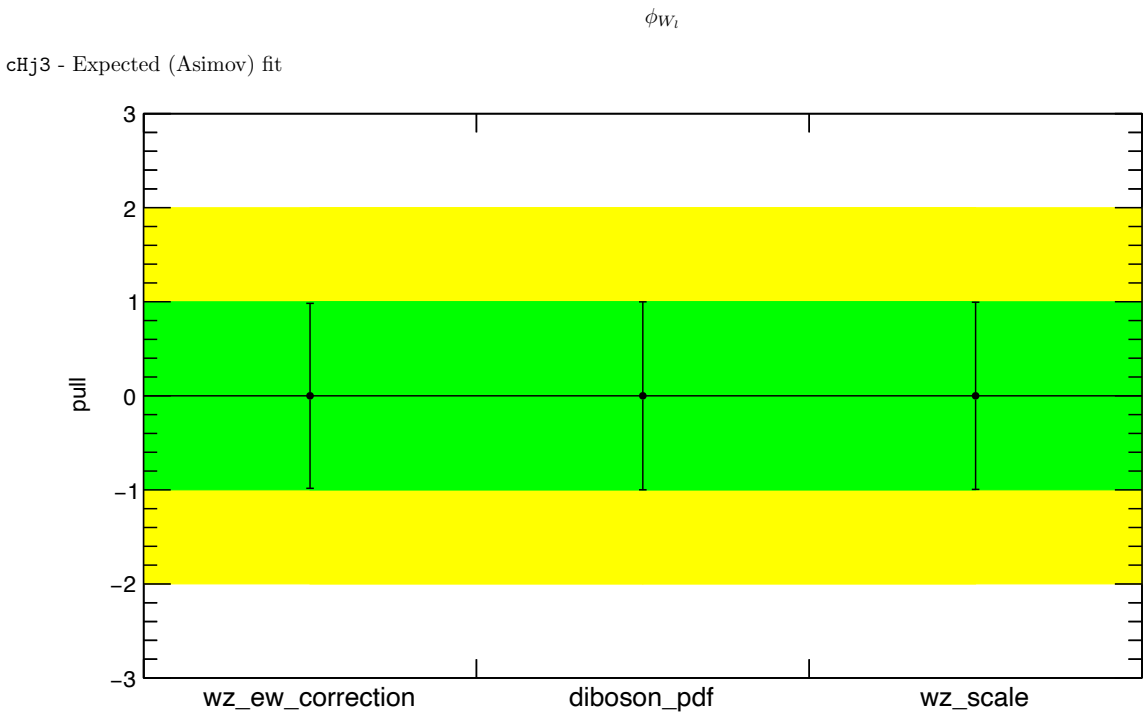

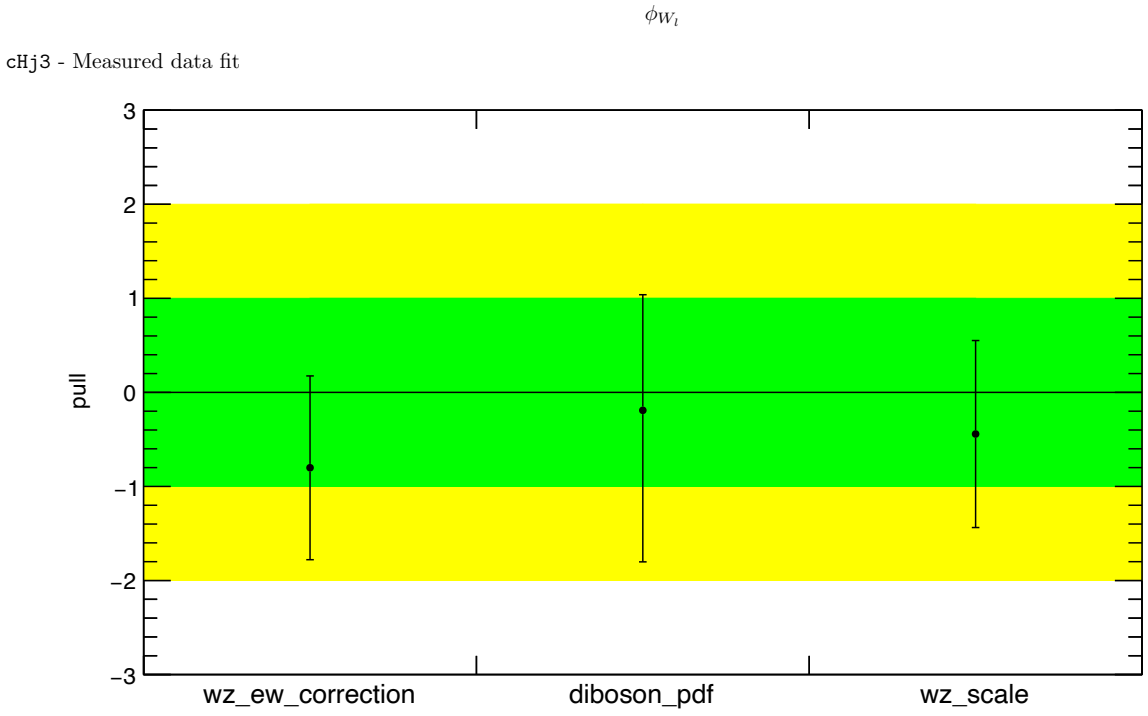

Figure E.6: *Pull plots of 1D fits for* `cHj3` *using the* ϕ_{W_l} *observable. Both Expected pulls (upper panel) and Measured pulls (lower panel) are shown.*

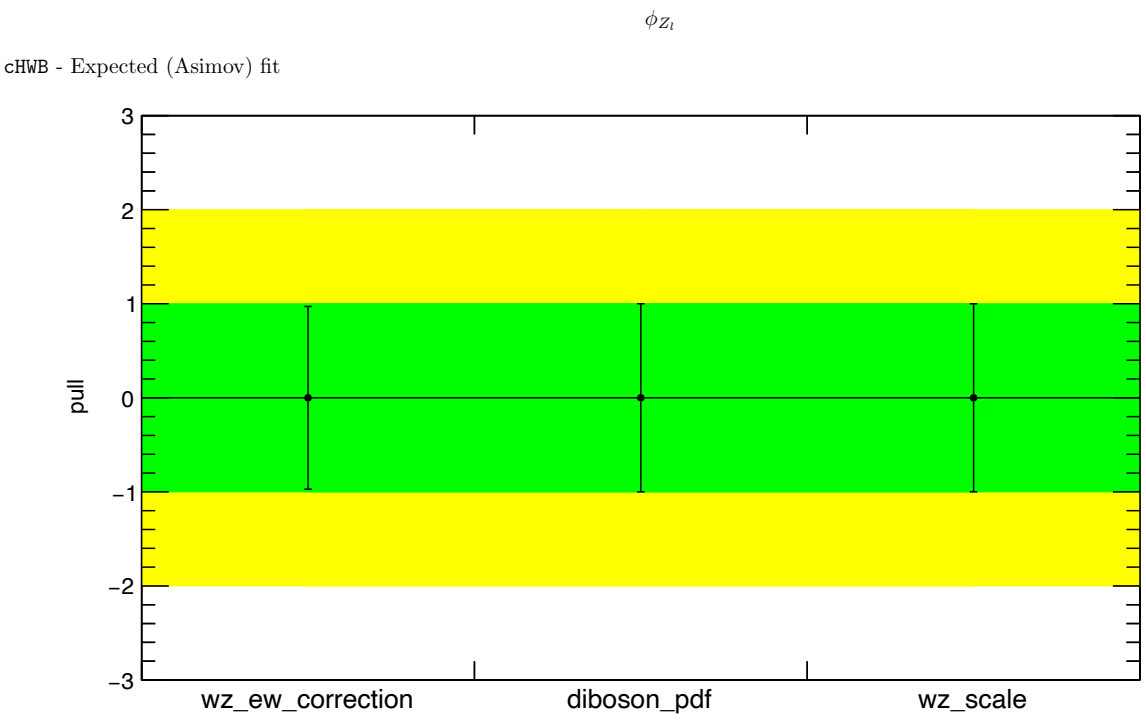

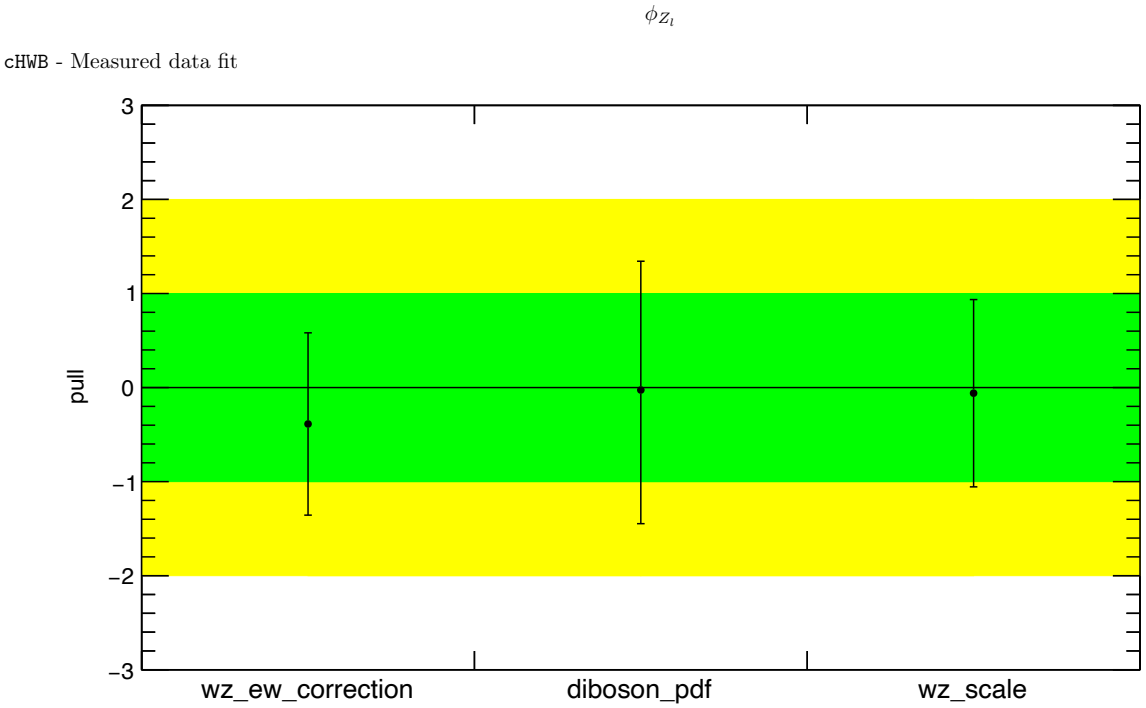

Figure E.7: *Pull plots of 1D fits for cHWB using the $\phi^*_{Z_\ell}$ observable. Both Expected pulls (upper panel) and Measured pulls (lower panel) are shown.*

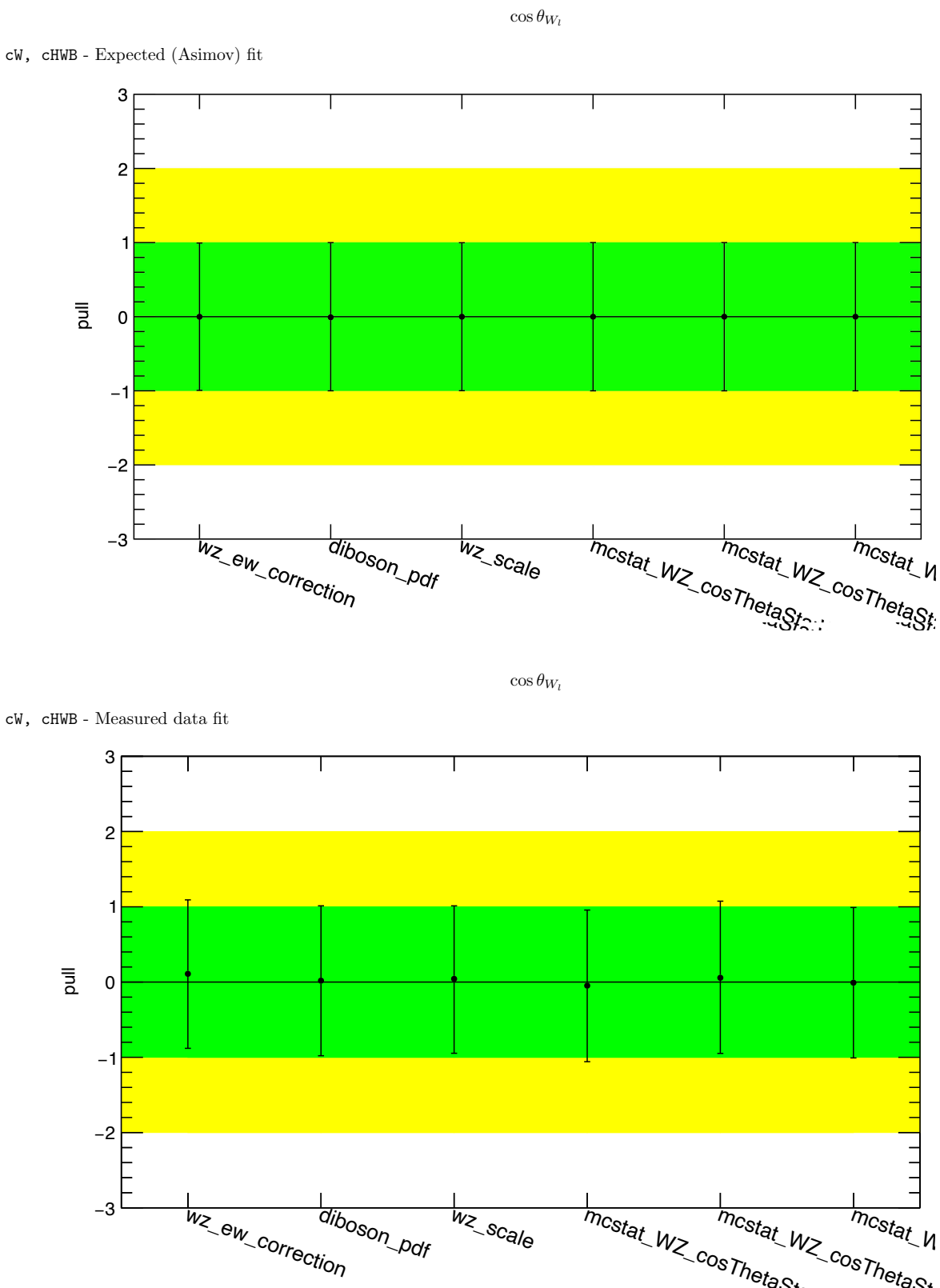

Figure E.8: *Pull plots of 2D fits for* `cW x cHWB` *using the* $\cos\theta^*_{W_\ell}$ *observable. Both Expected pulls (upper panel) and Measured pulls (lower panel) are shown.*

$\cos\theta_{Z_l}$

cHj3, cll1221 - Expected (Asimov) fit

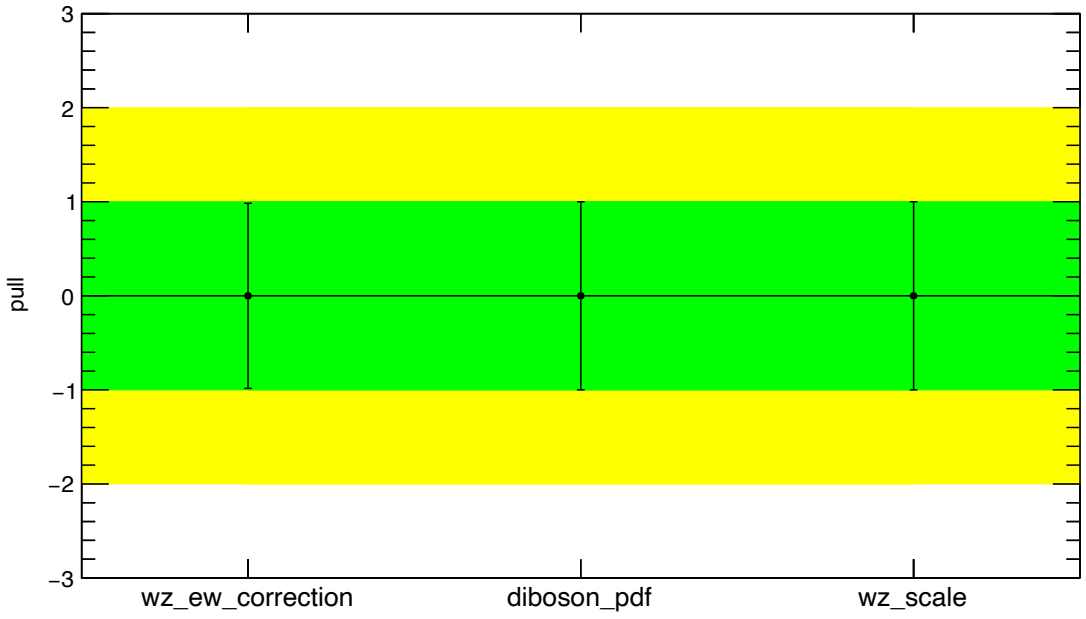

$\cos\theta_{Z_l}$

cHj3, cll1221 - Measured data fit

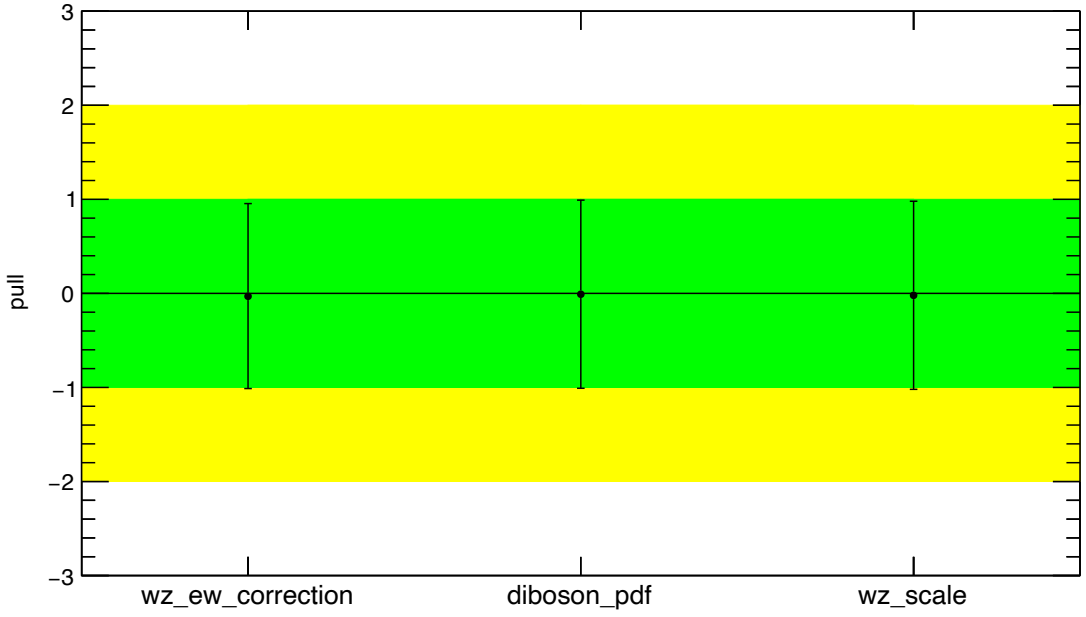

Figure E.9: *Pull plots of 2D fits for* `cHj3 x cll1221` *using the* $\cos\theta^*_{Z_\ell}$ *observable. Both Expected pulls (upper panel) and Measured pulls (lower panel) are shown.*

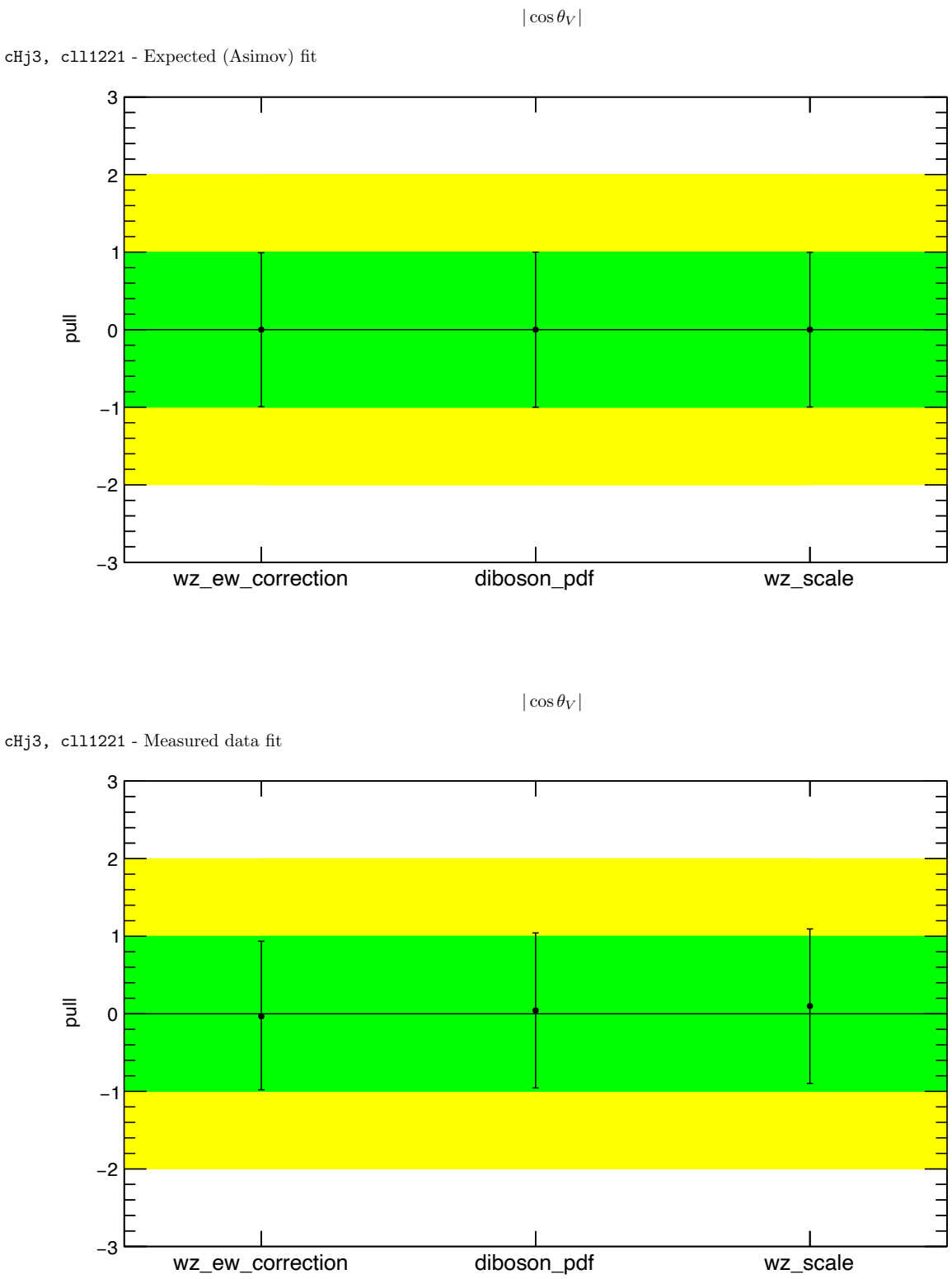

Figure E.10: *Pull plots of 2D fits for* `cHj3 x cll1221` *using the* $|\cos\theta_V|$ *observable. Both Expected pulls (upper panel) and Measured pulls (lower panel) are shown.*

m_T^{WZ}

cW, cHj3 - Expected (Asimov) fit

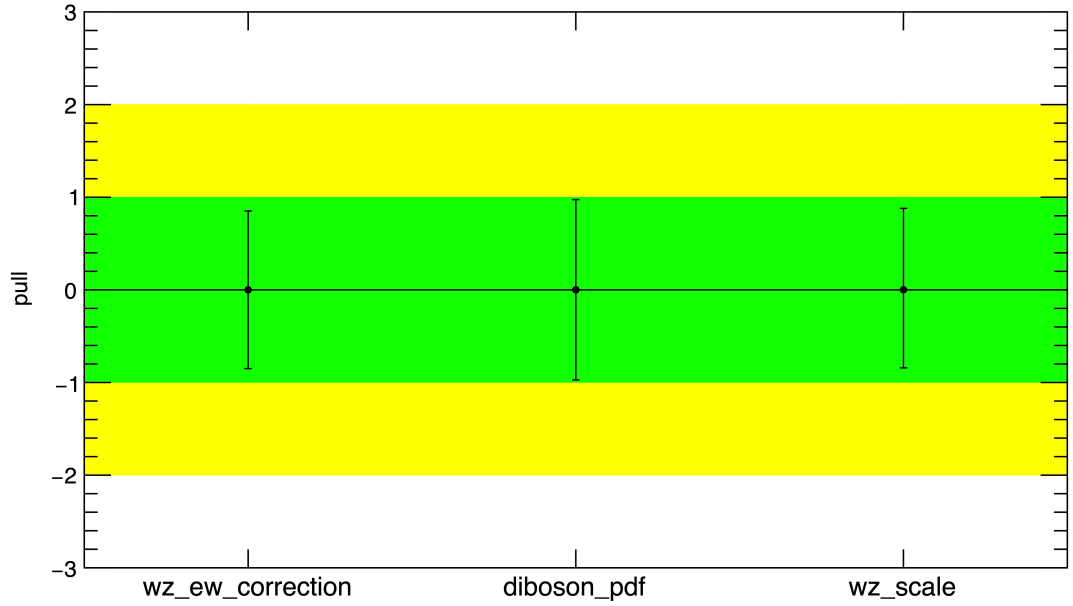

m_T^{WZ}

cW, cHj3 - Measured data fit

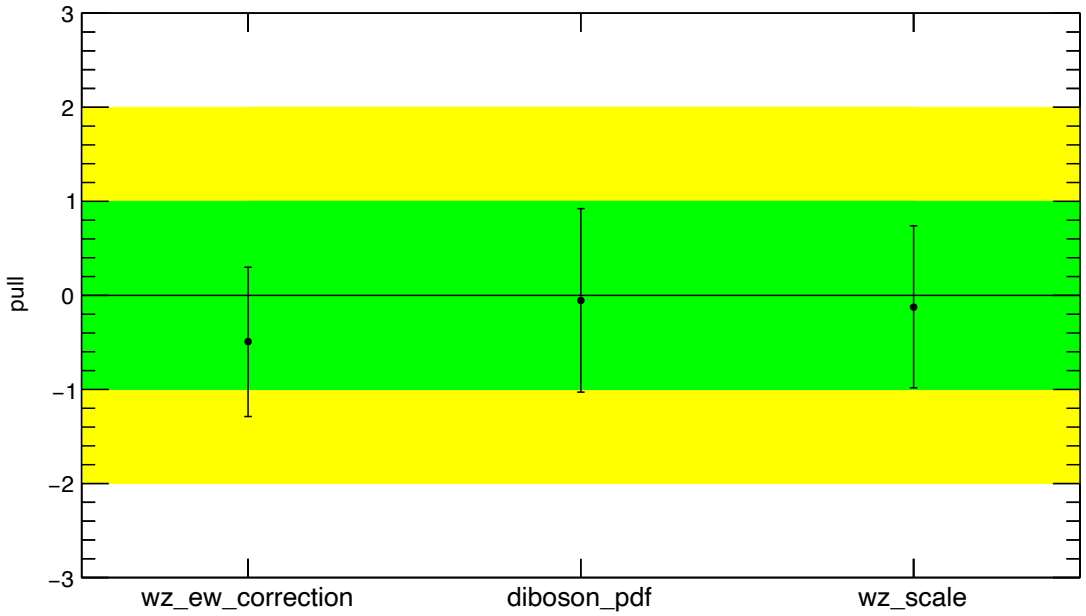

Figure E.11: *Pull plots of 2D fits for* `cW x cHj3` *using the* m_T^{WZ} *observable. Both Expected pulls (upper panel) and Measured pulls (lower panel) are shown.*

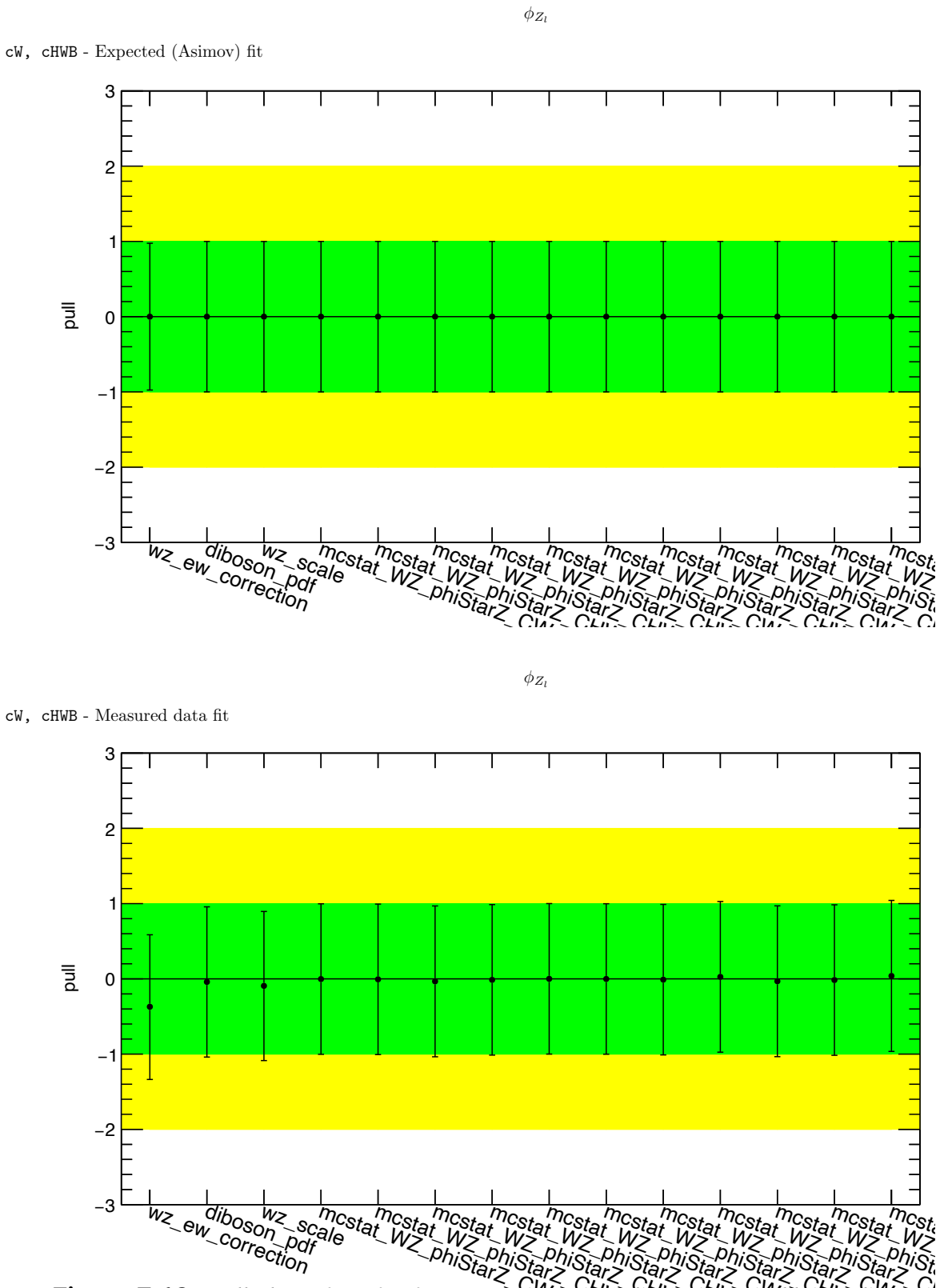

Figure E.12: *Pull plots of 2D fits for* `cW x cHWB` *using the* $\phi^*_{Z_\ell}$ *observable. Both Expected pulls (upper panel) and Measured pulls (lower panel) are shown.*

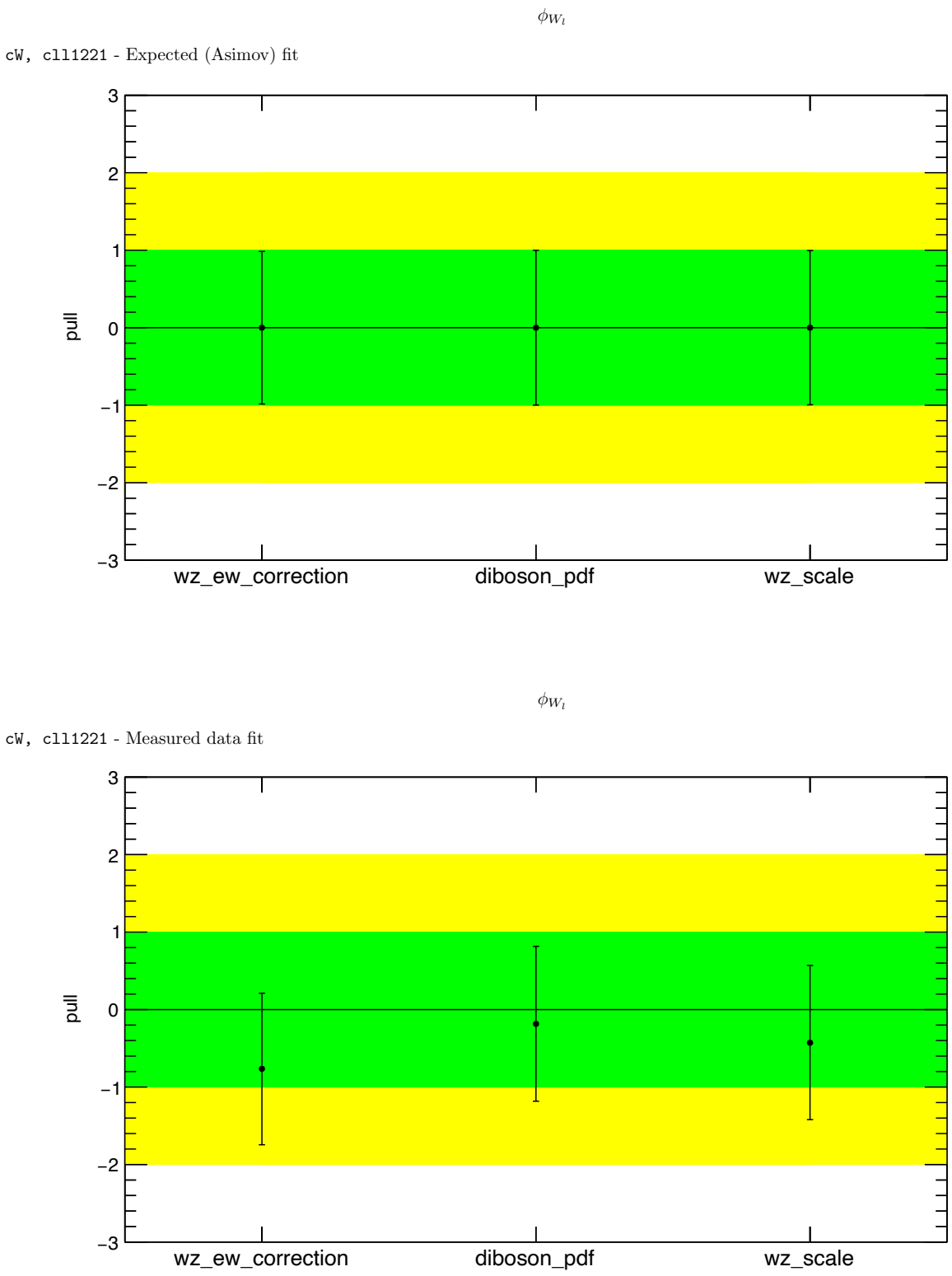

Figure E.13: *Pull plots of 2D fits for* `cW x cll1221` *using the* ϕ_{W_l} *observable. Both Expected pulls (upper panel) and Measured pulls (lower panel) are shown.*

APPENDIX F

Validation of only EFT terms: 0+1j vs SMEFTatNLO

In Chapter 7.4.2, the distributions for each observable of interest were compared for the 0+1j `SMEFTsim 3.0` LO generation to the state-of-the-art `SMEFTatNLO` generation. These comparisons included the SM + EFT prediction for both the generated samples.

EFT predictions alone can also be compared, as presented in this Appendix. Because `SMEFTatNLO` does not use the decomposition method (see Section 6.1.1), the EFT predictions are obtained by subtracting a pure `SMEFTatNLO` SM sample from the `SMEFTatNLO` full production. Through this, a reasonable estimation of how EFT predictions compare between the two models can be made.

The `SMEFTatNLO` data sample is privately generated and therefore statistically limited. The subtraction operation increases the statistical uncertainty in the `SMEFTatNLO` prediction.

The figures compare the differential distributions of the observables of interest for the parameters for `cHDD` (Figure F.1), `cHl111` (Figure F.2), `cHl122` (Figure F.3), `cHl311` (Figure F.4), `cHl322` (Figure F.5), `cHj3` (Figure F.6), `cHWB` (Figure F.7), `cll1221` (Figure F.8), and `cW` (Figure F.9) respectively.

Despite the statistical limitation, it can be noted that both the simulations have significant overlap and agreement in shape for their EFT predictions, despite being generated at different orders in QCD and using different models. This further validates the use of the 0+1j sample for the EFT terms as highlighted in 7.4.2.

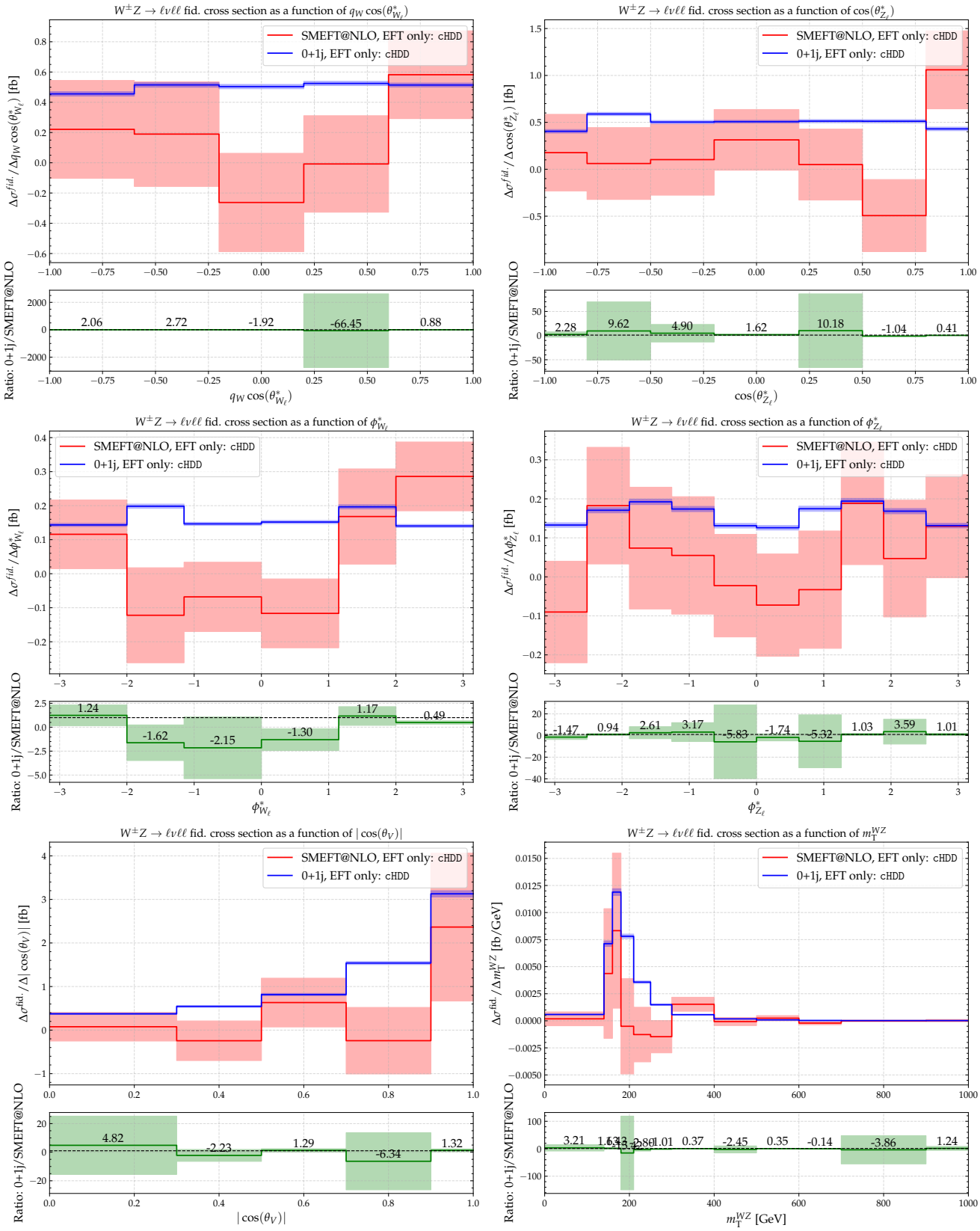

Figure F.1: *Comparison of the differential distributions of the observables of interest for* `SMEFTatNLO` *and 0+1j* `SMEFTsim 3.0` *LO, with* `cHDD=1`*. Only the linear + quadratic EFT contribution is shown. The ratio plot shows a bin-by-bin ratio between* `SMEFTatNLO` *and* `SMEFTsim` *LO. All uncertainty bands are statistical.*

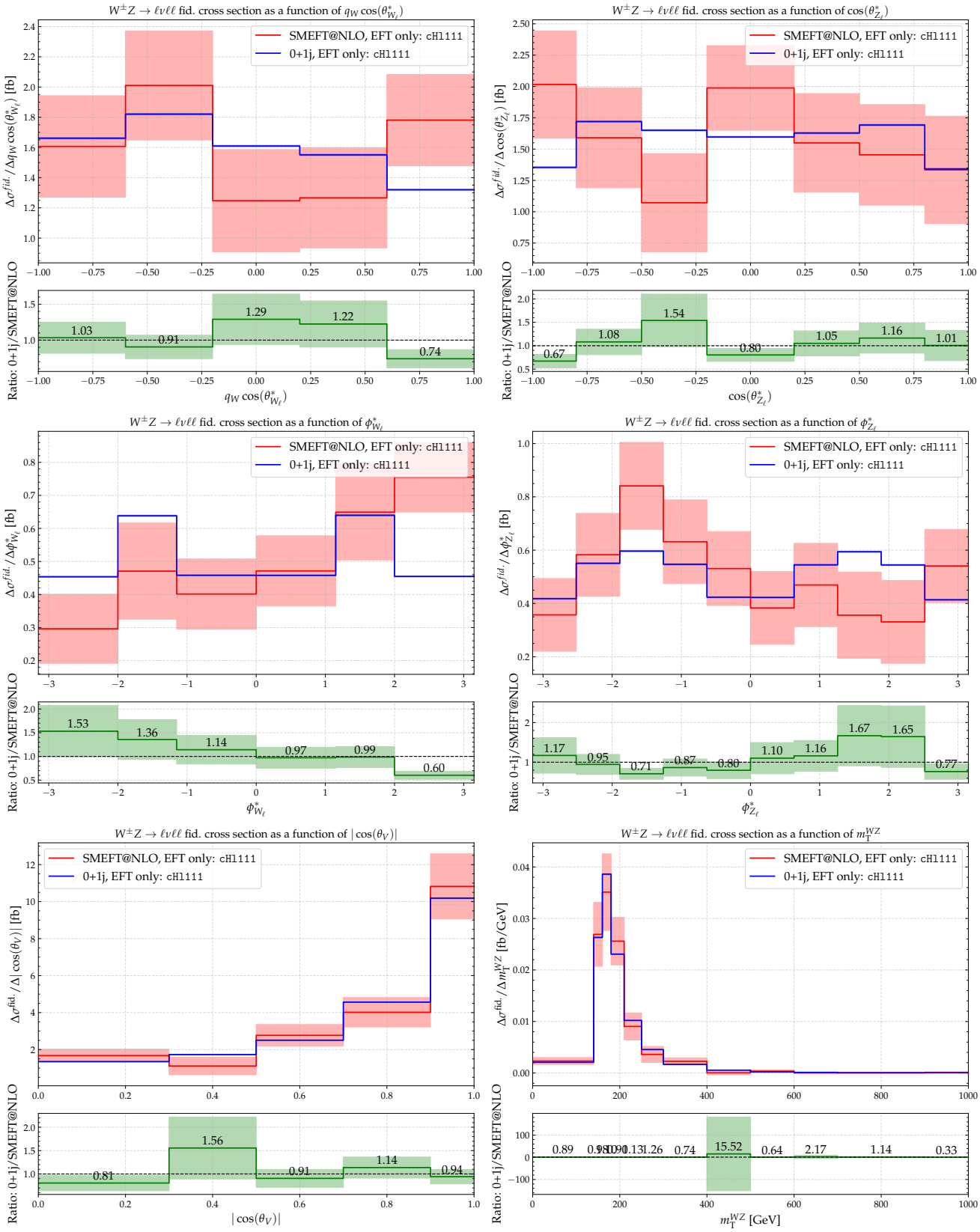

Figure F.2: *Comparison of the differential distributions of the observables of interest for* `SMEFTatNLO` *and 0+1j* `SMEFTsim 3.0` *LO, with* `cHl111=1`*. Only the linear + quadratic EFT contribution is shown. The ratio plot shows a bin-by-bin ratio between* `SMEFTatNLO` *and* `SMEFTsim` *LO. All uncertainty bands are statistical.*

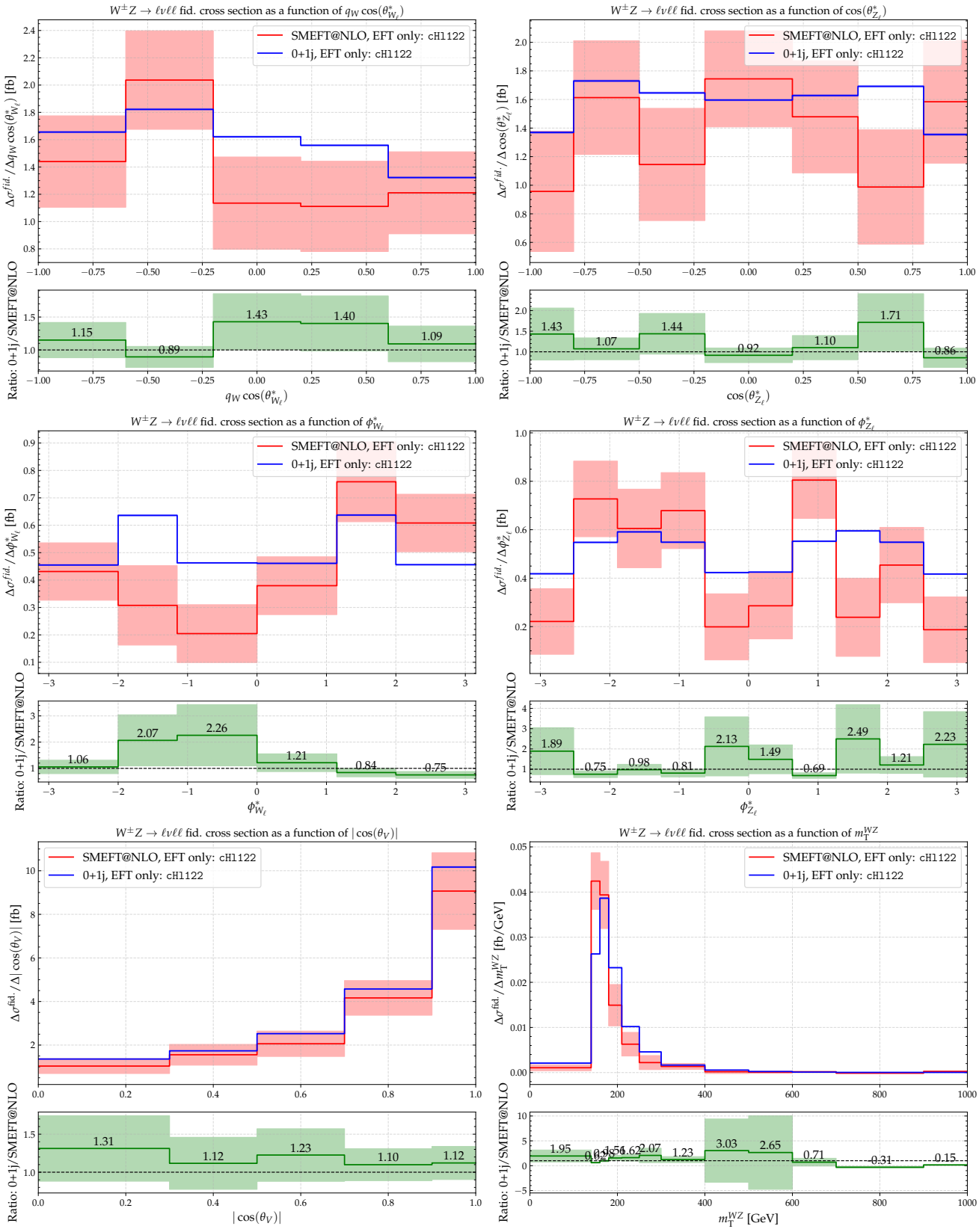

Figure F.3: *Comparison of the differential distributions of the observables of interest for* `SMEFTatNLO` *and 0+1j* `SMEFTsim 3.0` *LO, with* `cHl122=1`*. Only the linear + quadratic EFT contribution is shown. The ratio plot shows a bin-by-bin ratio between* `SMEFTatNLO` *and* `SMEFTsim` *LO. All uncertainty bands are statistical.*

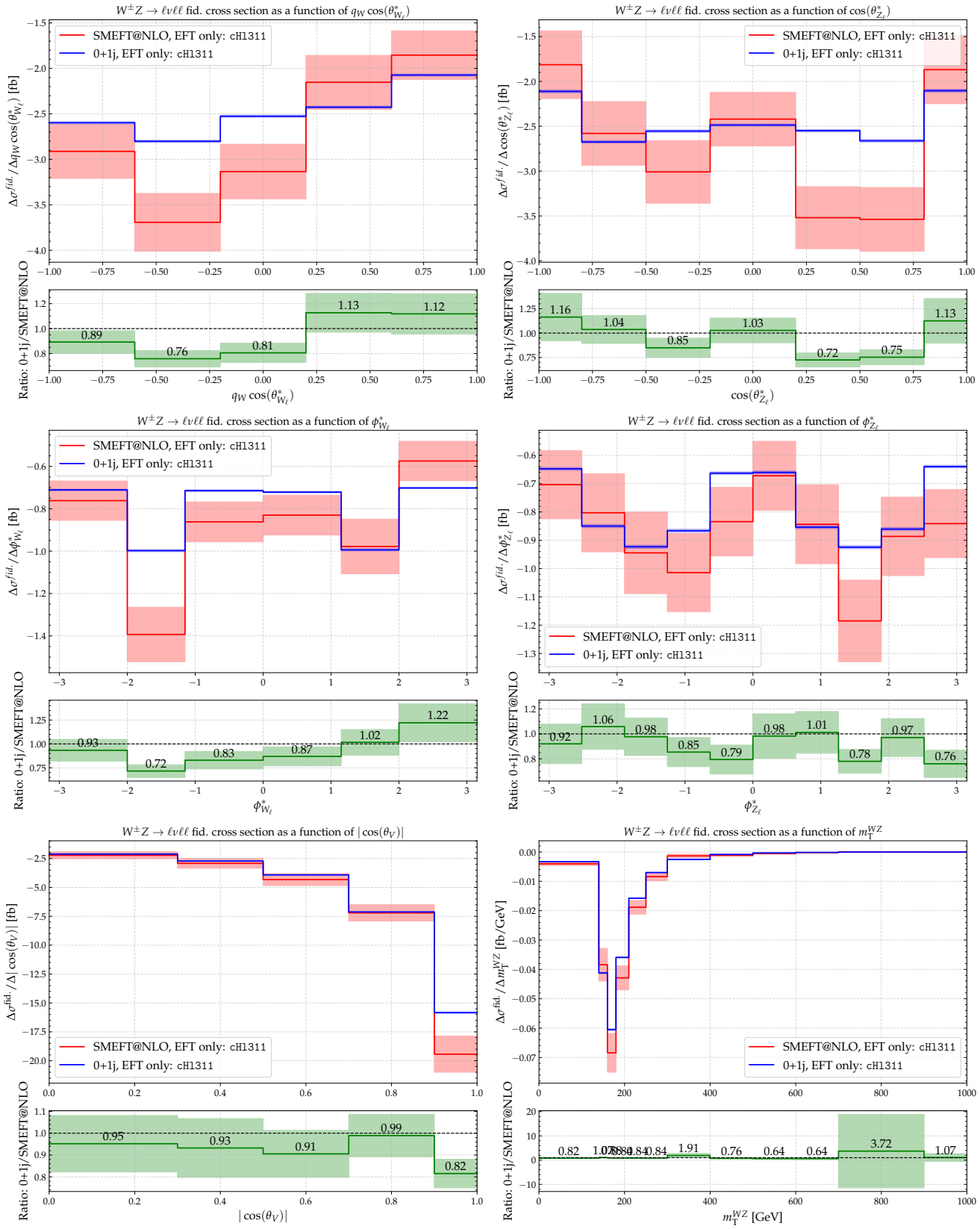

Figure F.4: *Comparison of the differential distributions of the observables of interest for* `SMEFTatNLO` *and 0+1j* `SMEFTsim 3.0` *LO, with* `cHl311=1`*. Only the linear + quadratic EFT contribution is shown. The ratio plot shows a bin-by-bin ratio between* `SMEFTatNLO` *and* `SMEFTsim` *LO. All uncertainty bands are statistical.*

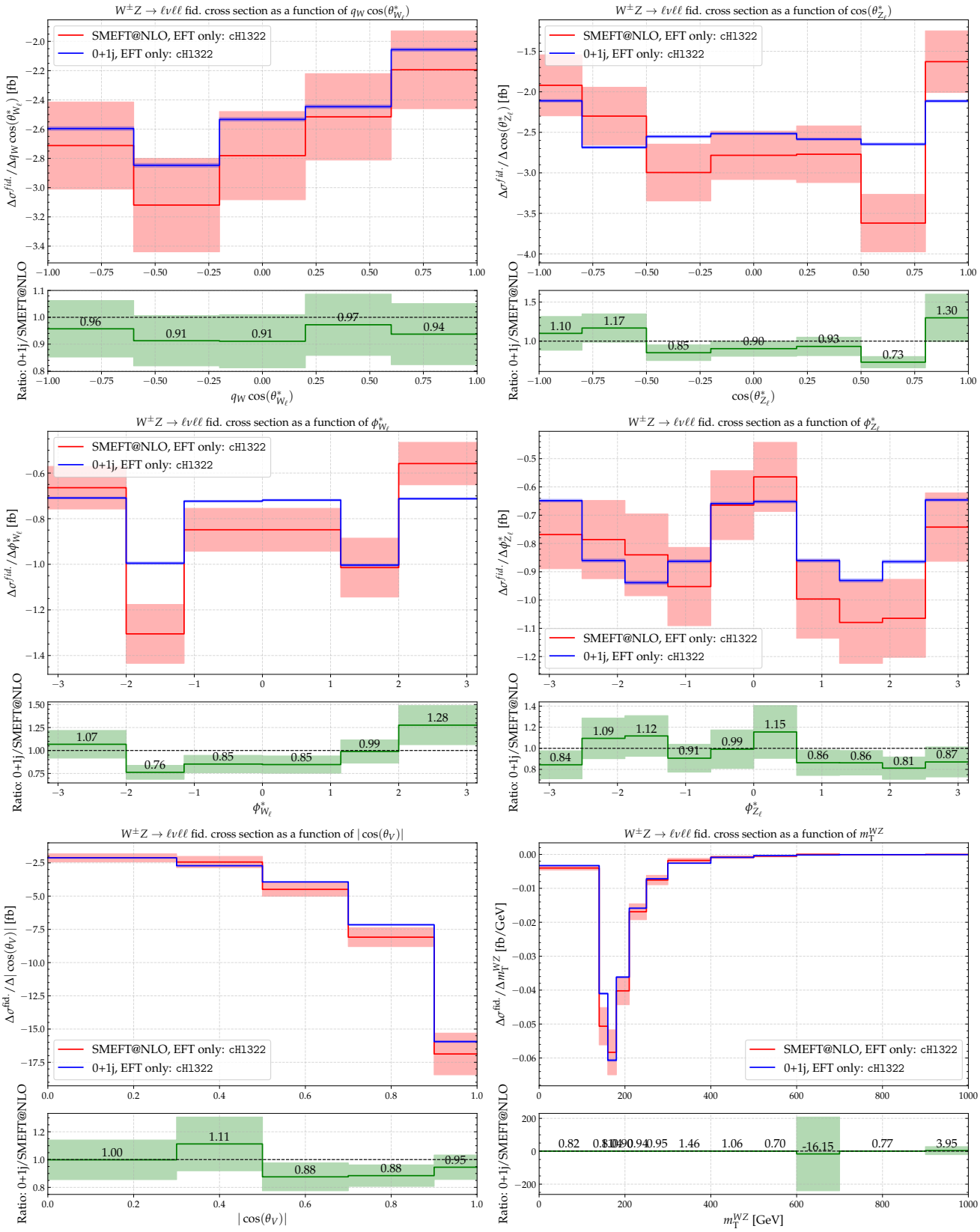

Figure F.5: *Comparison of the differential distributions of the observables of interest for* `SMEFTatNLO` *and 0+1j* `SMEFTsim 3.0` *LO, with* `cHl322=1`*. Only the linear + quadratic EFT contribution is shown. The ratio plot shows a bin-by-bin ratio between* `SMEFTatNLO` *and* `SMEFTsim` *LO. All uncertainty bands are statistical.*

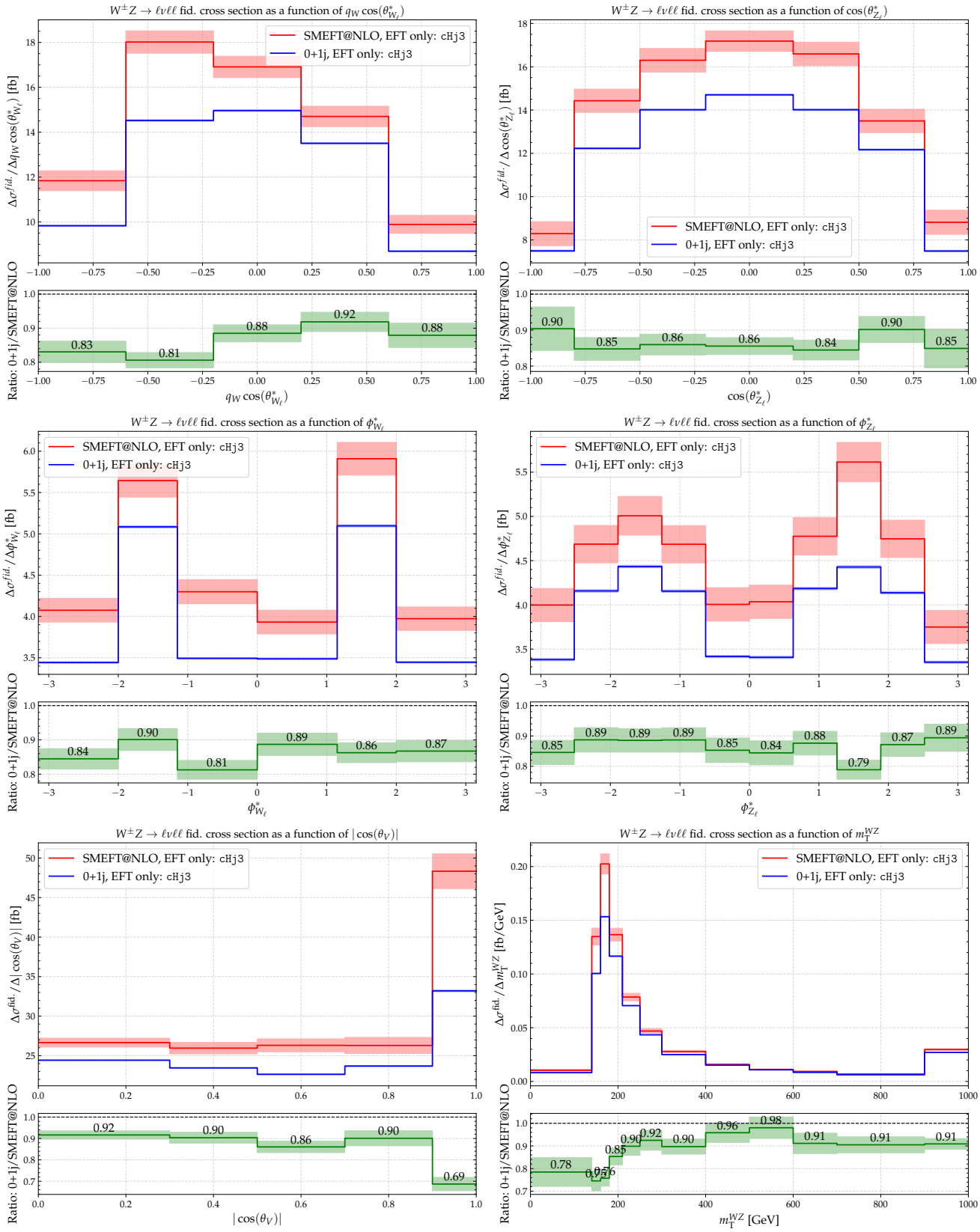

Figure F.6: *Comparison of the differential distributions of the observables of interest for* `SMEFTatNLO` *and 0+1j* `SMEFTsim 3.0` *LO, with* `cHj3=1`*. Only the linear + quadratic EFT contribution is shown. The ratio plot shows a bin-by-bin ratio between* `SMEFTatNLO` *and* `SMEFTsim` *LO. All uncertainty bands are statistical.*

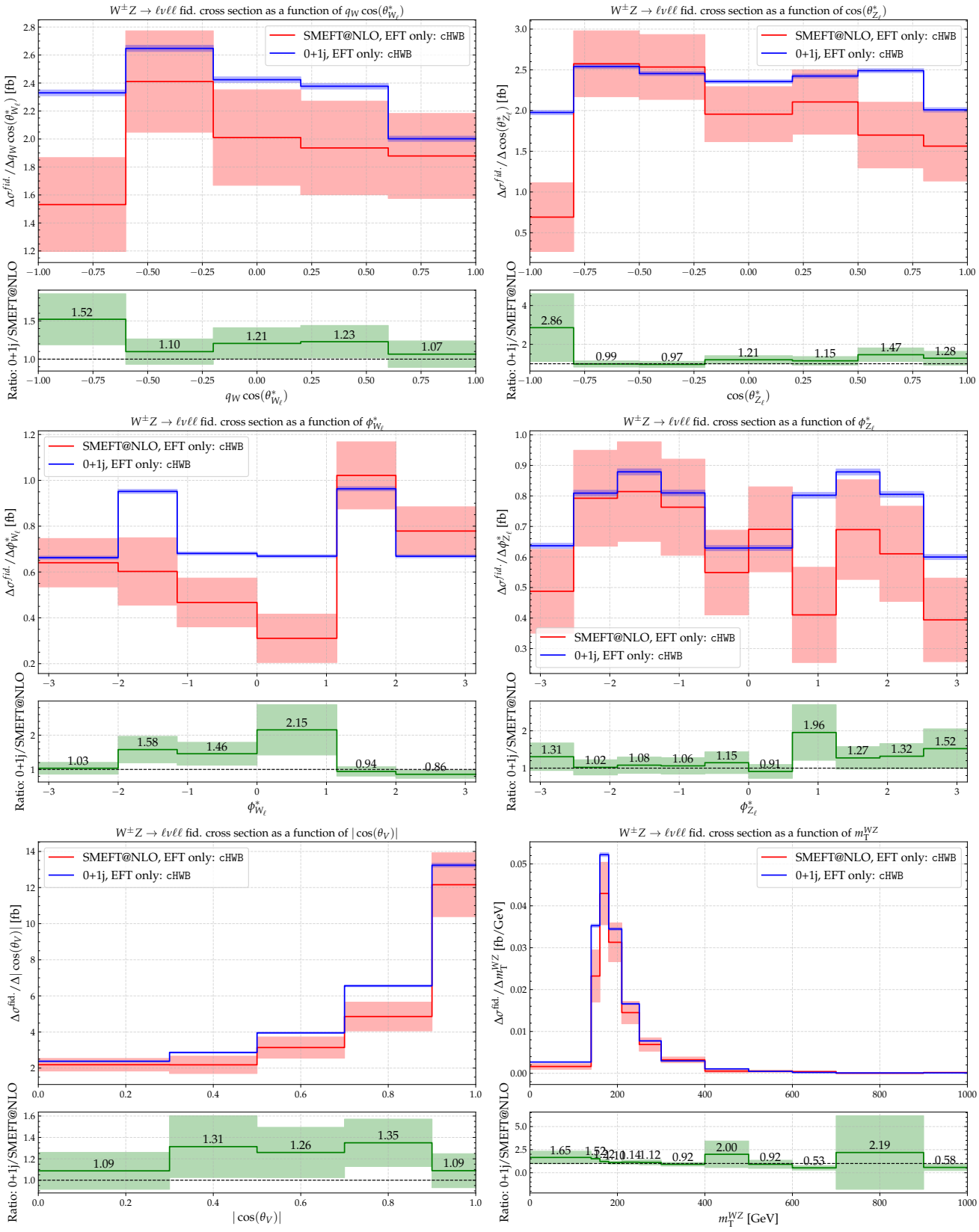

Figure F.7: *Comparison of the differential distributions of the observables of interest for* `SMEFTatNLO` *and 0+1j* `SMEFTsim 3.0` *LO, with* `cHWB=1`*. Only the linear + quadratic EFT contribution is shown. The ratio plot shows a bin-by-bin ratio between* `SMEFTatNLO` *and* `SMEFTsim` *LO. All uncertainty bands are statistical.*

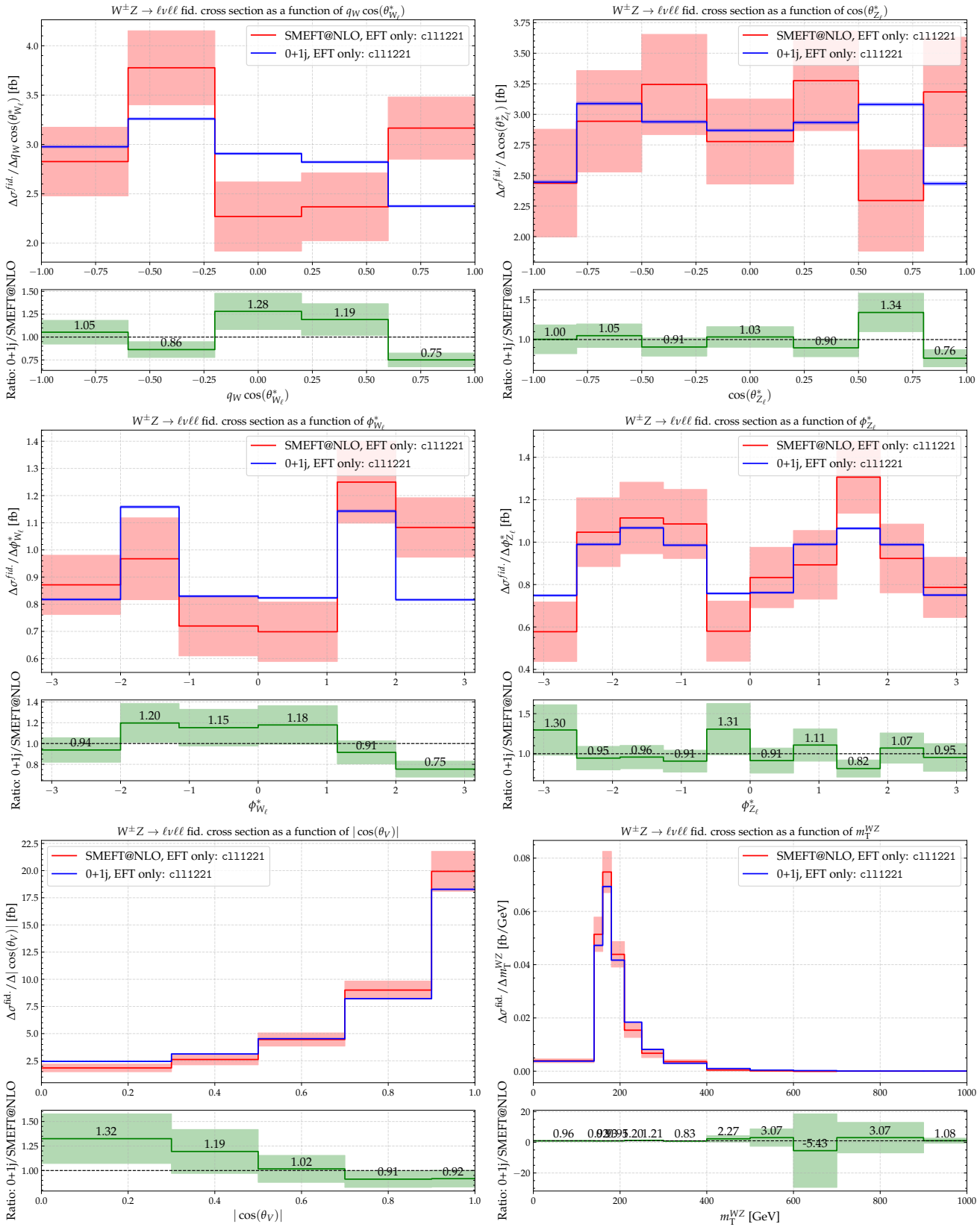

Figure F.8: *Comparison of the differential distributions of the observables of interest for* `SMEFTatNLO` *and 0+1j* `SMEFTsim 3.0` *LO, with* `cll1221=1`*. Only the linear + quadratic EFT contribution is shown. The ratio plot shows a bin-by-bin ratio between* `SMEFTatNLO` *and* `SMEFTsim` *LO. All uncertainty bands are statistical.*

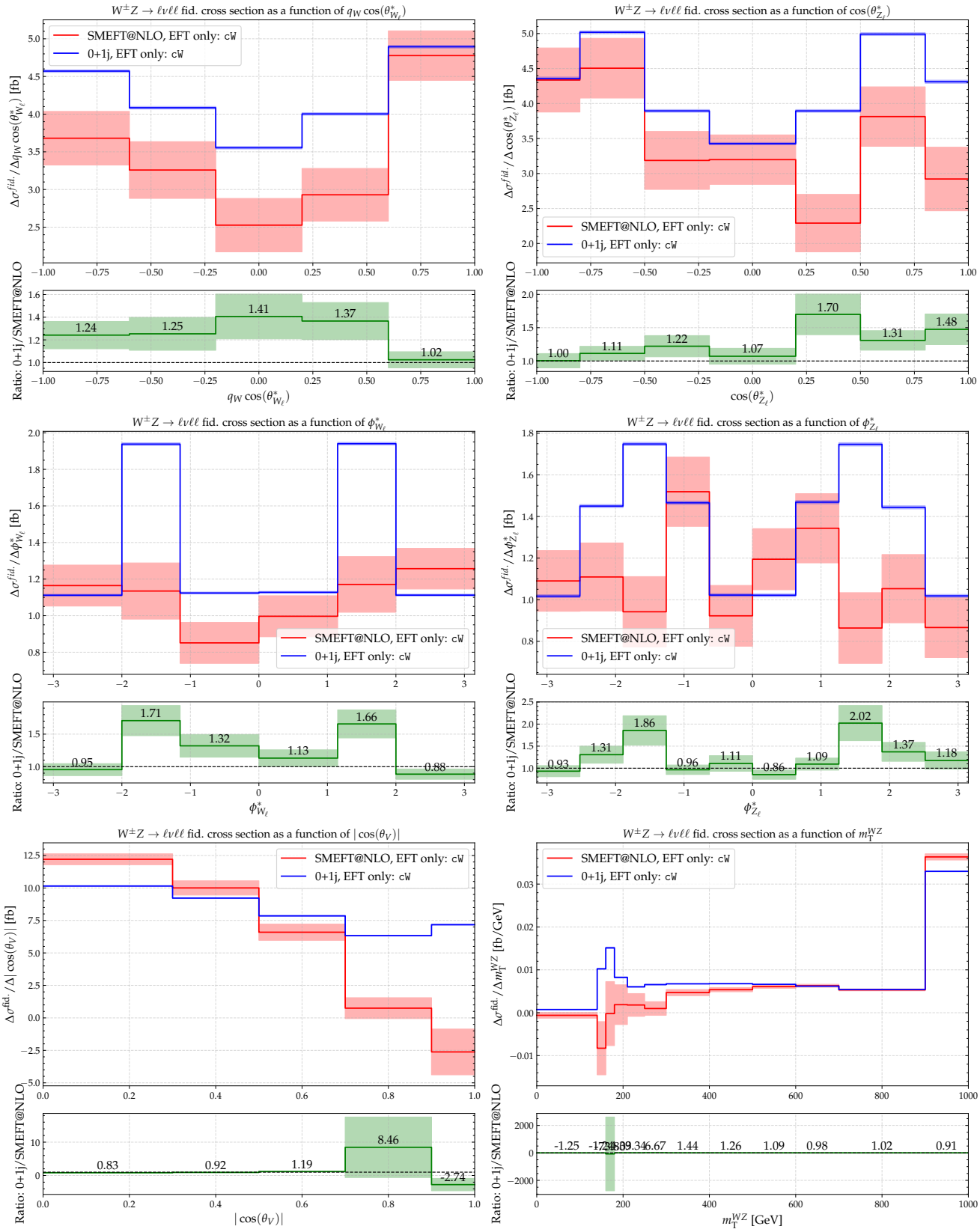

Figure F.9: *Comparison of the differential distributions of the observables of interest for* `SMEFTatNLO` *and 0+1j* `SMEFTsim 3.0` *LO, with* `cW=1`*. Only the linear + quadratic EFT contribution is shown. The ratio plot shows a bin-by-bin ratio between* `SMEFTatNLO` *and* `SMEFTsim` *LO. All uncertainty bands are statistical.*

APPENDIX G

The High-Luminosity LHC and the LAr Upgrade project.

A series of dedicated upgrades is planned to make the transition from LHC to the High Luminosity LHC (HL-LHC) [136]. The HL-LHC is planned to work at $\sqrt{s} = 14$ TeV and a peak luminosity of $L = 7 \times 10^{34}\text{cm}^{-2}\text{s}^{-1}$ (7 times the original LHC design) [136].

The motivation for this upgrade is to study very rare physics processes as well as improve precision measurements, both of which would result in significant scope for new high-energy physics findings.

The increase in luminosity, however, comes at the cost of increased pile-up. The HL-LHC will experience up to 200 overlapping collisions per bunch crossing [136, 137]. In this environment, distinguishing signal from noise becomes significantly more difficult. To address this, the ATLAS trigger and data acquisition system is undergoing substantial upgrades to handle higher data rates and improve event selection capabilities. For example, the Liquid Argon Calorimeter system, which was upgraded in Phase-I to provide higher-granularity inputs to the Level-1 trigger, will be further enhanced in Phase-II to allow full calorimeter data to be digitised and transmitted at 40 MHz. This ensures that detailed calorimeter information can be made available quickly enough to contribute to real-time trigger decisions, as well as for offline analysis.

G.1 LAr Phase-II Upgrade and LASP

The LAr calorimeter cells themselves are not going to be upgraded. The way the information from these cells is relayed and processed is however going to be upgraded [137]. In this respect, the LAr upgrade only affects the readout electronics. Both the On-detector and Off-detector electronics are to be upgraded. Figure G.1 shows a schematic of the LAr electronics after the Phase-II upgrade.

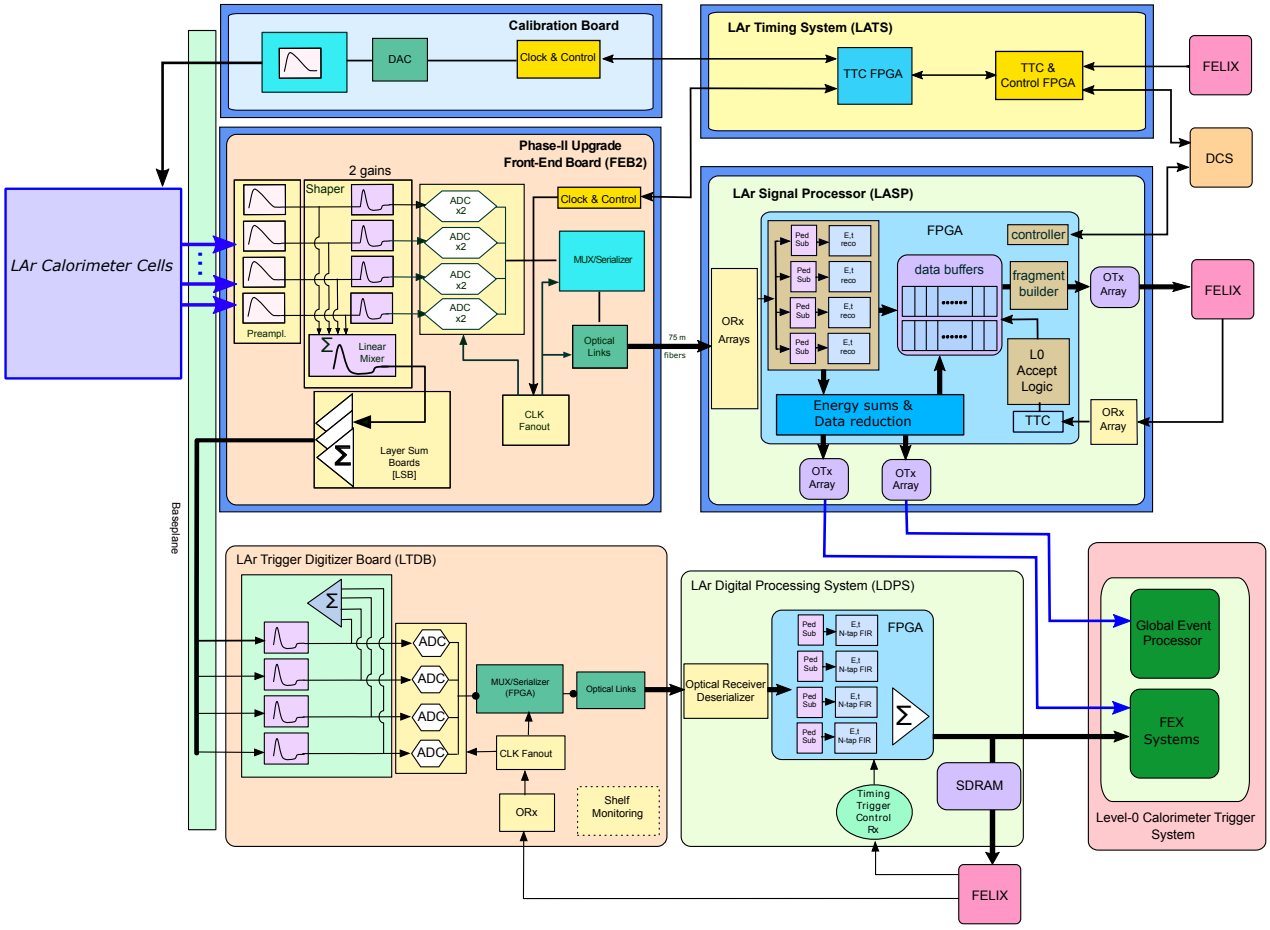

Figure G.1: *Schematic block diagram of the LAr calorimeter readout architecture for the Phase-II upgrade. Diagram taken from [137].*

On-detector electronics

Each FEB2 board reads signals from 128 calorimeter cells, and 1524 boards are needed for the entire LAr system. These signals are received through two connectors, each handling 64 signals.

Signal processing on the FEB2 involves pre-amplification, splitting into two gain scales, and shaping with an ASIC. The shaping time is adjustable to manage increased pileup at the HL-LHC. The processed signals are digitised by 14-bit ADCs for four channels in both gain scales, with a resolution such that the value corresponding to the least significant bit is smaller than the intrinsic noise of a typical LAr cell.

Operating at 40 MHz and synchronised with the LHC clock, the ADCs provide Bunch Crossing Identification (BCID) for synchronisation, resetting counters each orbit. The ADCs output 14-bit signals formatted into 16-bit words with BCID, transmitting serially at 640 Mbps.

Serializer chips then take these outputs and serialize them into a 10.24 Gbps bit-stream using lpGBT chips [138], which support two-way communication with fixed latency and error recovery. Each lpGBT chip has 14 input channels, with a setup where 2 lpGBT chips handle 3 ADC chips, leading to 22 lpGBT chips per FEB2 board.

Finally, the serialised data is converted from electrical to optical signals using Versatile Link+ (VL+) for transmission to off-detector parts.

A new calibration board system is also present which injects a known calorimeter pulse to calibrate the readout electronic chain. Two custom ASICs, one which creates this pulse and another which acts as a 16-bit Digital-to-Analogue converter (DAC), are used for this system.

Off-detector Electronics

The off-detector electronics include a new Liquid Argon Timing system (LATS), which will distribute the Trigger, Timing, and Control (TTC) signals to On-detector electronics.

The other major component of the Off-detector electronics is the Liquid Argon Signal Processor (LASP). The LASP receives data from ADCs from up to 6 FEB2s and applies digital filtering, calculates energy and time for each LHC bunch crossing (40 MHz), and transmits these values to trigger and DAQ.

The LASP units demand high input and output bandwidth along with flexible programming capabilities for data handling, digital filtering, and data reduction algorithms. Since many algorithms will be refined and optimised based on operational knowledge gained once the HL-LHC is running, the LASP is designed with Field Programmable Gate Arrays (FPGAs) as the main processing units. This technology provides the necessary flexibility to reprogram the hardware as needed.

G.2 The Injector Project

The LASP will not receive any input until the Phase II upgrade is fully integrated and completed. This lack of input poses a problem for the development cycle of the LASP, as it prevents verification of the proper functionality of individual LASP modules.

To address this, an Injector project provides FEB2-like data to the LASP, in the lpGBT protocol. From the LASP point-of-view, the data being received is exactly as it would be in HL-LHC operation. This provides an opportunity to test the LASP, and the firmware algorithms as it is being developed.

The Injector project is designed on an Intel Stratix 10 GX FPGA Development kit (devkit)

board, which uses technology similar to that for the LASP. The architecture for the project is broken down into four different sub-modules: data injection, data storage, and data retrieval and data transmission.

The injector employs Gigabit Ethernet (GbE) technology and can communicate with any device on a shared network. User-defined FEB2 formatted data is sent from a computer to the Injector FPGA via the GbE network. Once received, the Injector strips the extraneous Ethernet frame data and stores the ADC data in an external 2 GB memory storage device. Upon filling the 2 GB storage limit, or upon user-trigger, the Injector then retrieves the ADC data, and formats it in an lpGBT payload. This is then sent out of the Injector at the lpGBT speeds of 10.24 Gbps, emulating what a FEB2 would do. Figure G.2 is a schematic of how the project operates. Full details on the Injector project have been described in [139].

The Injector project described in [139] suffered from an extremely slow Ethernet throughput of 2.7 MBps. Improvements were made that allowed the Injector to harness the full potential of the Gigabit Ethernet technology:

- Removal of the NIOS-II system. The GbE IP is now instantiated in logic.
- Removal of TCP/IP protocol to UDP. TCP/IP protocol was implemented in software on a NIOS-II soft core. Removal of the NIOS-II system meant that the TCP/IP protocol was replaced by a UDP protocol, to accommodate a faster throughput, however at the expense of a higher chance of data loss. Since the network systems for the Injector use-case are relatively simple and usually peer-to-peer, data-loss is not an important factor.

The above changes have made the ("new") Injector project achieve Ethernet throughput of ~ 980 Mbps.

The implementation of the Ethernet as done in the Injector was also transferred to the LASP to improve its Ethernet functionality.

Another change to the Injector developed in [139], is that the Injector can now emulate all 3 different FEB2 data link types, which provides a more complete testbench for the LASP. Further, the injector now can send unique data on all channels, replicating real-life FEB2 behaviour.

Software changes to the Injector provide a lot of flexibility to the user in terms of the data they wish to send. The injector implements pre-defined data that can be used for quick sanity checks, as well as custom-defined data that can be used to test a whole variety of edge-cases. The injector software component also allows the user to either automatically send the BCID in the lpGBT payload or manually send one. The latter is helpful in diagnosing cases where the BCID may be incorrectly transmitted to the LASP.

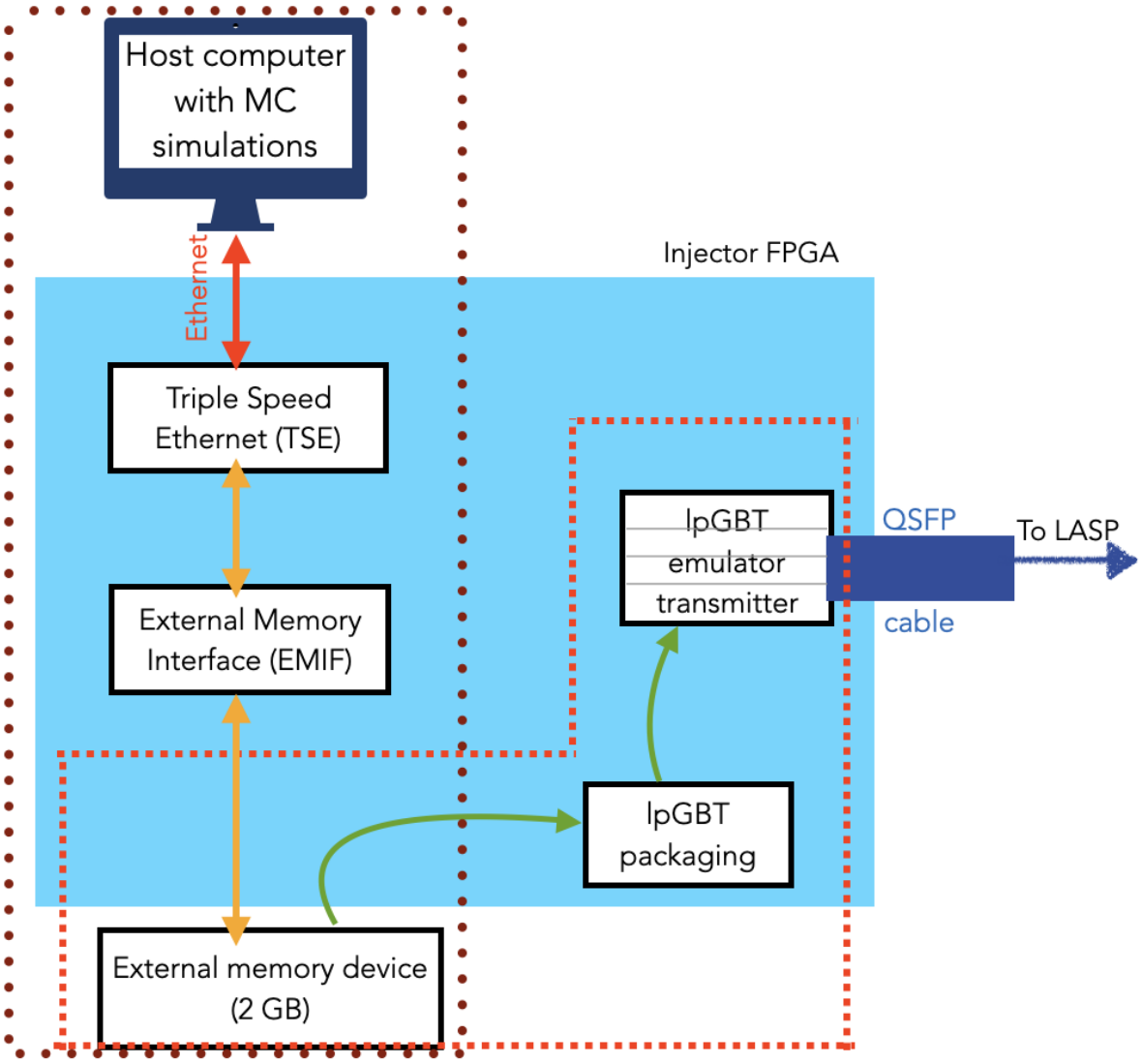

Figure G.2: *Schematic diagram of the Injector project and the flow of data. Block diagrams indicate distinct components in Firmware logic. The maroon dotted border includes the components involved in data injection and data storage, while the red dotted border includes the components for data retrieval and transmission*

G.3 Integration efforts at CERN

The LHC program foresees Run-3 to end in mid 2026, which will then be followed by the Long Shutdown 3 (LS3), from 2026-2028. During LS3, the detector will be upgraded to accommodate the HL-LHC environment. HL-LHC is planned to start data-taking in 2030.

Many of the components required for the LAr upgrade are designed, manufactured and tested in different laboratories worldwide. The LAr collaboration has created a facility test bench where

Electronic prototypes of different components are made to communicate and interface with each other, as they would in HL-LHC, to assist in the final integration process.

Integration efforts at the Electronics Maintenance Facility (EMF) at Point 1 at CERN have started.

To begin, two development kits with an Intel Stratix 10 FPGA were assembled at CERN to test the optical transmission from one FPGA to another at the lpGBT speeds. One FPGA was programmed with the injector and the other was programmed with the developmental LASP firmware. The injector transmitted data on 4 channels, which was then extended to 6 channels using a custom-made plug-in board. Figure G.3 illustrates this.

Figure G.3: *2 Intel Stratix 10 FPGA development kits connected together via fiber optic cables. One devkit acts as an Injector of FEB2 data while the other acts as a LASP.*

The LASP prototype was then also made available, which enabled testing and programming firmware directly on the board. The LASP prototype board contains 3 FPGAs: 1 Intel Stratix 10 SX FPGA, 1 Intel Stratix 10 MX FPGA and 1 Intel MAX 10 FPGA. The first 2 FPGAs are similar except for an increased memory storage capacity in the MX. They were used to see which would be a better choice for the LASP. The Intel MAX 10 FPGA is used for board control and monitoring. Figure G.4 shows the structure of the very dense LASP prototype board, with a few of its key components highlighted. Testing and validation of major components on the LASP board was also done at the EMF.

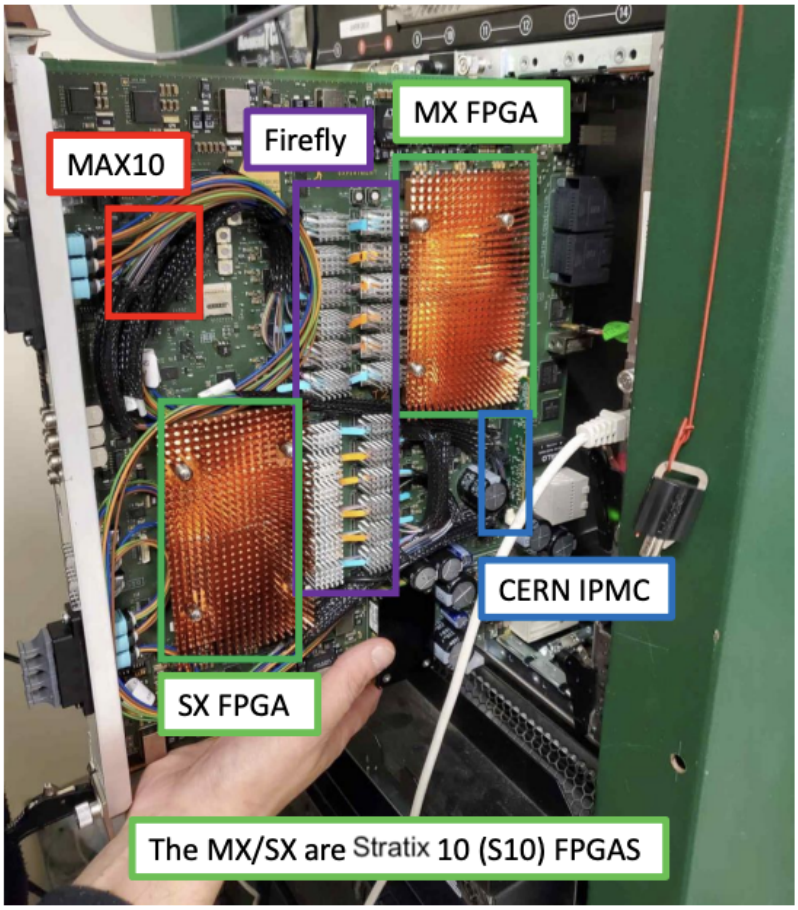

Figure G.4: *The LASP prototype board at the EMF, showing the Stratix 10 FPGAs as well as the MAX 10 FPGA for board control. Fireflies are the high-speed optical transceivers used for data communication to and from the board. The CERN IPMC is a custom card that allows for the communication of critical data with the outside world. The board is being plugged into an ATCA-type crate, where it is continuously cooled.*

A big advantage to the setup at CERN was the presence of a dedicated TTC (Trigger, Timing, and Control) signal, which is missing in the laboratories where components are manufactured. The TTC plays a key role as it is the signal that is synchronised with the LHC clock. All corresponding downstream electronic entities that are synchronous to the LHC clock rely on this signal. One such entity is the LASP. For LAr, the LATS board will receive the LHC signal and transmit the TTC to the LASP and the FEB2. This ensures that both the On-detector and Off-detector components are operating synchronously with each other.

At the EMF, a dedicated TTC signal is obtained and transferred via a FELIX to the LASP board and the Injector (mimicking FEB2). The FELIX also acts as a Data Acquisition (DAQ) machine, which can receive data after it is processed in the LASP.

Due to the availability of several FELIXs, a rigorous test was made to see if the LASP can

correctly function if provided a different TTC stream than that provided to the Injector. In this case, both the Injector and the LASP must recover the LHC clock from the TTC stream, and derive a clock synchronous to the recovered LHC clock for their operation. Such functionality is developed for both the Injector and the LASP firmware. Reduced firmware on the LASP has also been developed such that it could decode the data from an incoming lpGBT frame, and transmit it to another FELIX which acts as a DAQ. The full schema is shown in Figure G.5.

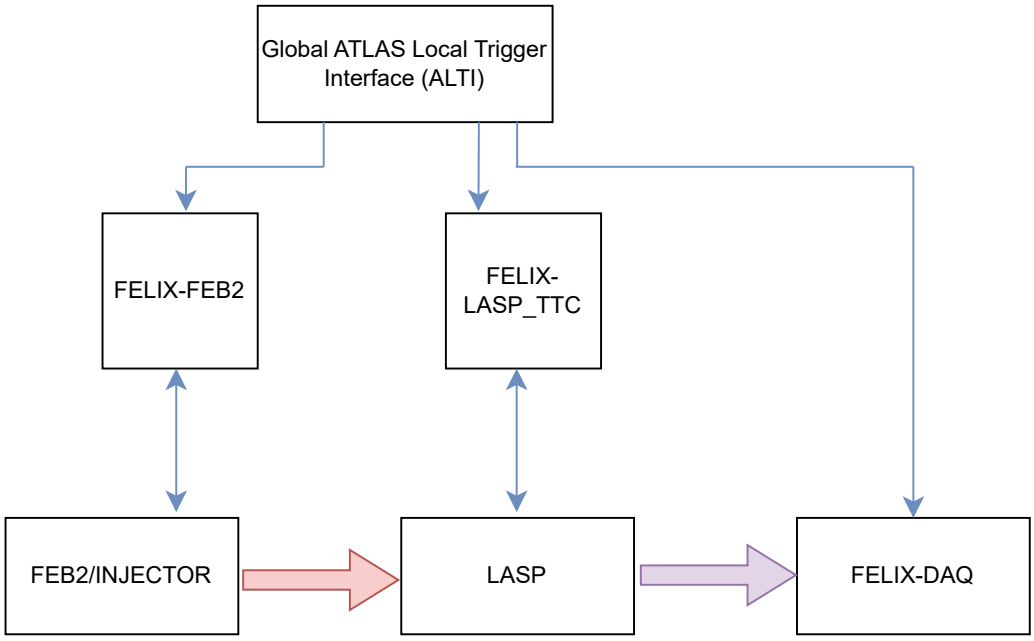

Figure G.5: *Schematic diagram showing the integration of different components at the EMF. Data being sent from the FEB2/Injector is then received and manipulated in the LASP, after which the useful ADC data is sent to the DAQ. All the FELIX receive a central global TTC signal. The FEB2/Injector and the LASP derive its clock from this TTC signal.*

The full plan illustrated in Figure G.5 was successfully executed in the EMF at CERN [140]. Custom data sent to the Injector was verified to exactly match the output of the LASP at the FELIX-DAQ, thus providing a full pathway demonstration with the components that had currently been manufactured. The system breaks down upon cutting one TTC pathway, as expected, proving that all the clocks are centrally connected.

The EMF has since acquired a prototype version of the FEB2 as well as a prototype version of the LATS. The FEB2 replaces the need for the Injector and the LATS replaces the need for the TTC transmitting FELIXs. The Injector still plays a critical role in providing custom data to the LASP and the possibility to test for various edge cases as this functionality is limited in the FEB2.